The rise of black shale giants: case studies on the Exshaw Shale and Bowland Shale

Sen Li

Submitted in accordance with the requirements of the degree of Doctor of Philosophy

The University of Leeds

School of Earth and Environment

Earth Surface Science Institute

June 2023

The candidate confirms that the work submitted is his own, except where work which has formed part of jointly authored publications has been included. The contribution of the candidate and the other authors to this work has been explicitly indicated below. The candidate confirms that appropriate credit has been given within the thesis where reference has been made to the work of others.

Contributions of the candidate and the other authors:

In all chapters the candidate (Sen Li) was the primary data gatherer and processor. All chapters were primarily written by the candidate with comments and suggested edits to the manuscripts provided by P.B. Wignall (all chapters), S. Poulton (Chapter 2 and 3) and J. Peakall (Chapter 4). Contribution to sample collection for Chapter 2 was provided by P.B Wignall. Fieldwork in Bowland Basin study in Chapter 3 and 4 was assisted by Professor Jeffrey Peakall, Dr. Kaixuan Ji, Yuxuan Wang, Dr. Yafang Song, Dr. Zhen Xu and Dr. Jed Atkinson. Minor lab work is also contributed by Dr. Tianchen He and Dr Yijun Xiong in Chapter 2 and 3.

Acknowledgements

Most importantly, my deepest gratitude goes to my supervisor Professor Paul Wignall whose guidance in the office and demonstration in the fieldwork are the invaluable experience in my academic life. I am touched by his enthusiasm in geology which is inseparable in his life. I still cannot imagine how I got through the lockdown during 2020. Staying at home and most of time in a room make me feel lost. But Paul's message, online meeting kept me on track. I am so grateful that every time Paul drove his grey car and took me to the field in 2020, 2021 and 2022. I always felt quite tired and fall asleep on the way back, but Paul still returned me home safely. It is my privilege to have you as my PhD supervisor.

Professor Simon Poulton is completely different supervisor who bring me not only the most professional insight on Fe, P cycle and redox analysis but also great fun in my spare time. There are hundreds of pictures in my smart phone showing the fun we had in bars and delicious cuisine in restaurants. I will long remember those nights playing snooker and karaoke. Also Dr. Yijun Xiong, my best friend who is also my aqueous geochemistry demonstrator in the lab. I was a freshman in lab in the first year, and it is him who trains me to have good command of every equipment in the lab. I could not have obtained such a high-quality data without his help. In addition, he is also a good housemate who teach me how to cook and enjoy Leeds.

For technical help, Harri Wyn Williams must be mentioned as he polished hundreds of nice thin sections for me. In the Cohen Lab, thanks also go to Andy Hobson for his countless notice to remind me how to perform lab work safely and Stephen Reid for the professional ICP analysis and AAS demonstration.

There are lots of friends including PGR students Yuxuan Wang, Chong he, Chiara Krewer, Yafang Song, visitors such as Yinggang Zhang, Aiguo Dong, Yang Liu, Zidong Peng, Zhihui An, Hailin Yang, Zhen Xu, Wei shi, He Zhao and Jingwei Cui as well as postdocs Tianchen He and Heping Wu. Thank you all for your accompany in Leeds and making my daily life colourful.

Finally, I also thanks my parents for providing unconditional financial support and my wife Han Liu who faced lonely and challenging work in Beijing that I cannot imagine. I owe you a lot and wish I can pay back in the rest of my life.

Abstract

The thickest developments of black shales are often found overlying shallow-water limestone, and mark fundamental changes in depositional environment. This is the case in the Carboniferous successions of the British Isles where thick black shale reserves belonging to the mid-Carboniferous Bowland Shale formations sit on Lower Carboniferous slope and platform carbonates. A similar transition is seen around the Devonian-Carboniferous boundary in western Canada where the Exshaw Shale overlies ramp carbonates. Intriguingly phosphate nodule beds often occur at this latter transition.

Comprehensive petrology and geochemical study of Jura Creek, a classic section in Western Canada Sedimentary Basin in western Laurentia shows that the onset of black shale deposition was preceded by intense pyritization of the topmost limestone suggesting deoxygenation began before shale deposition. The succeeding thin phosphate-rich bed was likely produced by internal wave action at a density interface within the water column. Following onset of black shale deposition in the lower Exshaw Shale Formation there was considerable redox variation. Elevation in Fe_{HR}/Fe_{T}, Fe_{py}/Fe_{HR}, pronounced enrichment in trace metals (Mo, U, V and Re) combined with tiny framboid populations indicate euxinia. This was followed by a transition to a ferruginous water column as confirmed by moderate enrichment in trace metals, but low Fe_{py}/Fe_{HR} and remarkably no framboidal pyrite. In addition, Mo-U covariation also suggests a preferential enrichment in Mo which could be associated with particulate shuttle (Fe cycle in ferruginous conditions). The Devonian-Carboniferous boundary saw the return of better ventilated conditions in the Exshaw Shale marked by a decrease in trace metal content and loss of syngenetic pyrite. The level of the Hangenberg Crisis at Jura Creek coincides with the improved ventilation, from euxinic to ferruginous conditions, a distinct contrast from European sections where anoxia intensifies at this level.

The Bowland Shale of the mid-Carboniferous Bowland Basin of northern England has been examined in 16 sections ranging from basin centre to basin margin sites. Based on calibrated redox threshold, it is found that the basin experienced a broad range of redox conditions from oxic, ferruginous, weakly euxinic ultimately to highly euxinic conditions. Initial deoxygenation in the Lower Bowland Shale (ferruginous and euxinic conditions) showed considerable local variation whilst carbonate productivity on adjacent platforms was maintained with the result that substantial volumes of carbonate detritus was supplied to the basin resulting in discrete calciturbidite fans composed of calcarenite and a substantial component of fine calcisilt in the interbedded shales. Much of this material was likely sourced from the Central Lancashire High (CLH), a small carbonate platform to the SE of the basin. The much more extensive platform on the Askrigg Block to the north of the Basin sourced little material probably because depositional dip was to the north. A major phase of onlap, associated with a transition from syn to post-rift conditions, saw black shales of the Upper Bowland Shale overlie the CLH carbonate platform. The extensive Upper Bowland Shales record intense euxinia indicated by presence of abundant tiny framboids, elevated enrichment in Mo ($Mo_{EF} > 40$), low ratio in U/Mo as well as $Fe_{py}/Fe_{HR} > 0.6$. The petrography of this euxinic facies is dominated by clay lenses (up to 0.4 mm in length) with organic filaments and pelagic components (syngenetic framboids, planktonic larval shells) and further clay in the interstitial sediment. Most recent studies have interpreted such clay lenses to be intraclasts transported as bedload or in low concentration sediment gravity

flows, but it is proposed that hemipelagic depositional processes dominate, as is likely the case for most organic-rich shales formed in euxinic conditions. The clay lenses are interpreted to be faecal pellets formed above the redoxcline before settling to the seabed.

By comparing the study of Exshaw Shale and Bowland Shale, it is found that the relationship between shallow-water carbonate demise and black shale deposition is complex. The basin morphology (whether it is a ramp or platform) is likely an important factor in controlling the timing of carbonate shutdown. Specifically, it is contended that a euxinic water body can more readily "poison" the lower reaches of a carbonate ramp than in a fault-bounded basin where water circulation is constrained. Only when the highly euxinic water body spills across a basin margin, perhaps due to basin margin collapse, can it shutdown carbonate production.

Insight from the Bowland Shale study enables a new model to be postulated that shows that input of warm saline bottom water provides an option to create an ideal environment for black shale deposition. Especially if the basins are surrounded by carbonate platform where potential reasons (e.g. elevated productivity, fresh water input) for black shale deposition cannot be adopted. However, it is ironic that the hydrogen sulphide produced by these strongly stratified and poorly circulated basinal waters may compromise the carbonate production on the platform in return. Furthermore the demise of carbonate production is destined in a basin-block setting.

Table of contents

Acknowledgments .... **V**

Abstract .... **Vii**

Table of contents .... **iX**

Appendices .... **Xii**

List of tables .... **XiV**

List of figures .... **XV**

Abbreviation .... **XXiV**

Chapter 1: Introduction **1**

- 1.1 Aims of the project 1
- 1.2 Rational for the project 2
- 1.3 Black shale formation 2
- 1.4 Black shale deposition model 4
- 1.5 Fine-grained sedimentary rock depositional process 6
- 1.6 Factors controlling carbonate production 8
  - 1.6.1 Tectonic subsidence 9
  - 1.6.2 Sea level variation 10
  - 1.6.3 Temperature variation 10
  - 1.6.4 Excess nutrients 11
  - 1.6.5 Salinity fluctuation 12
  - 1.6.6 Ocean acidification 13
  - 1.6.7 Anoxia 13
  - 1.6.8 Terrigenous input 14
- 1.7 Thesis outline 15
- References 16

Chapter 2: Carbonate shutdown, phosphogenesis and the variable style of marine anoxia in the late Famennian (Late Devonian) in western Laurentia **24**

- 2.1 Abstract 25
- 2.2 Introduction 26
- 2.3 Regional geology 30
- 2.4 Methods 32

2.4.1 Sample preparation and optical microscopy 33
2.4.2 Major elements 33
2.4.3 Fe phase partitioning 34
2.4.4 Framework for redox interpretations 36
2.5 Results 39
2.5.1 Lithofacies 39
2.5.2 Pyrite petrography 45
2.5.3 Geochemical proxies 49
2.6 Discussion 53
2.6.1 Depositional Conditions 53
2.6.2 Models for carbonate shutdown 61
2.6.3 Comparative latest Devonian redox history in other North American basins. 62
2.7 Conclusions 63
References 65
Chapter 3: Calibration of redox thresholds in black shale: Insight from a stratified Mississippian basin with warm saline bottom waters 73
3.1 Abstract 74
3.2 Introduction 75
3.3 Regional Setting 76
3.4 Methods and Approach 80
3.4.1 Sample collection and field area 80
3.4.2 Major elements 82
3.4.3 Fe phase partitioning 82
3.4.4 Framework for redox interpretation 83
3.5 Results 86
3.5.1 TOC variability 86
3.5.2 Total Fe and Fe phase partitioning 94
3.5.3 Mo and U systematics 99
3.5.4 Pyrite petrography 102
3.6 Discussion 103

3.6.1 Redox proxy threshold calibrations 103
3.6.2 Evolving redox trends during Bowland Basin development 108
3.6.3 Controls on oxygenation in the Bowland Basin 114
3.7 Conclusions 122
References 124
Chapter 4: Contrasting sediment sources and depositional processes in a black shale basin: the Mississippian Bowland Basin of northern England 132
4.1 Abstract 133
4.2 Introduction 134
4.3 Regional History 136
4.4 Methods and Approach 141
4.5 Results 141
4.5.1 Regional development of Bowland Shales 141
4.5.2 Carbonate Lithofacies (CLF) 150
4.5.3 Clastic Sandstones Lithofacies (CSF) 157
4.5.4 Mudrock Lithofacies 159
4.6 Discussion 164
4.6.1 Carbonate depositional processes and platform resilience 164
4.6.2 Clastic depositional process and sediment source 168
4.6.3 Eustatic influence? 171
4.7 Conclusions 173
Reference 174
Chapter 5 Conclusion and future work 181
5.1 Conclusion 184
5.2 Future work 188
Reference 190

Appendices

Appendix A: Field locations in Bowland Basin and on Craven Fault Belt. Locations are given with six figure national grid references……………………………………………………………………………..191
Appendix B: Framboidal pyrite date set on TLC, SM, RH and DH section………………………...193
Appendix C: geochemical data ……………………………………………………………………………………217
Appendix D: Detailed petrological logging in the field……………………………………………….233

List of tables

Table 2.1 Geochemical data for the Jura Creek samples. TOC = total organic carbon, AVS. = acid-volatile sulphide, ND = not determined. LQD = limit of quantification……………..35

Table 2.2 Pyrite morphology variation in different redox settings (Bond and Wignall, 2010)……………………………………………………………………………………………………..36

Table 2.3 Lithofacies, defined by petrographic features, and their interpreted environmental conditions from the Jura Creek section…………………………………..………….40

Table 2.4 Pyrite framboid diameter dataset. N = sample size for each sample. Ave = mean average framboid diameter. S.D. standard deviation……………….……………………….…..46

List of figures

Fig. 1.1 Remineralization of organic matter in different settings (Demaison & Moore 1980)……3

Fig. 1.2 Type example of anoxic sill basin, black sea where total organic matter content increase about tenfold after the onset of anoxic bottom water in the basin (Demaison & Moore 1980) ……4

Fig. 1.3 Mediterranean Sea anoxic intervals (Sapropels S1 to S9) identified by elevated primary productivity (Ba/Al), redox sensitive elements (U and Mo) and their connection with insolation (Hennekam et al., 2020)……5

Fig. 1.4 Simplified dynamics of a coastal upwelling systems and related deposition in local environment (Wignall 1994)……6

Fig. 1.5 Organic-rich mudstone from Kimmeridge Clay Formation. Organomineralic aggregation (oma) are ancient marine snow produced during elevated productivity in the water column. The interbedded between oma and homogenized layer suggests episodically depositional processes, particularly in association with algae bloom (Macquaker et al., 2010)……7

Fig. 1.6 A summary of the processes that produce lenticular lamination in shales via erosion and redeposition of water-rich mud clasts (Schieber et al., 2010)……8

Fig. 1.7 Different kinds of carbonate producer (photozoan and heterozoan association) can flourish in specific sea surface temperatures and productivity level (Halfar et al., 2004)……11

Fig. 1.8 Conceptual model illustrating how water clarity influences zonation of zooxanthellate corals (K is the extinction coefficient of light). Branching corals require about 60% of surface light, head corals about 20%, and plate corals about 4% (Hallock & Schlager 1986)……12

Fig. 1.9 (a)With oxygen-exhausted and potentially euxinic waters transported from the sub-basin to the ramp by upwelling currents. (b) This led to transgressive black shale deposition in middle to inner ramp settings and termination of carbonate production (Petrash et al., 2016)……14

Fig. 2.1 Correlation of latest Devonian- earliest Carboniferous stratigraphy from the Canadian Rocky Mountains (Caplan and Bustin 1998), Rhenish Basin, Germany

(Kaiser et al. 2016) and Williston Basin, Montana, the Dakotas and the southern prairies of Canada (Smith and Bustin 1998; Hogancamp and Pocknall, 2018). Mbr. =Member; Fm. =Formation; Carb. =Carboniferous. Correlation is achieved based on conodont biostratigraphy……………………………………………………………………………………..27

Fig. 2.2 Location of studied outcrop, stratigraphic log of the Jura Creek section and sample horizons. A simplified lithofacies column is introduced and used in the following figures. The approximate position of the Famennian-Tournaisian boundary is defined by Re-Os dating (Selby and Creaser 2005)……………………………………………………………….31

Fig. 2.3 Petrographic features of limestone in the Jura Creek section. (a) sample JC-2: packstone consisting of abundant bioclasts, mostly from echinoderm, within calcium mud matrix; (b) sample JC-3: middle part of limestone (see "f" area in Fig. 4a), packstone bearing limited bioclasts, bioclastic wackestone; (c) sample JC-3: bottom part of limestone (see "e" area in Fig. 4a), packstone bearing crinoid fragments (yellow arrows) and calcisphere (yellow circle); (d) sample JC-3: top part of limestone (see "g" area in Fig. 4a) showing crinoid fragments selectively replaced by pyrite (yellow arrows)……………………………………………………………………………………………….41

Fig. 2.4 Petrographic features of rudaceous limestone (sample JC-3). (a) sketch of lithofacies in limestone sample JC-3, consisting of bioclastic wackestone with intraclasts and abundant pyrite in the upper part. Black bar on the left side indicates a scale of 1 cm; positions of parts b, c and d are marked, and e, f and g refer to Fig. 3 parts c, b and d, respectively; (b) wackestone fabric within intraclast with small bioclast fragments; (c) bryozoan chamber infilled with quartz (cross polarized light). Dotted yellow line delineates the boundary of a wackestone intraclast; (d) large crinoid fragment with extensive siliceous replacement (cross polarized light)………42

Fig. 2.5 Petrographic features of sample JC-4 (facies 2). (a) sketch of the lithofacies in the sandstone, showing three distinct layers. The black bar indicates a scale of 1 cm; positions of b, c and d are marked; f is the position of the SEM image in Fig. 6f. Photomicrographs showing: (b) rhombic dolomite and reworked crinoid fragments (some examples circled in yellow), and pyrite gains (yellow arrows) seen at contact between layers 1 and 2; (c) quartz grains (yellow arrows) with bioclasts and rhombic dolomite; (d) sand grains of quartz and feldspar cemented by pyrite in layer 3; (e) phosphatic bioclasts (yellow arrows), likely fish bones, in sandstone of layer 3……..43

Fig. 2.6 SEM backscatter images of pyrite morphologies in limestone (sample JC-3) and sandstone (sample JC-4). (a) abundant pyrite crystals in sample JC-3; (b) pyrite cement between clastic grains (mainly quartz and feldspar) in sample JC-4; (c) polyframboid composed of framboids with pyrite microcrysts dominating the matrix in sample JC-4 (yellow arrows indicate truncated framboids at the margin); (d) polyframboid comprising framboids and pyrite crystals with a mostly cemented matrix of sphalerite (the brightest mineral, yellow arrow); (e) giant framboid composed of giant microcrysts of octahedral pyrite; (f) phosphate clasts in Fig. 5a consisting of bioclasts (dark area), partly replaced by pyrite crystals, and framboids (bright crystals circled by white dotted line). The matrix is phosphate-rich (medium grey area)………..44

Fig. 2.7 Petrographic features of shale samples from the Black Shale Member at Jura Creek. (a) sample JC-5: calcareous black shale consisting of organic-rich layers and calcite-rich laminations, facies 3; (b) sample JC-6: siliceous black shale bearing tiny, scattered quartz grains, facies 4; (c) sample JC-12: siliceous black shale bearing abundant radiolarians, facies 4; (d) sample JC-20: lenticular laminated shale consisting of compacted clay clasts and silt, facies 5; (e) sample JC-19: calcareous mudstone bearing ophiuroid and tiny carbonate bioclasts, facies 6; (f) sample JC-21: pyritic calcareous silt, facies 7…………………………………………………………………………………47

Fig. 2.8 SEM backscatter images of pyrite morphologies. (a) Sample JC-5: small framboids in calcareous black shale; (b) Sample JC-20 showing abundant pyrite crystals; (c) Sample JC-19: abundant framboids showing secondary pyrite overgrowth……..48

Fig. 2.9 Box-and-whisker plots of framboid size distributions from Jura Creek samples and mean value versus standard deviation plot. Blue, yellow and green circles represent statistic features of framboids in the second, third and fourth units, respectively. Data for samples JC-4-1 and JC-4-2 were collected from framboids within two polyframboids, while the framboid size distribution in sample JC-4-3 was collected from the sandstone matrix……………………………………………………………………………………49

Fig. 2.10 Geochemical profiles for total Fe (Fe_T), total P (P_T) and Fe speciation through the Jura Creek section. The dashed line on Fe_T plots represent the minimum Fe concentration (0.5 wt%) for application of Fe speciation. The dashed lines on Fe/Al plots represent the range of normal oxic shale (0.44-0.66) (Clarkson et al., 2014). The dashed line on Fe_{HR}/Fe_T plots represent the boundary for distinguishing anoxic water-column conditions. The dashed lines on Fe_{py}/Fe_{HR} plots represent the boundaries for distinguishing euxinic (> 0.8) and ferruginous (< 0.6) water-column conditions……………………………………………………………………………………………………….50

Fig. 2.11 Redox sensitive element profiles for the Jura Creek section. Black solid lines represent concentrations, and red lines with triangle icons represent variation in enrichment factors………………………………………………………………………………………………52

Fig. 2.12 Redox evolution and depositional history of the Devonian-Carboniferous transition in western Canada. Inset boxes show redox conditions at the Jura Creek study site (location indicated by triangle in main figures). The size of arrows is consistent with the amount of trace metal flux. SWI is sediment- water interface….54

Fig. 2.13 Mo-EF versus U-EF cross plot for the Jura Creek section. Unit 2 samples are labelled to show the progression of redox conditions through this unit. Cross plot is modified from Algeo and Tribovillard (2009) and Tribovillard et al. (2012)…………..….59

Fig. 3.1 (a) Mississippian (340 Ma) global palaeogeography (modified from Boucot et al., 2013), showing the northern England study area (black rectangle); (b) regional palaeogeography of northern England during the Asbian (336- 332 Ma), showing the occurrence of isolated basins surrounded by carbonate platforms and shelves (modified from Cope et al., 1992)……………………………………………………………………77

Fig. 3.2 Summary cross section through the Bowland Basin, Craven Fault Belt; ICS = International Commission on Stratigraphy, Serpukhov. – Serpukhovian, Hol. = Holkerian; dashed lines show the formation boundaries (after Earp et al., 1961; Aitkenhead et al., 1992; Waters et al., 2017)…………………………………………………….79

Fig. 3.3 Study area in the Bowland Basin, Craven Fault Belt, and the southern Askrigg Block. Outcrop locations are Dobson Brook (DB), Leagram Brook (LB), Smelthwaite Farm (SM), School Share (SS), Cow Close (CC), Moor Close Gill (MC), Dinckley Hall

(DH), River Hodder (RH), Light Clough (LC), Swarden Clough (SC), Clough Head Beck (CH), Tory Log Clough (TLC), and Fell Lane (FL)……………………………………………………81

Fig. 3.4 Geochemical profile for TOC, Fe speciation, trace metal systematics and framboid analyses through the SM (a) and RH (b) sections. The dashed lines on Fe_{HR}/Fe_{T} plots represent the boundaries for distinguishing anoxic (>0.38) and oxic (<0.22) water column conditions. The dashed lines on Fe_{py}/Fe_{HR} plots indicate the boundaries for distinguishing euxinic (>0.8) and ferruginous (<0.6) water column conditions, and the open circles reflect oxic samples (determined via combined consideration of Fe speciation and trace metal systematics), while closed circles represent anoxic samples. In U and Mo plots, black circles and the diamonds present enrichment factors and concentration respectively. Diamonds are shown at zero if the concentration is below instrument detection limits. The grey bar and the dash lines indicate calibrated redox thresholds for U_{EF} and Mo_{EF} respectively (see text)………..88

Fig. 3.5 Geochemical profiles for TOC, Fe speciation, trace metal systematics and framboid analysis at the TLC section. See Fig. 3.4 caption for additional information……………89

Fig. 3.6 Geochemical profiles for TOC, Fe speciation and trace metal systematics at the DB and LB sections. See Fig. 3.4 caption for additional information……………………………90

Fig. 3.7 Geochemical profiles for TOC, Fe speciation and trace metal systematics at the CH and SC sections. PL: Pendleside Limestone Formation. See Fig. 3.4 caption for additional information………………………………………………………………………………………91

Fig. 3.8 Geochemical profiles for TOC, Fe speciation, trace metal systematics and framboid analyses at the DH section. See Fig. 3.4 caption for additional information……………92

Fig. 3.9 Geochemical profiles for TOC, Fe speciation and trace metal systematics at the FL section. PL: Pendleside Limestone Formation. See Fig. 3.4 caption for additional information…………………………………………………………………………………………………..93

Fig. 3.10 Geochemical profiles for TOC, Fe speciation and trace metal systematics at the LC and SS sections. LBS: Lower Bowland Shale Formation; UBS: Upper Bowland Shale Formation. See Fig. 3.4 caption for additional information……………………………………..95

Fig. 3.11 Geochemical profiles for TOC, Fe speciation and trace metal systematics through the CC and MC sections. See Fig. 3.4 caption for additional information…………………97

Fig. 3.12 Wilkin Plot (mean framboid diameter against standard deviation) of framboid populations from the late Holkerian to early Pendleian of the Bowland Basin. Dashed line indicates the euxinic/oxic-dysoxic threshold, as determined in modern environments (Wilkin et al., 1996)……………………………………………………………………103

Fig. 3.13 Redox threshold calibrations based on proxy covariation; open, light grey, dark grey and black circles illustrate oxic, ferruginous, weakly euxinic and highly euxinic samples. (a) U_{EF} and Fe_{HR}/Fe_T cross plot, upper part showing data points and lower part showing statistical analysis in which Fe_{HR}/Fe_T data are displayed as mean values (± 1 S.D), where U_{EF} is <1, 1-2, 2-3 and >3. (b) Mo_{EF} and U_{EF} cross plot and its corresponding statistical analysis showing there is no Mo accumulation with U_{EF} <1.37, but that Mo enrichment increases rapidly as U_{EF} increases above 3.0. (c) Mo_{EF} and Fe_{py}/Fe_{HR} cross plot showing scattered Fepy/FeHR ratios for oxic and ferruginous samples, but with Fe_{py}/Fe_{HR} ratios dominantly falling in and above the possibly euxinic zone when Mo_{EF} is > 4.8. (d) framboid size distribution (points refer to mean value, and upper and lower limits represent the maximum and minimum framboid diameters) and Mo_{EF} cross plot showing a broad decline in framboid size as Mo_{EF} increases. Large framboids (mean value > 6 μm) occur when Mo_{EF} is below 10, while framboid mean sizes < 6 μm commonly occur with Mo_{EF} > 10. With Mo_{EF} > 40, all framboid populations are < 6 μm in mean diameter. LOD: limit of detection………..105

Fig. 3.14 Summary of the redox history of the Bowland Basin study sites showing a gradual increase in the extent and intensity of anoxia from the Asbian to the early Pendleian. The extent of Bowland Shale deposition also increases with onlap of the marginal Craven Fault Belt beginning in the Brigantian and extending onto the Askrigg Block in the late Brigantian-Pendleian……………………………………………………109

Fig. 3.15 Depositional model for the development of the Bowland Shale Formation from a carbonate ramp experiencing little oxygen restriction in the mid Asbian, to a fault-bounded syn-rift basin in the Brigantian with ferruginous-euxinic bottom waters, to a post-rift basin experiencing flank collapse and onlap of black shales onto the basin margin in the early Pendleian. Euxinic waters are envisaged to have been maintained beneath a salinity stratified water column in which warm saline bottom waters, generated on adjacent carbonate shelves, supplied the deep water……………………..115

Fig. 3.16 Mo/TOC plots of euxinic samples from the Brigantian to early Pendleian in the

Bowland Basin. The dash lines depict the gradients from three modern, euxinic basins (Algeo and Lyons, 2006)……………………………………………………………………..116

Fig. 4.1. (a) Global palaeogeography during the Mississippian showing location of the study region. (b) Regional palaeogeography showing location of the Bowland Basin amongst a series of fault-bounded block-and-basins. (c) Stratigraphy of the Bowland Basin. UBS Upper Bowland Shale Formation; LBS Lower Bowland Shale Formation; PL Pendleside Limestone Formation; HL Hodderense Limestone Formation; PSM Pendleside Sandstone Member; RLM Ravensholme Limestone Member; PLM Park Style Limestone Member. After Earp *et al*. (1961), Aitkenhead *et al*. (1992) and Waters *et al*. (2009). Abbreviated stages are Serpukhovian (Serpukhov) and Holkerian (Hol.)…………………………………………………………………………………………..137

Fig. 4.2 Study area in the Bowland Basin, Craven Fault Belt (between the South and North Craven Faults), and the southern Askrigg Block and location of study sections (see Table 1). MCF - Mid Craven Fault……………………………………………………………………..138

Fig. 4.3 Isopach map of the Lower Bowland Shale Formation showing the influence of structural features (Craven faults and the Slaidburn Anticline) on sediment thickness. Dots represent locations of thickness data, primarily derived from the records of Geological Survey memoirs…………………………………………………………………………………142

Fig. 4.4 Correlation panels for Bowland Shale sections along two NE-SW transects from the margins to the centre of the Bowland Basin (see Fig. 2 and Table 1 for outcrop details). RSM Ravensholme Limestone Member; PSM Pendleside Sandstone Member; MLF mudstone lithofacies; CLF carbonate lithofacies; CSF clastic sandstone lithofacies (see lithofacies section in main text)………………………………………………..143

Fig. 4.5 (a) Sedimentary log of the Lower Bowland Shale at Tory Log Clough (TLC), showing numerous limestone interbeds of the Ravensholme Limestone Member. The strata below 73 m height (not shown) belongs to the underlying Pendleside Limestone Formation; topmost bed at 110 m height marks the erosive-base base of the Pendleside Sandstone. (b) Sedimentary log of the basal Lower Bowland Shale developed at Fell Lane section showing interbeds of allochthonous limestones……144

Fig. 4.6 Cross section from the southern margin of the Askrigg Block to the southern-most outcrops of the Bowland Basin, showing the thick development of the Pendleside

Sandstone in the Lower Bowland Shale, and levels of main limestone units and the laterally equivalent lithologies of the Yoredale Group. See figure 2 for line of section. MLF for Mudstone Lithofacies, CLF is carbonate lithofacies and CSF is clastic sandstone lithofacies (see section of lithofacies in main text)……………………………….145

Fig. 4.7 Thickness variations in Pendleside Sandstone in the Bowland Basin. Isopachs are dashed where data density is low……………………………………………………………………….147

Fig. 4.8 Isopachs for carbonate bodies developed in the Bowland Shales and location of localised, limestone boulder beds………………………………………………………………………147

Fig. 4.9 Isopach map of the Upper Bowland Shale Formation in the Bowland Basin and Craven Fault Belt area showing principal depocentres adjacent to bounding faults……….149

Fig. 4.10 Field photographs of carbonate beds in the Bowland Shale. (a) coarse calcirudite bed (CLF 1), dominantly composed of crinoid columnals, P_{1b} zone, Fell Lane section. (b) limestone bed (CLF 4) displaying hummocky topography, E_{1b} zone, Dinckley Hall section. Yellow notebook is 20 cm in length. (c) CLF 2 bed displaying broad hummock (yellow arrows denote base), whilst topmost bed is graded, and nearly 1 m thick, B_{2b} zone, Dobson's Brook section. (d) Loose block of CLF 2 bed showing massive, graded lower part (T_a division) grading upwards into laminated strata (T_b division), B_{2b} zone, Dobson's Brook section……………………………………………………………………………………151

Fig. 4.11 Thin section photographs of limestone facies from the Bowland Shale. (a) CLF 1 coarse calcirudite with crinoid bioclasts and wackestone intraclast, P_{1b} zone, Fell Lane section. (b) CLF 1 coarse calcirudite with large brachiopod shell with broken spine attached. The matrix shows a mix of micrite and sparry patches, P_{1b} zone, Fell Lane section. (c) CLF 2 coarse calcarenite/grainstone composed dominated by peloids, with foram and crinoid bioclasts, basal P_{1a} zone, Tory Log Clough section. (d) CLF 2 coarse calcarenite composed of peloids, crinoid columnals (showing micrite envelopes), calcareous algae (*Koninckopora,* outlined) and forams. B_{2a} zone, basal Lower Bowland Shales, Dobson's Brook. (e) CLF 2 calcarenite dominated by peloids, intraclasts with micrite envelopes and rarer quartz grains, B_2 zone, basal-most Lower Bowland Shale, Swardean Clough. (f) CLF 2 fine calcarenite/ pack-grainstone with peloids, coated grains, forams and possible micritised brachiopod shells, B_2 zone topmost bed of the Pendleside Limestone, immediately below base of Lower Bowland Shale, Swardean Clough……………………………………………………………………….152

Fig. 4.12 Evolving composition of allochthonous carbonates (CLF 2) found within the Asbian- Brigantian in the Bowland Basin. River Hodder data are from the Pendleside Limestone, all other data from the Lower Bowland Shale. The three most abundant clast types are displayed whilst others are included as 'other bioclasts'………………..153

Fig. 4.13 Thin section photographs of limestone facies from the Bowland Shale. (a) CLF 3, calcisiltite with a fragment of bivalve shell showing prismatic structure, P_{1b} zone, Fell Lane. (b) CLF 3 calcisiltite with spar-filled ostracod, P_{1b} zone, Fell Lane. (c) CLF 4 micritic limestone displaying wavy lamination partially recrystallised to microspar, uppermost E_{1a} zone, Dinckley Hall. (d) CLF 4 Microspar consisting of laths/stumpy prisms orientated vertically and showing a weak radial or fan-like arrangement, basal P_{1c} zone, Smelthwaite Farm (e) CLF 5, ostracod and crinoids in wackestone, basal P_{1a} zone, Smelthwaite Farm. (f) CLF 3 bioclastic wackestone bearing calcispheres and a thin-shelled bivalve, B_{2b} zone, Dobson's Brook………………………………………………………156

Fig. 4.14 Thin section photographs of clastic sandstone lithofacies from the Bowland Shale. (a) CSF 1 well sorted, fine sandstone seen in cross-polars, P_{1d} zone, Tory Log Clough. (b) CSF 2, bioclast-rich sandstone with forams (yellow circle, *Archaediscus*), basal P_{1d} zone, Tory Log Clough. (c) CSF 2, bioclast-rich sandstone containing brachiopod fragments (central), crinoid fragments (yellow arrows) and a foram (yellow circle, *Archaediscus*), basal P_{1d} zone, Tory Log Clough. (d) CSF 1 medium-fine grained sandstone with poor sorting, lower E_{1b} zone, Dinckley Hall………………………158

Fig. 4.15 Stratigraphic variation of mudrock facies in selected Bowland Shale outcrops showing increasing importance of MLF 4 in younger strata. HOL - Holkerian………..160

Fig. 4.16 Thin section and SEM photographs of mudrock facies from the Bowland Basin. (a) MLF 2 calcareous, silty mudstone with common organic filaments, topmost Pendleside Limestone, B zone, Swardean Clough. (b) MLF 2 calcareous, silty mudstone with common bioclast fragments, B_{2a} Zone, basal Lower Bowland Shale, Dobson's Brook. (c) MLF 3 laminated, calcareous mudstone consisting of carbonate-rich and clay rich laminae, P_{1a} Zone, Swardean Clough. (d) MLF 3 laminated, calcareous mudstone consisting of carbonate-rich laminae composed of angular calcisilt (fragmented bioclasts?) with clay and organic-rich laminae, uppermost P_{1a} zone, Swardean Clough. (e) MLF 2 SEM image showing abundant carbonate grains (light grey), clay minerals (dark grey), organic matter (black) and pyrite (bright colour) in the form of small, spherical framboids and a pyrite lens incorporating carbonate clasts, P_{1b}-P_{1c} boundary, Smelthwaite Farm. (f) MLF 1 homogenous mudstone with bivalve fragment showing prismatic structure and partial pyritic replacement, B_2 zone, basal Lower Bowland Shale, Tory Log Clough……………………161

Fig. 4.17 Thin section and SEM photographs of lenticular, organic-rich mudrocks, MLF 4, from Dinckley Hall. (a) example showing thin, articulated bivalve prodissoconch (yellow arrow), basal E_{1a} zone. (b) example with scattered radiolarians (arrowed), P_{2b} zone. (c) example showing typical clay lens-rich layer fabric and a homogenous lamina consisting of clay and organic matter (arrows denote the base), mid E_{1a} zone. (d) example with phosphatic nodules (largest example arrowed), mid E_{1a} zone. (e) SEM image showing a clay lens lacking framboids (delineated by arrows) in a matrix with abundant small framboids (bright spots), lower E_{1a} zone. (f) example with several ammonitellas (larval goniatites) in a matrix rich in framboids and clay lenses, basal P_{1c} zone……………………………………………………………………………………………..163

Fig. 5.1 Conceptual model for black shale and carbonate production on different tectonic settings (Exshaw Shale Model and Bowland Shale Model)………………………………….182

Fig. 5.2 Depositional history in Bowland Basin spanning from Asbian to early Pendleian……………………………………………………………………………………………………184

Fig. 5.3 Model demonstrating the development of carbonate production and its termination on Central Lancashire High, which is succeeded by Upper Bowland Shale (modified from Evans & Kirby 1999); HMF: Hodderence Mudstone Formation; PdL: Pendleside Limestone Formation…………………………………………………………………….185

Fig. 5.4 WSBW circulation in block-and-basin in Northern England; with the progradation of deltaic sand coming from the North, black shale deposition is mainly found in the basins on the south (Fraser & Gawthorpe 1990 with modification)……………………………186

Abbreviations

C_{org}: mole value of organic carbon

Fe_{HR}: highly reactive Fe

Fe_{py}: pyrite Fe

Fe_{T}: total Fe

ICS: international commission on stratigraphy

LBS: Lower Bowland Shale Formation

LOD: Limit of detection

MCF: Mid- Craven Fault

Mo_{EF}: molybdenum enrichment factor

Myr: million years

NCF: Northern Craven Fault

OMZ: oxygen minimum zone

PL: Pendleside Limestone Formation

PLM: Park Style Limestone Member

P_{org}: mole value of phosphorus in organic carbon

P_{reac}: mole value of reactive phosphorus which refers to those phosphorus getting involved in the marine biogeochemical cycle and it usually includes authigenic apatite, Fe-bound phosphorus and phosphorus in organic carbon.

PSM: Pendleside Sandstone Member

P_{T}: total phosphorus

RLM: Ravensholme Limestone Member

SCF: Southern Craven Fault

SR: sedimentation rate

SWI: sediment- water interface

UBS: Upper Bowland Shale Formation

U_{EF}: uranium enrichment factors

WSBW: warm saline bottom water

yr: year

Chapter 1 Introduction

Carbonate platform formation is often abruptly terminated by the onset of thick black shale deposition. The reason(s) for this fundamental change in depositional style is unclear and contentious. Factors including tectonic movement, eustatic variation, elevated nutrient, salinity crisis and oxygen depletion (see section 1.6) could contribute to these events. On the other hand, phosphatisation is usually found on this sharp transition. However, its origin and significance are not well understood. Additionally, considering the special location where black shale is adjacent to carbonate production, traditional black shale deposition model of estuarine circulation may not fully explain its origin. Recent study of depositional process of fine-grained sediments are also challenging the foundation of geochemistry. It is proposed that some shale/mudstone deposition is associated with reworked intraclasts which do not preserve solid geochemical signal (Schieber et al., 2010).

To reveal these, two case studies are investigated here: the first from the Devonian-Carboniferous transition in western Canada where black shales overlie ramp carbonates. The second is from British mid-Carboniferous successions where thick black shale belonging to the Bowland Shale formations sit on Lower Carboniferous platform and slope carbonates.

1.1 Aims of the project

The thickest developments of black shales are often found overlying shallow-water limestone, and mark fundamental changes in depositional environment. However, the cause of these sudden lithological transitions is not well understood in terms of its timing, and the nature of the transitional environments. This project will attempt to answer the questions:

Q1: What environmental changes cause these transitions i.e., what causes the collapse of carbonate productivity? The study will investigate the connection between these transitions and tectonic movement and eustatic variation.

Q2: What are the associated redox condition changes during these transitions?

Q3: What is the significance of the phosphatisation during the carbonate-to-black shale transition?

Q4: What depositional processes are responsible for black shale accumulation and what role does sediment from adjoining shallow-water carbonate factories play?

1.2 Rationale for the project

The study focusses on Mid-Carboniferous outcrops of Northern England, and Devonian-Carboniferous outcrops in the Canadian Rockies. Detailed logging in the field, followed by thin section analysis provides information on evolution of sedimentary successions. Coupled with this, trace element behaviour, pyrite morphology and Fe speciation allows investigation of redox conditions. Furthermore, the role of redox variations and the development of phosphatic horizons at the transition in the Canadian example is clearly an important factor investigated here. Eventually, an understanding of tectonic, sedimentary and redox controls will be synthesized to explain the mechanisms of carbonate demise and black shale formation.

1.3 Black shale formation

Organic-rich shale or black shale is characterised by its dark grey to black colour, impoverished benthic fauna and trace metal enrichment (Arthur & Sageman 1994; Wignall 1994). They can form both in marine and lacustrine environments and have great economic significance as an important hydrocarbon source (Demaison & Moore 1980; Tissot et al., 1980; Carroll & Bohacs 2001; Fig. 1.1). Black shale deposition is often associated with palaeoenvironmental perturbations and Ocean Anoxic Events (Jenkyns 2010).

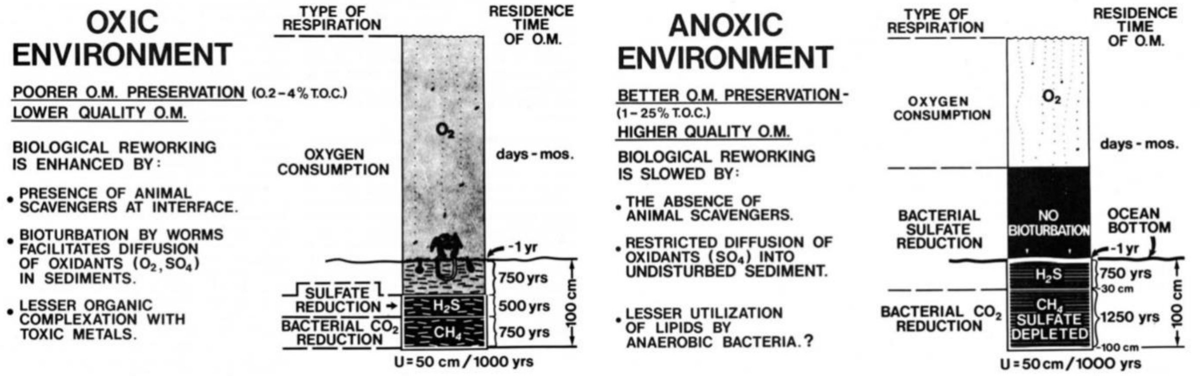

Fig. 1.1 Remineralization of organic matter in different settings (Demaison & Moore 1980)

In most modern marine environments, the seafloor is fully oxygenated thanks to ample oxygen supply outstripping oxygen demand (e.g., Gamo et al., 1986). Modern analogues of black shale deposition can only be found in specific area such as the poorly- circulated Black Sea. The key factors controlling oxygen levels are the rates of consumption and supply. If oxygen consumption via organic matter remineralization is intense then deoxygenation can be achieved. Such “organic overload” occurs in conditions of high primary productivity when abundant nutrients are supplied either by upwelling of nutrient-rich waters, or in coastal areas where abundant fluvial nutrient supply achieves the same effect (e.g. Jenkyns, 2010). Alternatively, oxygen supply can be restricted by the presence of a strong density interface (pycnocline) within the water column and/or limited lateral advection due to a silled basin configuration (e.g., Saanich Inlet, Black Sea; Fig. 1.2). As organic matter remineralization is less intense in anoxic conditions this scenario is known as the preservation model (Anderson & Devol 1973; Demaison & Moore, 1980; Tyson & Pearson, 1991; Wignall, 1994; Algeo et al., 2008; Fig. 1.1).

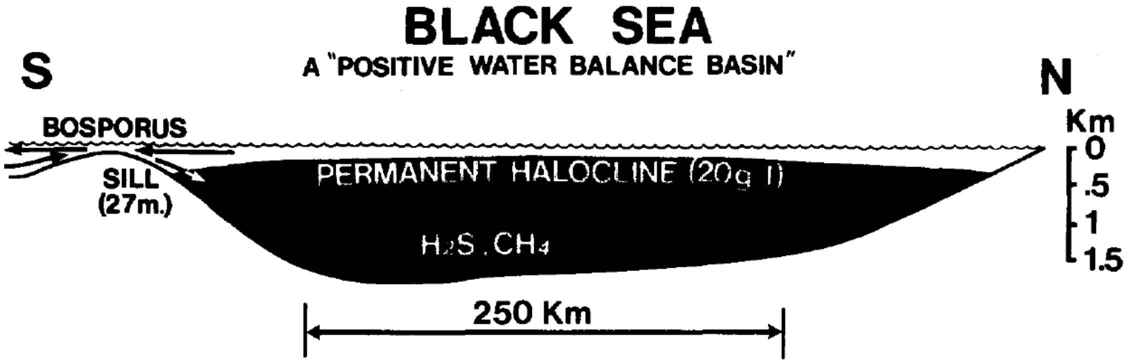

Fig. 1.2 Type example of anoxic sill basin, black sea where total organic matter content increase about tenfold after the onset of anoxic bottom water in the basin (Demaison & Moore 1980)

1.4 Black shale deposition model

There are several alternative models for black shale formation.

Salinity stratification model: salinity stratification creates a stable halocline in the water column and severely limits vertical water advection. Terrestrial run-off can produce a low salinity surface layer that stratifies the epeiric sea and results in bottom-water anoxia (e.g., the Eastern Mediterranean in the Pleistocene (Tyson & Pearson 1991)). In the past 250 kyr, nine layers of sapropel (organic-rich mudrock) formed in the deep waters of the Eastern Mediterranean in anoxic conditions (Matthews et al., 2017; Benkovitz et al., 2020; Hennekam et al., 2020). Each sapropel coincides with enhanced isolation of bottom waters caused by increased run-off from the Nile (Martine et al., 1982; Rohling & Hilgen 2007; Hennekam et al., 2020; Fig. 1.3). Salinity stratification is also encountered in the modern Black Sea, the largest permanently euxinic basin in the modern world (Murray et al., 1989), where ingression of Mediterranean seawater through the shallow Bosphorus supplies the deeper water column whilst riverine influx supplies the lower density surface waters (Ryan et al., 1997; Hiscott et al., 2007).

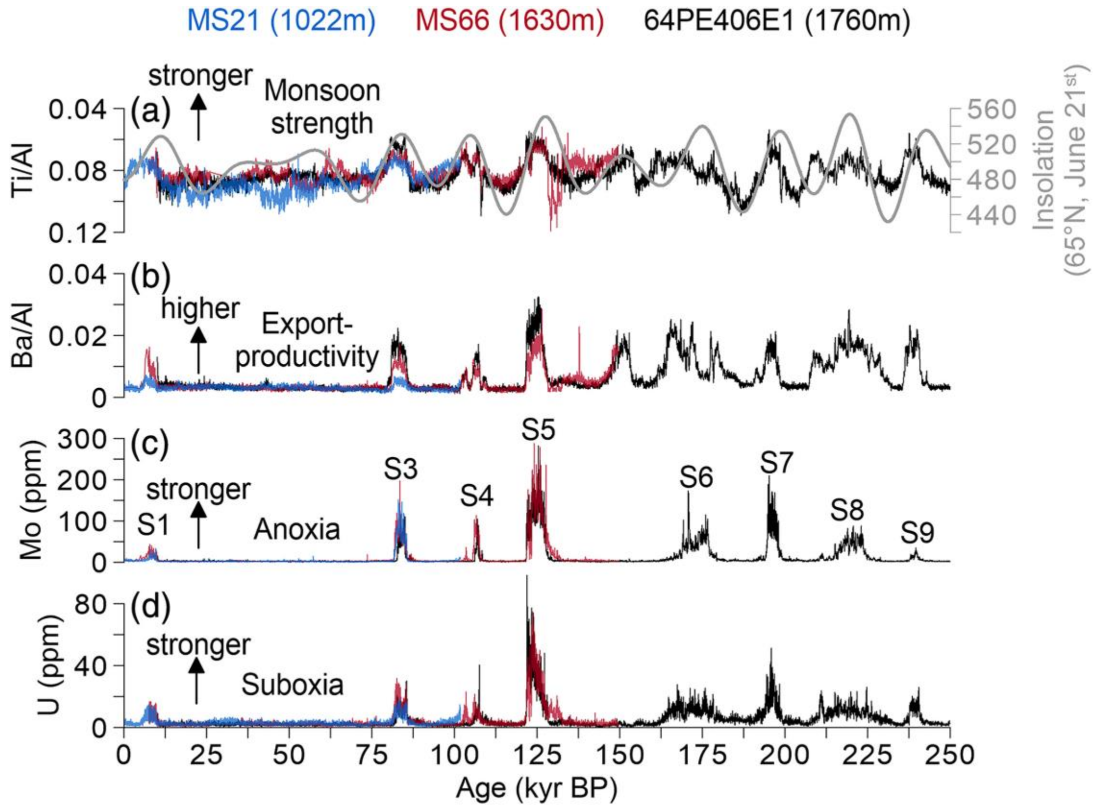

Fig. 1.3 Mediterranean Sea anoxic intervals (Sapropels S1 to S9) identified by elevated primary productivity (Ba/Al), redox sensitive elements (U and Mo) and their connection with insolation (Hennekam et al., 2020)

In both the Eastern Mediterranean and Black Sea examples the water column structure has less dense, more brackish surface waters above more saline, denser waters. However, a warm saline bottom water model has also been proposed for intervals of anoxic ocean in the Phanerozoic (Brass et al. 1982). In this model seawater experiences high evaporation in low latitude shelf seas that generates dense, warm and saline water that sinks into the adjacent deep oceans (Railsback et al., 1990). During the Cretaceous Friedrich et al. (2008) contended that a combination of warm saline waters and restricted palaeogeography probably acted as preconditioning factors for the prolonged period of anoxia and black-shale formation in the equatorial proto-North Atlantic Ocean.

Upwelling Zone model: Upwelling, typically on west-facing continental margins, leads to high nutrient delivery and thus elevated productivity (Tyson & Pearson 1991; Fig. 1.4). As a result, the supply of oxygen cannot compete with its consumption via organic matter remineralization and an oxygen minimum zone forms in the mid-water column (Nameroff et al., 2002; Böning et al., 2004, 2005; Levin et al., 2009). Nutrient-driven ocean anoxia has been frequently proposed e.g. in the Late Ordovician (Qiu et al., 2022).

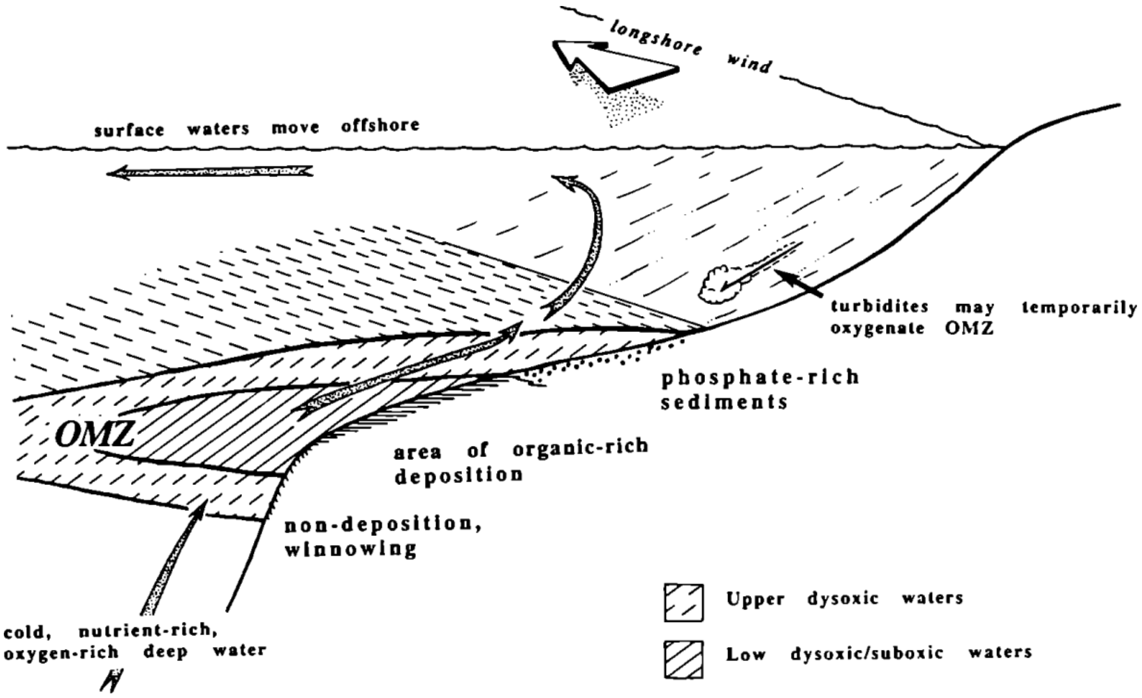

Fig. 1.4 Simplified dynamics of a coastal upwelling systems and related deposition in local environment (Wignall 1994)

1.5 Fine-grained sedimentary rock depositional process

Black shales are typically unbioturbated and as a result they provide a detailed record of fine-grained depositional processes for which there are many, often conflicting, models. Stow & Piper (1984) proposed that fine grain sediment deposition is related to turbidity current, contourite and pelagic/hemipelagic deposition with each producing distinct sedimentary structure. The depositional process of pelagic/hemipelagic has drawn great attention. Settling velocity via Stoke’s law ensures that fine-grained sediment can remain in suspension for a long time resulting in an extremely low theoretical sedimentation rate which is much slower than observed in in modern environments (e.g. Shanks & Trent 1980). In order to reconcile the difference between theoretical calculation and modern observation, other sedimentary processes including entrapment of particles on marine snow and faecal pellets are required for fine-grained sediment sedimentation (e.g. Alldredge & Silver 1988; Cuomo & Bartholomew, 1991; Macquaker et al., 2010; Turner 2015; Fig. 1.5). Marine snow is organic matter derived from various components including phytoplankton, phytodetritus, and microbial and faecal matter (Alldredge & Silver 1988). It is usually larger than 500 µm and is widespread in the modern ocean (Macquaker et al., 2010; Turner 2015).

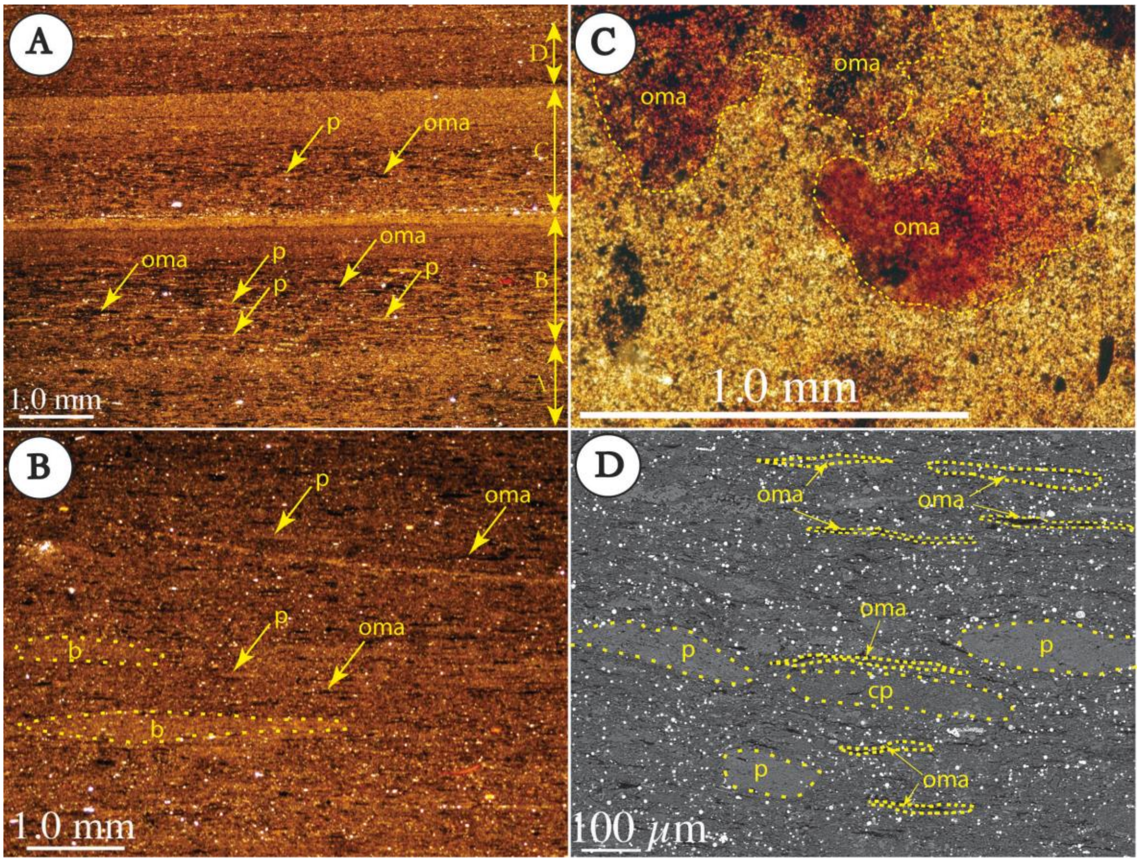

Fig. 1.5 Organic-rich mudstone from Kimmeridge Clay Formation. Organomineralic aggregation (oma) are ancient marine snow produced during elevated productivity in the water column. The interbedded between oma and homogenized layer suggests episodically depositional processes, particularly in association with algae bloom (Macquaker et al., 2010).

Basinal mudstone deposition has traditionally been ascribed to hemipelagic processes with planktonic organic matter/marine snow settling through the water column along with fine-grained clays and wind-blown fine silt (e.g., Wignall, 1994; Gorsline et al., 1996). In recent years, however, the application of flume experiments has challenged the notion that mudrocks are mostly suspension-deposition products. Schieber et al., (2007) proposed that deposition of clay floccules occurs at flow velocities that transport and deposit sand, providing an alternative origin for ancient mudstone.

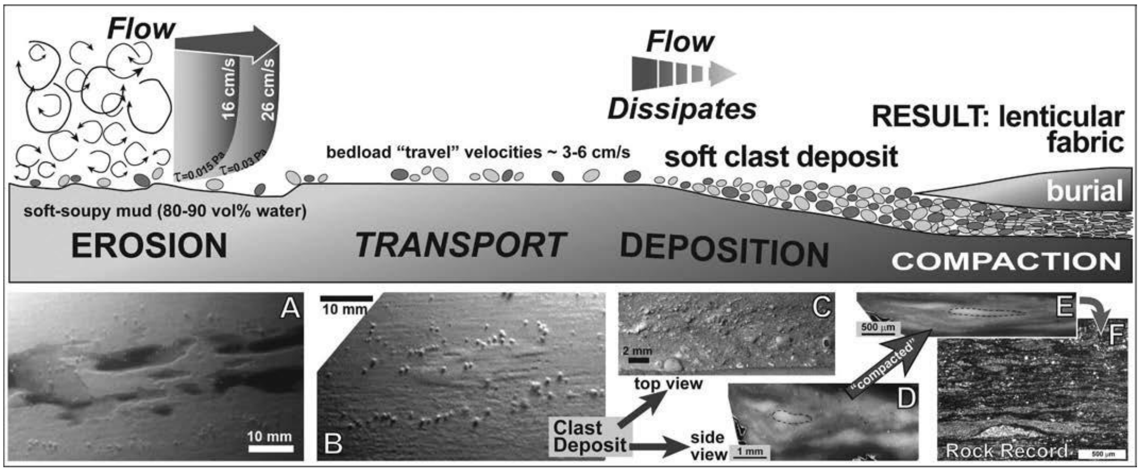

Fig. 1.6 A summary of the processes that produce lenticular lamination in shales via erosion and redeposition of water-rich mud clasts (Schieber et al., 2010).

Using evidence from flume experiments it is proposed erosion and transport of water-rich mud clasts could result in the mudrocks showing lenticular lamination being the product of transport by sediment gravity flows (e.g., Schieber et al., 2010; Fig. 1.6). Many subsequent studies have adopted this notion that mudrocks consist of transported intraclasts sourced from shallow-water environments (e.g., Konitzer et al., 2014; Emmings et al., 2020; Peng 2021). Such an origin challenges the assumption of many geochemical studies that basinal shales provide a reliable in-situ signal of basinal redox.

1.6 Factors controlling carbonate production

Drowning of carbonate platforms occurred commonly throughout Phanerozoic history (Schlager 1981; Hallock & Schlager 1986) and carbonate accumulation rates are outpaced by base-level rise (Schlager 1981, 1999). This can occur if the rate of relative sea-level rise is able to outpace carbonate aggradation (Schlager 1999), or rapid tectonic subsidence, can achieve the same end (e.g. Blanchon & Shaw 1995).

The growth potential of carbonate platforms through geological history has shown great variation as the principal carbonate-producers have changed. During the Triassic, for instance, the average carbonate platform accumulation rate was up to 230 m/Myr while the average rate in the Cretaceous was ~186 m/Myr, and only 75 m/Myr in Carboniferous (Kiessling et al., 2003). By contrast, it is conservatively estimated that average growth potential of modern platforms and reefs is extremely high by Phanerozoic standards: 1000 µm/yr (1000 m/Myr) (Schlager 1981). However, it is important to note that the carbonate production rate in the Holocene is time averaged on a scale of thousand years, a high resolution that cannot be achieved in deep time where rates are derived from longer time spans which will likely include more hiatuses/depositional breaks. Accordingly, long-term study of carbonate shutdown is complicated by inaccurate estimation of depositional rates.

Palaeoenvironmental stresses can suppress carbonate production, and include temperature variation, eutrophication, salinity fluctuation and ocean acidification in short time-scale (e.g. Halfar et al., 2004). With compromised productivity, carbonate platforms are more susceptible to be drowned under small-scale relative sea-level variation (e.g. Schlager 1981; Erlich et al., 1990; Betzler et al., 1995).

1.6.1 Tectonic subsidence

Rapid relative sea-level rise during times of accelerated subsidence has been proposed to cause carbonate drowning in several cases, e.g. the Mid-Devonian shallow-water carbonate platforms in the Moravo-Silesian Basin in central Europe (Bábek et al., 2007); late Barremian to early Aptian platform carbonates in Vocontian Basin, France, saw four drowning events coincide with four episodes of rifting (Masse & Fenerci-Masse 2013).

1.6.2 Sea level variation

Eustatic rise is often considered a cause of carbonate platform drowning. Schlager (1981) showed that elevated sea-level rise in early Holocene coincides with depressed carbonate production, while in late Holocene, slow down of sea-level rise saw a recovery of carbonate deposition. The last glacial to interglacial transition involved three transgressive pulses which caused three reef and carbonate drowning events (Blanchon & Shaw 1995). It is estimated that during the Holocene peak deglaciation caused rates of sea-level rise in excess 45 mm/yr, while the carbonate sedimentation rate was only 13 mm/yr (Bard et al., 1990). Other examples occur in deeper time. In the Cenomanian, sea-level variation is assigned a crucial role in the evolution and demise of a shallow marine carbonate deposition in northern Cantabria (Wilmsen 2000) where three successive 3rd-order sea-level rises resulted in backstepping and drowning of a carbonate platform.

1.6.3 Temperature variation

Sea surface temperature (SST) has long been recognized as a major influence on carbonate production and grain associations (Schlager 1992; Halfar et al., 2004; Wilson & Vecsei 2005; Fig. 1.7). Modern areas with abundant hermatypic coral and calcareous green algae thrive in temperatures of 20- 28°C (Adams et al., 1990), while heterozoan faunas can flourish even at temperatures below 15°C (Halfar et al., 2004). Additionally, temperature controls CO_2 solubility and therefore the saturation of $CaCO_3$ in water column, which favours increased carbonate production in warmer waters (Mutti & Hallock 2003). Cooling is generally regarded to induce carbonate platform deterioration. On the other hand, abnormally high SST (e.g. temperatures above 30°C) may negatively impact on carbonate production e.g. coral bleaching events (Brown 1997) and decrease carbonate production (Warner et al., 1996; Kwiatkowski et al., 2015). In the geological record, high SSTs have been blamed for the demise of carbonate production (Wilson et al., 1998; Scheibner & Speijer 2008).

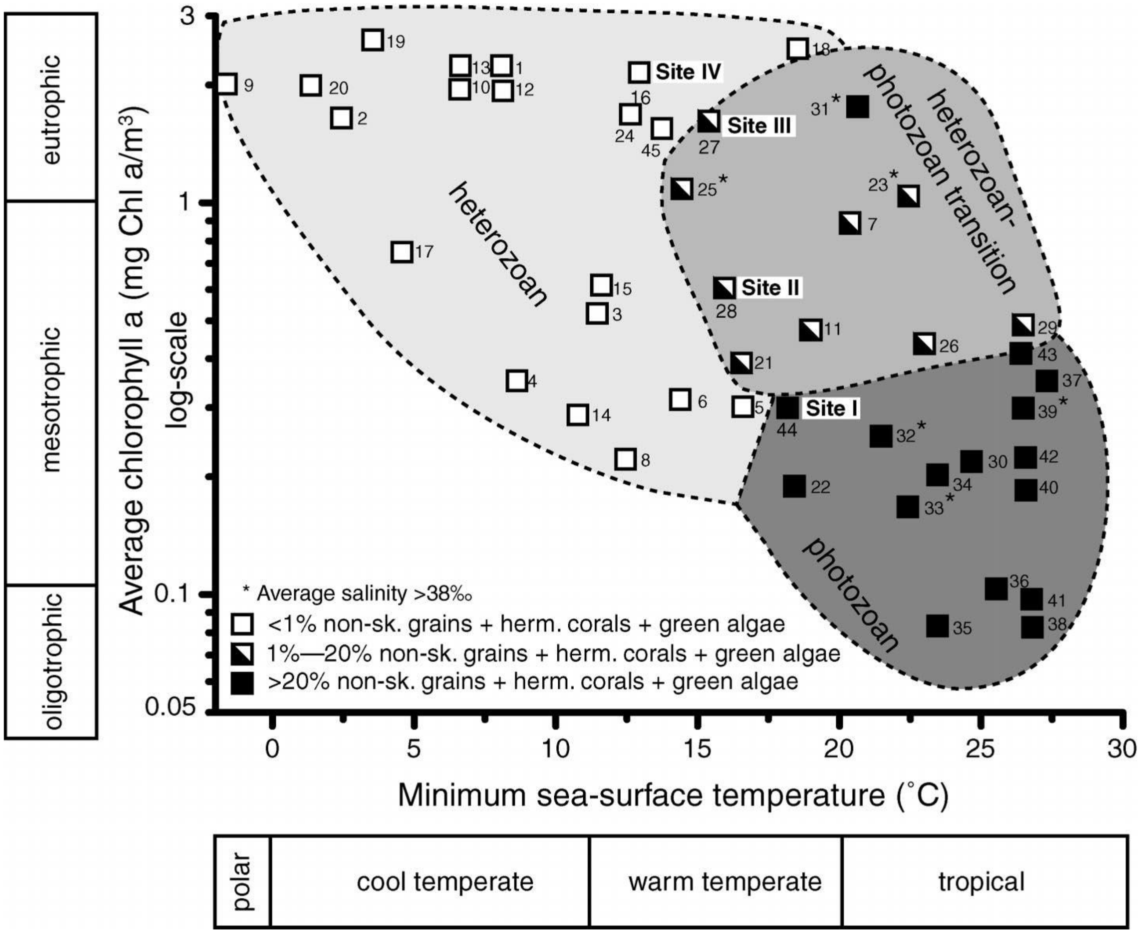

Fig. 1.7 Different kinds of carbonate producer (photozoan and heterozoan association) can flourish in specific sea surface temperatures and productivity level (Halfar et al., 2004).

1.6.4 Excess nutrients

Eutrophication can lead to the termination of carbonate production (Schlager 1988). In modern environments carbonate-producing photozoans can only persist in oligotrophic and slightly mesotrophic settings, with heterotrophic organisms becoming more competitive as nutrient levels increase (Halfar et al., 2004, 2006). These include molluscs, bryozoan and some benthic and planktic forams that out-compete photozoan carbonate producers but lead to low sedimentation rates (Hallock 1988; Halfar et al., 2006; Reijme 2021). Elevated nutrients input will also stimulate the flourishment of plankton. On the one hand, the water transparency could be reduced to compromise phototrophic carbonate production (Hallock & Schlager 1986; Fig. 1.8). On the other, the thrive of plankton will also promote the multiplication of bioeroders as plankton is their preferential food both in their larval and adult stage (Hutchings 1986; Birkeland 1988; Hallock 1988).

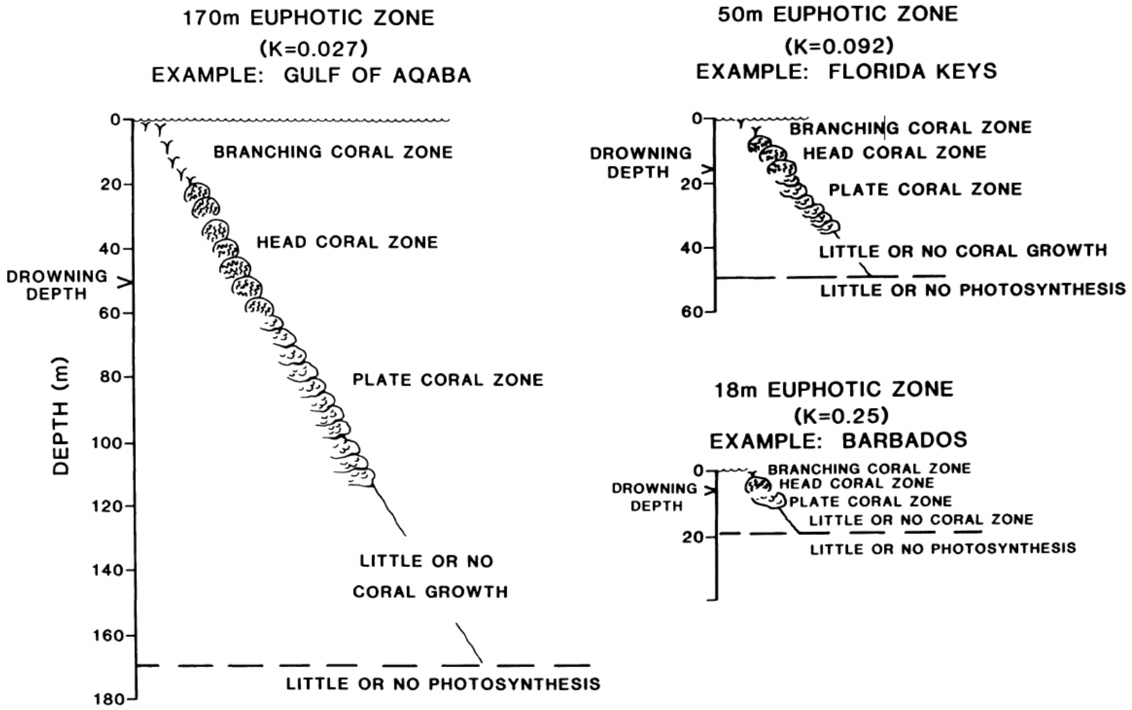

Fig. 1.8 Conceptual model illustrating how water clarity influences zonation of zooxanthellate corals (K is the extinction coefficient of light). Branching corals require about 60% of surface light, head corals about 20%, and plate corals about 4% (Hallock & Schlager 1986).

1.6.5 Salinity fluctuation

Salinity is another important factor that controls carbonate deposition and has a clear impact on global carbonate distribution especially within the tropics (Wilson 2008). Lee (1975) showed that salinity controls the development of non-skeletal associations, especially oolith/aggregate production, which only occurs when salinity exceeds 35.8%. Indeed, marine salinity plays a large role in carbonate equilibrium and precipitation (Opdyke & Wilkinson 1990; Saraswat et al., 2015). High salinity has a detrimental influence on foraminifers (Saraswat et al., 2015) whilst reduced salinity hinders aragonite reef formation and promoted calcitic larger foraminifera (Wilson 2008).

1.6.6 Ocean acidification

Carbonate accretion is currently facing a threat from ocean acidification (OA) with numerous groups, such as bivalves, coralline algae and gastropods thought to be susceptible (Anthony et al., 2008; Hall-Spencer et al., 2008; Vihtakari 2015). In geological history, many carbonate crises have been linked with OA (Kump et al., 2009; Kiessling & Simpson 2011). They have found that the elevated CO2 concentration of seawater both in modern and deep time restricts the calcification of corals and prohibit its growth rate (Kiessling & Simpson 2011). For instance, Paleocene- Eocene Thermal Maximum (PETM), the latest global warming event witnessed a short-lived OA supported by shallowing of carbonate conpensation depth (Zachos et al., 2005). A response to this OA is that a transition in carbonate producer from coral- algal reefs to large- foraminifera-dominated platforms occurs showing compromised carbonate production (Scheibner & Speijer, 2008).

1.6.7 Anoxia

Many carbonate-producers are suppressed by oxygen-poor conditions and as noted above, carbonate platforms are often overlain by black shales formed in anoxic conditions. However, in many cases it is unclear if the anoxia only became established after platform collapse allowed the expansion of deep-water oxygen-poor conditions. Some have attributed the carbonate demise to the upwelling of oxygen-poor waters into shallow-water settings thus suggesting a cause-and-effect link for black shale development (Petrash et al., 2016, Fig. 1.9). In contrast, a Devonian/Carboniferous carbonate platform in Poland was shut-down following tectonic extension and volcanism before black shale deposition ensued (Szulczewski et al., 1996).

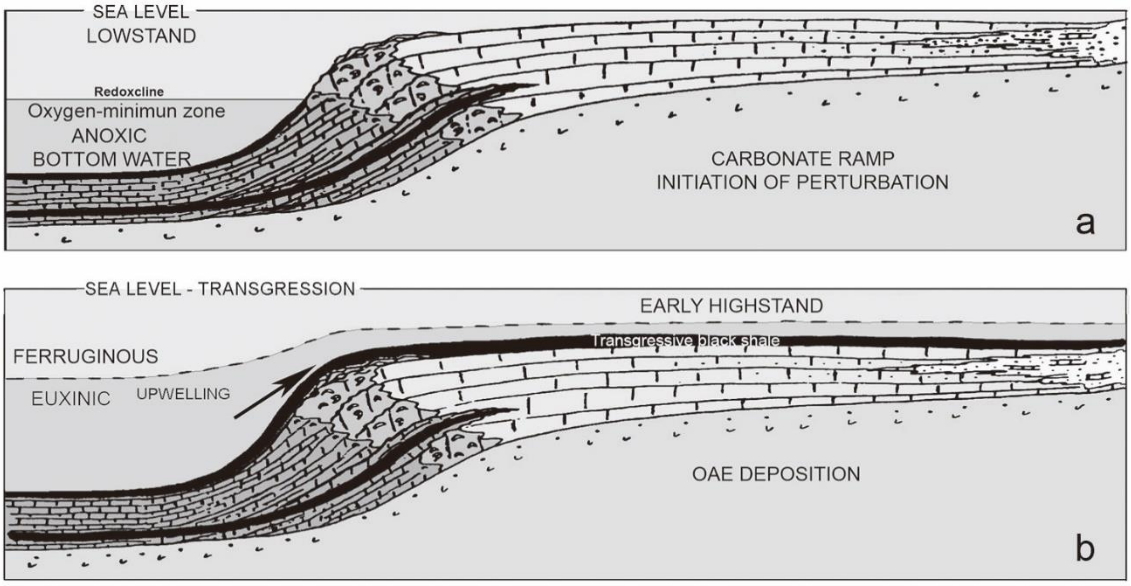

Fig. 1.9 (a)With oxygen-exhausted and potentially euxinic waters transported from the sub-basin to the ramp by upwelling currents. (b) This led to transgressive black shale deposition in middle to inner ramp settings and termination of carbonate production (Petrash et al., 2016)

1.6.8 Terrigenous input

Clastic input from land also hinders carbonate production. Sediments influx is associated with nutrients, resulting in eutrophication (see above). Fine sediment in suspension reduces water transparency and hinders photozoan carbonate production (Hallock 1988). The Askrigg Block on the north of Bowland Basin shows a carbonate-dominated sequence before Brigantian (Dean et al., 2011). However, with the delta progradation coming from the north, its deposition shows a great shift from carbonate section (Great Scar Limestone Group) to a mixed sequence (Yoredale Group) recording cycles of marine to fluvio-deltaic sedimentation (Dunham and Wilson 1985). Eventually there is no more carbonate production and it is replaced by Millstone Grit Group, a sequence dominated by sandstone deposition (Waters et al., 2014). Another case refers to the Carnian Pluvial event (CPE) in late Triassic when the whole of Pangea experienced extremely heavy precipitation (Simms & Ruffell, 1990). Huge amount of terrestrial sediment was transported to the shelf and many carbonate platform were drowned during this process showing that carbonate deposition is directly overlaid by fluvial sandstone (e.g. Bechstädt & Schweizer 1991; Mutti & Weissert 1995; Hornung & Krystyn 2007; Arche & Lopez- Gomez 2014).

1.7 Thesis outline

The thesis is divided into several chapters, two are accepted and published papers and one is currently in review. Chapter 2, published in *Palaeogeography Palaeoclimatology Palaeoecology* in 2022, provides a detailed petrography and geochemical study on the Jura Creek of western Canada which investigates the transition from a carbonate ramp to a black shale and the origin of a phosphate-rich bed. The redox history of the black shale is compared with other records of the Hangenberg Event. Chapter 3, accepted and available online in the *Geological Society of America Bulletin* provides a comprehensive redox study of the Bowland Basin covering Pendleside Limestone Formation (which records conditions immediately prior to basinal anoxia), Lower Bowland Shale Formation (onset of black shale) and Upper Bowland Shale Formation (wide spread of black shale). Combined Fe speciation, trace metals systematics (Mo, U) and pyrite morphology, establish redox thresholds for trace metals in order to refine redox conditions. The control of redox variation has been discussed, and a new model of warm saline bottom water is proposed to explain the onset of anoxia. Chapter 4, submitted to *Sedimentology* presents detailed lithofacies analysis of the Bowland Shale in which five carbonate facies, two sandstone facies and four mudstone facies are identified, and diverse sedimentary processes are discussed. Special attention is paid to the origin of lenticular mudstone (clay lens-rich shale). In addition, based on the redox history revealed in Chapter 3, the relationship between carbonate production and redox history is also investigated. Chapter 5 provides a summary of the key results found in the case studies and outlines future research questions.

References

Adams, C.G., Lee, D.E., Rosen, B.R. 1990. Conflicting isotopic and biotic evidence for tropical sea-surface temperatures during the Tertiary. *Palaeogeography, Palaeoclimatology, Palaeoecology*, **77(3-4)**, 289-313, https://doi.org/10.1016/0031-0182(90)90182-7.

Algeo, T.J., & Ingall, E. 2007. Sedimentary Corg: P ratios, paleocean ventilation, and Phanerozoic atmospheric pO2. *Palaeogeography, Palaeoclimatology, Palaeoecology*, **256(3-4)**, 130-155, https://doi.org/10.1016/j.palaeo.2007.02.029.

Algeo, T.J., Heckel, P.H., Maynard, J.B., Blakey, R., Rowe, H., Pratt, B.R., & Holmden, C. 2008. Modern and ancient epeiric seas and the super-estuarine circulation model of marine anoxia. Dynamics of Epeiric seas: sedimentological, paleontological and geochemical perspectives. *St. John's, Canada: Geological Association of Canada, Special Publication*, **48**, 7-38.

Alldredge, A.L., & Silver, M.W. 1988. Characteristics, dynamics and significance of marine snow. *Progress in oceanography*, **20(1)**, 41-82, https://doi.org/10.1016/0079-6611(88)90053-5.

Anderson, J.J., & Devol, A.H. 1973. Deep water renewal in Saanich Inlet, an intermittently anoxic basin. *Estuarine and Coastal Marine Science*, **1(1)**, 1-10, https://doi.org/10.1016/0302-3524(73)90052-2.

Anthony, K.R., Kline, D.I., Diaz-Pulido, G., Dove, S., & Hoegh-Guldberg, 2008. Ocean acidification causes bleaching and productivity loss in coral reef builders. *Proceedings of the National Academy of Sciences*, **105(45)**, 17442-17446, https://doi.org/10.1073/pnas.0804478105.

Arche, A., & Lopez-Gomez, J. 2014. The Carnian pluvial event in Western Europe: new data from Iberia and correlation with the Western Neotethys and eastern North America–NW Africa regions. *Earth-Science Reviews*, **128**, 196-231.

Arthur, M.A., & Sageman, B.B. 1994. Marine black shales: depositional mechanisms and environments of ancient deposits. *Annual Review of Earth and Planetary Sciences*, **22(1)**, 499-551, https://doi.org/10.1146/annurev.ea.22.050194.002435.

Bábek, O., Přikryl, T., Hladil, J. 2007. Progressive drowning of carbonate platform in the Moravo-Silesian Basin (Czech Republic) before the Frasnian/Famennian event: facies, compositional variations and gamma-ray spectrometry. *Facies*, **53(2)**, 293-316.

Bard, E., Hamelin, B., Fairbanks, R.G., Zindler, A. 1990. Calibration of the 14 C timescale over the past 30,000 years using mass spectrometric U-Th ages from Barbados corals. *Nature*, **345(6274)**, 405-410.

Bass, G.W., Southam, J.R., & Peterson, W.H. 1982. Warm saline bottom water in the ancient ocean. *Nature*, **296(5858)**, 620-623.

Bechstädt, T., & Schweizer, T. 1991. The carbonate—clastic cycles of the East-Alpine Raibl group: Result of third-order sea-level fluctuations in the Carnian. *Sedimentary Geology*, **70(2-4)**, 241-270.

Benkovitz, A., Matthews, A., Teutsch, N., Poulton, S. W., Bar-Matthews, M., & Almogi-Labin, A. 2020. Tracing water column euxinia in Eastern Mediterranean Sapropels S5 and S7. *Chemical Geology*, **545**, 119627, https://doi.org/10.1016/j.chemgeo.2020.119627.

Betzler, C., Brachert, T.C., Kroon, D. 1995. Role of climate in partial drowning of the Queensland Plateau carbonate platform (northeastern Australia). *Marine Geology*, **123(1-2)**, 11-32, https://doi.org/10.1016/0025-3227(95)80002-S.

Birkeland, C. 1987. Nutrient availability as a major determinant of differences among coastal hard-substratum communities in different regions of the tropics. *UNESCO Reports in Marine Science*, **46**, 45-97.

Blanchon, P., & Shaw, J. 1995. Reef drowning during the last deglaciation: evidence for catastrophic sea-level rise and ice-sheet collapse. *Geology*, **23(1)**, 4-8, https://doi.org/10.1130/0091-7613(1995)023<0004:RDDTLD>2.3.CO;2.

Böning, P., Brumsack, H.J., Böttcher, M.E., Schnetger, B., Kriete, C., Kallmeyer, J., & Borchers, S.L. 2004. Geochemistry of Peruvian near-surface sediments. *Geochimica et cosmochimica acta*, **68(21)**, 4429-4451, https://doi.org/10.1016/j.gca.2004.04.027.

Böning, P., Cuypers, S., Grunwald, M., Schnetger, B., & Brumsack, H.J. 2005. Geochemical characteristics of Chilean upwelling sediments at∼ 36° S. *Marine Geology*, **220(1-4)**, 1-21, https://doi.org/10.1016/j.margeo.2005.07.005.

Brown, B.E. 1997. Coral bleaching: causes and consequences. *Coral reefs*, **16(1)**, S129-S138.

Carroll, A. R., & Bohacs, K. M. 2001. Lake-type controls on petroleum source rock potential in nonmarine basins. *AAPG bulletin*, **85(6)**, 1033-1053, https://doi.org/10.1306/8626CA5F-173B-11D7-8645000102C1865D.

Cuomo, M.C., & Bartholomew, P.R. 1991. Pelletal black shale fabrics: their origin and significance. *Geological Society, London, Special Publications*, ***58*****(1)**, 221-232, http://doi.org/10.1144/GSL.SP.1991.058.01.15.

Dean, M.T., Browne, M.A.E., Waters, C.N. & Powell, J.H., 2011. A lithostratigraphical framework for the Carboniferous successions of northern Great Britain (onshore). British Geological Survey.

Demaison, G.J., & Moore, G.T. 1980. Anoxic environments and oil source bed genesis. *AAPG Bulletin*, **64(8)**, 1179-1209, https://doi.org/10.1306/2F91945E-16CE-11D7-8645000102C1865D.

DiCaprio, L., Müller, R.D., & Gurnis, M. 2010. A dynamic process for drowning carbonate reefs on the northeastern Australian margin. *Geology*, **38(1)**, 11-14, https://doi.org/10.1130/G30217.1.

Dunham, K.C. & Wilson, A.A., 1985. Geology of the Northern Pennine Orefield, Vol. 2: Stainmore to Craven. Economic Memoir of the British Geological Survey.

Emmings, J.F., Davies, S.J., Vane, C.H., Moss-Hayes, V., & Stephenson, M. H. 2020. From marine bands to hybrid flows: Sedimentology of a Mississippian black shale. *Sedimentology*, **67(1)**, 261-304, https://doi.org/10.1111/sed.12642.

Erlich, R.N., Barrett, S.F., Ju, G.B. 1990. Seismic and geologic characteristics of drowning events on carbonate platforms. *AAPG bulletin*, **74(10)**, 1523-1537, https://doi.org/10.1306/0C9B250B-1710-11D7-8645000102C1865D.

Fraser, A.J., & Gawthorpe, R.L. 1990. Tectono-stratigraphic development and hydrocarbon habitat of the Carboniferous in northern England. *Geological Society London Special Publications*, **55(1)**, 49-86.

Friedrich, O., Erbacher, J., Moriya, K., Wilson, P.A., & Kuhnert, H. 2008. Warm saline intermediate waters in the Cretaceous tropical Atlantic Ocean. *Nature Geoscience*, **1(7)**, 453-457, https://doi.org/10.1038/ngeo217.

Gamo, T., Nozaki, Y., Sakai, H., Nakai, T., & Tsubota, H. 1986. Spacial and temporal variations of water characteristics in the Japan Sea bottom layer. *Journal of Marine Research*, **44(4)**, 781-793.

Gonthier, E.G., Faugères, J.C., & Stow, D.A.V. 1984. Contourite facies of the Faro drift, Gulf of Cadiz. *Geological Society London Special Publications*, **15(1)**, 275-292.

Gorsline, D.S., Nava-Sanchez, E., & de Nava, J.M. 1996. A survey of occurrences of Holocene laminated sediments in California Borderland Basins: products of a variety of depositional processes. *Geological Society London Special Publications*, **116(1)**, 93-110.

Halfar, J., Godinez-Orta, L., Mutti, M., Valdez-Holguín, J. E., Borges, J. M. 2004. Nutrient and temperature controls on modern carbonate production: an example from the Gulf of California, Mexico. *Geology*, **32(3)**, 213-216, https://doi.org/10.1130/G20298.1.

Halfar, J., Godinez-Orta, L., Mutti, M., Valdez-Holguin, J.E., Borges, J.M. 2006. Carbonates calibrated against oceanographic parameters along a latitudinal transect in the Gulf of California, Mexico. *Sedimentology*, **53(2)**, 297-320, https://doi.org/10.1111/j.1365-3091.2005.00766.x.

Hallock, P. 1988. The role of nutrient availability in bioerosion: consequences to carbonate buildups. *Palaeogeography, Palaeoclimatology, Palaeoecology*, **63(1-3)**, 275-291, https://doi.org/10.1016/0031-0182(88)90100-9.

Hallock, P., Schlager, W. 1986. Nutrient excess and the demise of coral reefs and carbonate platforms. *Palaios*, 389-398, https://doi.org/10.2307/3514476.

Hall-Spencer, J.M., Rodolfo-Metalpa, R., Martin, S., Ransome, E., Fine, M., Turner, S. M., Buia, M.C. 2008. Volcanic carbon dioxide vents show ecosystem effects of ocean acidification. *Nature*,**454(7200)**, 96-99, https://doi:10.1038/nature07051.

Hennekam, R., van der Bolt, B., van Nes, E.H., de Lange, G.J., Scheffer, M., & Reichart, G.J. 2020. Early-warning signals for marine anoxic events. *Geophysical Research Letters*, **47(20)**, e2020GL089183, https://doi.org/10.1029/2020GL089183.

Hiscott, R. N., Aksu, A. E., Mudie, P. J., Marret, F., Abrajano, T., Kaminski, M. A., & Yaşar, D. 2007. A gradual drowning of the southwestern Black Sea shelf: evidence for a progressive rather than abrupt Holocene reconnection with the eastern Mediterranean Sea through the Marmara Sea Gateway. *Quaternary International*, **167**, 19-34, https://doi.org/10.1016/j.quaint.2006.11.007.

Hornung, T., Krystyn, L., & Brandner, R. 2007. A Tethys-wide mid-Carnian (Upper Triassic) carbonate productivity crisis: evidence for the Alpine Reingraben event from Spiti (Indian Himalaya)? *Journal of Asian Earth Sciences*, **30(2)**, 285-302.

Hutchings, P.A. 1986. Biological destruction of coral reefs. *Coral reefs*, **4(4)**, 239-252.

Jenkyns, H. C. 2010. Geochemistry of oceanic anoxic events. *Geochemistry, Geophysics, Geosystems*, **11(3)**, https://doi.org/10.1029/2009GC002788.

Kiessling, W., & Simpson, C. 2011. On the potential for ocean acidification to be a general cause of ancient reef crises. *Global Change Biology*, **17(1)**, 56- 67, https://doi.org/10.1111/j.1365-2486.2010.02204.x.

Kiessling, W., Flügel, E., Golonka, J.A.N. 2003. Patterns of Phanerozoic carbonate platform sedimentation. *Lethaia*, **36(3)**, 195-225, https://doi.org/10.1080/00241160310004648.

Könitzer, S.F., Davies, S.J., Stephenson, M.H., & Leng, M.J. 2014. Depositional controls on mudstone lithofacies in a basinal setting: implications for the delivery of sedimentary organic matter. *Journal of Sedimentary Research*, **84(3)**, 198-214, https://doi.org/10.2110/jsr.2014.18.

Kump, L.R., Bralower, T.J., Ridgwell, A. 2009. Ocean acidification in deep time. *Oceanography*, **22(4)**, 94-107.

Kwiatkowski, L., Cox, P., Halloran, P.R., Mumby, P.J., Wiltshire, A.J. 2015. Coral bleaching under unconventional scenarios of climate warming and ocean acidification. *Nature Climate Change*, **5(8)**, 777-781, https://doi.org/10.1038/NCLIMATE2655.

Lees, A. 1975. Possible influence of salinity and temperature on modern shelf carbonate sedimentation. *Marine Geology*, **19(3)**, 159-198, https://doi.org/10.1016/0025-3227(75)90067-5.

Levin, L.A., Whitcraft, C.R., Mendoza, G.F., Gonzalez, J.P., & Cowie, G. 2009. Oxygen and organic matter thresholds for benthic faunal activity on the Pakistan margin oxygen minimum zone (700–1100 m). *Deep Sea Research Part II: Topical Studies in Oceanography*, **56(6-7)**, 449-471, https://doi.org/10.1016/j.dsr2.2008.05.032.

Macquaker, J.H., Keller, M.A., & Davies, S.J. 2010. Algal blooms and “marine snow”: Mechanisms that enhance preservation of organic carbon in ancient fine-grained sediments. *Journal of sedimentary Research*, **80(11)**, 934-942, https://doi.org/10.2110/jsr.2010.085.

Maria Mutti, & Helmut Weissert. 1995. Triassic monsoonal climate and its signature in Ladinian-Carnian carbonate platforms (Southern Alps, Italy). *Journal of Sedimentary Research*, **65 (3b)**, 357–367.

Martine, R.S. 1982. Petroleum Origin: Heavy Rains, River Plume, Ocean Stratification. *AAPG Bulletin*, **66(5)**, 625-626, https://doi.org/10.1306/03B5A15B-16D1-11D7-8645000102C1865D.

Masse, J.P., Fenerci-Masse, M. 2013. Drowning events, development and demise of carbonate platforms and controlling factors: The Late Barremian–Early Aptian record of Southeast France. *Sedimentary Geology*, **298**, 28-52, https://doi.org/10.1016/j.sedgeo.2013.09.004.

Matthews, A., Azrieli-Tal, I., Benkovitz, A., Bar-Matthews, M., Vance, D., Poulton, S. W., & Archer, C. 2017. Anoxic development of sapropel S1 in the Nile Fan inferred from redox sensitive proxies, Fe speciation, Fe and Mo isotopes. *Chemical Geology*, **475**, 24-39, https://doi.org/10.1016/j.chemgeo.2017.10.028.

Murray, J.W., Jannasch, H.W., Honjo, S., Anderson, R.F., Reeburgh, W.S., Top, Z., & Izdar, E. 1989. Unexpected changes in the oxic/anoxic interface in the Black Sea. *Nature*, **338(6214)**, 411-413.

Mutti, M., & Hallock, P. 2003. Carbonate systems along nutrient and temperature gradients: some sedimentological and geochemical constraints. *International Journal of Earth Sciences*, **92(4)**, 465-475.

Nameroff, T.J., Balistrieri, L.S., & Murray, J.W. 2002. Suboxic trace metal geochemistry in the eastern tropical North Pacific. *Geochimica et Cosmochimica Acta*, **66(7)**, 1139-1158, https://doi.org/10.1016/S0016-7037(01)00843-2.

Opdyke, B.N., & Wilkinson, B.H. 1988. Surface area control of shallow cratonic to deep marine carbonate accumulation. *Paleoceanography*, **3(6)**, 685-703, https://doi.org/10.1029/PA003i006p00685.

Peng, J. 2021. Sedimentology of the Upper Pennsylvanian organic-rich Cline Shale, Midland Basin: From gravity flows to pelagic suspension fallout. *Sedimentology*, **68(2)**, 805-833, https://doi.org/10.1111/sed.12811.

Petrash, D.A., Gueneli, N., Brocks, J.J., Méndez-Dot, J.A., Gonzalez-Arismendi, G., Poulton, S. W., Konhauser, K.O. 2016. Black shale deposition and early diagenetic dolomite cementation during Oceanic Anoxic Event 1: the mid-Cretaceous Maracaibo Platform, northwestern South America. *American Journal of Science*, **316(7)**, 669-711, https://doi.org/10.2475/07.2016.03.

Qiu, Z., Zou, C., Mills, B. J., Xiong, Y., Tao, H., Lu, B., & Poulton, S. W. 2022. A nutrient control on expanded anoxia and global cooling during the Late Ordovician mass extinction. *Communications Earth & Environment*, **3(1)**, 82, https://doi.org/10.1038/s43247-022-00412-x.

Railsback, L.B., Ackerly, S.C., Anderson, T.F., & Cisneti, J.L. 1990. Palaeontological and isotope evidence for warm saline deep waters in Ordovician oceans. *Nature*, **343(6254)**, 156-159.

Reijmer, J.J. 2021. Marine carbonate factories: review and update. *Sedimentology*, **68(5)**, 1729-1796, https://doi.org/10.1111/sed.12878.

Rohling, E.J., & Hilgen, F.J. 2007. The eastern Mediterranean climate at times of sapropel formation: a review. *Netherlands Journal of Geosciences.*

Ryan, W.B., Pitman III, W.C., Major, C.O., Shimkus, K., Moskalenko, V., Jones, G. A., & Yüce, H. 1997. An abrupt drowning of the Black Sea shelf. *Marine geology*, **138(1-2)**, 119-126, https://doi.org/10.1016/S0025-3227(97)00007-8.

Saraswat, R., Kouthanker, M., Kurtarkar, S.R., Nigam, R., Naqvi, S.W.A., Linshy, V.N. 2015. Effect of salinity induced pH/alkalinity changes on benthic foraminifera: A laboratory culture experiment. *Estuarine, Coastal and Shelf Science*, **153**, 96-107, https://doi.org/10.1016/j.ecss.2014.12.005.

Scheibner, C., & Speijer, R.P. 2008. Late Paleocene–early Eocene Tethyan carbonate platform evolution- A response to long-and short-term paleoclimatic change. *Earth-Science Reviews*, **90(3-4)**, 71-102, https://doi.org/10.1016/j.earscirev.2008.07.002.

Schieber, J., Southard, J., & Thaisen, K. 2007. Accretion of mudstone beds from migrating floccule ripples. *Science*, **318(5857)**, 1760-1763, https://doi.org/10.1126/science.1147001.

Schieber, J., Southard, J.B., & Schimmelmann, A. 2010. Lenticular shale fabrics resulting from intermittent erosion of water-rich muds—interpreting the rock record in the light of recent flume experiments. *Journal of Sedimentary Research*, **80(1)**, 119-128, https://doi.org/10.2110/jsr.2010.005.

Schlager, W. 1981. The paradox of drowned reefs and carbonate platforms. *Geological Society of America Bulletin*, **92(4)**, 197-211, https://doi.org/10.1130/0016-7606(1981)92<197:TPODRA>2.0.CO;2.

Schlager, W. 1999. Scaling of sedimentation rates and drowning of reefs and carbonate platforms. *Geology*, **27(2)**, 183-186, https://doi.org/10.1130/0091-7613(1999)027<0183:SOSRAD>2.3.CO;2.

Shanks, A.L., & Trent, J.D. 1980. Marine snow: sinking rates and potential role in vertical flux. *Deep Sea Research Part A. Oceanographic Research Papers*, **27(2)**, 137-143, https://doi.org/10.1016/0198-0149(80)90092-8.

Simms, M.J., & Ruffell, A.H. 1990. Climatic and biotic change in the late Triassic. *Journal of the Geological Society*, **147(2)**, 321-327.

Speed, R.C., & Sleep, N.H. 1982. Antler orogeny and foreland basin: A model. *Geological Society of America Bulletin*, **93(9)**, 815-828, https://doi.org/10.1130/0016-7606(1982)93<815:AOAFBA>2.0.CO;2.

Stow, D.A.V., & Piper, D.J.W. 1984. Deep-water fine-grained sediments: facies models. *Geological Society London Special Publications*, **15(1)**, 611-646.

Szulczewski, M., Belka, Z., Skompski, S. 1996. The drowning of a carbonate platform: an example from the Devonian-Carboniferous of the southwestern Holy Cross Mountains, Poland. *Sedimentary Geology*, **106(1-2)**, 21-49, https://doi.org/10.1016/0037-0738(95)00145-X.

Tissot, B., Demaison, G., Masson, P., Delteil, J. R., & Combaz, A. 1980. Paleoenvironment and petroleum potential of middle Cretaceous black shales in Atlantic basins. *AAPG Bulletin*, **64(12)**, 2051-2063, https://doi.org/10.1306/2F919738-16CE-11D7-8645000102C1865D.

Turner, J.T. 2015. Zooplankton fecal pellets, marine snow, phytodetritus and the ocean's biological pump. *Progress in Oceanography*, **130**, 205-248, https://doi.org/10.1016/j.pocean.2014.08.005.

Tyson, R.V., & Pearson, T.H. 1991. Modern and ancient continental shelf anoxia: an overview. *Geological Society London Special Publications*, **58(1)**, 1-24.

Vihtakari, M. 2015. Bivalves as indicators of environmental perturbations related to climate and ocean acidification. PhD thesis, The Arctic University of Norway.

Warner, M.E., Fitt, W.K., Schmidt, G.W. 1996. The effects of elevated temperature on the photosynthetic efficiency of zooxanthellae in hospite from four different species of reef coral: a novel approach. *Plant, Cell & Environment*, **19(3)**, 291-299, https://doi.org/10.1111/j.1365-3040.1996.tb00251.x.

Waters, C.N., Millward, D., & Thomas, C.W. 2014. The Millstone Grit group (pennsylvanian) of the northumberland–solway basin and alston block of northern England. *Proceedings of the Yorkshire Geological Society*, **60(1)**, 29-51.

Wignall, P.B. 1994. *Black shale*. Oxford University Press: New York, NY, USA.

Wilson, M.E.J., & Vecsei, A. 2005. The apparent paradox of abundant foramol facies in low latitudes: their environmental significance and effect on platform development. *Earth-Science Reviews*, **69(1-2)**, 133-168, https://doi.org/10.1016/j.earscirev.2004.08.003.

Wilson, P.A., Jenkyns, H.C., Elderfield, H., Larson, R.L. 1998. The paradox of drowned carbonate platforms and the origin of Cretaceous Pacific guyots. *Nature*, **392(6679)**, 889-894.

Zirks, E., Krom, M., Schmiedl, G., Katz, T., Xiong, Y., Alcott, L. J., & Goodman-Tchernov, B. 2021. Redox evolution and the development of oxygen minimum zones in the Eastern Mediterranean Levantine basin during the early Holocene. *Geochimica et Cosmochimica Acta*, **297**, 82-100, https://doi.org/10.1016/j.gca.2021.01.009.

Chapter 2: Carbonate shutdown, phosphogenesis and the variable style of marine anoxia in the late Famennian (Late Devonian) in western Laurentia

Published on Palaeogeography, Palaeoclimatology, Palaeoecology

Li, S., Wignall, P. B., Poulton, S. W., Hedhli, M., & Grasby, S. E. (2022). Carbonate shutdown, phosphogenesis and the variable style of marine anoxia in the late Famennian (Late Devonian) in western Laurentia. Palaeogeography, Palaeoclimatology, Palaeoecology, 589, 110835.

Carbonate shutdown, phosphogenesis and the variable style of marine anoxia in the late Famennian (Late Devonian) in western Laurentia

Sen Li[1], Paul B. Wignall[1], Simon W. Poulton[1], Makram Hedhli[3], Stephen E. Grasby[2,3]

[1]University of Leeds, School of Earth and Environment, Leeds, LS2 9JT, UK

[2]University of Calgary, Department of Geoscience, 2500 University Drive NW, Calgary, Alberta T2N 1N4, Canada

[3]Geological Survey of Canada, 3303-33rd Street NW, Calgary, Alberta T2L 2A7, Canada

2.1 Abstract

The shutdown of carbonate productivity and its replacement by black shale deposition is often observed in the geological record and yet the factors driving such a change are debated. The latest Famennian of western Laurentia (present day North America) provides a good example of a limestone – black shale transition that is roughly contemporaneous with the global Hangenberg Crisis – a series of environmental and biotic changes associated with the widespread development of black shale deposition. However, in western Laurentia limestone deposition ceased and black shale deposition began prior to this crisis. Examining the type section of the Exshaw Formation at Jura Creek (Alberta) reveals that declining seafloor oxygen levels were likely responsible for the loss of carbonate productivity, followed by phosphogenesis of the youngest carbonates. The top surface of the limestone is a hard ground that was reworked, possibly by internal wave action, producing a lag of phosphatic clasts and pyrite grains including giant framboids (reaching 100 µm diameter) and polyframboids. The subsequent redox history of the lower Exshaw Formation shows substantial variations. Initially, the occurrence of small framboids, and elevated Fe_{HR}/Fe_T and Fe_{py}/Fe_{HR} combined with enhanced U, Mo and Re concentrations indicates intense euxinia in the water column. These conditions were replaced by ferruginous anoxic conditions recorded in radiolarian-rich black shales that have moderate concentrations of trace metals, and low pyrite content, as confirmed both by low Fe_{py}/Fe_{HR} ratios and scanning electron microscope observation. Mo-U covariation trends suggest that Mo enrichment under ferruginous conditions was promoted by drawdown in association with Fe minerals precipitated in the water column. The return of better ventilated conditions around the Devonian/Carboniferous boundary is marked by a decrease in trace metal content and the loss of syngenetic pyrite. The Hangenberg Crisis is thus marked by an improvement in ventilation, from euxinic to ferruginous conditions in our study, and evidence from other basins in western North America suggests an even greater increase in oxygenation at this time.

Keywords: carbonate demise; framboidal pyrite; Exshaw Formation; Hangenberg crisis; black shale

2.2 Introduction

The demise of carbonate platforms can be due to a number of factors including the encroachment of siliciclastic sediment (e.g. Wilmsen, 2000) and salinity changes (e.g. Hornung et al., 2007). However, in many cases carbonates are overlain by a hiatal surface – suggesting little sediment influx – and black shales (e.g. Caplan et al., 1996; Petrash et al., 2016). In these circumstances it is tempting to explain the shutdown of carbonate productivity to the development of the anoxic environments in which black shales accumulate. This could either be driven by nutrient influx and elevated primary productivity or a change in circulation regime and a decline in bottom water oxygen renewal. Often it is difficult to truly assess such shutdown mechanisms because the key evidence lies at a hiatal surface and so is associated with little or no sedimentary record. Here we address this issue with a detailed study of one such limestone-to-black shale transition: the boundary between the Palliser Formation carbonates and Exshaw Formation black shales from the latest Devonian of western Canada (Johnstone et al., 2010). This changeover was part of a widespread transition that encompasses the Hangenberg Crisis – an interval that also saw the widespread loss of carbonate deposition in Europe (Kaiser et al., 2016).

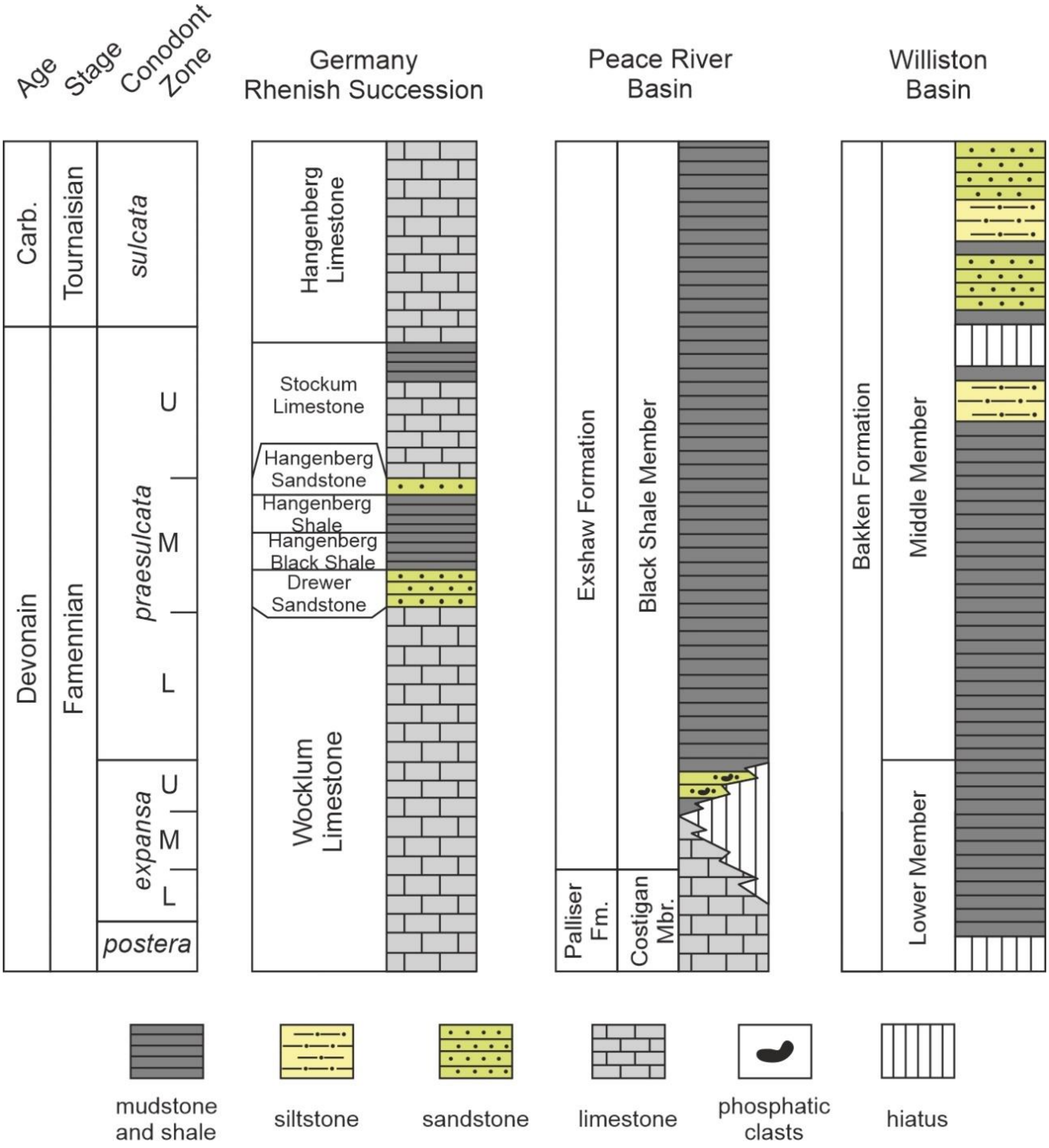

Fig.2.1 Correlation of latest Devonian- earliest Carboniferous stratigraphy from the Canadian Rocky Mountains (Caplan and Bustin 1998), Rhenish Basin, Germany (Kaiser et al. 2016) and Williston Basin, Montana, the Dakotas and the southern prairies of Canada (Smith and Bustin 1998; Hogancamp and Pocknall, 2018). Mbr. =Member; Fm. =Formation; Carb. =Carboniferous. Correlation is achieved based on conodont biostratigraphy.

The latest Devonian was marked by major biotic and environmental events, including a mass extinction, major sea-level oscillations linked to glaciation in the southern hemisphere, and widespread anoxia and shutdown of carbonate productivity (Becker, 1993; Walliser, 1996; Carmichael et al., 2016; Kaiser et al., 2016). This series of events is known as the Hangenberg Crisis, named after stratigraphic units in Germany (Fig. 2.1). The crisis began in the late Famennian following a brief sea-level fall around the end of the Lower *S. praesulcata* Zone (Fig. 2.1). This is thought to have been of glacioeustatic origin, and saw the Drewer Sandstone replace the Wocklum Limestone in Germany (Sandberg et al., 2002). Subsequent transgression and deepening in the early part of the Mid *praesulcata* Zone was associated with the spread of black shales, such as the Hangenberg Black Shale (Walliser, 1996; Caplan and Bustin, 1999; Kumpan et al., 2019). These organic-rich strata replaced limestones in many regions, with carbonate productivity generally being low throughout the Hangenberg Crisis. A contemporaneous, positive excursion in the δ^{238}U record suggests extensive U drawdown linked to the development of globally extensive anoxia (Zhang et al., 2020) for up to 80 kyr (Myrow et al., 2013). Deposition of Hangenberg anoxic facies was terminated in the late Mid *praesulcata* Zone, either due to increased siliciclastic input producing the Hangenberg Sandstone, or by the development of marls and oolites (Fig. 2.1). Carbonate deposition only resumed in Europe with the Stockum Limestone (Fig. 2.1) in the Upper *praesulcata* Zone (Bábek et al., 2016).

Extensive black shales also occur in the Devonian-Carboniferous transitional strata in western North America, where they too overlie extensive carbonate deposits (Savoy, 1992; Smith et al., 1995; Savoy et al., 1999; Hart and Hofmann, 2018; Over, 2021). Similar to the European anoxic facies, there is much debate over the cause of this transition in North America. Regionally, two black shale units developed across several depocentres in the region (Fig. 2.1), specifically in the lower member of the Bakken Formation and the lower part of the Exshaw Formation (Smith and Bustin, 2000; Johnston et al., 2010). However, based on conodont biostratigraphy data it appears that black shale deposition began earlier than in Europe and persisted for longer (Johnston et al., 2010) (Fig. 2.1). It is thus unclear whether deposition of the Hangenberg black shales in Europe reflects a global intensification of anoxia driven by a unified driver (such as climate change or eustasy), or if it was a coincidence of local causes.

Links between glaciation and the development of Hangenberg anoxia include the possibility that enhanced circulation in cooler oceans may have led to increased nutrient supply and elevated productivity, thereby creating water column anoxia (Caplan and Bustin, 1999, 2001; Sageman et al. 2003; Bábek et al., 2016; Kumpan et al., 2019). In western North America factors, such as tectonism and the degree of basin isolation may provide an alternative explanation for the occurrence of the anoxic facies that are only partly contemporaneous with the Hangenberg Crisis. The notion that limited circulation in semi-isolated basins was responsible for black shale deposition is supported by geochemical proxies for restriction (Richards et al., 2002; Algeo et al., 2007). However, other researchers favour a model in which eustatic transgression and deepening allowed oceanic nutrients to invade the North American epicontinental basins, fostering high productivity and black shale development (Savoy, 1992; Smith and Bustin, 1998; Caplan and Bustin, 1999, 2001). These debates also link to discussion on the water depth at which black shales form: some models envisage black shales forming in shallow lagoons beneath a stratified water column (Raasch, 1956; Petty, 2019), while others favour deposition beneath hundreds of metres of water (Webster, 1984; Savoy, 1992; Smith and Bustin, 1998).

Explaining the origin of a thin, phosphatic sandstone bed found at the base of the Exshaw Formation black shale (Fig. 2.1) may help in understanding why carbonate deposition was replaced with black shale accumulation. The phosphate-rich level has been attributed to four alternative circumstances: 1) as a result of a regression that terminated carbonate production prior to onlap and black shale development (Smith et al., 1995); 2) as a product of eutrophication that elevated primary productivity and caused the demise of carbonate production (Caplan et al., 1996); 3) as a storm deposit formed after carbonate shut down (Richards and Higgins, 1988; Egenhoff and Fishman, 2013); or 4) as a lag deposit formed by dissolution of underlying carbonate as a deep-water chemocline transgressed over a carbonate ramp (Caplan and Bustin, 1999, 2001). These scenarios all have very different implications for the cause of carbonate shut-down and black shale development.

In order to investigate these debates, we have undertaken an integrated petrographic and geochemical study of sedimentary facies and redox changes at the type location of the Exshaw Formation's lower member in western Alberta, Canada. We aim to assess how redox conditions evolved and how they may have contributed to carbonate deposition shutdown.

2.3 Regional geology

Important and much debated tectonic events associated with the Antler Orogeny occurred in western North America during the Late Devonian – Early Carboniferous (Root, 2001). There were several major depocenters in western Laurentia most notably the hydrocarbon-rich Williston Basin (Richards and Higgins, 1988; Hogencamp and Pocknall, 2018; Hart and Hofmann, 2018). This straddled the United States/ Canadian border and is found in present day North Dakota, South Dakota, easternmost Montana, and southern Saskatchewan and saw the deposition of the Bakken Formation. The lower member records the development of anoxic-euxinic conditions in the late Famennian *postera – praesulcata* zonal interval and was succeeded by a more heterolithic, burrowed, middle member following a short hiatus around the Devonian-Carboniferous boundary (Fig. 2.1) (Smith and Bustin, 2000; Egenhoff, 2017; Hogencamp and Pocknall, 2018). This in turn is overlain by another argillaceous unit, the Upper Bakken black shale, that records anoxic-dysoxic conditions (Borcovsky et al., 2017). West of the Williston Basin, in

Montana, the Sappington Basin also contains a Devonian-Carboniferous black shale unit, the Sappington Formation (di Pasquo et al. 2019; Browne et al., 2020). Like the Bakken Formation, the Sappington black shales occur as two separate members separated by more oxygenated facies developed during the Devonian-Carboniferous boundary interval.

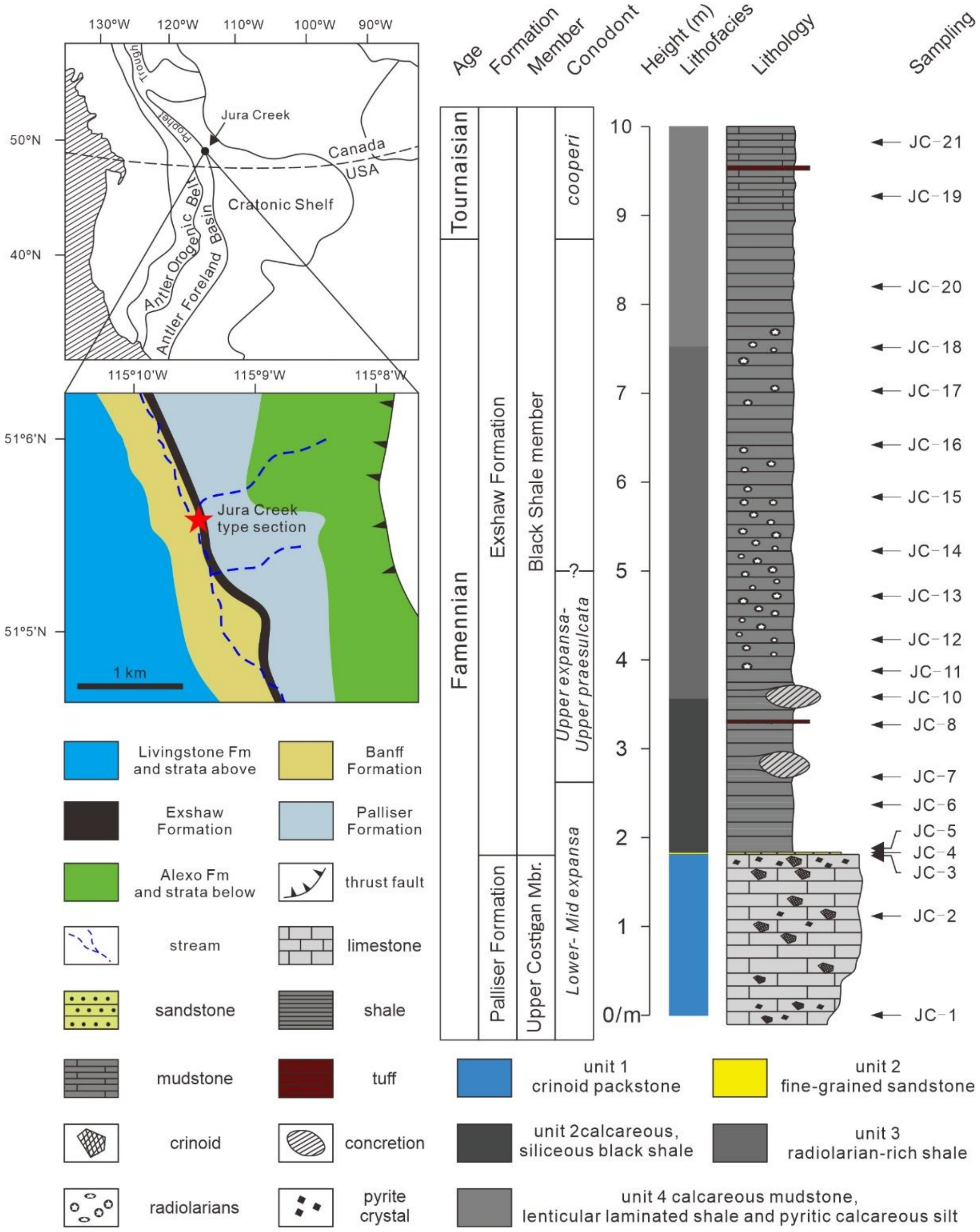

Fig. 2.2 Location of studied outcrop, stratigraphic log of the Jura Creek section and sample horizons. A simplified lithofacies column is introduced and used in the following figures. The approximate position of the Famennian-Tournaisian boundary is defined by Re-Os dating (Selby and Creaser 2005).

A separate depocenter, the Western Canada Sedimentary Basin, was also the locus of deposition of two black shale units separated by an organic-poor siltstone (Caplan and Bustin, 1999; Smith and Bustin, 2000; Johnston et al., 2010; Over, 2021). In this region, a Black Shale Member of the Exshaw Formation overlies carbonates of the Palliser Formation (Fig. 2.2), with a hiatus spanning up to three conodont Zones at the contact (Johnston et al., 2010). The conodont fauna of the Exshaw Formation indicates that the onset of black shale deposition began in the earlier part of the *expansa* Zone (Richards et al., 1994; Johnston et al., 2010). This is roughly contemporaneous with the onset of black shale deposition in the adjacent Williston Basin although it clearly predates Hangenberg anoxia in western Europe (Fig. 2.1). However, anoxic deposition persisted into the Carboniferous in the Western Canada Sedimentary Basin and the upper part of the Black Shale Member thus records the Hangenberg Event.

Our study focusses on the type section of the Exshaw Formation at Jura Creek, a tributary to the Bow River, western Alberta (Richards and Higgins, 1988; Richards et al., 1994; Fig. 2.2). A thin, phosphatic sandstone, of highly debated origin (see above), separates carbonates of the upper Costigan Member of the Palliser Formation from the overlying black shales of the Exshaw Formation (Fig. 2.2). The phosphatic sandstone is overlain by nearly 10 m of black shale that becomes calcareous in the upper third. Conodonts indicate that the lower, non-calcareous black shales belong to the lower part of the *expansa* Zone, with the central part ranging to the upper *praesulcata* zones, whilst the Devonian-Carboniferous boundary occurs within a ~4m-thick interval (Richards and Higgins, 1988; Richards et al., 1994; Over, 2021; Fig. 2.2).

2.4 Methods

2.4.1 Sample preparation and optical microscopy

A total of 21 shale and carbonate samples were collected from the Jura Creek section (Fig. 2.2). Minor weathered surfaces were removed and samples with visible signs of alteration and/or veining were rejected at this point. An agate mortar was used to crush samples into homogeneous powder (< 60 µm) for geochemical analyses. Microfacies analyses of carbonates and shales were also performed via petrographic microscopy and SEM. Nineteen polished blocks of around 5 cm^2 were prepared, coated in carbon, and examined using a TESCAN VEGA3 SEM under backscatter mode.

2.4.2 Major elements

Total organic carbon (TOC) analyses were determined on a LECO Carbon-Sulfur analyzer. Samples were de-carbonated prior to analysis using 50 vol% HCl. Replicate analyses of certified reference material (Soil LCRM with carbon content of 10.8 ± 0.26 wt%) gave a relative standard deviation (RSD) of 1%, and accuracy was ensured by analyses within 1% of reported values. Other major and trace elements were analysed following a total dissolution (Alcott et al., 2020). After ashing at 550 °C for 8 h, samples were quantitatively digested using concentrated HNO_3, HF and $HClO_4$, and left to dry before addition of H_3BO_3 to prevent the formation of Al complexes. Finally, the residues were re-dissolved with near-boiling HNO_3 and diluted with ultrapure 18MΩ H_2O prior to analysis by ICP-OES (major elements) and ICP-MS (trace elements). Accuracy and precision, estimated from repeat analyses of USGS (United State Geological Survey) standard SGR-1b (Green River Shale), were better than 5%. Enrichment factors (EF) were used to assess the behaviour of Mo, U, V and Re in siliciclastic intervals (i.e. carbonates from unit 1 and the phosphatic sandstone from unit 2 were excluded), where $EF = (metal/Al)_{sample}/(metal/Al)_{AUC}$, and AUC represents average upper crust (McLennan, 2001).

2.4.3 Fe phase partitioning

Sequential Fe extractions were performed according to the technique of Poulton and Canfield (2005). The procedure targets different operationally-defined Fe pools that are considered highly reactive (Fe_{HR}) towards dissolved sulphide in anoxic surface environments

(Raiswell and Canfield, 1998; Poulton and Canfield, 2005; Poulton, 2021). The first step targets carbonate-associated iron (Fe_{carb}) via a 1 M sodium acetate extraction performed at pH 4.5 and 50 °C for 48 h. This was followed by a sodium dithionite extraction (2 h at room temperature), which targets Fe (oxyhydr)oxide minerals (Fe_{ox}). Finally, a 0.2 M ammonium oxalate/0.17 M oxalic acid solution was used (6 h at room temperature) to target magnetite (Fe_{mag}). The concentration of Fe phases was determined using a Thermo Scientific iCE-3000 series flame atomic absorption spectrometer. Acid volatile sulphide (AVS) and pyrite (Fe_{py}) were determined on a separate sub-sample via a two-step chromous chloride distillation (Canfield et al., 1986), with the liberated sulphide trapped as Ag_2S and concentrations of sulphide determined gravimetrically. Replicate extractions of an international reference material (WHIT; Alcott et al., 2021) gave a RSD of <5% for each Fe pool, with analyses within 2% of reported values.

Acid volatile sulphide was present at very low concentration in four samples, with only one sample (JC-4) containing a high concentration (Table 2.1). Sample JC-4 is a sandstone within the phosphatic horizon and has a high Zn concentration (Table 2.1), with petrographic observations demonstrating that much of this Zn is in the form of ZnS (which would be dissolved during the AVS extraction) (see *Pyrite petrography* section). Thus, we assign the AVS in this sample to ZnS, rather than FeS. For consistency, we also consider the minor AVS present in the four samples with low concentrations to dominantly reflect metal sulphides other than FeS. Note, however, that for these four samples, the low AVS concentrations mean that our results are unaffected by whether we assign the AVS to FeS or to other metal monosulphides. Given these considerations, we hereon define Fe_{HR} as the sum of $Fe_{carb} + Fe_{ox} + Fe_{mag} + Fe_{py}$ (Poulton et al., 2004; Poulton and Canfield, 2011).

Table 2.1 Geochemical data for the Jura Creek samples. TOC = total organic carbon, AVS. = acid-volatile sulphide, ND = not determined. LQD = limit of quantification

Unit	Sample	Lithofacies No.	Height (m)	TOC (wt%)	Fe$_{carb}$ (wt%)	Fe$_{ox}$ (wt%)	Fe$_{mag}$ (wt%)	Fe$_{py}$ (wt%)	AVS (wt%)	Fe$_{T}$ (wt%)	Al (wt%)	P (ppm)	Mo (ppm)	U (ppm)	V (ppm)	Re (ppb)	Zn (ppm)
4	JC-21	6	9.82	0.22	0.59	0.02	0.02	1.18	0.03	1.96	2.95	420.4	0.79	1.12	58.69	14.59	10.57
	JC-19	7	9.22	0.65	0.75	0.04	0.02	1.52	0.05	2.37	3.75	482.0	3.47	2.04	69.92	4.65	31.34
	JC-20	5	8.22	1.77	0.44	0.06	0.02	2.57	0.00	3.68	7.66	523.2	7.70	2.39	221.1	12.64	76.20
3	JC-18	4	7.52	3.81	0.04	0.37	0.02	0.15	0.00	0.81	5.58	89.00	53.80	10.23	1122	60.51	124.8
	JC-17		7.02	4.36	0.07	0.55	0.02	0.14	0.00	1.27	7.21	128.1	78.20	11.38	1576	83.34	188.5
	JC-16		6.42	4.19	0.18	0.73	0.02	0.15	0.00	1.36	5.28	192.6	69.51	10.77	1289	49.68	183.8
	JC-15		5.82	4.44	0.03	0.31	0.02	0.16	0.00	0.82	5.6	68.03	69.53	10.61	1400	71.78	65.79
	JC-14		5.22	4.36	0.03	0.39	0.03	0.09	0.00	0.72	3.62	81.00	79.24	9.72	1167	31.95	93.68
	JC-13		4.72	3.91	0.02	0.24	0.02	0.12	0.00	0.58	3.29	107.2	74.03	8.09	1093	39.86	73.56
	JC-12		4.22	3.60	0.05	0.22	0.01	0.09	0.00	0.56	3.76	57.42	39.82	9.25	1205	28.35	35.56
	JC-11		3.87	4.20	ND	ND	ND	ND	ND	0.21	3.00	LQD	53.55	6.51	1147	34.98	26.74
	JC-10		3.57	3.48	0.07	0.84	0.02	0.16	0.00	1.31	3.86	330.1	72.12	13.49	1466	37.88	240.2
2	JC-8		3.27	4.04	0.23	0.30	0.01	1.84	0.00	2.86	4.26	513.7	141.6	30.36	1855	174.2	153.6
	JC-7		2.67	4.15	0.11	0.14	0.01	0.58	0.00	1.04	3.78	106.4	53.15	13.07	479.2	34.03	17.39
	JC-6		2.37	5.11	0.22	0.16	0.01	1.30	0.00	1.97	4.16	259.2	79.59	20.15	386.0	31.14	17.56
	JC-5	3	1.87	4.00	0.63	0.01	0.01	2.65	0.00	3.12	3.22	375.5	76.59	22.57	173.1	61.23	227.9
	JC-4	2	1.82	0.61	0.96	0.02	0.02	9.00	1.23	9.22	3.15	12090	199.6	31.57	16.47	1065	27374
1	JC-3	1	1.8	0.12	0.38	0.03	0.01	6.54	0.07	6.8	0.65	1075	3.71	11.22	10.86	16.95	250.3
	JC-2		1.1	0.10	ND	ND	ND	ND	ND	0.28	0.38	179.2	2.40	0.78	5.46	6.65	12.97
	JC-1		0	0.07	ND	ND	ND	ND	ND	0.43	0.76	244.8	0.19	0.35	8.87	3.67	5.67

2.4.4 Framework for redox interpretations

We have combined three independent approaches for reconstructing water column and porewater redox conditions during deposition of the Jura Creek succession: pyrite framboid petrography, Fe speciation and trace metal systematics. Pyrite framboid sizes have been widely utilized to diagnose redox condition (Table 2.2), especially euxinic (anoxic, sulfidic water column) conditions (Wilkin et al., 1996; Wilkin and Barnes, 1997; Wignall and Newton, 1998; Wignall et al., 2010). In modern euxinic environments framboids form in the water column and only achieve a small size with narrow distribution (Wilkin et al., 1996), whereas framboids can grow larger and are accompanied by higher proportions of diagenetic pyrite in dysoxic conditions (Wilkin and Arthur, 2001; Wignall et al., 2010).

Table 2.2 Pyrite morphology variation in different redox settings (Bond and Wignall, 2010)

Redox conditions	Framboid parameters
Euxinic (persistently sulfidic lower water column)	small (mean 3- 5 μm), abundant, with narrow size range. Framboids dominate pyrite fraction.
Anoxic (no oxygen in the bottom water for long period)	Small (mean 4- 6 μm), abundant, with a few, larger framboids. Framboids dominate pyrite fraction.
Lower dysoxic (weakly oxygenated bottom water)	Mean 6- 10 μm, moderately common, with a few, larger framboids and some crystalline pyrite.
Upper dysoxic (partial oxygen restriction in bottom water)	Moderately common to rare, broad range of sizes, only a small proportion
Oxic (no oxygen restriction)	No framboids, rare pyrite crystals

We also use Fe speciation (Poulton and Canfield, 2005) to provide more detailed insight into the redox state of the water column. This technique is used to distinguish oxic, ferruginous (anoxic, Fe-containing) and euxinic water column conditions, whereby ratios of Fe_{HR} normalized to total Fe (Fe_T) < 0.22 suggest an oxic water column and Fe_{HR}/Fe_T ratios > 0.38 suggest anoxic water column conditions (Raiswell and Canfield, 1998; Raiswell et al., 2001; Poulton, 2002). Ratios of 0.22-0.38 are considered to be equivocal (Poulton and Canfield, 2011; Poulton, 2021). For samples deposited under anoxic water column conditions, Fe_{py}/Fe_{HR} ratios are used to distinguish euxinic from ferruginous conditions, whereby Fe_{py}/Fe_{HR} > 0.8 suggests euxinia, ratios of 0.6-0.8 are considered to potentially reflect euxinic depositional conditions, and $Fe_{py}/Fe_{HR} < 0.6$ implies ferruginous water column conditions (Poulton et al., 2004; Poulton and Canfield, 2011; Benkovitz et al., 2020; Poulton, 2021).

The different, redox-dependent behaviour of Mo, U, V and Re provides further insight into redox conditions. Molybdenum is delivered to the ocean as the largely unreactive molybdate anion (MoO_4^{2-}), and under oxic conditions may be removed to the sediments (generally at low concentration) through uptake by Fe-Mn (oxyhydr)oxide minerals at the sea bed (Bertine and Turekian, 1973). Under ferruginous conditions, extensive water column precipitation of Fe minerals such as Fe (oxyhydr)oxides or green rust (e.g. Zegeye et al., 2012) may draw down higher concentrations of Mo through a particulate shuttle mechanism (e.g. Algeo and Tribovillard, 2009; Tribovillard et al., 2012). By contrast, when a critical threshold of free H_2S is met under euxinic conditions, the molybdate anion is converted to particle-reactive thiomolybdate (Helz et al., 1996), commonly resulting in significant Mo enrichment in the sediments (Emerson and Huested, 1991; Helz et al., 1996; Erickson and Helz, 2000).

Uranium reduction primarily occurs in anoxic sediments rather than in the water column, and U is therefore enriched beneath anoxic bottom waters, regardless of whether euxinic or ferruginous conditions dominate (Anderson et al., 1989; Klinkhammer and Palmer, 1991; Partin et al., 2013). By contrast, vanadium is commonly incorporated into sediments as the vanadate ion ($H_2V(VI)O_4^-$) adsorbed onto Mn oxides, and may be released from sediments during Mn oxide reduction under dysoxic porewater conditions (Emerson and Huested, 1991; Nameroff et al., 2002). Under anoxic conditions, however, the vanadate released following Mn oxide reduction is reduced to the vanadyl ion ($V(IV)O_2^+$), which is highly surface-reactive and tends to be retained in the sediment (Emerson and Huested, 1991).

Rhenium is efficiently sequestered in the sediment under both euxinic and ferruginous conditions, as well as under dysoxic conditions when O_2 penetrates < 1 cm below the sediment–water interface (Crusius et al., 1996; Morford and Emerson, 1999). This specific behaviour has led to the use of elevated Re/Mo ratios as an indicator of dysoxic conditions at the sediment-water interface (e.g. Kendall et al., 2010; Schobben et al., 2020), which is predicated on the fact that Mo enrichments only occur under fully anoxic conditions, either through drawdown of particle-reactive thiomolybdate in the presence of dissolved sulphide (Emerson and Huested, 1991; Helz et al., 1996; Erickson and Helz, 2000), or via the particulate shuttle mechanism outlined above (Algeo and Tribovillard, 2009; Tribovillard et al., 2012). However, in the absence of a strong particulate shuttle for Mo under fully anoxic conditions, which would be typical of an anoxic, non-sulphidic setting where the precipitation and depositional flux of Fe minerals from the water column was not high, elevated Re/Mo ratios would potentially occur under anoxic, as well as dysoxic, water column conditions. Given that this particular scenario was likely a common feature of ancient anoxic, non-sulphidic (commonly ferruginous) marine environments, where large expanses of the sea floor constituted a source of Fe^{2+} to the water column, rather than being a sink for Fe_{HR} minerals (Poulton, 2021; Poulton and Canfield, 2011), we here consider the additional use of Re/U ratios. Re/U ratios have the potential to provide more robust insight into the development of dysoxic conditions in the water column and at the sediment-water interface, since sequestration of U only requires anoxic porewater conditions (Anderson et al., 1989; Klinkhammer and Palmer, 1991), and hence dysoxic conditions will specifically be characterised by elevated Re/U.

2.5 Results

2.5.1 Lithofacies

Based on petrological examination, we have divided the Jura Creek section into four informal units (Fig. 2.2). The first/lowest unit consists of limestone of the Costigan Member in Palliser Formation (at 0 – 1.87 m); the second includes a 10 cm-thick, phosphatic, sandstone bed at the base, as well as an overlying calcareous and siliceous black shale (1.87 – 3.57 m) of the basal Exshaw Formation, which contains large carbonate concretions (Fig. 2.2); the third unit is a siliceous (radiolarian-rich) shale (3.57 – 7.52 m) with concretions at the base; the fourth unit consists of lenticular-laminated shale, calcareous mudstone and pyritic calcareous silt (7.52 – 9.82 m).

Within these four units we define seven lithofacies based on petrographic observations (Table 2.3). The first unit is dominated by crinoidal packstone (Fig. 2.3a; Facies 1). Other than crinoid columnals, other bioclasts include ophiuroid fragments and echinoid spines (Figs. 2.3a, c). In the uppermost bed of unit 1 (sample JC-3) the crinoidal packstone also contains intraclasts of rounded wackestone, around 1 cm in diameter (Figs. 2.4a, b), and shows heterogenous distributed bioclasts (Figs. 2.3b, c). Extensive pyrite replacement occurs in the uppermost bed especially of echinoderm grains (Figs. 2.3d, 2.4a). Siliceous replacement was also observed in two forms: abundant dark, chert concretions in the topmost limestone, and chalcedonic quartz infilling voids within bioclasts (Figs. 2.4c, d).

The thin, phosphatic sandstone bed (sample JC-4; Facies 2) separating the Costigan Member and the Exshaw black shale consists of three distinct layers (Fig. 2.5a). A lower carbonate layer (L1) consists of irregular shaped (possibly abraded) fragments of echinoderms in a fine dolomitic matrix (Fig. 2.5b). The overlying layer (L2), a phosphatic sandstone, is dominated by angular, fine

Table 2.3 Lithofacies, defined by petrographic features, and their interpreted environmental conditions from the Jura Creek section.

Lithofacies No.	Lithofacies	Petrological description	Dominant clasts	Mineral composition	Distribution	Pyrite content	Environmental Interpretation
1	Crinoidal packstone	Bioclasts and micrite matrix	Echinoderms, calcisphere and ophiuroid (Figs. 2.3a, c)	Mainly calcite, some pyrite and chert replacement	Topmost part of Costigan Member (JC-1 to JC-3)	Lower content in JC-1 and JC-2 but high in JC-3	Mid-ramp
2	Phosphatic sandstone	Grained supported with pyrite and calcite cement	Quartz, feldspar and pyrite, phosphatised clasts and bone fragments (Fig. 2.5)	Quartz, feldspar, phosphate, pyrite and calcite cement	Basal bed of Lower Exshaw Shale Member (JC-4)	Abundant pyrite both as cement, giant framboids and polyframboids	Transgressional lag in a mid- ramp setting
3	Black calcareous shale	Laminae of clay-rich and calcite-rich layers with organic matter	Mostly clay-grade sediment but with calcite microcrystals (Fig. 2.7a)	Clay, calcite and pyrite	Basal part of Lower Exshaw Shale (JC-5)	Abundant small framboids	Euxinic, basinal setting
4	Black siliceous shale	scattered silty quartz or radiolarian	Mostly clay-grade sediment but with radiolarians, and silt-grade quartz, (Figs. 2.7b,c)	Clay, silica and pyrite	Middle and upper part of the Lower Exshaw Shale (JC-6 to JC-8; JC-10 to 18)	Some samples have abundant small framboids, other samples are pyrite free	euxinic bottom waters but pyrite-free samples recording ferruginous conditions, all in a basinal setting
5	Lenticular laminated shale	Thin beds and lenticular laminae consisting of flattened lenses of clay clasts	Mostly clay-grade sediment but with silt-grade quartz (Fig. 2.7d)	Clay, silica and pyrite	Upper part of Lower Exshaw Shale (JC-20)	Common pyrite, in form of both euhedral crystals and framboids	Dysoxic bottom waters with sulfidic sediment
6	Calcareous mudstone	Well-sorted calcite grains with small amount of bioclasts	Ophiuroid, bivalves and calcite microcrystal (Fig. 2.7e)	Clay and calcite	Top part of section (JC-19)	Common pyrite, in form of both euhedral crystals and framboids	Dysoxic bottom waters with sulfidic sediment
7	Pyritic calcareous silt	Well-sorted sand grains (calcite crystal)	Calcite microcrystasl (Fig. 2.7f)	Calcite, pyrite	Top part of section (JC-21)	Rare pyrite, mainly occurs as scattered crystals	Weakly dysoxic bottom waters with sulfidic sediment

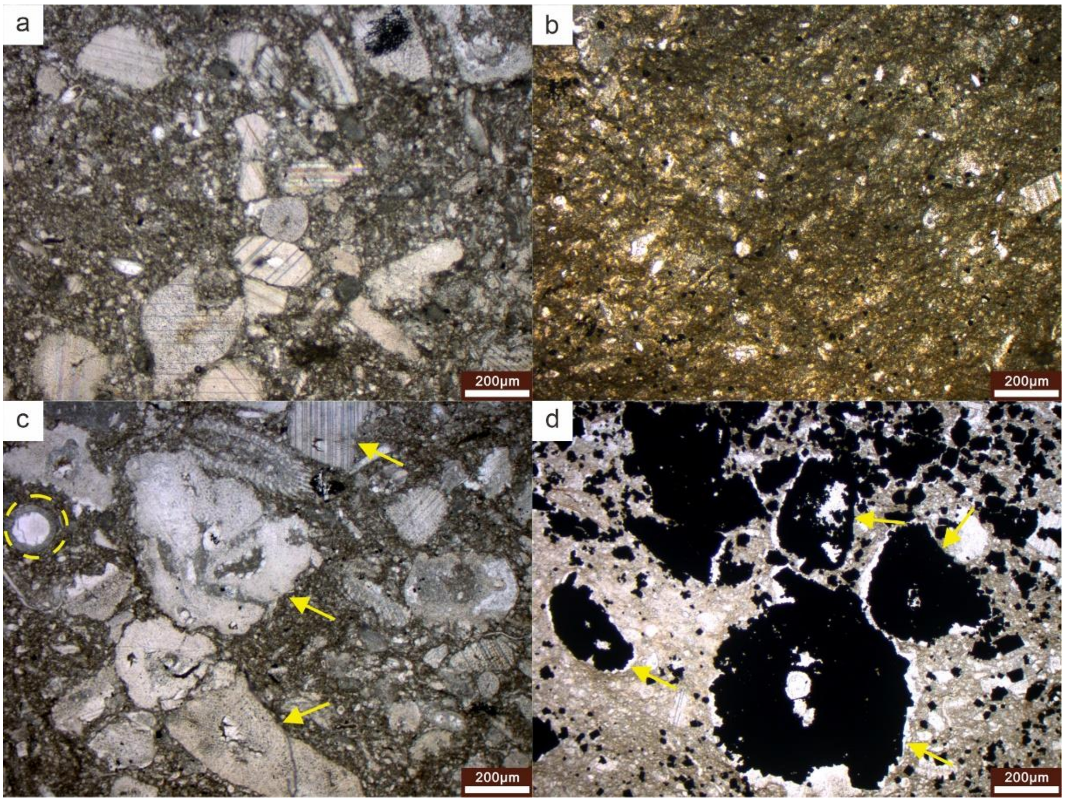

Fig. 2.3 Petrographic features of limestone in the Jura Creek section. (a) sample JC-2: packstone consisting of abundant bioclasts, mostly from echinoderm, within calcium mud matrix; (b) sample JC-3: middle part of limestone (see "f" area in Fig. 2.4a), packstone bearing limited bioclasts, bioclastic wackestone; (c) sample JC-3: bottom part of limestone (see "e" area in Fig. 2.4a), packstone bearing crinoid fragments (yellow arrows) and calcisphere (yellow circle); (d) sample JC-3: top part of limestone (see "g" area in Fig. 2.4a) showing crinoid fragments selectively replaced by pyrite (yellow arrows).

sand-size grains of quartz and feldspar, plus phosphate and pyrite grains (Fig. 2.5b). The contact between L1 and L2 is sharp, although sand grains are intermixed with dolomite rhombs at the transition, indicating that L1 was not lithified prior to deposition of L2 (Fig. 2.5c). Within L2, rounded phosphate clasts, up to 1.5 cm in length, are also seen (Fig. 2.5a). These contain bioclast fragments (replaced by pyrite) suggesting that they are phosphatised limestone clasts (Fig. 2.6f). Apart from the phosphatised clasts, L2 is dominated by sand grains and pyrite polyframboids and has a calcite cement. In the upper layer (L3), the cement is dominated by pyrite (Figs. 2.5d, 2.6b), except in the topmost part where calcite cement again occurs (Fig. 2.5e). L3 contains quartz,

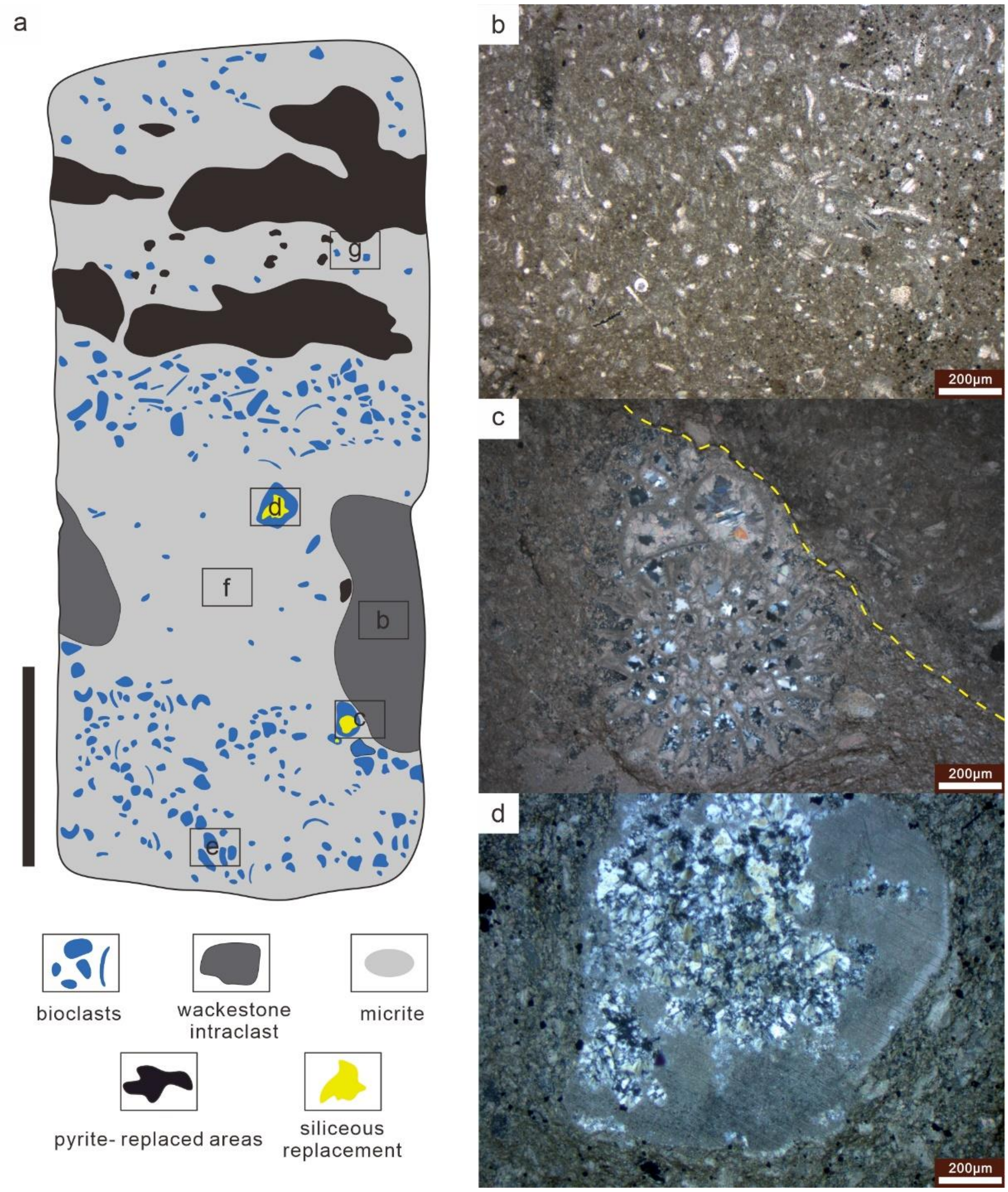

Fig. 2.4 Petrographic features of rudaceous limestone (sample JC-3). (a) sketch of lithofacies in limestone sample JC-3, consisting of bioclastic wackestone with intraclasts and abundant pyrite in the upper part. Black bar on the left side indicates a scale of 1 cm; positions of parts b, c and d are marked, and e, f and g refer to Fig. 2.3 parts c, b and d, respectively; (b) wackestone fabric within intraclast with small bioclast fragments; (c) bryozoan chamber infilled with quartz (cross polarized light). Dotted yellow line delineates the boundary of a wackestone intraclast; (d) large crinoid fragment with extensive siliceous replacement (cross polarized light).

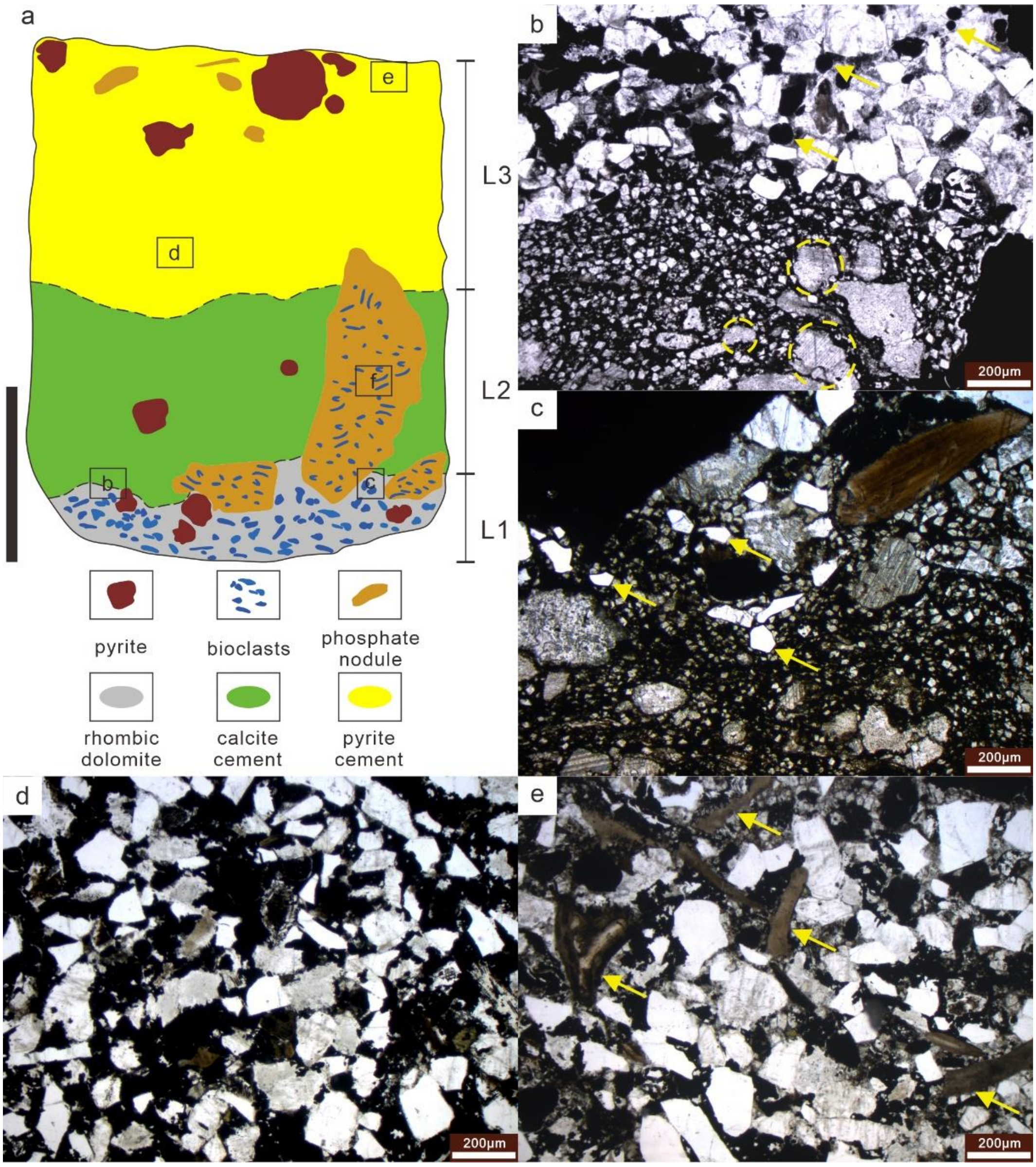

Fig. 2.5 Petrographic features of sample JC-4 (facies 2). (a) sketch of the lithofacies in the sandstone, showing three distinct layers. The black bar indicates a scale of 1 cm; positions of b, c and d are marked; f is the position of the SEM image in Fig. 2.6f. Photomicrographs showing: (b) rhombic dolomite and reworked crinoid fragments (some examples circled in yellow), and pyrite gains (yellow arrows) seen at contact between layers 1 and 2; (c) quartz grains (yellow arrows) with bioclasts and rhombic dolomite; (d) sand grains of quartz and feldspar cemented by pyrite in layer 3; (e) phosphatic bioclasts (yellow arrows), likely fish bones, in sandstone of layer 3.

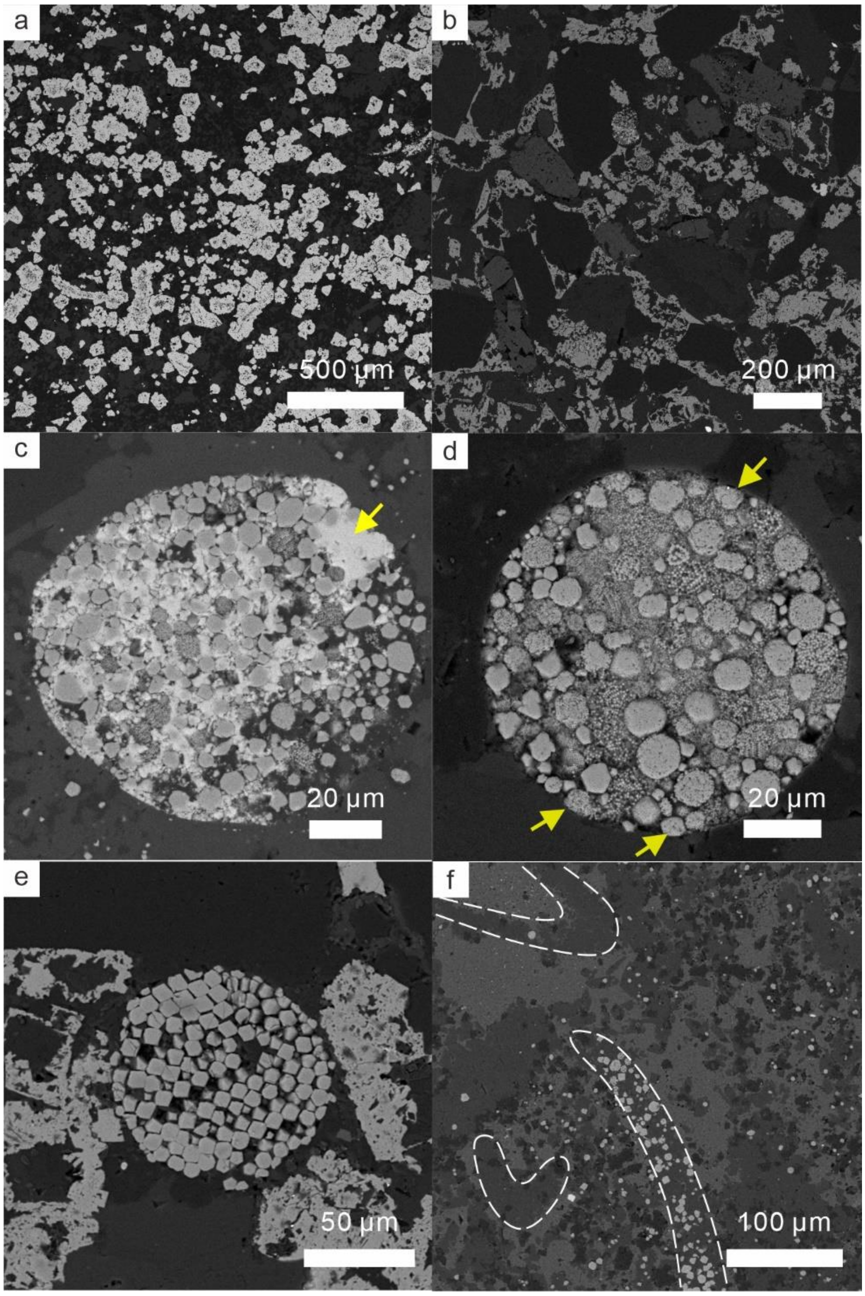

Fig. 2.6 SEM backscatter images of pyrite morphologies in limestone (sample JC-3) and sandstone (sample JC-4). (a) abundant pyrite crystals in sample JC-3; (b) pyrite cement between clastic grains (mainly quartz and feldspar) in sample JC-4; (c) polyframboid composed of framboids with pyrite microcrysts dominating the matrix in sample JC-4 (yellow arrows indicate truncated framboids at the margin); (d) polyframboid comprising framboids and pyrite crystals with a mostly cemented matrix of sphalerite (the brightest mineral, yellow arrow); (e) giant framboid composed of giant microcrysts of octahedral pyrite; (f) phosphate clasts in Fig. 2.5a consisting of bioclasts (dark area), partly replaced by pyrite crystals, and framboids (bright crystals circled by white dotted line). The matrix is phosphate-rich (medium grey area).

feldspar, pyrite polyframboids and phosphate clasts, similar to those in L2, together with elongate and curved phosphate grains that are likely fish ribs (Fig. 2.5e).

The petrography of the Black Shale Member shows a clear vertical evolution. The onset of calcareous black shale (Facies 3) in the second unit is marked by alternating laminations of organic-rich clay and calcisilt (Fig. 2.7a). The latter laminae range from 20 to 70 µm thickness and show horizontal persistence and low amplitude current ripples. Higher in the second unit, the calcite content declines whilst the siliceous content, in the form of scattered silt-grade quartz, increases (Fig. 2.7b, Facies 4). The third unit marks the transition to radiolarian-rich black shale, containing compacted radiolarian tests in a dark, organic-rich matrix that lacks lamination (Fig. 2.7c, Facies 4). The fourth unit consists of lenticular-laminated shale consisting of compacted clay clasts (Fig. 2.7d, Facies 5), calcareous mudstone bearing tiny shell fragments and ophiuroid ossicles (Fig. 2.7e, Facies 6), and pyrite-rich, calcisilt laminae (Fig. 2.7f, Facies 7).

2.5.2 Pyrite petrography

SEM analysis reveals that pyrite crystals are common in the topmost bed of the Costigan Member (JC-3) (Fig. 2.6a) and overlying phosphatic sandstone (JC-4), where it also occurs as a cement (Fig. 2.6b). Framboidal pyrite occurs in the second and fourth units (Fig. 2.8), where their sizes were measured (Table 2.4; Fig. 2.9), but framboidal pyrite was not present in the Costigan limestone nor in unit 3 (with the exception of sample JC-17). Within the phosphatic sandstone, exceptionally large framboids, up to 100 µm in diameter, were seen (Fig. 2.6e). These had large constituent microcrysts reaching up to 10 µm. Both of these dimensions are an order of magnitude larger than typical framboids (Wignall and Newton, 1998). The large framboids occur alongside equally large, composite, spherical grains of pyrite, around 80 – 100 µm in diameter, that resemble polyframboids. However, unlike typical polyframboids, which consist solely of spherical clusters of framboids (Love, 1971; Love and Vanguestaine, 1973; Wei et al., 2016), the polyframboids in JC-4 are composed of both framboids and a range of other components; predominantly pyrite microcrysts, a few microns in size, that form the matrix between the

Table 2.4 Pyrite framboid diameter dataset. N = sample size for each sample. Ave = mean average framboid diameter. S.D. standard deviation.

ID		size of framboids (μm)																														N	Ave	S.D.
		2	2.5	3	3.5	4	4.5	5	5.5	6	6.5	7	7.5	8	8.5	9	9.5	10	10.5	11	11.5	12	12.5	13	13.5	14	14.5	15	15.5	16	>16			
JC-1				no framboids																														
JC-2				no framboids																														
JC-3				no framboids																														
JC-4	polyframboid 1	0	0	0	2	1	2	4	3	4	8	5	1	3	3	0	3	1	0	0	0	0	0	1								41	6.7	1.9
	polyframboid 2	0	0	0	0	0	1	2	0	1	2	5	0	3	1	2	3	0	2	1												23	7.8	1.8
	framboids in matrix	0	0	1	1	3	3	6	8	6	3	5	1	2	2	4	2	0	2	2	0	0	1	0	0	0	0	0	2	0	1	55	8.7	12.6
JC-5		0	4	9	24	27	26	24	13	11	9	6	7	5	0	0	1	1	1	0	0	1	0	0	2	1	1	1				174	5.2	2.2
JC-6		0	1	12	25	26	23	22	8	8	8	5	4	0	1	0	0	0	2													145	4.7	1.4
JC-7				no framboids																														
JC-10		2	5	12	6	10	13	14	5	4	3	1	1	0	2	1																79	4.5	1.4
JC-11				no framboids																														
JC-12				no framboids																														
JC-13				no framboids																														
JC-14				no framboids																														
JC-15				no framboids																														
JC-16		0	1	4	8	12	10	18	10	7	3	1	4	1	1	2	0	0	1													83	5.1	1.5
JC-17				no framboids																														
JC-18		0	0	1	4	5	7	10	5	1	1	1	1	0	2	0	0	0	0	0	0	0	1	1								40	5.5	2.1
JC-19		1	3	1	6	5	10	16	15	19	14	10	5	1	1	1	1	0	0	2	0	1	0	0	1	1						114	5.9	1.9
JC-20		0	2	11	37	24	27	15	15	3	8	2	1	1	0	1	1	1	1	1	0	0	0	0	0	0	0	0	0	2		153	4.7	1.9
JC-21				no framboids																														

framboids (Fig. 2.6c), together with larger pyrite crystals (5-10 μm in size) and, in some cases, patches of sphalerite cement (Fig. 2.6d). The margins of the near-perfectly spherical grains are sharp, with framboids at the outer edge of the polyframboid being truncated (Fig. 2.6c). More ovoid polyframboids (Fig. 2.6d) also occur (possibly due to compaction) together with concentrations of framboids with more diffuse boundaries that may be partially disintegrated polyframboids or examples caught at the moment of coalescing.

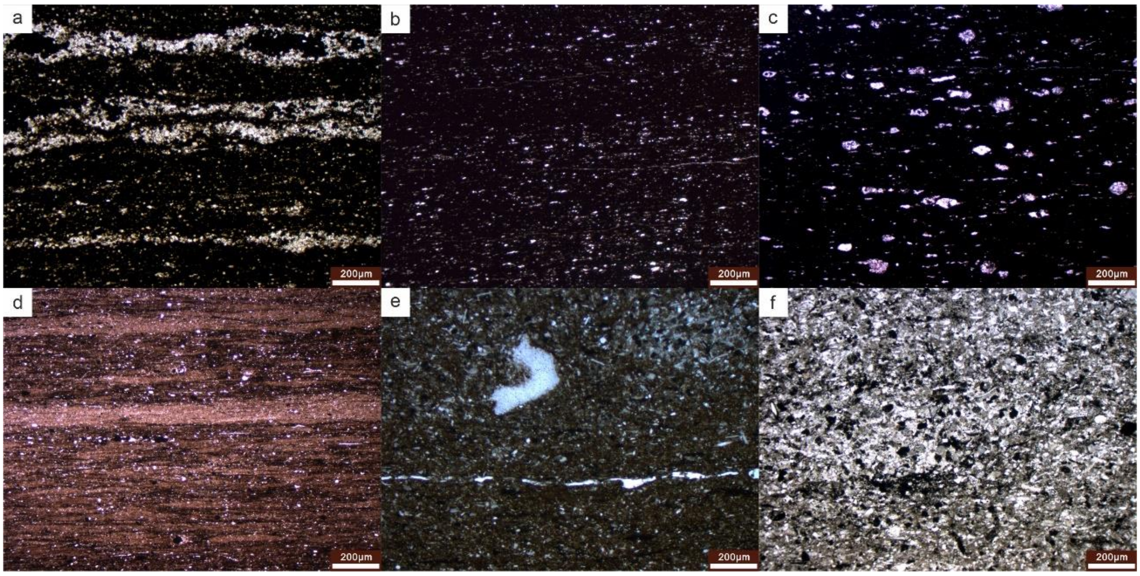

Fig. 2.7 Petrographic features of shale samples from the lower Exshaw Shale member at Jura Creek. (a) sample JC-5: calcareous black shale consisting of organic-rich layers and calcite-rich laminations, facies 3; (b) sample JC-6: siliceous black shale bearing tiny, scattered quartz grains, facies 4; (c) sample JC-12: siliceous black shale bearing abundant radiolarians, facies 4; (d) sample JC-20: lenticular laminated shale consisting of compacted clay clasts and silt, facies 5; (e) sample JC-19: calcareous mudstone bearing ophiuroid and tiny carbonate bioclasts, facies 6; (f) sample JC-21: pyritic calcareous silt, facies 7.

The framboids in unit 2 are small, with a mean diameter of ~4 μm, and they occur with small pyrite crystals (Fig. 2.8a), although one sample (JC-7) lacked framboids (Fig. 2.9). Unusually for a black shale, samples of unit 3 lack framboids or indeed any form of visible pyrite (JC-11 to JC-15, and JC-17). Only at the top of the unit do a limited amount of framboids re-appear (sample JC-16, JC-18), together with common pyrite crystals. The pyrite content of unit 4 is dominated by euhedral crystals, although framboids are also common (Fig. 2.8b). Minor, secondary overgrowth of crystalline pyrite is common on framboid margins, although their central cores are still clear (Fig. 2.8c).

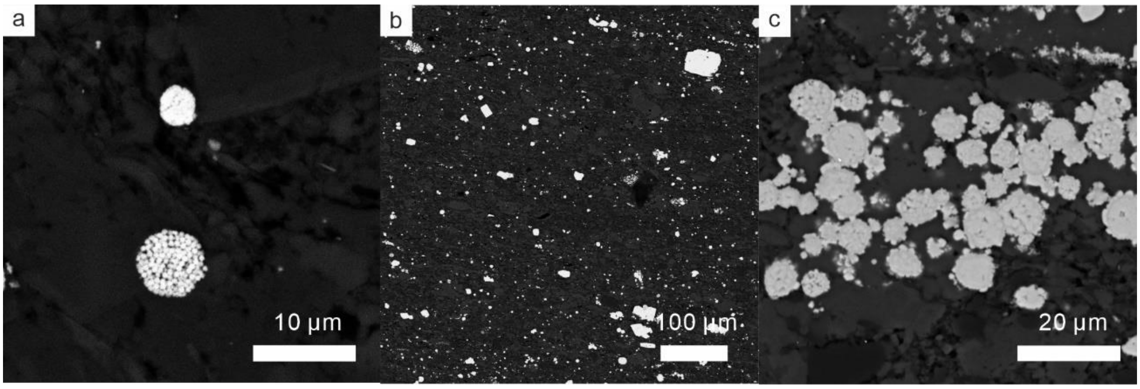

Fig. 2.8 SEM backscatter images of pyrite morphologies. (a) Sample JC-5: small framboids in calcareous black shale; (b) Sample JC-20 showing abundant pyrite crystals; (c) Sample JC-19: abundant framboids showing secondary pyrite overgrowth.

Plotting the framboids’ mean diameter versus standard deviation (Fig. 2.9) shows that they mostly fall in the field typical of framboids from modern euxinic environments (Wilkin et al., 1996). In the phosphatic sandstone, the diameter of the framboids found within the polyframboids was measured separately to the isolated framboids found within the matrix (Table 2.4). The framboids found in the polyframboids (samples JC-4-1, JC-4-2) display a similar average size with a narrow size distribution, and plot close to the euxinic-dysoxic/oxic boundary in the size-standard deviation plot (Fig. 2.9). By contrast, the framboids in sandstone matrix (JC-4-3) are considerably larger in size and show a broader size distribution, and thus plot in the dysoxic/oxic field (Fig. 2.9). The framboids in the black shale of unit two (and the single, framboid-bearing sample from unit 3) have a small size and narrow distribution, and plot in the euxinic field (Fig. 2.9). The framboids from unit 4 are somewhat larger and more variable in size, and plot close to the euxinic/dysoxic boundary (Fig. 2.9). Framboids do not occur in the topmost sample (JC-21), although some pyrite crystals are present.

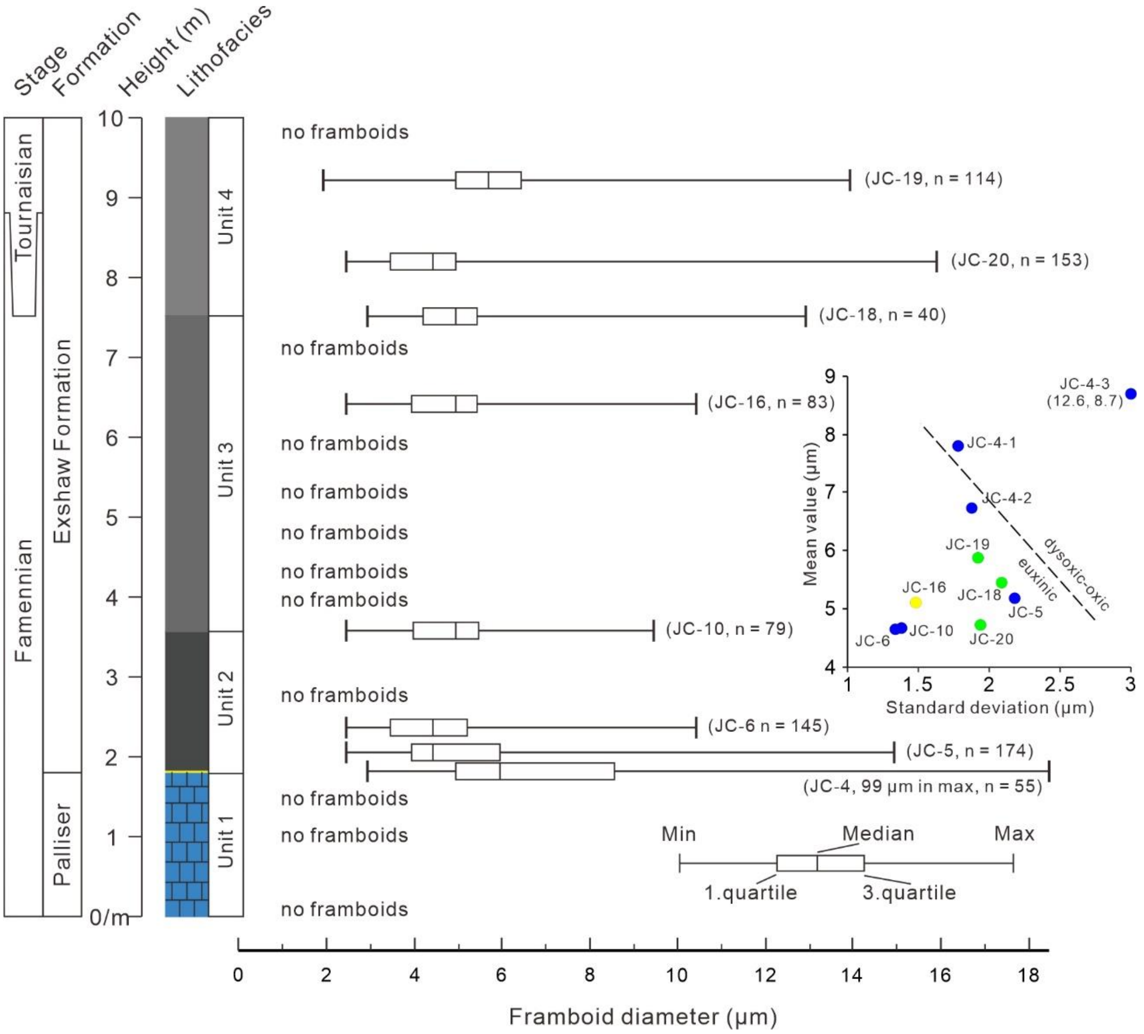

Fig. 2.9 Box-and-whisker plots of framboid size distributions from Jura Creek samples and mean value versus standard deviation plot. Blue, yellow and green circles represent statistic features of framboids in the second, third and fourth units, respectively. Data for samples JC-4-1 and JC-4-2 were collected from framboids within two polyframboids, while the framboid size distribution in sample JC-4-3 was collected from the sandstone matrix.

2.5.3 Geochemical proxies

TOC variability

TOC values in the Costigan carbonate are low, with an average of 0.09 ± 0.02 wt.%, followed by a small increase in the phosphatic sandstone to 0.61 wt.% (Table 2.1; Fig. 2.10). The onset of black shale in the Exshaw Formation shows a sharp increase in TOC to 4.00 wt.% and remains high, with average values of 4.12 ± 0.39 wt.% throughout units 2 and 3. TOC levels in unit 4 decline to a value of 0.22 wt.% at the top of succession (Table 2.1; Fig. 2.10).

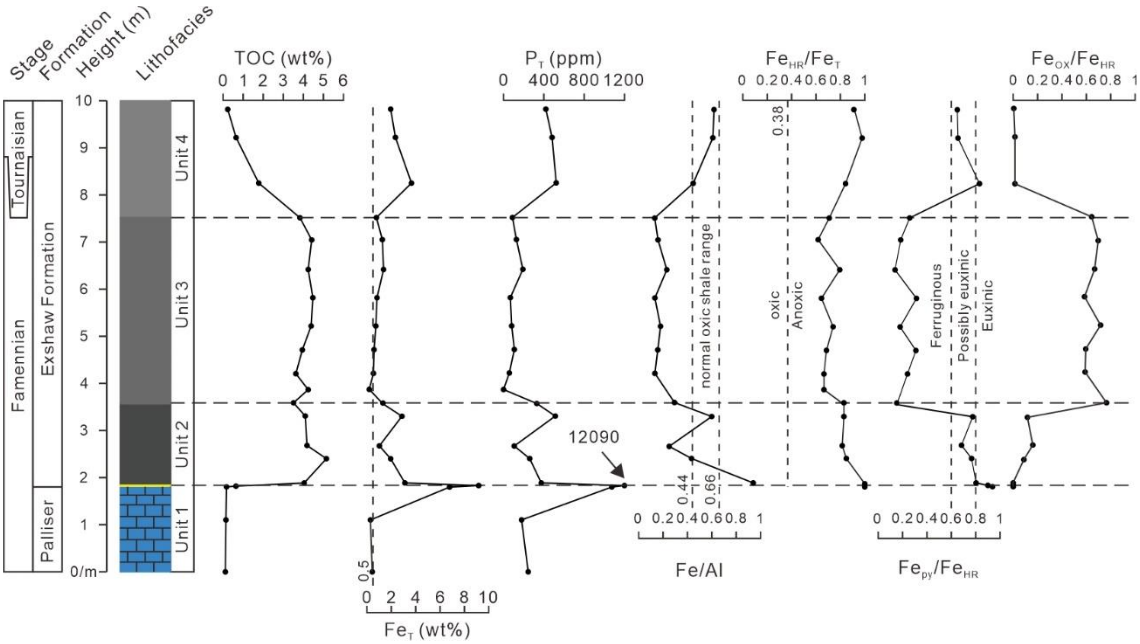

Fig. 2.10 Geochemical profiles for total Fe (Fe_T), total P (P_T) and Fe speciation through the Jura Creek section. The dashed line on Fe_T plots represent the minimum Fe concentration (0.5 wt%) for application of Fe speciation. The dashed lines on Fe/Al plots represent the range of normal oxic shale (0.44-0.66) (Clarkson et al., 2014). The dashed line on Fe_{HR}/Fe_T plots represent the boundary for distinguishing anoxic water-column conditions. The dashed lines on Fe_{py}/Fe_{HR} plots represent the boundaries for distinguishing euxinic (>0.8) and ferruginous (<0.6) water-column conditions.

Total Fe, total P and Fe phase partitioning

Samples from the Costigan Member have a low total iron (Fe_T) content (< 0.5 wt.%), with the exception of the sample from the topmost bed, where Fe_T is 6.80 wt.% (Table 2.1, Fig. 2.10). These typically low carbonate Fe_T values are below the threshold generally considered to provide reliable Fe speciation and Fe/Al data for palaeoredox analysis (Clarkson et al., 2014), and thus are not considered further in this context. The Fe_T content increases dramatically in the phosphatic sandstone bed (to 9.22 wt.%), and the black shales of unit 2 have an average of 2.25 ± 0.82 wt.%. This is followed by lower values in the radiolarian-rich shale of unit 3, ranging from 0.21 – 1.36 wt.%, and there is another sample (JC-11), containing low Fe_T, which will not be considered in Fe associated redox analysis (Table 2.1, Fig. 2.10). Concentrations of Fe_T increase again in the shales of unit 4, reaching 3.68 wt.% before decreasing to 1.96 wt.%.

The stratigraphic trend in Fe_T/Al, which may provide insight into variability in water column redox conditions (Lyons and Severmann, 2006; Clarkson et al., 2014), closely follows the trend seen in Fe_T through the Exshaw Shale, with a decline at the top of unit 2, stable and low values in unit 3, and an increase in unit 4 (Fig. 2.10). Variations in the proportions of Fe_{ox}/Fe_{HR} and Fe_{py}/Fe_{HR} show inverse trends, whereby Fe_{py} is high in the second and fourth interval, but low in the third, and Fe_{ox} is the main Fe_{HR} fraction in the third unit (Fig. 2.10; Table 2.1). The concentration of Fe_{carb} is also particularly low in unit 3, while Fe_{mag} is consistently low in all samples, averaging only 0.017 ± 0.006 wt.% (Table 2.1). Fe_{HR}/Fe_T ratios are elevated (> 0.38), representing the threshold for distinguishing deposition beneath anoxic bottom waters (Raiswell and Canfield, 1998; Raiswell et al., 2001; Poulton, 2002) throughout the section, but with a slight decrease in unit 3 (Fig. 2.10).

Total phosphorus displays a similar trend to total Fe (Fig. 2.10). In detail, P is low throughout most of unit 1 (212 ± 32 ppm), but there is an increase to 1080 ppm in the topmost limestone sample, with a subsequent major increase to 12,090 ppm in the phosphatic sandstone (Table 2.1). Total P then returns to lower values of 313 ± 150 ppm in the black shale of unit 2, followed by particularly low average values of 131 ± 85 ppm in unit 3, and then an increase to 475 ± 42 ppm in unit 4.

Trace metals (Mo, U, V and Re)

Redox sensitive trace metal concentrations are low in carbonates of the Costigan Member, but Mo, U, V and Re all increase slightly towards the top (Fig. 2.11; Table 2.1). There are then large increases in Mo (to ~200 ppm), U (to ~32 ppm) and Re (to ~1065 ppb), and a smaller increase in V (to ~16 ppm), in the phosphatic sandstone of unit 2. The overlying calcareous black shale of unit 2 is characterized by overall high values of Mo (87.7 ± 32.8 ppm), U (21.5 ± 6.2 ppm) and Re (75.1 ± 58.4 ppb), but with significant scatter, while V progressively increases to reach a peak of

~1855 ppm around the level where large carbonate concretions occur (Fig. 2.11). Trace metal concentrations decline to relatively stable values in unit 3 (Mo = 65.5 ± 12.6 ppm; U = 10.0 ± 1.9 ppm; V = 1274 ± 161 ppm; Re = 48.7 ± 18.1 ppb). Unit 4 is characterized by markedly lower trace metal concentrations, although values tend to be higher than in the carbonates of unit 1 (Fig. 2.11; Table 2.1).

Enrichment factors for Mo, U, V and Re tend to closely follow the trends in the concentration data, although enrichment factors for Mo, U and V show a slight overall decrease through unit 3, which contrasts with concentration data for these elements (Fig. 2.11). Enrichment factors for all of the trace metals are particularly elevated (> 1) through units 2 and 3, indicating enhanced drawdown and sequestration in the sediment. We also use Re/U and Re/Mo ratios to evaluate water column and porewater redox conditions (see below). Both parameters decrease through unit 1, but show strong peaks in the phosphatic sandstone of unit 2 (Fig. 2.11). Values then remain relatively constant, but with a slight overall increase, through units 2, 3 and 4, followed by peaks in both Re/U and Re/Mo in the uppermost sample of unit 4.

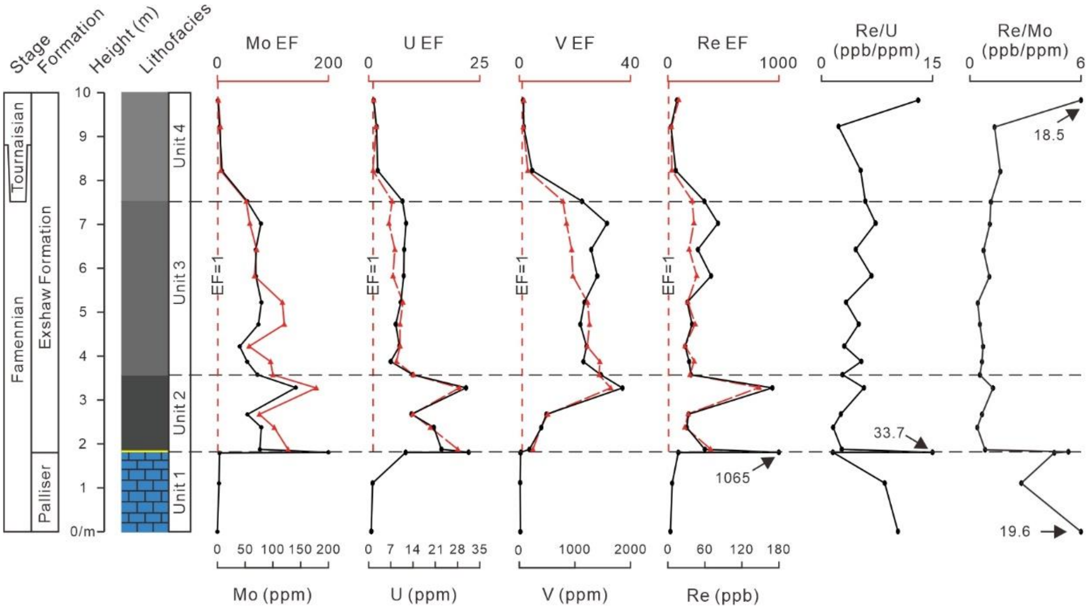

Fig. 2.11 Redox sensitive element profiles for the Jura Creek section. Black solid lines represent concentrations, and red lines with triangle icons represent variation in enrichment factors.

2.6 Discussion

2.6.1 Depositional Conditions

Unit 1

The top 2 m of the Costigan Member at Jura Creek is a crinoidal wackestone to packstone developed in a mid-ramp setting (Richards and Higgins, 1988; Savoy, 1992). The limestone contains low concentrations of Mo, U and V (Fig. 2.11), suggesting well-oxygenated bottom waters. In support of this contention, relatively high Re/U and Re/Mo ratios through most of the unit suggest that dysoxic conditions were likely limited to pore waters close to the sediment-water interface (Fig. 2.12a). However, during deposition of this unit, a progressive decrease in Re/U and an overall decrease in Re/Mo are accompanied by slight increases in the concentrations of U and Re in the uppermost sample (Fig. 2.10). These trends suggest that the redox state of the system was beginning to change, leading to the development of anoxic pore waters closer to the sediment-water interface during the final stages of unit 1 deposition (Fig. 2.12a). However, the lack of any significant increase in [V] in the uppermost sample (Fig. 2.10) suggests that the pore waters remained dysoxic at the sediment-water interface. This relatively minor redox progression in the sediment, with strong evidence for oxic water column conditions, is in accord with the abundant and diverse benthic fauna seen in this unit (Fig. 2.3, 2.12a).

At the top of unit 1, the occurrence of reworked limestone pebbles (Fig. 2.2) suggests partial seafloor lithification and reworking, perhaps as accommodation space declined. Indeed, a depositional hiatus is reported between the top of the Costigan Member of the Palliser Formation and the base of the Exshaw Formation in the region (Savoy et al., 1999; Johnston et al., 2010), raising the possibility that carbonate production in the region was terminated by emergence (Smith et al., 1995). However, such a scenario appears unlikely given the ramp geometry during deposition of the Palliser Formation (Savoy, 1992), because a base-level fall would be unlikely to shut down deposition in the lower reaches of the ramp.

Additionally, considering the high P concentrations in the topmost sample (JC-3) of the limestone (Fig. 2.10, Table 2.1) and the phosphatic limestone clasts in the overlying sandstone (JC-4) (Fig. 2.5), it is reasonable to speculate that the top of the carbonate was intensively phosphatised and then eroded with the resultant clasts preserved in the overlying sandstone. Phosphogenesis commonly coincides with carbonate shut-down because sediment starvation allows time for this process to occur (e.g. Föllmi et al., 1994; Föllmi, 1996, 2016).

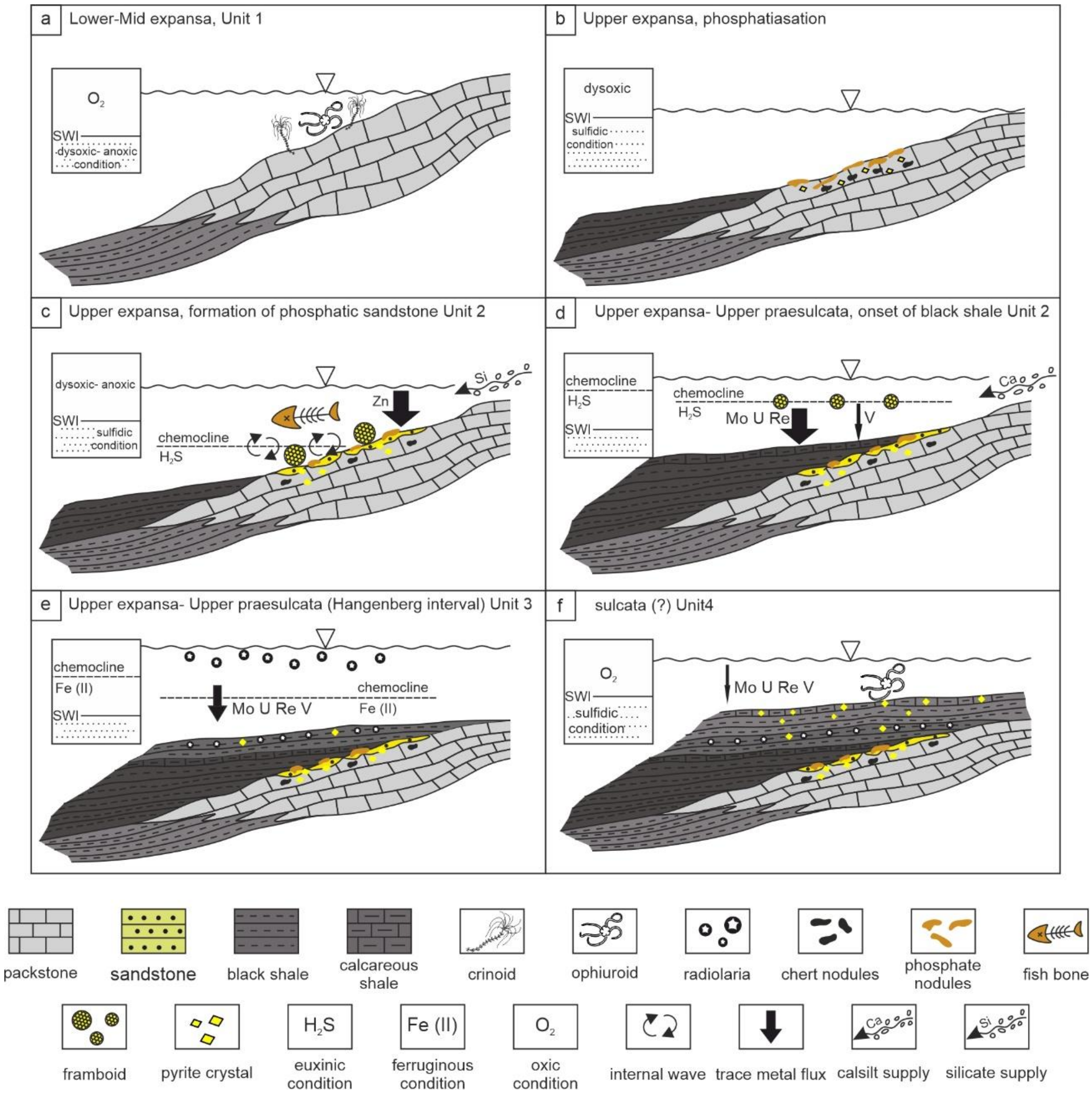

Fig. 2.12 Redox evolution and depositional history of the Devonian-Carboniferous transition in western Canada. Inset boxes show redox conditions at the Jura Creek study site (location

indicated by triangle in main figures). The size of arrows is consistent with the amount of trace metal flux. SWI is sediment- water interface.

Pronounced sulphide replacement (see Fig. 2.4) combined with elevated Fe_{py}/Fe_{HR} (Fig. 2.10) suggests that pore waters became highly sulphidic below the sediment-water interface (Fig. 2.12b). Under such conditions, P associated with organic matter would have been released during remineralization via sulphate-reducing microbes (Ingall and Cappellen, 1990; Ruttenberg and Berner, 1993), while iron-bound P would also have become available during sulphide-promoted reductive dissolution of Fe (oxyhydr)oxide minerals (Sundby et al., 1992). This released P may have undergone extensive recycling through re-adsorption to Fe (oxyhydr)oxide minerals at the sediment-water interface, followed by subsequent re-release during early diagenesis (Slomp et al., 1996), ultimately leading to the P accumulation at the top of this unit (Fig. 2.12b).

Unit 2

As discussed above, the uppermost part of the Costigan Member experienced a gradual intensification of oxygen depletion in surface sediments. This appears to have been a progressive transition that became more oxygen deficient during deposition of the phosphatic sandstone as highly elevated [Re], combined with high Re/U and Re/Mo ratios alongside low [V] (Fig. 2.11), suggest the more expansive development of dysoxic conditions into the water column. However, elevated [U] (Fig. 2.11), combined with high Fe_T/Al and Fe_{HR}/Fe_T ratios in this unit (Fig. 2.10), suggest that the water column likely fluctuated between dysoxic and anoxic conditions on relatively short timescales. Although [Mo] and Fe_{py}/Fe_{HR} are also highly elevated in the phosphatic sandstone and could be taken to indicate euxinic depositional conditions, the nature of the sulphide mineralization supports dominantly dysoxic or anoxic non-sulphidic water column conditions (see below). Thus, while we cannot discount periodic development of water column euxinia, elevated Mo contents more likely reflect drawdown by the particulate shuttle mechanism (Algeo and Tribovillard, 2009; Tribovillard et al., 2012) during the periodic development of ferruginous conditions. This may have combined with fixation in the sediment via the thiomolybdate pathway (Helz et al., 1996) during extensive diagenetic sulphidation of Fe_{HR} (see below). Whatever the precise mechanism responsible for the elevated Mo content of the phosphatic sandstone, there is clear evidence for an overall deterioration in water column oxygenation that was likely the major factor in suppressing carbonate production.

Having been phosphatised, the seabed underwent erosion resulting in production of reworked phosphate clasts that co-occur with polyframboids, giant framboids and pyrite crystals (Fig. 2.12c). The polyframboids are likely to have formed at this stage, since they are regularly associated with sediment reworking and transportation (Love, 1971; Baird and Brett, 1991). The constituent framboids within the polyframboids are small and suggestive of euxinic conditions, although there may have been a selectivity for smaller sizes during polyframboid formation (Fig. 2.9). The precise process, whereby the various polyframboid constituents are “glued” together is unclear, although Schieber and Baird (1991) have proposed a model based on the occurrence of pyrite spheres found in Devonian black shales in eastern USA. These range from 0.1 – 0.9 mm in diameter and consist of a mixture of framboids and crystals. They are argued to be the pyrite infill of *Tasmanites* cysts although commonly, they were only half filled before compaction collapsed the cysts, resulting in lunate, half spheres (Schieber and Baird, 2001, Fig. 2.5a). The Jura Creek polyframboids are not directly comparable to the *Tasmanites* infills because they are substantially smaller (they do not exceed 0.1 mm diameter), do not show half-filled examples, and lack the organic coating of the Schieber and Baird examples (although such material could have been removed by abrasion). Nonetheless, a *Tasmanites*-fill model for the Jura Creek polyframboids cannot be ruled out. Whatever their origin, it is clear that they have been subject to erosion and abrasion (Fig. 2.7c).

The process of erosion and polyframboid formation likely occurred in anoxic waters otherwise sulphide oxidation would have occurred. Similar examples of phosphate-and-pyrite-rich lag deposits, with polyframboids (and *Tasmanites* infills), are seen at the base of black shale successions from the Devonian of eastern USA, for which Baird and Brett (1991) developed an internal wave-erosion model. Such waves develop at the density interface in stratified basins, and can separate an anoxic lower water column from a better mixed upper water column. Wave erosion combined with carbonate dissolution is envisaged to be intense, resulting in a remnant lag of phosphate and pyrite grains (Baird and Brett, 1991).

The phosphatic sandstone bed on Jura Creek only differs from the examples described by Baird and Brett (1991) in its siliciclastic component, which is envisaged to derive from a western, volcanic source (Savoy, 1992). The angularity of the grains suggests their transport distances were short (Fig. 2.5). The phosphatic sandstone also contains substantial amounts of biogenic phosphate (fish bones) that are likely to have accumulated slowly from a pelagic rain (Fig. 2.12c). During this stage a series of diagenetic phases formed within the sandstone, comprising dolomite rhombs (Fig. 2.5b), calcite and pyrite cement (Fig. 2.7b), and sphalerite cement within some polyframboids (Fig. 2.7d).

The subsequent onset of calcareous black shale deposition records a quiescent depositional environment, with occasional currents introducing calcisilt laminae as bed load or dense suspension (Fig. 2.6a). The calcisilt was derived from up-dip, implying that the carbonate factory was weakly re-established in shallower settings at this time (Fig. 2.12d). Thus, the phosphatic sandstone records the onset of water column deoxygenation, whilst the overlying siliceous black shales of unit 2 formed as these conditions intensified. A sharp increase in TOC at the base of the black shale coincides with elevated Fe/Al, Fe_{HR}/Fe_T and Fe_{py}/Fe_{HR} (Fig. 2.10), as well as enrichments in Mo and U (Fig. 2.11). In combination with the small size and narrow range of pyrite framboids in this interval (Fig. 2.9, Table 2.4), these observations provide strong support for a transition to euxinic water column conditions (Fig. 2.12d). Given this redox reconstruction, the low V_{EF} values at this horizon likely reflect the lack of a Mn shuttle under euxinic conditions, which, as observed in some modern euxinic environments, would limit transport of V to the sediment (Bennett and Canfield, 2020).

There is a progressive decrease in Mo_{EF}, U_{EF} and Re_{EF} (Fig. 2.11) towards the middle part of unit 2 (samples JC-5 to JC-7), and pyrite framboids are absent in samples of JC-7 (Fig. 2.9). By contrast, Fe_{HR}/Fe_T and Fe_{py}/Fe_{HR} ratios remain elevated (Fig. 2.10), while V_{EF} values increase through this part of the succession (Fig. 2.10). This implies that water column redox conditions fluctuated through unit 2, with an overall progression to less intense euxinia, and likely ferruginous conditions (but with the development of sulphidic porewaters during diagenesis resulting in elevated Fe_{py}/Fe_{HR}), towards the middle of the unit. In this context, the low Fe_T/Al ratios in the middle of unit 2, which are substantially depleted relative to average shale (Fig. 2.10), may partly represent intense recycling of Fe_{HR} between the sediments and water column, whereby short-term delivery of Fe_{HR} to the sediment by water column precipitation under ferruginous conditions was followed by Fe recycling during diagenesis and Fe^{2+} supply back to the water column (Poulton and Canfield, 2011; Poulton, 2021). Such a scenario, likely requiring variable redox conditions on short timescales (which would be integrated over the timescale recorded by our sampling strategy), could potentially account for the complex redox signal recorded at this horizon, but does imply that the Fe_T/Al ratio of the detrital sediment supplied to this region was low relative to average shale.

The upper half of unit 2 then records the re-establishment of more intense euxinia (as indicated by elevated Mo_{EF}, U_{EF}, V_{EF} and Re_{EF} values; Fig. 2.10), prior to the boundary with unit 3. This overall evolution of redox conditions is supported by the co-behaviour of Mo_{EF} and U_{EF} (Fig.

2.13), whereby the samples through the lower half of unit 2 (samples JC-5 to JC-7) transition from the euxinic field to the particulate shuttle field, with a return to the euxinic field in the upper half of unit 2 (sample JC-8), before a return to the particulate shuttle field at the boundary between units 2 and 3 (Fig. 2.13).

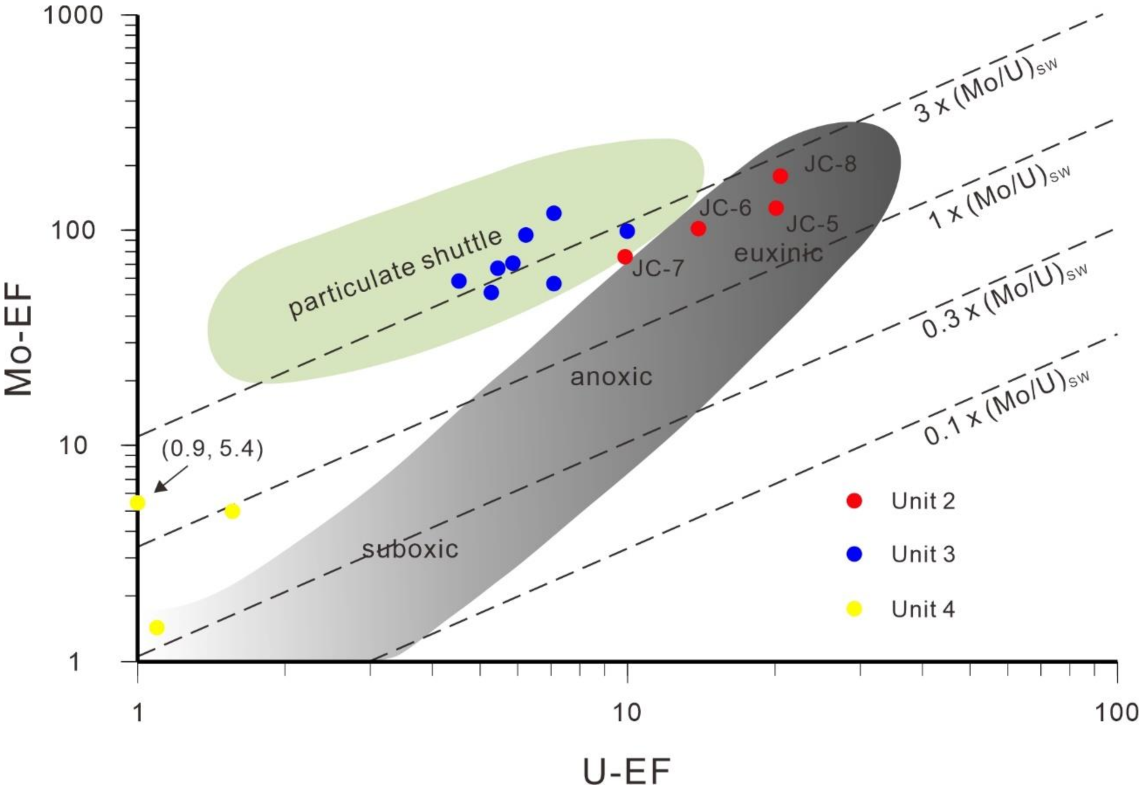

Fig. 2.13 Mo-EF versus U-EF cross plot for the Jura Creek section. Unit 2 samples are labelled to show the progression of redox conditions through this unit. Cross plot is modified from Algeo and Tribovillard (2009) and Tribovillard et al. (2012).

Unit 3

Radiolarians are typically oceanic taxa although they can also occur in coastal regions (e.g. Lampitt et al., 2009). The appearance of radiolarians in unit 3, at a level within the *praesulcata* Zone (and thus equivalent to the Hangenberg Event in Europe (Richards and Higgins, 1988)), suggests improved oceanic connectivity, probably associated with continued deepening (Fig. 2.12e). Unit 3 is characterised by high Fe_{HR}/Fe_T and low Fe_{py}/Fe_{HR} ratios (Fig. 2.10) and an absence of pyrite framboids, suggesting anoxic, ferruginous, water column conditions. This redox state is supported by the moderate Mo_{EF}, U_{EF}, V_{EF} and Re_{EF} values (Fig. 2.11), and in particular, the Mo_{EF}

and U_{EF} data that plot in the particulate shuttle region (Algeo and Tribovillard, 2009), suggesting elevated Mo drawdown through uptake by Fe minerals precipitating in a ferruginous water column (Fig. 2.13).

As with the development of ferruginous conditions in the middle part of unit 2, ferruginous condition in unit 3 are associated with very low Fe_T/Al ratios (Fig. 2.10). As discussed above, the Fe_T/Al ratio of detrital sediment delivered to this region may have been particularly low relative to average shale, thus partially explaining the lack of enrichment in Fe_T. However, we also note that low Fe_T/Al ratios often occur in deep-water siliceous sediments deposited under ferruginous conditions and could potentially be generated through diagenesis. During diagenesis of biogenic silica in sediment, dissolution of detrital minerals (clay minerals) releases dissolved Al to pore waters, which then becomes structurally incorporated into the deposited biogenic silica (Van Cappellen and Qiu, 1997; Dixit et al., 2001; Van Cappellen et al., 2002). The dissolution of detrital minerals would also release dissolved Fe^{2+}, which would be retained in the sediment as Fe_{HR} under oxic conditions. However, in contrast to Al, under ferruginous conditions the mobilised Fe would have the potential to diffuse into the water column (Poulton and Canfield, 2011; Poulton, 2021), particularly in non-sulphidic sediments where precipitation of pyrite would not act as a sink for the Fe^{2+}. This scenario would be expected in the radiolarian-rich sediments of unit 3, whereby an Fe_{HR} mineral shuttle sequestered Mo in the sediment, but recycling back to the water column of a portion of this Fe_{HR} under non-sulphidic conditions close to the sediment-water interface, along with the Fe^{2+} released through detrital mineral dissolution, would result in the distinct combination of elevated Fe_{HR}/Fe_T ratios and low Fe_T/Al ratios. Indeed, we note that generation of this combined Fe signal may be a distinctive and possibly even a diagnostic feature of biogenic silica-rich sediments deposited under ferruginous conditions.

Unit 4

The appearance of bioclasts in the calcareous mudstone indicates improved benthic oxygenation of the sea floor during deposition of unit 4 at the start of the Carboniferous. A decline in Mo_{EF}, U_{EF}, V_{EF} and Re_{EF} (Fig. 2.11), combined with the Mo_{EF}-U_{EF} cross-plot systematics (Fig. 2.13), all support progressive oxygenation. Increases of Re/U and Re/Mo in the topmost sample suggest a transition from anoxic to dysoxic pore waters close to the sediment-water interface, thus providing further evidence for a progressive return to a well-oxygenated marine environment (Fig. 2.12f). However, Fe_{HR}/Fe_T and Fe_{py}/Fe_{HR} are high (and Fe_T/Al also increases) in this unit, with SEM observations suggesting that the pyrite comprises euhedral crystals and is therefore diagenetic in origin (Fig. 2.8). Consequently, the high Fe_{py}/Fe_{HR} ratio reflects intense sulphide production deeper in the pore waters (Poulton, 2021), with the elevated Fe_{HR}/Fe_T and Fe_T/Al ratios likely arising from water column precipitation of Fe minerals during upwelling of deeper ferruginous waters into the shallower dysoxic waters.

2.6.2 Models for carbonate shutdown

Carbonate demise in the western Laurentia during the Famennian has been attributed to the role of increased nutrient supply from upwelling, with the increased productivity and declining seafloor oxygenation being responsible for carbonate shutdown (e.g. Savoy, 1992; Caplan et al., 1996; Caplan and Bustin, 1999). Here we show evidence of increasing dysoxia in the uppermost levels of the Costigan Member and the associated phosphogenesis provides substantial support for this scenario. However, the reliance on upwelling to elevate nutrient levels is questionable. The Devonian-Carboniferous transition along the western North American margin coincides with the Antler Orogeny and the development of a foreland basin (Root, 2001); such a transition would likely have restricted the region's connectivity with the global ocean and its nutrients. Potentially any decline in connection may have been overridden by an increase in oceanic circulation. Global cooling and glaciation in the latest Famennian are frequently argued to have invigorated upwelling and so lead to the development of Hangenberg anoxia (Caplan and Bustin, 1999; Bábek et al., 2016; Kumpan et al., 2019). The best evidence for glaciation occurs in the mid-*praesulcata* Zone where sea-level fall lead to incision and valley fill (e.g. the Hangenberg Sandstone; Fig. 2.1), but these events postdate carbonate shutdown in Canada. Rather than upwelling, nutrients may have been derived from land; the occurrence of terrestrial grains in the phosphatic sandstone supports this possibility. It is interesting to note that, by the time of Hangenberg black shale development in Europe, the Jura Creek section showed peak water depths (radiolarian-rich black shale) which potentially could have had improved oceanic connectivity and access to upwelled nutrients. Instead, water column redox conditions changed from euxinic to ferruginous anoxic around this time, indicating slight improvement in oxygenation. Clearly, the redox conditions in western Laurentia were not entirely driven by variations in nutrient supply. The semi-isolation of the deep-water basins was likely a key factor (e.g. Caplan et al., 2001; Algeo et al., 2007).

2.6.3 Comparative latest Devonian redox history in other North American basins

The redox history of other basins in North America during the Devonian-Carboniferous transition bears some comparison with the Western Canada Sedimentary Basin albeit with regional differences. The Lower Bakken Formation of the Williston Basin is both organic-carbon rich (total organic carbon values average 9.7 wt.%) and trace metal rich suggesting euxinic deposition possibly with sulphidic conditions developed within the photic zone (Scott et al., 2017). This is broadly comparable with the euxinic-style deposition proposed for the contemporaneous black shales of unit 2 at the base of the Exshaw Formation at Jura Creek. In contrast, the Middle Member of the Bakken Formation, a succession of mixed carbonate-siliciclastic beds (roughly coeval with units 3 and 4 at Jura Creek), records substantially better ventilation than seen in the Western Canada Sedimentary Basin likely due to a shallower depositional setting (Egenhoff, 2017;

Hogencamp and Pocknall, 2018; Hart and Hofmann, 2018). The Sappington Basin also saw intense euxinic deposition during deposition of the Lower Sappington Formation in the Mid *expansa* Zone (di Pasquo et al., 2019; Browne et al., 2020), and again this of broadly comparable age to unit 2 at Jura Creek. Following a hiatus in the Sappington Basin, the resumption of deposition in the Upper *expansa* Zone saw better oxygenated carbonates and siliciclastics developed in a basin interpreted to be brackish rather than fully marine (Browne et al., 2020).

What the basins of western North America do not show is an intensification of anoxia comparable to that seen during the Hangenberg crisis in Europe. It seems likely that this signal was substantially overprinted by regional controls on basin development, that are no doubt linked to the ongoing Antler orogeny. In most sections the most anoxic conditions are developed earlier, during the *expansa* Zone, whilst the Hangenberg Crisis, in the *praesulcata* interval saw the transition from euxinic to ferruginous conditions in our Western Canada Sedimentary Basin study and an even greater improvement of oxygenation in the Sappington and Williston Basins.

2.7 Conclusions

The trigger of anoxia and its impact on the carbonate ramp in western Laurentia during the latest Famennian has been subject to considerable debate. Evidence from the Jura Creek type section of the Exshaw Formation shows that the final stages of limestone deposition in the Costigan Member of the Palliser Formation were likely caused by declining oxygen levels (shown by decreasing Re/U and Re/Mo levels) and associated phosphogenesis. This suggests eutrophication with increased nutrient flux driving the change. It is unlikely the nutrients were sourced from oceanic upwelling, given the restricted connections to the global ocean due to the existence of a physical barrier to the west. Following the shutdown of carbonate productivity, the subsequent passage of a dissolutional pycnocline caused deflation of the top surface of the limestone and the formation of a thin lag of phosphate and pyrite clasts in a sandstone. The latter include extraordinarily large framboids and polyframboids that accreted in agitated, anoxic bottom waters.

The redox history of the Black Shale Member shows considerable variations. Euxinic conditions became established during deposition of the lowest part of the Shale as indicated by enriched U and Mo values, elevated Fe/Al, Fe_{HR}/Fe_T and Fe_{py}/Fe_{HR} and the presence of populations of small framboids. Only V is not enriched, which may reflect the lack of a Mn shuttle in the sulfidic water column. The middle part of the Black Shale Member is contemporaneous with the Hangenberg black shale event in Europe and, unusually for a black shale, it lacks any pyrite framboids. This petrographic observation is supported by the very low Fe_{py}/Fe_{HR} values at this level, although Fe_{HR}/Fe_T are high and Fe_T/Al low. These are the attributes of ferruginous anoxic conditions in which much remobilised Fe escapes to the water column. Redox history from other basins in western North America (the Sappington and Williston basins) show even greater improvements in basin ventilation. The Hangenberg anoxic event is barely manifest in the region. The younger, Carboniferous levels of the Black Shale Member record a transition to dysoxic conditions. Despite the diverse history of redox change recorded in this study, the organic carbon values of the Black Shale Member at Jura Creek remained remarkably constant at values of ~ 4 wt.% TOC, before declining in the uppermost dysoxic level.

Acknowledgements

Dr. Yijun Xiong and Dr. Tianchen He are acknowledged for their support in geochemical analysis. Our gratitude also extends to Lisa Neville who helped with field work and sample collection. We thank an anonymous reviewer and Song Huyue for their comments during the review process.

References

Alcott, L.J., Krause, A.J., Hammarlund, E.U., Bjerrum, C.J., Scholz, F., Xiong, Y., Hobson, A.J., Neve, L., Mills, B.J.W., März, C., Schnetger, B., Bekker, A., & Poulton, S.W., 2020. Development of Iron Speciation Reference Materials for Palaeoredox Analysis. *Geostand. Geoanalytical Res*. **44**, 581–591. https://doi.org/10.1111/ggr.12342.

Algeo, T.J., Lyons, T.W., Ronald, B., & Over, D.J., 2007. Hydrographic conditions of the Devono–Carboniferous North American Seaway inferred from sedimentary Mo–TOC relationships. *Palaeogeography, Palaeoclimatology, Palaeoecology*, **256**, 204–230. https://doi. org/10.1016/j.palaeo.2007.02.035.

Algeo, T.J., & Tribovillard, N., 2009. Environmental analysis of paleoceanographic systems based on molybdenum-uranium covariation. *Chemical Geology*, **268**, 211–225. https://doi.org/10.1016/j.chemgeo.2009.09.001.

Anderson, R.F., Lehuray, A.P., Fleisher, M.Q., & Murray, J.W., 1989. Uranium deposition in Saanich Inlet sediments, Vancouver Island. *Geochimica et Cosmochimica Acta*, **53**, 2205–2213. https://doi.org/10.1016/0016-7037(89)90344-X.

Bábek, O., Kumpan, T., Kalvoda, J., & Matys Grygar, T., 2016. Devonian/Carboniferous boundary glacioeustatic fluctuations in a platform-to-basin direction: A geochemical approach of sequence stratigraphy in pelagic settings. *Sedimentary Geology*, **337**, 81–99. https://doi.org/10.1016/j.sedgeo.2016.03.009.

Baird, G.C., & Brett, C.E., 1991. Submarine erosion on the anoxic sea floor: stratinomic, palaeoenvironmental, and temporal significance of reworked pyrite and bone deposits. *Geological Society of London, Special Publication*, **58**, 233–257. https://doi.org/10.1144/GSL.SP. 1991.058.01.16.

Becker, R.T., 1993. Anoxia, eustatic changes, and Upper Devonian to Lowermost Carboniferous global ammonoid diversity. In: House, M.R. (ed.) The Ammonoidea, environment, ecology, and evolutionary change. System Association Special Volume 47. Clarendon Press, Oxford, 115-164.

Benkovitz, A., Matthews, A., Teutsch, N., Poulton, S.W., Bar-Matthews, M., & Almogi-Labin, A., 2020. Tracing water column euxinia in eastern Mediterranean sapropels S5 and S7. *Chemical Geology*, **545**, 119627, https://doi.org/10.1016/j.chemgeo.2020.119627.

Bennett, W.W., & Canfield, D.E., 2020. Redox-sensitive trace metals as paleoredox proxies: A review and analysis of data from modern sediments. *Earth-Science Review*, **204**, 103175. https://doi.org/10.1016/j.earscirev.2020.103175.

Bertine, K.K., & Turekian, K.K., 1973. Molybdenum in marine deposits. *Geochim. Cosmochimica Acta* 37, 1415–1434, https://doi.org/10.1016/0016-7037(73)90080-X.

Borcovsky, D., Egenhoff, S., Fishman, N., Maletz, J., Boehlke, A., & Lowers, H., 2017. Sedimentology, facies architecture, and sequence stratigraphy of a Mississippian black mudstone—The upper member of the Bakken Formation, North Dakota, United States.

AAPG Bulletin. **101**, 1625-1673, https://doi.org/10.1306/01111715183.

Browne, T.N., Hofmann, M.H., Malkowski, M.A., Wei, J., & Sperling, E.A., 2020. Redox and paleoenvironmental conditions of the Devonian-Carboniferous Sappington Formation, southwestern Montana, and comparison to the Bakken Formation, Williston Basin. Palaeogeography Palaeoclimatology Palaeoecology, **560**, 110025. https://doi.org/10.1016/j.palaeo.2020.110025.

Canfield, D.E., Raiswell, R., Westrich, J.T., Reaves, C.M., & Berner, R.A., 1986. The use of chromium reduction in the analysis of reduced inorganic sulfur in sediments and shales. *Chemical Geology*, **54**, 149–155. https://doi.org/10.1016/0009-2541(86)90078-1

Caplan, M.L., & Bustin, R.M., 1999. Devonian-Carboniferous Hangenberg mass extinction event, widespread organic-rich mudrock and anoxia: causes and consequences. P*alaeogeography Palaeoclimatology Palaeoecology*, **148**, 187–207. https://doi.org/10.1016/S0031-0182(98)00218-1.

Caplan, M.L., & Bustin, R.M., 2001. Palaeoenvironmental and palaeoceanographic controls on black, laminated mudrock deposition: example from Devonian-Carboniferous strata, Alberta, Canada. *Sedimentary Geology*, **145**, 45–72. https://doi.org/10.1016/S0037-0738(01)00116-6

Caplan, M.L., Bustin, R.M., & Grimm, K.A., 1996. Demise of a Devonian-Carboniferous carbonate ramp by eutrophication. *Geology*, **24**, 715–718, https://doi.org/10.1130/0091-7613(1996)024<0715:DOADCC>2.3.CO;2.

Carmichael, S.K., Waters, J.A., Batchelor, C.J., Coleman, D.M., Suttner, T.J., Kido, E., Moore, L.M., & Chadimová, L., 2016. Climate instability and tipping points in the Late Devonian: detection of the Hangenberg Event in an open oceanic island arc in the Central Asian Orogenic Belt. *Gondwana Research*, **32**, 213–231, https://doi.org/10.1016/j.gr.2015.02.009.

Clarkson, M.O., Poulton, S.W., Guilbaud, R., & Wood, R.A., 2014. Assessing the utility of Fe/Al and Fe-speciation to record water column redox conditions in carbonate-rich sediments. *Chemical Geology*, **382**, 111–122, https://doi.org/10.1016/j.chemgeo.2014.05.031.

Crusius, J., Calvert, S., Pedersen, T., & Sage, D., 1996. Rhenium and molybdenum enrichments in sediments as indicators of oxic, suboxic and sulfidic conditions of deposition. *Earth Planetary Science Letter*, **145**, 65–78. https://doi.org/10.1016/s0012-821x(96)00204-x

di Pasquo, M., Grader, G.W., Kondas, M., Doughty, P.T., Filipiak, P., Rice, B.J., & Isaacson, P.E., 2019. Lower Sappington Formation palynofacies in Montana confirm upper famennian black shale paleoenvironments and sequences across western North America. *Palaeogeography Palaeoclimology Palaeoecology*, **536**, 109370. https://doi.org/10.1016/j.palaeo.2019.109370.

Dixit, S., Van Cappellen, P., & Van Bennekom, A.J., 2001. Processes controlling solubility of biogenic silica and pore water build-up of silicic acid in marine sediments. *Marine*

Chemistry, **73**, 333–352. https://doi.org/10.1016/S0304-4203(00)00118-3.

Egenhoff, S.O., 2017. The lost Devonian sequence – sequence stratigraphy of the middle Bakken member, and the importance of clastic dykes in the lower Bakken member shale, North Dakota, USA. *Marine Petroleum Geology*, **81**, 278- 293, https://doi.org/10.1016/j.marpetgeo.2017.01.015.

Egenhoff, S.O., & Fishman, N.S., 2013. Traces in the dark-sedimentary processes and facies gradients in the upper shale member of the Upper Devonian-Lower Mississippian Bakken Formation, Williston Basin, North Dakota, U.S.A. *Jouranl of Sedimentary Research*, **83**, 803–824, https://doi.org/10.2110/jsr.2013.60.

Emerson, S.R., & Huested, S.S., 1991. Ocean anoxia and the concentrations of molybdenum and vanadium in seawater. *Marine Chemistry*, **34**, 177–196, https://doi.org/10.1016/0304-4203(91)90002-E.

Erickson, B.E., & Helz, G.R., 2000. Molybdenum(VI) speciation in sulfidic waters. *Geochimica et Cosmochimica Acta*, **64**, 1149–1158, https://doi.org/10.1016/s0016-7037(99)00423-8.

Föllmi, K.B., 1996. The phosphorus cycle, phosphogenesis and marine phosphate-rich deposits. *Earth-Science Review*, **40**, 55– 124, https://doi.org/10.1016/0012-8252(95)00049-6.

Föllmi, K.B., 2016. Sedimentary condensation. Earth-Science Review, **152**, 143–180. https://doi.org/10.1016/j.earscirev.2015.11.016.

Föllmi, K.B., Weissert, H., Bisping, M., & Funk,H. 1994. Phosphogenesis, carbon-isotope stratigraphy, and carbonate-platform evolution along the Lower Cretaceous northern Tethyan margin. *Geological Society of America Bulletin*, **106(6)**, 729-746, https://doi.org/10.1130/0016-7606(1994)106<0729: PCISAC>2.3.CO;2.

Hart, B., & Hofmann, M. 2018. The Late Devonian ice age and the giant Bakken oil field. *The Sedimentary Record*, **18(1)**, 4-9.

Helz, G.R., Miller, C. V., Charnock, J.M., Mosselmans, J.F.W., Pattrick, R.A.D., Garner, C.D., & Vaughan, D.J., 1996. Mechanism of molybdenum removal from the sea and its concentration in black shales: EXAFS evidence. *Geochimica et Cosmochimica Acta,* **60**, 3631–3642, https://doi.org/10.1016/0016-7037(96)00195-0.

Hogancamp, N.J., & Pocknall, D.T., 2018. The biostratigraphy of the Bakken Formation: a review and new data. *Stratigraphy*, **15**, 197-224.

Hornung, T., Brandner, R., Krystyn, L., Joachimski, M.M., & Keim, L. 2007. Multistratigraphic constraints on the NW Tethyan “Carnian crisis”, *The Global Triassic*, **41**, 59-67.

Ingall, E.D., & Cappellen, P. Van, 1990. Relation between sedimentation rate and burial of organic phosphorus and organic carbon in marine sediments. *Geochimica et Cosmochimica Acta* **54**, 373–386. https://doi.org/10.1016/0016-7037(90)90326-G.

Johnstone, D.I., Henderson, C.M., & Schmidt, M.J. 2010. Upper Devonian to Lower

Mississippian conodont biostratigraphy of uppermost Wabamun Group and Palliser Formation to lowermost Banff and Lodgepole formations, southern Alberta and southeastern British Columbia, Canada: implications for correlations and sequence stratigraphy. *Bulletin of Canadian Petroleum Geology*, **58(4)**, 295-341, https://doi.org/10.2113/gscpgbull.58.4.295.

Kaiser, S.I., Aretz, M., & Becker, R.T., 2016. The global Hangenberg Crisis (Devonian-Carboniferous transition): Review of a first-order mass extinction. *Geological Society Speical Publication,* **423**, 387–437. https://doi.org/10.1144/SP423.9.

Kendall, B., Reinhard, C.T., Lyons, T.W., Kaufman, A.J., & Poulton, S.W., Anbar, A.D., 2010. Pervasive oxygenation along late Archaean ocean margins. *Nature Geoscience*, **3**, 647–652, https://doi.org/10.1038/ngeo942.

Klinkhammer, G.P., & Palmer, M.R., 1991. Uranium in the oceans: where it goes and why. *Geochimica et Cosmochimica Acta,* **55**, 1799–1806, https://doi.org/10.1016/0016-7037(91)90024-Y.

Lampitt, R.S., Salter, I., & Johns, D., 2009. Radiolaria: major exporters of organic carbon to the deep ocean. *Global Biogeochemical Cycles*, **23**, 1–9, https://doi.org/10.1029/2008GB003221.

Love, L.G., 1971. Early diagenetic polyframboidal pyrite, primary and redeposited, from the Wenlockian Denbigh Grit Group, Conway, North Wales, U.K. *Journal of Sedimentary Research*, **41**, 1038–1044.

Love, L.G., & Vanguestaine, M. 1973. Polyframboidal pyrite of the Rochelinval pyrite beds (Belgian Ardennes). *Annales de la Société géologique de Belgique*.

Lyons, T.W., & Severmann, S., 2006. A critical look at iron paleoredox proxies: New insights from modern euxinic marine basins. *Geochimica et Cosmochimica Acta,* **70**, 5698–5722. https://doi.org/10.1016/j.gca.2006.08.021.

McLennan, S.M., 2001. Relationships between the trace element composition of sedimentary rocks and upper continental crust. *Geochemistry Geophysics Geosystems*, **2**, 1021. https://doi.org/10.1029/2000GC000109.

Morford, J.L., & Emerson, S., 1999. The geochemistry of redox sensitive trace metals in sediments. *Geochimica et Cosmochimica Acta,* **63**, 1735–1750, https://doi.org/10.1016/S0016-7037(99)00126-X.

Myrow, P.M., Hanson, A., Phelps, A.S., Creveling, J.R., Strauss, J. V., Fike, D.A., & Ripperdan, R.L., 2013. Latest Devonian (Famennian) global events in western Laurentia: Variations in the carbon isotopic record linked to diagenetic alteration below regionally extensive unconformities. *Palaeogeography Palaeoclimatology Palaeoecology*, **386**, 194–209, https://doi.org/10.1016/j.palaeo.2013.05.021.

Nameroff, T.J., Balistrieri, L.S., & Murray, J.W., 2002. Suboxic trace metal geochemistry in the eastern tropical North Pacific. *Geochimica et Cosmochimica Acta,* **66**, 1139–1158, https://doi.org/10.1016/S0016-7037(01)00843-2.

Over, D.J. 2021. The Devonian-Carboniferous boundary in the United States. *Palaeobiodiversity and Palaeoenvironments*, **101**, 529-540, https://doi.org/10.1007/s12549-020-00428-1.

Partin, C.A., Bekker, A., Planavsky, N.J., Scott, C.T., Gill, B.C., Li, C., Podkovyrov, V., Maslov, A., Konhauser, K.O., Lalonde, S. V., Love, G.D., Poulton, S.W., & Lyons, T.W., 2013. Large-scale fluctuations in Precambrian atmospheric and oceanic oxygen levels from the record of U in shales. *Earth Planetary Science Letter*, **369–370**, 284–293, https://doi.org/10.1016/j.epsl. 2013.03.031.

Petrash, D.A., Gueneli, N., Brocks, J.J., Mendez-Dot, J.A., González-Arismendi, G., Poulton, S.W., & Konhauser, K.O., 2016. Black shale deposition and early diagenetic dolomite cementation during oceanic anoxic event 1: the Mid-Cretaceous Maracaibo Platform, northwesern South America. *American Journal of Science*, **316**, 669-711, https://doi.org/10.2475/07.2016.03.

Petty, D.M. 2019. An alternative interpretation for the origin of black shale in the Bakken Formation of the Williston Basin. *Bulletin of Canadian Petroleum Geology*, **67(1)**, 47-70.

Poulton, S.W., 2021. The iron speciation paleoredox proxy. Cambridge Elements: Geochemical tracers in Earth system science. https://doi.org/10.1017/9781108847148

Poulton, S.W., & Canfield, D.E., 2005. Development of a sequential extraction procedure for iron: Implications for iron partitioning in continentally derived particulates. *Chemical Geology*, **214**, 209–221, https://doi.org/10.1016/j.chemgeo.2004.09.003.

Poulton, S.W., & Canfield, D.E., 2011. Ferruginous conditions: a dominant feature of the ocean through Earth's history. *Elements*, **7**, 107–112, https://doi.org/10.2113/gselements. 7.2.107.

Poulton, S.W., Fralick, P.W., & Canfield, D.E., 2004. The transition to a sulphidic ocean ∼1.84 billion years ago. *Nature*, **431**, 173–177, https://doi.org/10.1038/nature02912.

Poulton, S.W., & Raiswell, R., 2002. The low-temperature geochemical cycle of iron : From continental fluxes to marine sediment deposition. *American Journal of Science*, **302**, 774–805, https://doi.org/10.2475/ajs.302.9.774.

Raasch, G.O., 1956 Late Devonian and/or Mississippian faunal succession in Stettler Area, Alberta. *Bulletin of Canadian Petroleum Geology*, **4**, 112-118.

Raiswell, R., & Canfield, D.E., 1998. Sources of iron for pyrite formation in marine sediments. *American Journal of Science,* **298**, 219–245, https://doi.org/10.2475/ajs.298.3.219.

Raiswell, R., Newton, R., & Wignall, P.B., 2001. An indicator of water-column anoxia: resolution of biofacies variations in the kimmeridge clay (upper Jurassic, U.K.). *Journal of Sedimentary Research*, **71**, 286–294, https://doi.org/10.1306/070300710286.

Richard, B.C., Ross, G.M., & Utting, H., 2002. U-Pb geochronology, lithostratigraphy and biostratigraphy of tuff in the upper Famennian to Tournaisian Exshaw Formation: evidence for a mid-Paleozoic magmatic arc on the northwestern margin of North America. *Canadian Society of Petroleum Geologists, Memoir*, **19**, 158-207.

Richards, B.C., Bamber, E.W., Henderson, C.M., Higgins, A.C., Johnstone, D.I., Mamet, B.L., & Meijer-Drees, N.C., 1994. Uppermost Devonian (Famennian) and Lower Carboniferous (Tournaisian) at Jura Ceek and Mount Rundle, southwestern Alberta. *Geological Survey of Canada*, Open File 2866, 79 pp.

Richards, B.C., & Higgins, A.C., 1988. Devonian-Carboniferous boundary beds of the Palliser and Exshaw formations at Jura Creek, Rocky Mountains, southwestern Alberta. *Canada Society of Petroleum Geological Memior*, **14**, 399–412.

Root, K.G., 2001. Devonian Antler fold and thrust belt and foreland basin development in the southern Canadian Cordillera: Implications for the Western Canada Sedimentary Basin. *Bulletin of Canadian Petroleum Geology*, **49**, 7–36, https://doi.org/10.2113/49.1.7.

Ruttenberg, K.C., & Berner, R.A., 1993. Authigenic apatite formation and burial in sediments from non-upwelling, continental margin environments. *Geochimica et cosmochimica acta*, **57**, 991–1007, https://doi.org/10.1016/0016-7037(93)90035-U.

Sageman, B.B., Murphy, A.E., Werne, J.P., Ver Straeten, C.A., Hollander, D.J., & Lyons, T.W., 2003. A tale of shales: the relative roles of production, decomposition, and dilution in the accumulation of organic-rich strata, Middle-Upper Devonian, Appalachian basin. *Chemical Geology*, **195**, 229–273, https://doi.org/10.1016/S0009-2541(02)00397-2.

Sandberg, C.A., Morrow, J.R., & Ziegler, W., 2002. Late Devonian sea-level changes, catastrophic events, and mass extinctions. *Special papers-geological society of America*, **356**, 473–487, https://doi.org/10.1130/0-8137-2356-6.473.

Savoy, L.E., 1992. Environmental record of Devonian-Mississippian carbonate and low- oxygen facies transitions, southernmost Canadian Rocky Mountains and northwesternmost Montana. *Geological Society of America Bulletin*, **104**, 1412–1432, https://doi.org/10.1130/0016-7606(1992)104<1412:ERODMC>2.3.CO;2.

Savoy, L.E., Harris, A.G., & Mountjoy, E.W., 1999. Extension of lithofacies and conodont biofacies models of Late Devonian to Early Carboniferous carbonate ramp and black shale systems, southern Canadian Rocky Mountains. *Canadian Journal of Earth Sciences*, **36**, 1281–1298, https://doi.org/10.1139/cjes-36-8-1281.

Schieber, J., & Baird, G., 2001. On the origin and significance of pyrite spheres in Devonian black shales of North America. *Journal Sedimentary Research*, **71**, 155-166.

Schobben, M., Foster, W.J., Sleveland, A.R.N., Zuchuat, V., Svensen, H.H., Planke, S., Bond, D.P.G., Marcelis, F., Newton, R.J., Wignall, P.B., & Poulton, S.W., 2020. A nutrient control on marine anoxia during the end-Permian mass extinction. *Nature Geoscience*, **13**, 640–646, https://doi.org/10.1038/s41561-020-0622-1.

Scott, C., Slack, J.F., & Kelley, K.D. 2017. The hyper-enrichment of V and Zn in black shales of the Late Devonian-Early Mississippian Bakken Formation (USA). *Chemical Geology*, **452**, 24-33, https://doi.org/10.1016/j.chemgeol.2017.01.026.

Selby, D., & Creaser, R.A., 2005. Direct radiometric dating of the Devonian-Mississippian time-scale boundary using the Re-Os black shale geochronometer. *Geology*, **33**, 545–548, https://doi.org/10.1130/G21324.1.

Slomp, C.P., Epping, E.H.G., Helder, W., & Van Raaphorst, W., 1996. A key role for iron-bound phosphorus in authigenic apatite formation in North Atlantic continental platform sediments. *Journal of marine Research*, **54**, 1179–1205, https://doi.org/10.1357/0022240963213745.

Smith, M.G., & Bustin, R.M., 1998. Production and preservation of organic matter during deposition of the Bakken Formation (Late Devonian and Early Mississippian), Williston Basin. *Palaeogeography, Palaeoclimatology, Palaeoecology*, **142**, 185–200, https://doi.org/10. 1016/S0031-0182(98)00063-7.

Smith, M.G., & Bustin, R.M., 2000. Late Devonian and Early Mississippian Bakken and Exshaw black shale source rocks, Western Canada sedimentary basin: A sequence stratigraphic interpretation. *AAPG Bulletin*, **84**, 940–960, https://doi. org/10.1306/a9673b76-1738-11d7-8645000102c1865d.

Smith, M.G., Bustin, R.M., & Caplan, M.L., 1995. Sequence Stratigraphy of the Bakken and Exshaw Formations: A Continuum of Black Shale Formations in the Western Canada Sedimentary Basin. Seventh Int. Willist. *Williston Basin Symposium*. 399–409.

Sundby, B., Gobeil, C., Silverberg, N., & Mucci, A., 1992. The phosphorus cycle in coastal marine sediments. Limnology and oceanography, 37, 1129-1145, https://doi.org/10.4319/lo.1992.37. 6.1129.

Tribovillard, N., Algeo, T.J., Baudin, F., & Riboulleau, A., 2012. Analysis of marine environmental conditions based on molybdenum-uranium covariation-Applications to Mesozoic paleoceanography. *Chemical Geology*, **324**, 46–58, https://doi.org/10.1016/j. chemgeo.2011.09.009.

Van Cappellen, P., Dixit, S., & van Beusekom, J., 2002. Biogenic silica dissolution in the oceans: reconciling experimental and field-based dissolution rates. *Global Biogeochemical Cycles,* **16**, 1075, https://doi.org/10.1029/2001gb001431.

Van Cappellen, P., & Qiu, L., 1997. Biogenic silica dissolution in sediments of the Southern Ocean. II. Kinetics. *Deep Sea Research Part II: Topical Studies in Oceanography*, **44**, 1129–1149, https://doi.org/10.1016/S0967-0645(96)00112-9.

Walliser, O.H., 1996. Global Events in the Devonian and Carboniferous, in: Walliser, O.H. (Ed.), Global Events and Event Stratigraphy in the Phanerozoic: Results of the International Interdisciplinary Cooperation in the IGCP-Project 216 ‘Global Biological Events in Earth History’. Springer Berlin Heidelberg, pp. 225–250, https://doi.org/10.1007/978-3-642-79634-0_11.

Webster, R.L., 1984. Petroleum source rocks and stratigraphy of Bakken Formation in North Dakota, *AAPG Bulletin*, **68**, 953, https://doi.org/10. 1306/AD46166F-16F7-11D7-8645000102C1865D.

Wei, H., Wei, X., Qiu, Z., Song, H., & Shi, G., 2016. Redox conditions across the G–L boundary in South China: Evidence from pyrite morphology and sulfur isotopic compositions. *Chemical Geology*, **440**, 1–14. https://doi.org/10.1016/j.chemgeo.2016.07.009.

Wignall, P.B., Bond, D.P.G., Kuwahara, K., Kakuwa, Y., Newton, R.J., & Poulton, S.W., 2010. An 80 million year oceanic redox history from Permian to Jurassic pelagic sediments of the Mino-Tamba terrane, SW Japan, and the origin of four mass extinctions. *Global Planetary Change*, **71**, 109–123. https://doi.org/10.1016/j.gloplacha.2010.01.022

Wignall, P.B., & Newton, R., 1998. Pyrite framboid diameter as a measure of oxygen deficiency in ancient mudrocks. *American Journal of Science*, **298**, 537–552. https://doi.org/10.2475/ajs.298.7.537.

Wilkin, R.T., & Arthur, M.A., 2001. Variations in pyrite texture, sulfur isotope composition, and iron systematics in the black sea: Evidence for late pleistocene to holocene excursions of the O2-H2S redox transition. *Geochimica et Cosmochimica Acta*, **65**, 1399–1416, https://doi.org/10.1016/S0016-7037(01)00552-X.

Wilkin, R.T., & Barnes, H.L., 1997. Formation processes of framboidal pyrite. *Geochimica et Cosmochimica Acta,* **61**, 323–339, https://doi.org/10.1016/S0016-7037(96)00320-1.

Wilkin, R.T., Barnes, H.L., & Brantley, S.L., 1996. The size distribution of framboidal pyrite in modern sediments. *Geochimica et Cosmochimica Acta,* **60**, 3897–3912, https://doi.org/10. 1016/0016-7037(96)00209-8.

Wilmsen, M. 2000. Evolution and demise of a mid-Cretaceous carbonate shelf: the Altamira Limestones (Cenomanian) of northern Cantabria (Spain). *Sedimentary Geology*, **133**, 195-226.

Zegeye, A., Bonneville, S., Benning, L.G., Sturm, A., Fowle, D.A., Jones, C.A., Canfield, D.E., Ruby, C., MacLean, L.C., Nomosatryo, S., Crowe, S.A., & Poulton, S.W., 2012. Green rust formation controls nutrient availability in a ferruginous water column. *Geology*, **40**, 599–602, https://doi.org/10.1130/G32959.1.

Zhang, F., Dahl, T.W., Lenton, T.M., Luo, G., Shen, S. zhong, Algeo, T.J., Planavsky, N., Liu, J., Cui, Y., Qie, W., Romaniello, S.J., & Anbar, A.D., 2020. Extensive marine anoxia associated with the Late Devonian Hangenberg Crisis. *Earth Planetary Science Letter*, **533**, 115976, https://doi.org/10.1016/j.epsl.2019.115976.

Chapter 3: Calibration of redox thresholds in black shale: Insight from a stratified Mississippian basin with warm saline bottom waters

Accepted by Geological Society of America Bulletin

Li, S., Wignall, P. B., Xiong, Y., & Poulton, S. (2023). Calibration of redox thresholds in black shale: Insight from a stratified Mississippian basin with warm saline bottom waters. Geological Society of America Bulletin.

Calibration of redox thresholds in black shale: Insight from a stratified Mississippian basin with warm saline bottom waters

Sen Li, Paul B. Wignall, Yijun Xiong, Simon W. Poulton

School of Earth and Environment, University of Leeds, Leeds, LS2 9JT, UK

3.1 Abstract

Depositional models for black shale formation rely on detailed understanding of redox conditions and how they relate to basin development. Here we calibrate multiple redox proxies (Fe speciation, U and Mo systematics, pyrite framboid distributions) in the Bowland Shale, a major hydrocarbon unit in the Mississippian of northern England and develop a depositional model for black shale deposition in basins adjacent to extensive carbonate platforms. The transition from deep ramp carbonates to basinal mudrocks initially occurred under oxic conditions, before anoxic conditions began to expand from basin centre locations. By the end of Bowland Shale deposition, ~10 million years later, black shale deposition extended from the basin into shallow-water settings, the former being sites of platform-edge carbonates. By this stage, euxinic conditions were widespread throughout the Bowland Shale. The prolonged persistence of euxinia during younger Bowland Shale deposition, and the sharp transition to fully oxygenated facies at the basin margin, suggests there was a well-developed water column pycnocline. Black shale development in silled basins is traditionally interpreted to form beneath a halocline with a positive water balance caused by freshwater run-off (estuarine circulation). This model is not considered appropriate in this case. Bowland Shale deposition was terminated by the onset of turbidite deposition supplied by a major deltaic system, but for most of its history the basin was surrounded by carbonate platforms that are unlikely to have experienced brackish conditions. The encroachment of the clastic system saw the rapid improvement of basinal oxygenation in the uppermost Bowland Shale, and even minor turbidite sandstones within the black shales coincided with a weakening in the intensity of euxinia, suggesting that sediment-laden fresher waters flushed out and oxygenated the basin. We therefore suggest a warm saline bottom water model for black shale deposition, with basinal waters generated on the adjacent carbonate platforms due to evaporation. Such a scenario is likely more broadly applicable to basinal black shales developed adjacent to shallow-water carbonate successions.

Key words: Black shale, Framboidal pyrite, Euxinic, Fe phase partitioning, Warm saline bottom water, Redox-sensitive elements

3.2 Introduction

Controls on the extent and nature of oxygen-depleted (anoxic) deposition in marine depositional environments constitute a key debate in paleoenvironmental research (Demaison and Moore, 1980; Arthur and Sageman, 1994; Wignall, 1994). Oxygen levels reflect a balance between supply and demand, with two end-member scenarios that can both lead to anoxic, organic-rich sediment deposition. Firstly, elevated productivity can lead to “organic overload”, where intense oxygen consumption by decaying, planktonic organic matter lowers the redox level in the water column. Such conditions can produce an intense mid-water oxygen-minimum zone either at the basin margin, where upwelling of nutrient-rich waters fosters high productivity, or adjacent to coastal areas where abundant terrigenous nutrient supply achieves the same effect (e.g. Jenkyns, 2010). Secondly, restricted vertical advection due to the presence of a strong density interface (pycnocline) within the water column, and/or restricted lateral advection due to a silled basin configuration, can hinder oxygen supply and lead to organic-rich sedimentation in settings where primary production is not unusually high (Demaison and Moore, 1980; Tyson and Pearson, 1991; Wignall, 1994; Algeo et al., 2008).

Typically, stratification is controlled by salinity, in which freshwater surface runoff isolates more saline, deeper waters, or by temperature whereby warmer surface waters overlie colder and denser deep waters (Tyson and Pearson, 1991; Wignall, 1994; Algeo et al., 2008). Surface water evaporation can also generate warm but dense saline waters that sink into deeper waters. Such warm saline bottom waters (WSBWs) are seen in the present-day Mediterranean, which is well-oxygenated at depth (Demaison and Moore, 1980), but oceanic anoxia in the Cretaceous and the Silurian has been attributed to WSBW stratification (e.g. Brass et al., 1982; Munnecke et al., 2003). Distinguishing between these scenarios (high productivity or restricted circulation) is a difficult undertaking in the geological record because productivity indicators are often ambivalent and water column stratification is difficult to diagnose. Here we examine the spatio-temporal redox record in a basin where a prolonged history of anoxic, organic-rich deposition produced one of the major black shale units of British stratigraphy, the Bowland Shale, and evaluate possible depositional models for this economically important source rock.

3.3 Regional Setting

Mississippian deposition in central northern England occurred in a series of interlinked, tectonically-active basins surrounded by shallow-water carbonate platforms at low southerly paleolatitudes (Fig. 3.1A). The Bowland Basin, now exposed in northern England, was one of the largest of these basins and was bordered to the north by an extensive carbonate platform developed on the Askrigg Block, with the Craven Fault belt marking the sharp transition between shallow-water carbonates and finer-grained basinal strata (Fig. 3.1B; Kirby, 2000). Carbonate shelf seas also fringed the basin to the south and east.

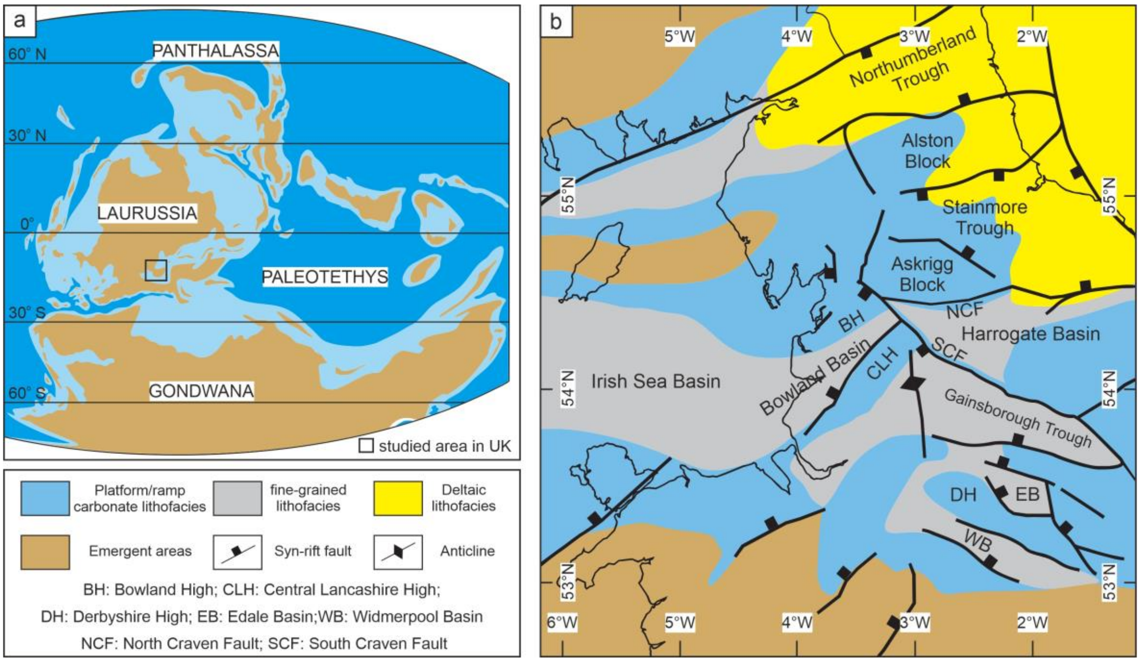

Fig. 3.1 (a) Mississippian (340 Ma) global paleogeography (modified from Boucot et al., 2013), showing the northern England study area (black rectangle); (b) regional paleogeography of northern England during the Asbian (336- 332 Ma), showing the occurrence of isolated basins surrounded by carbonate platforms and shelves (modified from Cope et al., 1992).

The initial phase of Bowland Basin infill consisted of fine-grained carbonate deposition interbedded with carbonate debris flow and sedimentary slide/slump deposits (the Pendleside Limestone Formation; Gawthorpe, 1986, 1987). The latter were especially common during two periods of tectonic activity that occurred in the late Tournaisian and the late Visean. Using the regional stage names, the latter phase of tectonism occurred during the Asbian to early Brigantian. This transformed the Bowland Basin (and others in the region) from one with extensive carbonate ramps to a basin with fault-bounded, steep margins, surrounded by carbonate platforms developed on both horsts and tilt blocks. (Gawthorpe, 1986; 1987; Ebdon et al., 1990; Fraser and Gawthorpe, 1990; Kirby, 2000; Manifold et al., 2021).

The increased subsidence rate during late Visean tectonism coincides with a diachronous transition from carbonate-dominated to dark grey shale-dominated deposition of the Lower Bowland Shale Formation in basinal areas (Fig. 3.2; Kirby, 2000). Several local, allochthonous limestones occur within the early Brigantian portion of this Formation, whilst thin sandstones make an appearance in the late Brigantian (Fig. 3.2). The latter are harbingers of a much-increased clastic influx into the Bowland Basin that would ultimately see shale deposition replaced by a thick succession of turbidite sandstones in the early Serpukhovian/late Pendleian stage (Waters et al., 2009; Kane, 2010). Prior to this, the transition from active rifting to more passive thermal subsidence around the Brigantian/Pendleian boundary caused the margins of the basin to subside following minor inversion, and dark grey shales of the Upper Bowland Shale Formation onlapped onto the southern margins of the Askrigg Block – an area that was previously the site of shallow-water carbonate deposition (Waters et al., 2017).

The geological history of the Bowland Basin is closely comparable to that seen in contiguous basins developed along strike. For example, in the Dublin Basin, 250 km to the west, the dark grey shales of the Donore Shale onlapped adjacent carbonate platforms during the Brigantian (Pickard et al., 1994; Kirby, 2000). The combined Lower and Upper Bowland Shale formations range from several hundred meters to more than a kilometer in

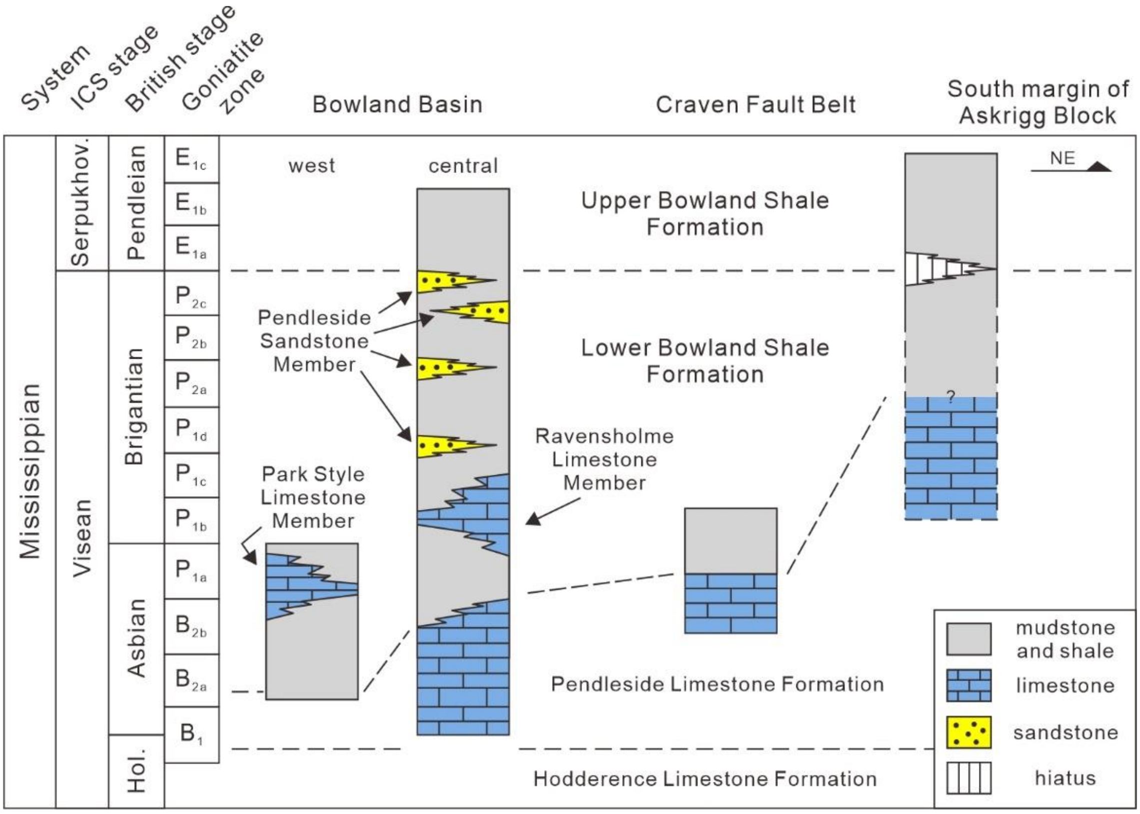

Fig. 3.2 Summary cross section through the Bowland Basin, Craven Fault Belt; Hol. = Holkerian; Serpukhov. = Serpukhovian; ICS stands for International Commission on Stratigraphy; dashed lines show the formation boundaries (after Earp et al., 1961; Aitkenhead et al., 1992; Waters et al., 2017).

thickness, making them one of the thickest black shale successions in the onshore stratigraphy of the British Isles (de Jonge-Anderson and Underhill, 2020) and they have great economic importance as a potential source of shale gas and known hydrocarbon prospects. Unsurprisingly, the Bowland Shale has been the subject of numerous studies mainly focused on organic matter types (e.g. Gross et al., 2015; Fauchille et al., 2017; Hennissen et al., 2017; Newport et al., 2018; de Jonge-Anderson and Underhill, 2020). However, the controls on redox conditions and organic enrichment during the ~10-million-year history of Bowland Shale deposition have been surprisingly little investigated. Emmings et al. (2020) reported that Upper Bowland Shale deposition in the NW region of the basin occurred beneath ferruginous anoxic and occasionally euxinic waters and suggested sea-level fluctuations were an important control. In order to evaluate the long history of redox development prior to and during deposition of the Lower and Upper Bowland Shale formations, we present a study of multiple redox proxies from numerous sections around the Bowland Basin and its margin and develop a model for the development of this economically important source rock.

3.4 Methods and Approach

3.4.1 Sample collection and field area

Fieldwork investigations (sedimentary logging and sample collection) were undertaken at 13 locations, mostly comprising stream and river outcrops: Dobson Brook (DB), Leagram Brook (LB), Smelthwaite Farm (SM), School Share (SS), Cow Close (CC), Moor Close Gill (MC), Dinckley Hall (DH), River Hodder (RH), Light Clough (LC), Swardean Clough (SC), Clough Head Beck (CH), Tory Log Clough (TLC), and Fell Lane (FL) (Fig. 3.3 and Supplementary appendix A). These locations record deposition in settings ranging from basin centre to basin margin. The two most extensive basinal sections were sampled at TLC and DH, and their combined record ranges from the mid Pendleside Limestone (Asbian Stage) to the Upper Bowland Shale (Pendleian Stage). A further seven, shorter sections, were also examined, thereby allowing the temporal and spatial variation of redox changes within the basin to be fully determined. Finally, additional study of four sites (SS, CC, MC and FL) from the Craven Fault Belt system on the northern margin of the Bowland Basin, allowed the redox conditions of the Bowland Shale Formation to be examined at a level where it onlaps platform carbonates on the southern margin of the Askrigg Block (Fig. 3.3). The study sections contain the Hodderense Limestone, Pendleside Limestone, and the Lower and Upper Bowland Shale formations, spanning the interval from the late Holkerian to early Pendleian (Fig. 3.2). High resolution correlation of sections is possible because of the associated goniatite fauna reported (see Supplementary appendix A). This long-established scheme utilises multiple lineages of goniatites (e.g. *Eumorphoceras*) and a short-hand, letter-number scheme (e.g. E_{1c} is the youngest zone of the Bowland Shale and has the zonal goniatite *Cravenoceras malhamense* and *Eumorphoceras* spp. present) to designate biozones (Waters and Condon, 2012).

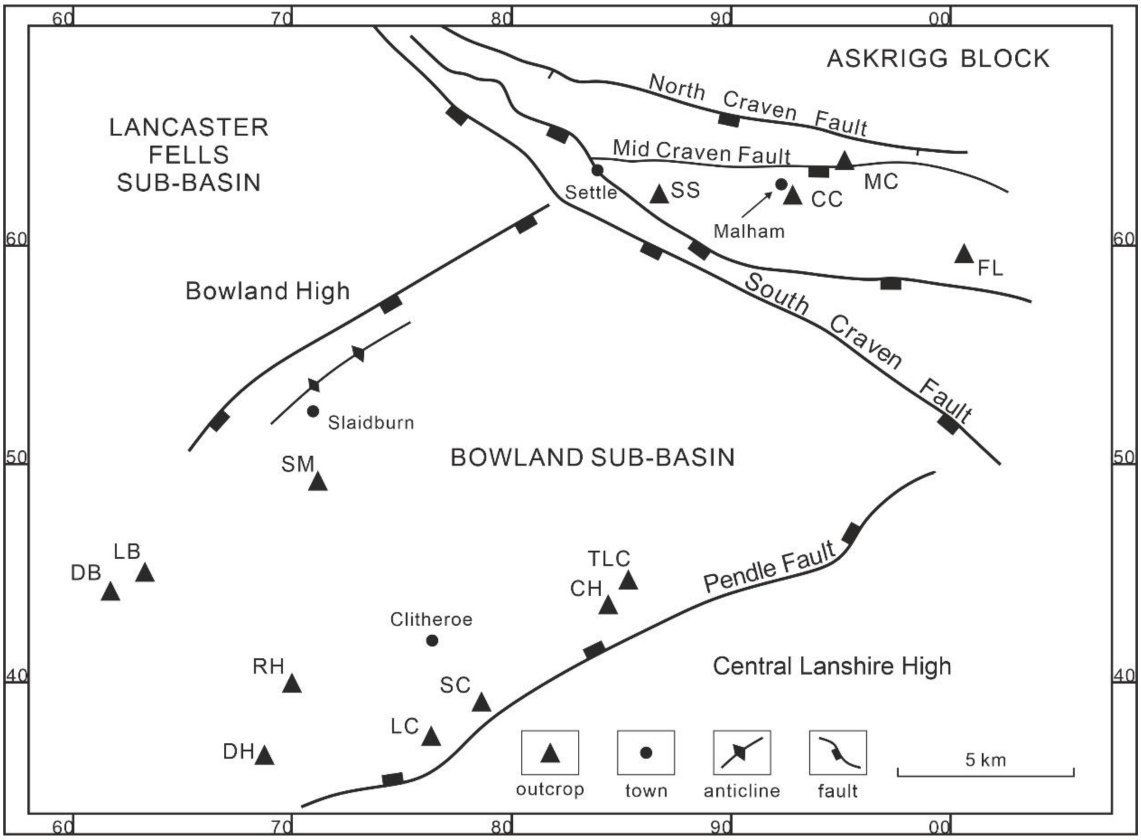

Fig. 3.3 Study area in the Bowland Basin, Craven Fault Belt, and the southern Askrigg Block. Outcrop locations are Dobson Brook (DB), Leagram Brook (LB), Smelthwaite Farm (SM), School Share (SS), Cow Close (CC), Moor Close Gill (MC), Dinckley Hall (DH), River Hodder (RH), Light Clough (LC), Swarden Clough (SC), Clough Head Beck (CH), Tory Log Clough (TLC), and Fell Lane (FL).

Fresh samples were collected to avoid oxidation and to obtain detailed petrological and geochemical information, and in all cases, samples with visible evidence of later stage diagenetic or post-depositional overprints (e.g. veins, nodules, concretions, secondary euhedral pyritization) were avoided. An agate mortar was used to crush samples into homogeneous powder (<60 μm) for geochemical analyses. Selected samples were polished before carbon-coating to perform pyrite morphology analyses on a TESCAN VEGA3 Scanning

Electron Microscope (SEM) using the backscatter mode. Framboidal pyrite data set refers to supplementary appendix B.

3.4.2 Major elements

Total organic carbon (TOC) analyses were determined on a LECO Carbon-Sulfur Analyzer. Samples were de-carbonated prior to analysis using 10% HCl. Replicate analyses of certified reference material (Soil LCRM with carbon content of 10.8 ± 0.26 wt%) gave a relative standard deviation (RSD) of <1.5%, and accuracy was ensured by analyses within 1% of reported values. In terms of other major and trace elements, samples were ashed at 550°C for 8 h, followed by quantitative digestion using concentrated HNO_3, HF and $HClO_4$. H_3BO_3 was added to prevent the formation of Al hexafluorate complexes. Finally, the residues were re-dissolved with near-boiling HNO_3 and diluted with ultrapure 18MΩ H_2O prior to analysis by ICP-OES (Inductively Coupled Plasma Optical Emission spectroscopy) for major elements and ICP-MS (Inductively coupled plasma mass spectrometry) for trace elements. Accuracy and precision, estimated from the repeat analyses of United State Geological Survey standard SGR-1b (Green River Shale), were better than 5%. Enrichment factors (EF) were used to assess the behaviour of Mo and U in siliciclastic intervals, where $element_{EF} = (element/Al)_{sample}/(element/Al)_{AUC}$, and AUC represents average upper crust concentrations (McLennan, 2001).

3.4.3 Fe phase partitioning

Sequential Fe extractions were performed according to the technique of Poulton and Canfield (2005). The procedure targets different operationally-defined Fe pools that are considered highly reactive (Fe_{HR}) towards dissolved sulfide in anoxic conditions under near-surface conditions (Raiswell and Canfield, 1998; Poulton and Canfield, 2005). Firstly, 1 M sodium acetate (pH 4.5) was used to extract carbonate-associated iron (Fe_{carb}) at 50°C for 48

h. Subsequently, Fe (oxyhydr)oxide minerals (Fe_{ox}) were extracted by sodium dithionite (2 h at room temperature), followed by magnetite (Fe_{mag}) extraction via a 0.2 M ammonium oxalate/0.17 M oxalic acid solution (6 h at room temperature). All Fe concentrations were measured on a Thermo Scientific iCE-3000 series flame Atomic Absorption Spectrometer (AAS). Pyrite (Fe_{py}) and acid volatile sulfide (AVS) were measured on a separate sub-sample via a two-step chromous chloride distillation (Canfield et al., 1986). Liberated hydrogen sulfide was trapped as Ag_2S and its concentration was quantified gravimetrically. Replicate extractions of an international reference material (WHIT; Alcott et al., 2020) gave a RSD of <5% for each Fe pool, with analyses within 5% of reported values. No AVS was detected and therefore, Fe_{HR} in this study is defined as the sum of $Fe_{carb} + Fe_{ox} + Fe_{mag} + Fe_{py}$ (Poulton et al., 2004; Poulton and Canfield, 2011). All geochemical data is tabulated in the Supplementary appendix C.

3.4.4 Framework for redox interpretation

We use three independent approaches to assess water column redox conditions: pyrite petrography, iron speciation and trace metal systematics. Pyrite framboid sizes have been widely utilized to diagnose redox conditions, and are particularly useful for identifying euxinic (anoxic, sulfidic) conditions (Wilkin et al., 1996; Wilkin and Barnes, 1997; Wignall and Newton, 1998; Wignall et al., 2010). In modern euxinic environments, framboids form in the water column and only achieve a small size with narrow distribution (Wilkin et al., 1996), whereas under anoxic-dysoxic conditions, framboids can grow larger and are accompanied by higher proportions of diagenetic pyrite (Wilkin and Arthur, 2001; Wignall et al., 2010; Li et al., 2022).

Iron speciation data potentially allow oxic water column conditions to be distinguished from ferruginous (anoxic, Fe(II)-containing) and euxinic conditions (Poulton and Canfield, 2011; Poulton, 2021). Oxic conditions are indicated when highly reactive Fe over total Fe (Fe_{HR}/Fe_T) ratios are <0.22, and anoxic conditions are suggested if this ratio is >0.38 (Raiswell and Canfield, 1998; Poulton and Canfield, 2011). Ratios of 0.22-0.38 are considered equivocal, and further consideration is required to evaluate such samples (see below). For samples diagnosed as anoxic, Fe_{py}/Fe_{HR} ratios are applied to distinguish euxinia (>0.8) from ferruginous conditions (<0.6). Ratios in the range 0.6-0.8 are considered to potentially reflect euxinic depositional conditions, but again, further consideration is required (Poulton et al., 2004; Poulton and Canfield, 2011; Benkovitz et al., 2020; Poulton, 2021). We note recent challenges to the utilization of Fe speciation in reconstructing ocean redox conditions (Pasquier et al., 2022), and indeed, a number of considerations must be evaluated when applying the technique. For example, Fe speciation may not provide reliable results when applied to sediments with low Fe contents (<0.5 wt% Fe_T; Clarkson et al., 2014), sediments experiencing rapid deposition (e.g. turbidites; Canfield et al., 1996), and those in proximity to hydrothermal inputs (Raiswell et al., 2018) or directly adjacent to (sub)tropical mountainous regions, where highly weathered sediment may supply a high proportion of Fe_{HR} directly onto the continental margin (Wei et al., 2021), thus circumventing the preferential trapping of Fe_{HR} that usually occurs in inner shore environments (Poulton and Raiswell, 2002). These caveats have been well described in the literature, but were ignored in the analysis of Pasquier et al. (2022). In addition, the Fe speciation framework has been independently calibrated against ancient marine rocks that have by definition undergone diagenesis (e.g. Raiswell et al., 2021; Clarkson et al., 2014), in contrast to the modern sediments that were solely investigated by Pasquier et al. (2022). As also described in the literature, Fe speciation is best used in combination with other indications of water column redox chemistry (e.g. pyrite framboid and redox sensitive trace metal systematics) and within the context of the sedimentological conditions of the depositional environment (Poulton, 2021). This is done here, and is typically done in the literature, providing the most accurate assessment of the chemical conditions of deposition. Indeed, we also note that pyrite framboid sizes (see below) and pyrite-sulfur isotope systematics (Emmings et al., 2020) are entirely consistent with syngenetic or very early diagenetic pyrite formation, which is factored into the Fe speciation proxy.

We utilize the redox-dependent behaviour of Mo and U to provide further independent insight into redox conditions. Molybdenum accumulation in the sediment is highly dependent on redox conditions, where uptake of Mo via Fe-Mn (oxyhydr)oxide minerals is the major removal mechanism under oxic conditions (Bertine and Turekian, 1973). Under ferruginous conditions, Mo accumulation can be promoted by a particulate shuttle mechanism (e.g. Algeo and Tribovillard, 2009; Tribovillard et al., 2012) via uptake during the water column precipitation of Fe minerals such as Fe (oxyhydr)oxides or green rust (e.g. Zegeye et al., 2012). However, with the presence of H_2S in the water column, the molybdate anion is converted to particle-reactive thiomolybdate (Helz et al., 1996), leading to pronounced Mo accumulation in the sediment, once a dissolved sulfide threshold of ~11 µM is passed (Emerson and Huested, 1991; Helz et al., 1996; Erickson and Helz, 2000). By contrast, uranium reduction primarily occurs in anoxic sediments rather than in the water column, and U is therefore enriched beneath anoxic bottom waters, regardless of whether euxinic or ferruginous conditions dominate (Anderson et al., 1989; Klinkhammer and Palmer, 1991). Therefore, when combined with other indicators of the water column redox state (e.g. Fe speciation and pyrite framboid systematics), U/Mo ratios can be used to provide further support for either euxinic water column conditions (i.e. low U/Mo ratios) or anoxic non-sulfidic conditions (i.e. moderate to highly elevated U/Mo ratios).

3.5 Results

3.5.1 TOC variability

Holkerian-Asbian

The carbonate-dominated units of the Hodderense Limestone and Pendleside Limestone generally have relatively low concentrations of TOC compared to the overlying Lower Bowland Shale. For example, the oldest strata in the RH section have TOC concentrations averaging 0.78 ± 0.28 wt% in 6 samples (Fig. 3.4). Similarly, at the TLC location, TOC concentrations average 0.66 ± 0.34 wt% in 26 samples of calcareous mudstone and micritic limestone from the Pendleside Limestone (Fig. 3.5). The onset of the Lower Bowland Shale is generally marked by an increase in TOC, although concentrations and trends are quite variable at this transition. At DB, TOC is 2.03 ± 1.04 wt% in the B_{2a} zone, but becomes slightly higher in the B_{2b} zone (3.20 ± 1.11 wt%; Fig. 3.6). A more pronounced increase is seen at the LB section, where low TOC values (0.57 ± 0.17 wt% in the lowermost 6 samples) in the B_{2a} zone are followed by a sharp increase to 3.41 ± 1.25 wt% in the upper B_{2a} zone and through the B_{2b} zone (Fig. 3.6). By contrast, at TLC, TOC values remain low (0.70 ± 0.38 wt%) until the P_{1a} Zone of the Lower Bowland Shale where it reaches a peak of

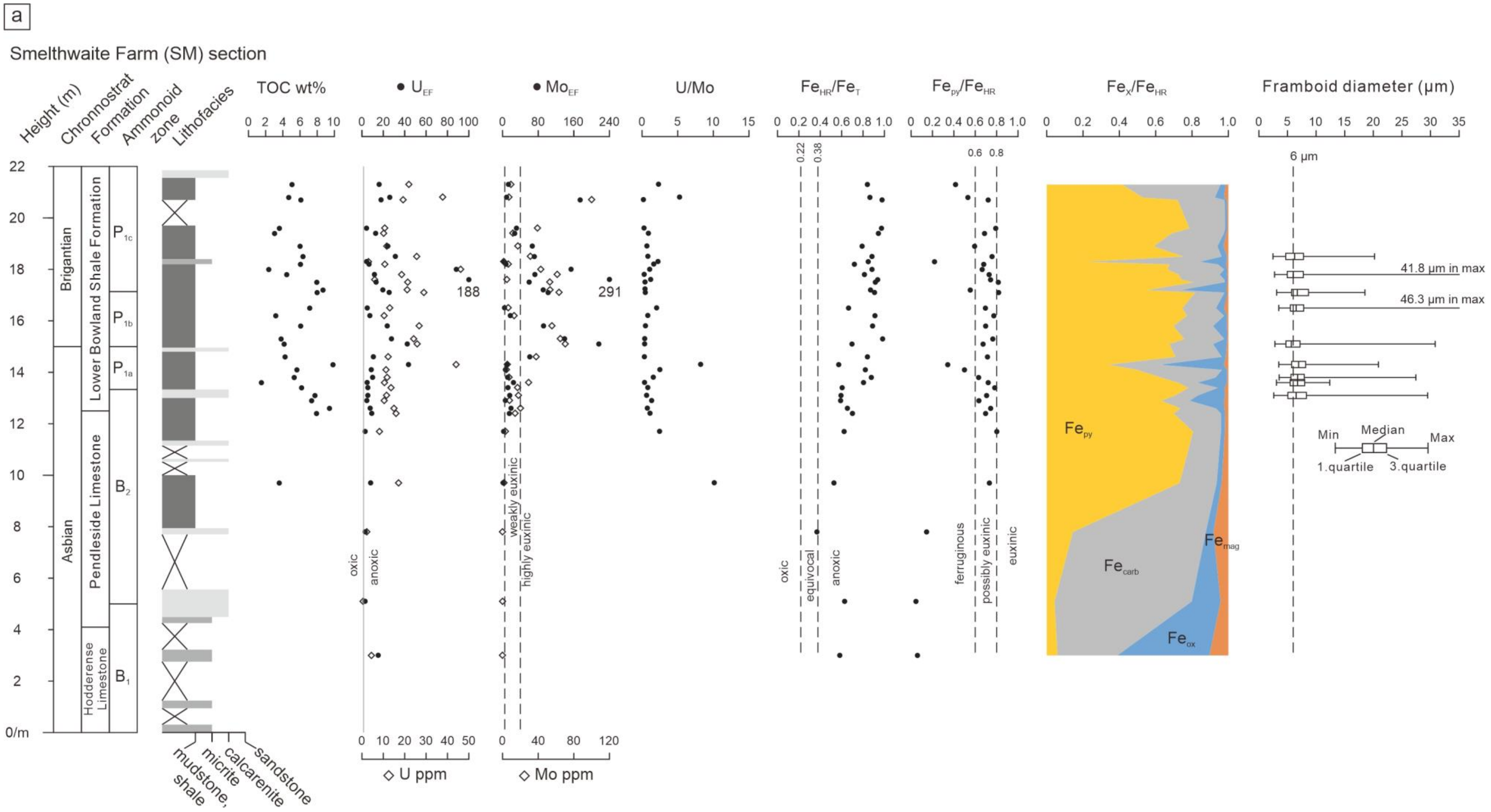
a
Smelthwaite Farm (SM) section
Height (m)
Chronnostrat
Formation
Ammonoid zone
Lithofacies
TOC wt%
● U_EF
● Mo_EF
U/Mo
Fe_HR/Fe_T
Fe_py/Fe_HR
Fe_X/Fe_HR
Framboid diameter (µm)
0 2 4 6 8 10
0 20 40 60 80 100
0 80 160 240
0 5 10 15
0 0.2 0.4 0.6 0.8 1.0
0 0.2 0.4 0.6 0.8 1.0
0 0.2 0.4 0.6 0.8 1.0
0 5 10 15 20 25 30 35
22 20 18 16 14 12 10 8 6 4 2 0/m
Brigantian
Asbian
Lower Bowland Shale Formation
Pendleside Limestone
Hodderense Limestone
P1c
P1b
P1a
B2
B1
mudstone, shale
micrite
calcarenite
sandstone
188
291
oxic
anoxic
weakly euxinic
highly euxinic
0.22
0.38
equivocal
0.6
0.8
ferruginous
possibly euxinic
euxinic
Fe_py
Fe_carb
Fe_mag
Fe_ox
6 µm
41.8 µm in max
46.3 µm in max
Min
Median
Max
1.quartile
3.quartile
0 10 20 30 40 50
◇ U ppm
0 40 80 120
◇ Mo ppm

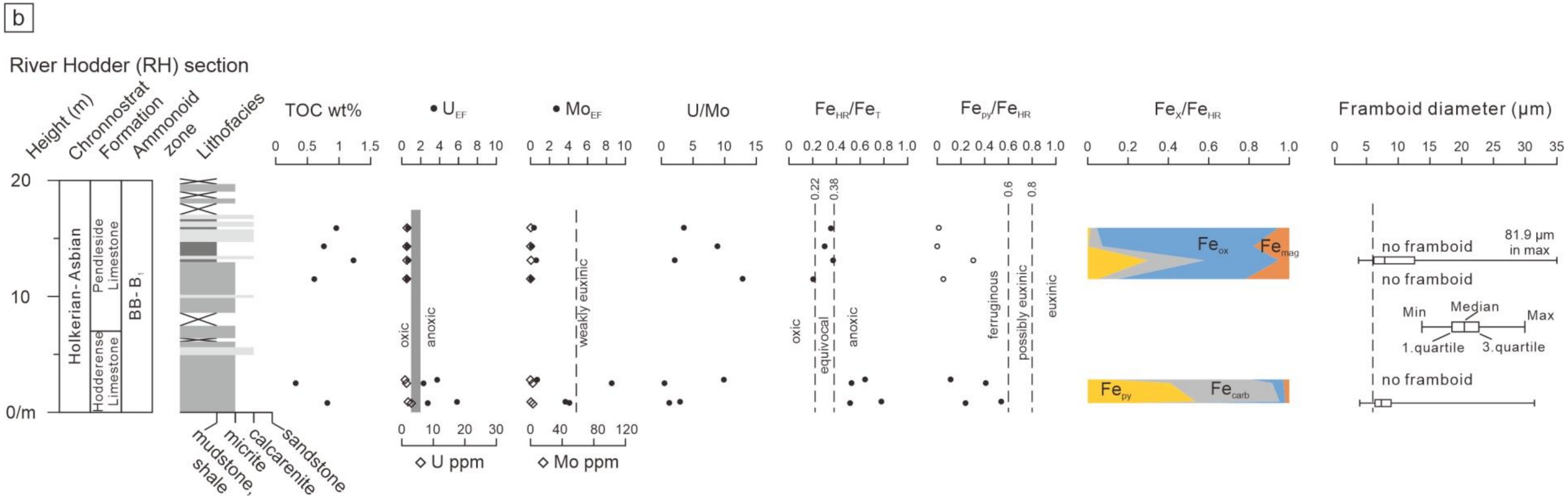

Fig. 3.4 Geochemical profile for TOC, Fe speciation, trace metal systemactics and framboid analyses through the SM (a) and RH (b) sections. The dashed lines on Fe_{HR}/Fe_{T} plots represent the boundaries for distinguishing anoxic (>0.38) and oxic (<0.22) water column conditions. The dashed lines on Fe_{py}/Fe_{HR} plots indicate the boundaries for distinguishing euxinic (>0.8) and ferruginous (<0.6) water column conditions, and the open circles reflect oxic samples (determined via combined consideration of Fe speciation and trace metal systematics), while closed circles represent anoxic samples. In U and Mo plot, black circles and the diamonds present enrichment factors and concentration respectively and diamonds are only shown presenting zero if its concentration is below detection limits. The grey bar and the dashed lines indicate calibrated redox thresholds for U_{EF} and Mo_{EF} respectively (see text).

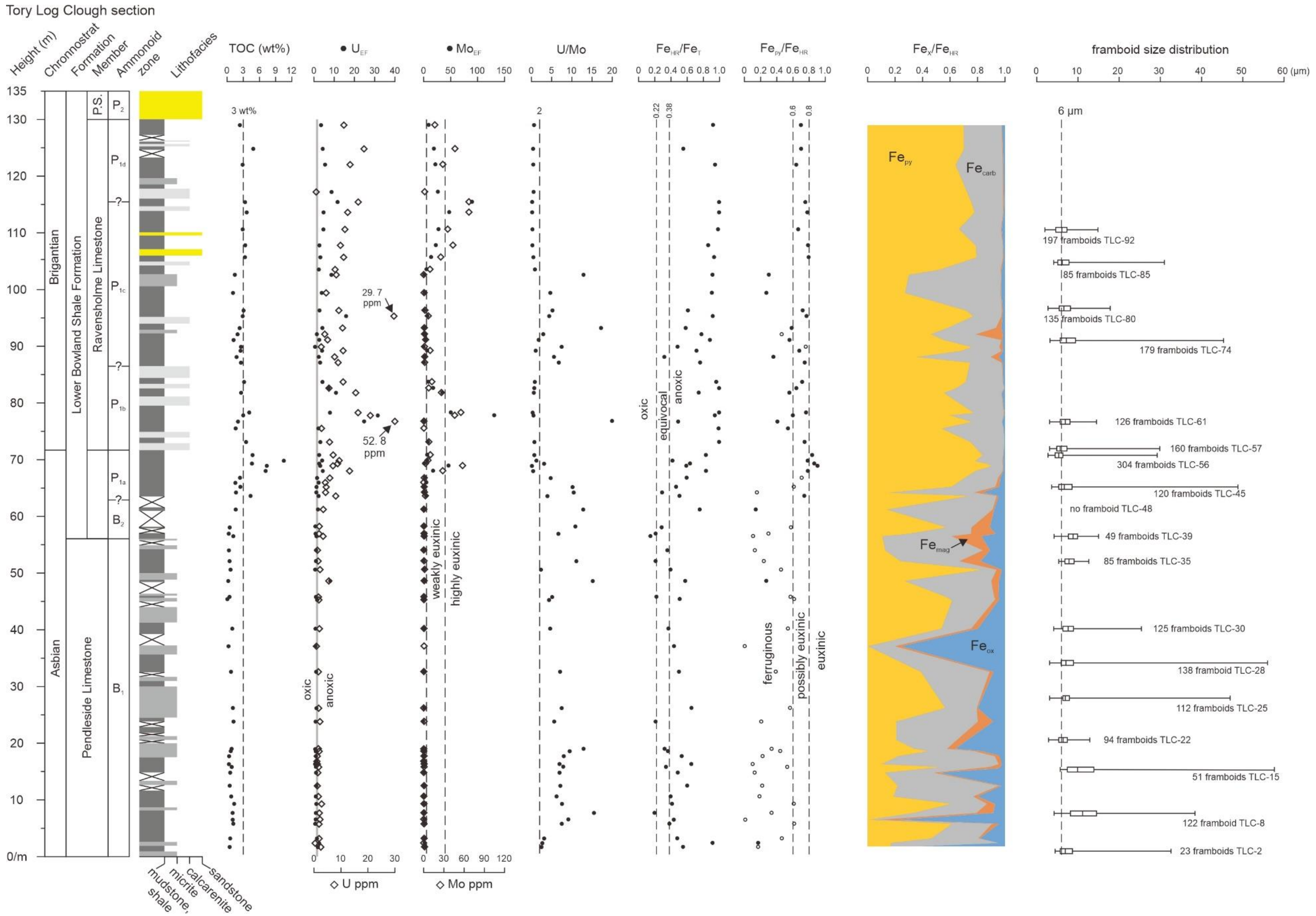

Fig. 3.5 Geochemical profiles for TOC, Fe speciation, trace metal systematics and framboid analysis at the TLC section. See Fig. 3.4 caption for additional information.

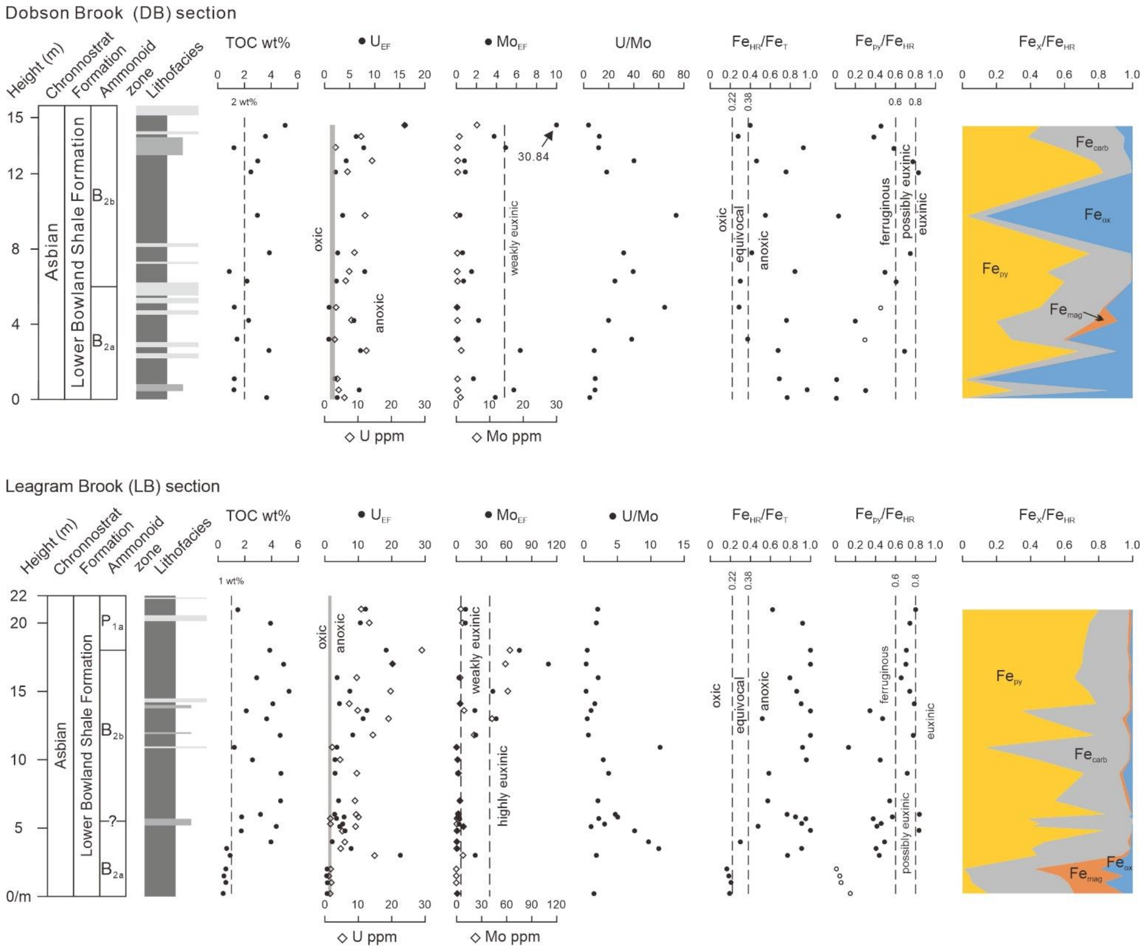

Fig. 3.6 Geochemical profiles for TOC, Fe speciation and trace metal systematics at the DB and LB sections. See Fig. 3.4 caption for additional information.

10.54 wt% (Fig. 3.5). The SM section, on the other hand, displays a pronounced increase in TOC concentrations to 9.45 wt% with the onset of Lower Bowland Shale in the late B_2 zone, succeeded by a gradual decline to 3.80 wt% at the end of the P_{1a} zone (Fig. 3.4). An overall increase is also found in the SC section, ranging from 1.71 to 3.27 wt% (Fig. 3.7). By contrast, low TOC concentrations (0.49 ± 0.26 wt% in 12 samples) are recorded in the P_{1a} zone of the Ravensholme Limestone in the CH section (Fig. 3.7).

Early Brigantian (P_{1b-d} zones)

The shale-dominated units in the lower part of the Lower Bowland Shale display moderate to elevated TOC values. At the start of the DH section, shale samples in the P_{1b} zone have relatively consistent TOC values, averaging 3.42 ± 0.45 wt% (10 samples) with a peak of 5.82 wt% (Fig. 3.8). Concentrations remain around 3 wt% (2.92± 0.17 wt%) in the P_{1c} zone (e.g. at the DH (Fig. 3.8) and TLC sections (Fig. 3.5). The SM section is condensed and has elevated but variable TOC concentrations (5.56 ± 1.84 wt% in 16 samples) through the P_{1b} - P_{1c} zones (Fig. 3.4).

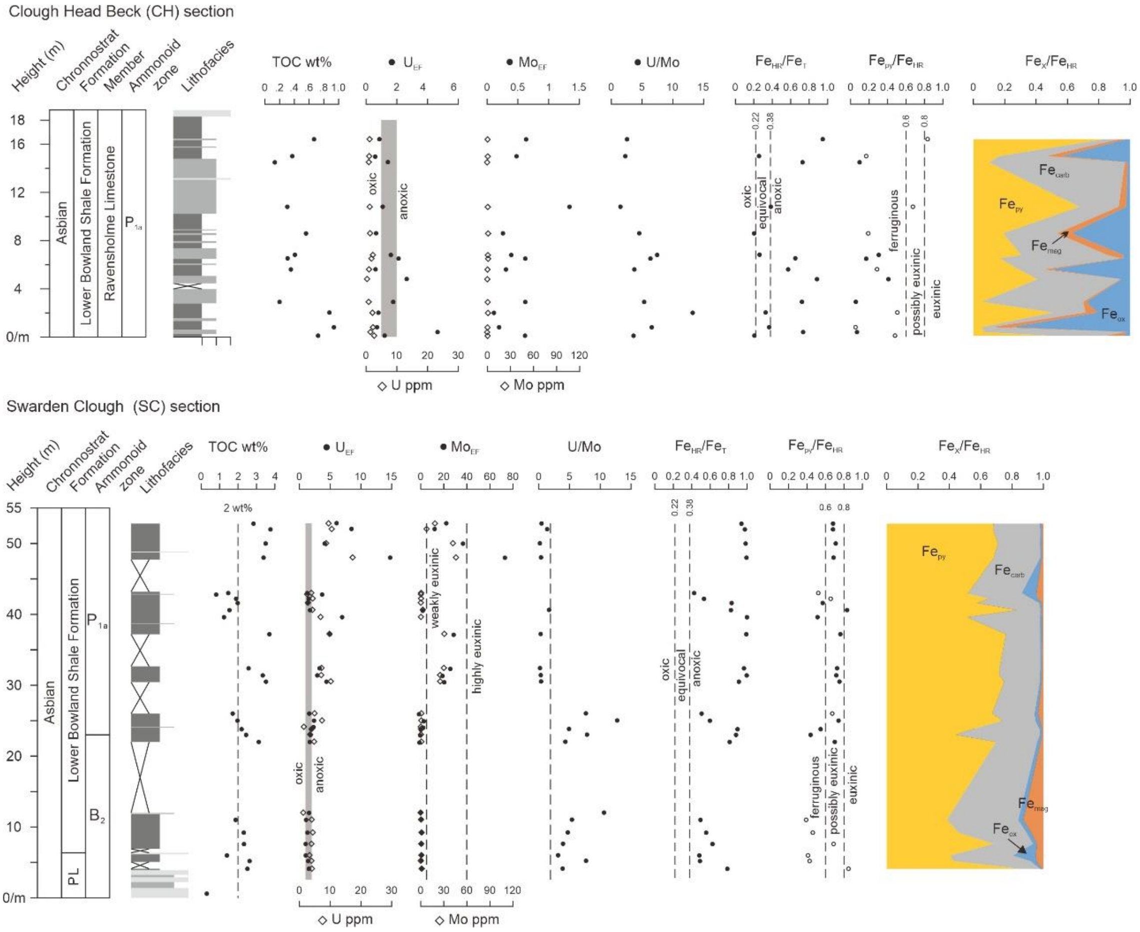

Fig. 3.7 Geochemical profiles for TOC, Fe speciation and trace metal systematics at the CH and SC sections. PL: Pendleside Limestone Formation. See Fig. 3.4 caption for additional information.

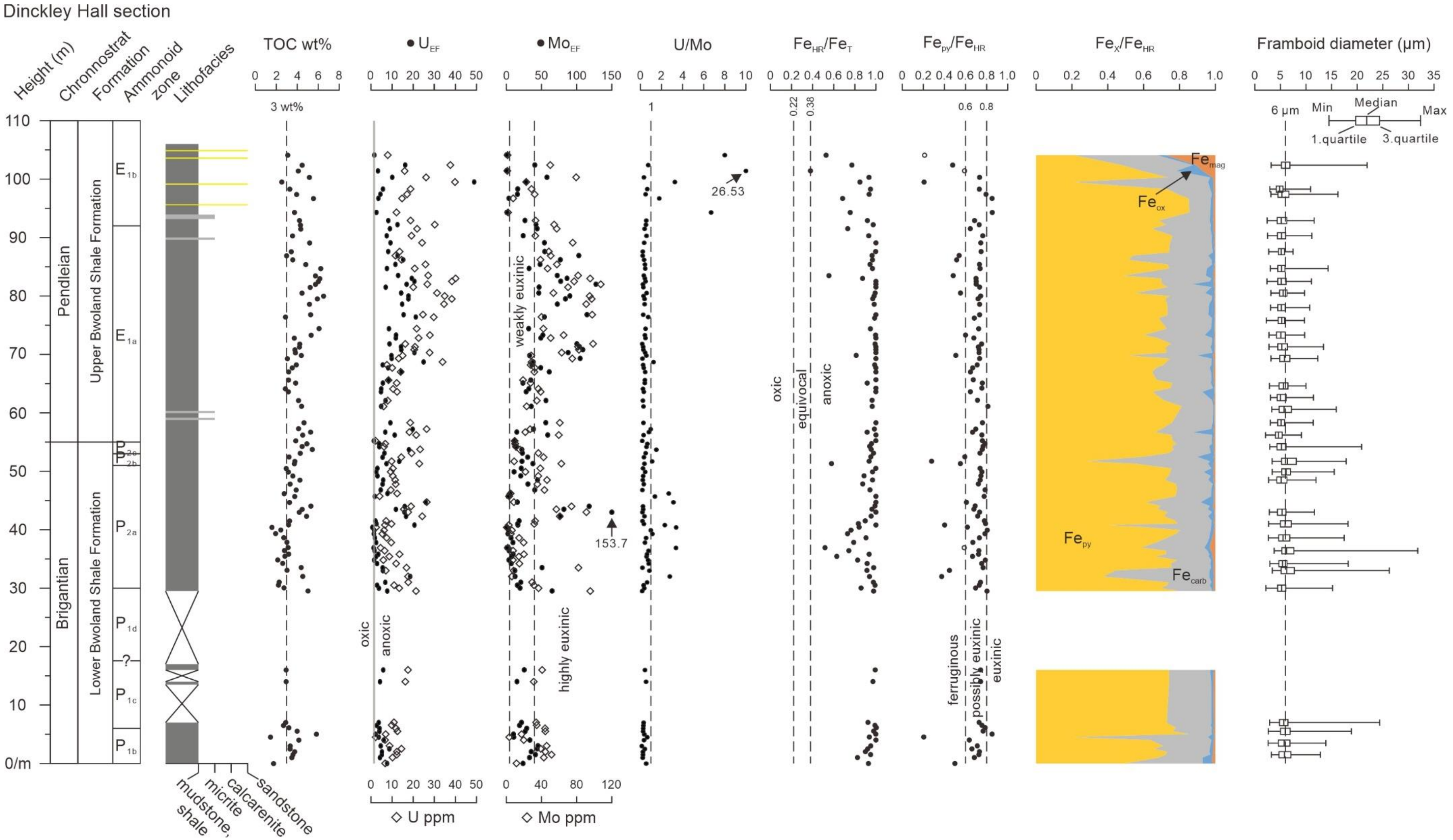

Fig. 3.8 Geochemical profiles for TOC, Fe speciation, trace metal systematics and framboid analyses at the DH section. See Fig. 3.4 caption for additional information.

The FL section was deposited on the northern edge of the Lower Bowland Shale outcrop on the margins of the Bowland Basin (Fig. 3.9), and interestingly the TOC values in the early Brigantian are amongst the highest seen anywhere in the basin at that time (Fig. 3.9). In the zone of P_{1b}, TOC values average 5.23 ± 1.10 wt% (9 samples) in shales, while the interbedded micritic limestones average 2.38 ± 0.93 wt% (5 samples) (Fig. 3.9). The TOC values decline somewhat in the overlying P_{1c} shales at FL and are generally around 3 wt% (2.81 ± 0.91 wt%), a value typical for this level throughout the basin.

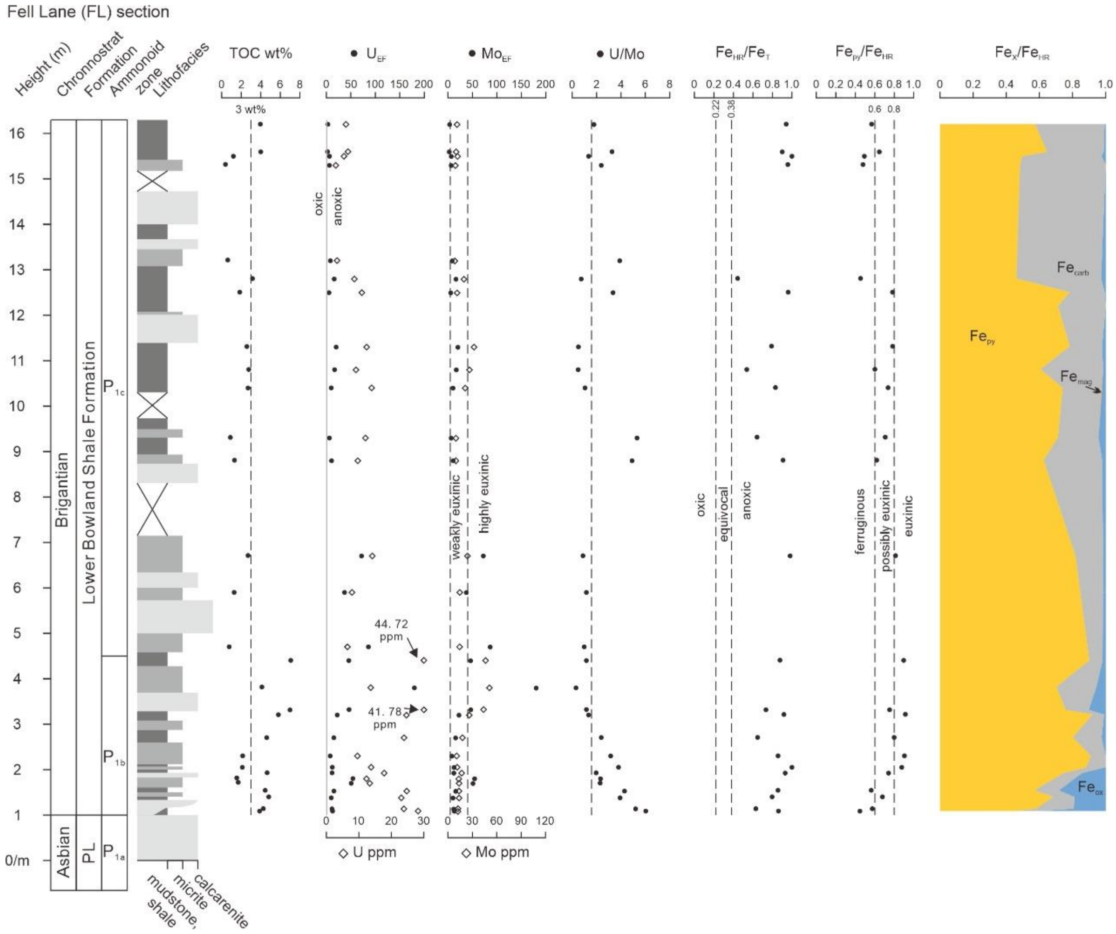

Fig. 3.9. Geochemical profiles for TOC, Fe speciation and trace metal systematics at the FL section. PL: Pendleside Limestone Formation. See Fig. 3.4 caption for additional information.

Late Brigantian (P_2 zones)

The DH section provides the most continuous section of the late Brigantian portion of the Lower Bowland Shale (Fig. 3.8). This exhibits a long-term trend of TOC enrichment (averaging 3.42 ± 0.93 wt% in 39 samples), reaching peak values in the late P_{2c} zone at 5.43 wt%, although there is a low point in the mid P_{2a} zone where the concentrations for a few samples drops below 2 wt% (Fig. 3.10). Shales from the P_{2c} zone are also seen in the expanded LC section, and they too show increasing TOC concentrations in the mid- to upper-part of the Lower Bowland Shale (rising from around 3.0 wt% to 5.27 wt%), before a gradual decline to 1.85 wt% in topmost meters of the P_{2c} strata (Fig. 3.10). P_{2c} shales at SS, on the margin of the Bowland Basin, have TOC values of 2.75 ± 0.21 wt% (Fig. 3.10).

Pendleian (E_1 zones)

TOC values in the Upper Bowland Shale have moderate to high values, albeit with considerable variation from sample-to-sample. At DH, E_{1a} shales have average TOC concentrations of 4.38 ± 1.04 wt%, which decline slightly to 4.02 ± 0.88 wt% (11 samples) in the E_{1b} zone (Fig. 3.8). TOC values are similar in the nearby LC section (Fig. 3.10). In contrast to the high, but variable, concentrations of TOC in the basinal sections, TOC levels from the northern margin of the Bowland Basin show more consistency (e.g. at SS, TOC = 2.82 ± 0.22 wt% in 12 samples, and at MC, TOC = 2.59 ± 0.34 wt% in 14 samples, Fig. 3.11), although values at CC peak at 4.92 wt% (Fig. 3.11).

3.5.2 Total Fe and Fe phase partitioning

Holkerian-Asbian

The Hodderense Limestone Formation has an average Fe_T content of 1.18 ± 0.33 wt% (RH section; Fig. 3.4), whereas the calcareous mudstone samples of the Pendleside Limestone Formation show variable Fe_T, from 1.4 to 6.2 wt% in both the RH and TLC sections (Figs. 3.4 and 3.5). Thus, these samples contain sufficient Fe_T for reliable analyses of Fe speciation to be undertaken (Clarkson et al., 2014).

In the RH section, the Hodderense Limestone data show elevated values of Fe_{HR}/Fe_T above 0.38 (0.62 ± 0.32, 4 samples, Fig. 3.4). The overlying Pendleside Limestone has persistently low values (0.32 ± 0.16) falling in the equivocal oxic/anoxic zone for the RH section, with more scatter and a higher ratio (0.44 ± 0.19 in 30 samples) in the TLC section (fluctuating between the equivocal and anoxic regions; Figs. 3.4, 3.5). Fe_{py}/Fe_{HR} ratios generally show considerable scatter, but all are below 0.6 (0.32 ± 0.16 in the Hodderense Limestone and 0.09 ± 0.12 in the Pendleside Limestone of the RH section; 0.33 ± 0.23 in the Pendleside Limestone of the TLC section).

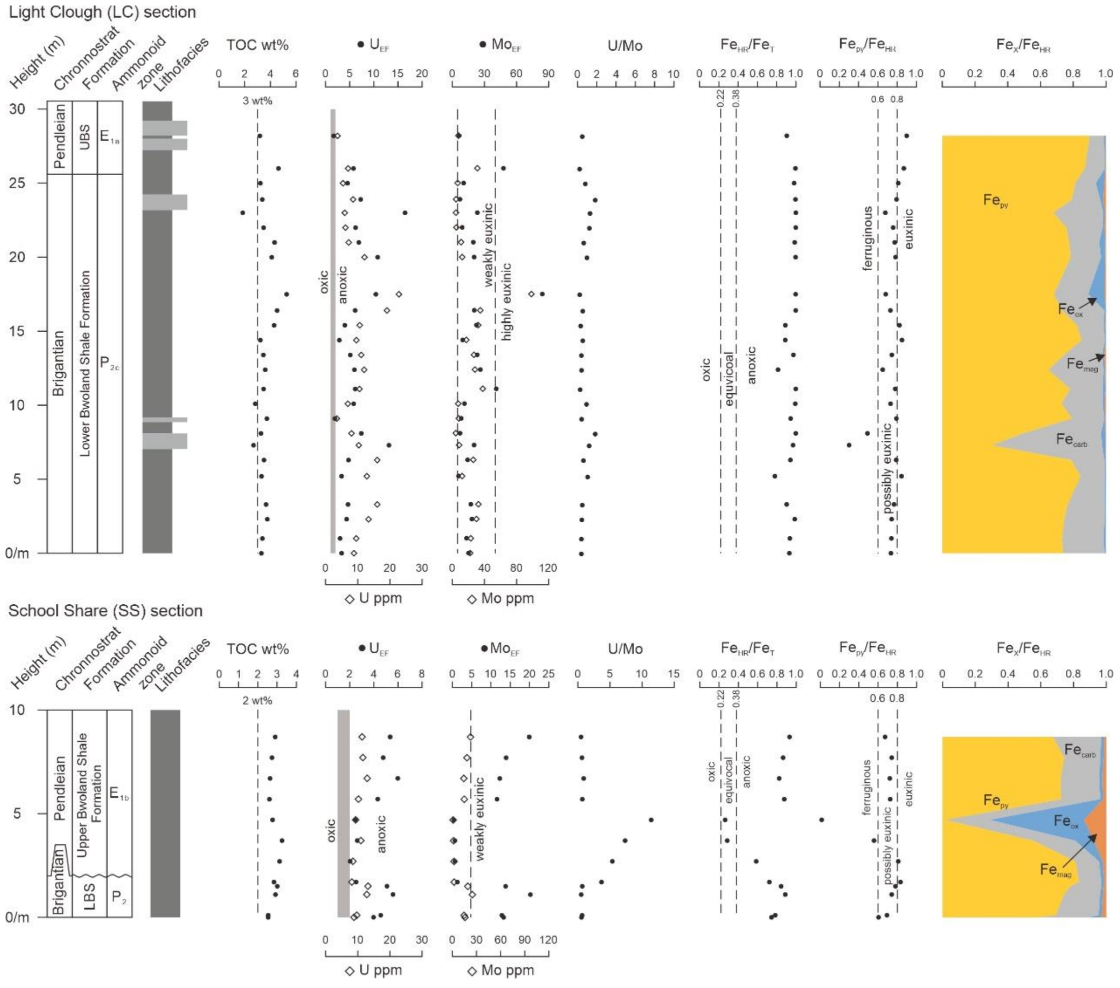

Fig. 3.10 Geochemical profiles for TOC, Fe speciation and trace metal systematics at the LC and SS sections. LBS: Lower Bowland Shale Formation; UBS: Upper Bowland Shale Formation. See Fig. 3.4 caption for additional information.

The transition to the Lower Bowland Shale in the late Asbian is marked by an overall increase in Fe_{HR}/Fe_T ratios, to values that commonly greatly exceed the threshold indicative of anoxic conditions. At the TLC section, the onset of organic-rich shale in the P_{1a} zone sees a rapid increase both in Fe_{HR}/Fe_T (reaching 1.0 in the anoxic zone) and in Fe_{py}/Fe_{HR} (reaching 0.8 in the euxinic zone; Fig. 3.5). Correspondingly, an elevated Fe_{HR}/Fe_T (0.87 ± 0.15 in 12 samples) in the anoxic zone is also evident in the LB section, and Fe_{py}/Fe_{HR} ratios fluctuate (0.61 ± 0.20 in 12 samples) between ferruginous and possibly euxinic (Fig. 3.6). By the end of the Asbian, all sections have high ratios, both in Fe_{HR}/Fe_T, which plot in the anoxic zone, and in Fe_{py}/Fe_{HR} ratios, which lie between 0.6- 0.8 throughout the Bowland Basin (Figs. 3.6, 3.7). The exception occurs at CH where the dark shales of the Bowland Shale are replaced in the P_{1a} zone by the calcareous shales and micritic limestones of the Ravensholme Limestone Member (Fig. 3.7). Here, the Fe_T content fluctuates between 1.32 and 3.45 wt% (2.42 ± 0.70 in 14 samples), giving suitable concentrations for Fe speciation analyses. The Fe_{HR}/Fe_T ratios straddle the equivocal and anoxic regions (0.52 ± 0.25 in 14 samples), while variable Fe_{py}/Fe_{HR} ratios are commonly below 0.8 (0.31 ± 0.24 in 14 samples) (Fig. 3.7).

Early Brigantian (P_1 zones)

Generally, early Brigantian strata (P_1 zones) has an Fe_T content of 2-4 wt%. In basinal settings, there are consistently high Fe_{HR}/Fe_T ratios (0.87 ± 0.10 for the SM section; 0.95 ± 0.05 for the DH section) that fall in the anoxic zone (Figs. 3.4, 3.5 and 3.8). The exception occurs in the early P_{1c} zone at TLC, where values decline to 0.32 (the equivocal zone) but bounce back rapidly (0.83 ± 0.20; Fig. 3.5). This trend is not seen in other sections. Fe_{py}/Fe_{HR} ratios dominantly fall in the possibly euxinic zone, while a few samples are below 0.6 (0.67 ± 0.14 for the SM section; 0.69 ± 0.15 for the DH section) (Fig. 3.5). A scattering of lower values below 0.6 (0.61 ± 0.18) is seen at the TLC section, at the same level where Fe_{HR}/Fe_T

ratios plot in the equivocal zone (Fig. 3.5). At the FL section, on the northern basin margin, Lower Bowland Shale deposition began at the start of the Brigantian with shales onlapping onto the shallow-water limestones of the Pendleside Limestone Formation (Fig. 3.9). The shales here have elevated Fe_{HR}/Fe_T ratios (0.83 ± 0.15) falling in the anoxic zone and Fe_{py}/Fe_{HR} ratios (0.69 ± 0.14) that mainly plot in the possibly euxinic zone (Fig. 3.9).

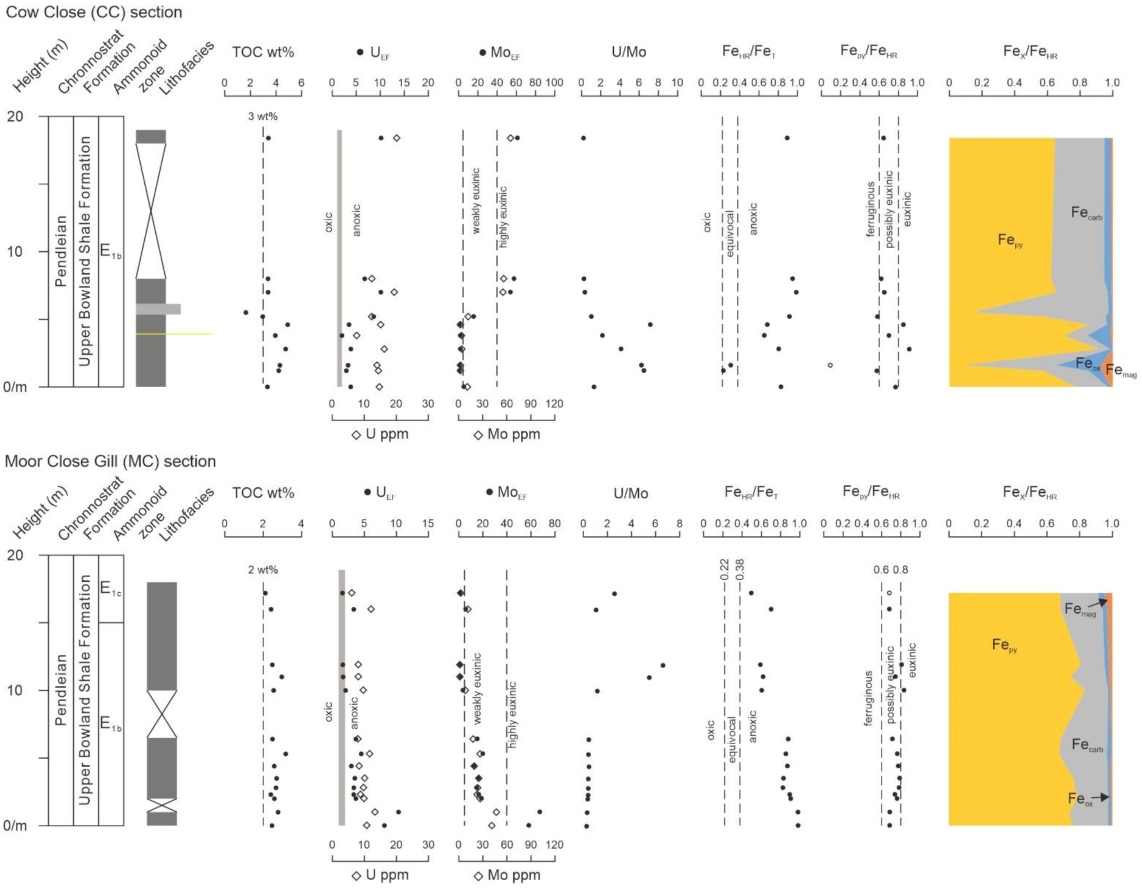

Fig. 3.11 Geochemical profiles for TOC, Fe speciation and trace metal systematics through the CC and MC sections. See Fig. 3.4 caption for additional information.

Late Brigantian (P_2 zones)

With the exception of Fe_T concentrations, which show considerable variability, the Fe_{HR}/Fe_T and Fe_{py}/Fe_{HR} ratios of late Brigantian strata maintains the relative stability established in the early Brigantian, falling in the anoxic and possibly euxinic zones, respectively. The basin-centre sections at DH and LC have high Fe_{HR}/Fe_T values (0.90 ± 0.12 in 40 samples at the DH section; 0.95 ± 0.05 in 25 samples from the LC section) plotting in the anoxic zone (Fig. 3.8, 3.10). The high proportion of reactive iron is due to the pyrite-rich nature of the sediment (e.g. at LC, Fe_{py}/Fe_{HR} is 0.74 ± 0.12 in 25 samples; at DH, Fe_{py}/Fe_{HR} is 0.69 ± 0.12 in 40 samples). At SS, on the basin margin, the P_2 black shales also display elevated ratios both in Fe_{HR}/Fe_T (0.72 ± 0.06 in 5 samples) and Fe_{py}/Fe_{HR} (0.73 ± 0.08 in 5 samples).

Pendleian (E_1 zones)

There is no major change in lithology at the transition to the Upper Bowland Shale Formation; dark grey and black shales persist. In biozone E_{1a}, Fe_{HR}/Fe_T and Fe_{py}/Fe_{HR} ratios exhibit persistently high values, plotting in the anoxic and possibly euxinic zones, respectively. At the DH section, Fe_{HR}/Fe_T is 0.96 ± 0.08 and Fe_{py}/Fe_{HR} is 0.69 ± 0.10 in 45 samples, and both ratios are 1.0 at the LC section (Fig. 3.10). However, values fall in the succeeding E_{1b} zone, as seen in the basinal DH section, where Fe_{HR}/Fe_T declines from peak ratios of 0.97 to approaching 0.38, and there is a corresponding fall in Fe_{py}/Fe_{HR} ratios from 0.86 to 0.21 (Fig. 3.8). This decline is associated with the appearance of thin beds of turbidite sandstone (Fig. 3.8). Ratios of Fe_{HR}/Fe_T in the equivocal zone also occur at this level in the early E_{1b} zone in basin margin locations: Fe_{HR}/Fe_T drops to 0.26 and 0.22 at the SS and CC sections, respectively. The decline is short-lived, however, and values increase in the late E_{1b} zone (e.g. 0.87 ± 0.04 for Fe_{HR}/Fe_T and 0.72 ± 0.03 for Fe_{py}/Fe_{HR} at the SS section; 0.83 ± 0.14 for Fe_{HR}/Fe_T and 0.75 ± 0.04 for Fe_{py}/Fe_{HR} at the MC section; Figs. 3.10, 3.11). These increased values are not seen at DH, probably because the younger part of the E_{1b} zone was not sampled there. The youngest levels of the Upper Bowland Shale (E_{1c} zone) were only sampled at MC, where Fe_{HR}/Fe_T ratios (0.71 and 0.50) plot in the anoxic zone, and Fe_{py}/Fe_{HR} ratios are 0.68 on average (Fig. 3.11).

3.5.3 Mo and U systematics

Holkerian-Asbian

The pink and light grey micrites of the Hodderense Limestone have low concentrations of Mo and U at RH (peak values of 2.88 and 2.93 ppm, respectively; see Supplemental Material C), which result in low enrichment factors (Fig. 3.4). The succeeding Pendleside Limestone shows a slight decline to even lower Mo and U concentrations. For example, at RH in four samples Mo is 0.40 ± 0.27 ppm and U is 1.65 ± 0.06 ppm, and at TLC Mo is 0.32 ± 0.23 ppm in 24 samples and U is 1.82 ± 0.91 ppm in 27 samples (Fig. 3.5).

The transition to the Lower Bowland Shale, within the B_2- P_{1a} zones, is marked by the appearance of dark grey shales, although the boundary is gradational because thin beds of micritic limestones and calcarenites persist above the formational boundary in several sections (e.g. the TLC section). A gradational upwards increase in redox-sensitive trace metal concentrations is evident in most sections. At the expanded TLC section, the lowest shales in the B_2 zone do not show enrichment in Mo and U, but all values increase slightly in the latest Asbian P_{1a} zone (Fig. 3.5). In the shale-dominated SC section (Fig. 3.7), Mo and U concentrations are similarly low in the B_2 and earliest P_{1a} zone (Mo is 0.70 ± 0.31 ppm in 10 samples, U is 3.51 ± 1.01 ppm in 11 samples) whilst U/Mo values are consistently above 2. Concentrations increase substantially in the late P_{1a} zone to peak values not seen at any other section in the basin at this level (Mo reaches values of 58.0 ppm, U reaches 13.2 ppm, with correspondingly high EFs) whilst U/Mo drops below 2 (Fig. 3.7). In contrast to the shale-dominated record at SC, the P_{1a} zone at CH records the development of the Ravensholme Limestone, and the interbedded mudrocks show little trace metal enrichment: Mo values remain below 0.8 ppm, U concentrations are below 3 ppm and U/Mo is above 2 (Fig. 3.7). The B_{2a} - early P_{1a} trend at LB is different again, with little evidence of trace metal enrichment in the lowest part of the section, although U (but not Mo) increases in the mid-B_{2a} zone and remains at near-constant levels above this, whilst U/Mo ratios are variable but generally >2 (Fig. 3.6). At the condensed SM section, U and Mo are only modestly enriched in the B_2 zone, but values rise late in the P_{1a} zone (Fig. 3.4). Overall, trace metal trends in the lower part of the Lower Bowland Shales show upwards enrichment, but the timing of this increase varies considerably throughout the basin, as do the peak concentrations.

Brigantian (P_{1b} — P_2 zones)

The Brigantian portion of the Lower Bowland Shale generally has more elevated trace metal concentrations than the Asbian portion, although once again the limestone-dominated section at TLC shows the lowest values (Fig. 3.5). Modest trace metal enrichments occur in the early P_{1b} zone at TLC, before values decline to around 5 ppm and 9 ppm for Mo and U, respectively and U/Mo ratios are below 2. By contrast, the P_{1b} strata in the SM section has strong trace metal enrichments, with Mo values around 70 ppm and U values around 20 ppm (Fig. 3.4).

The DH section provides a shale-dominated section of the entire Brigantian part of the Lower Bowland Shale, and shows high trace metal enrichment values throughout (Fig. 3.8). Mo concentrations are typically around 40 ppm for much of the section, but concentrations decline substantially in the early P_{2a} zone to ~10 ppm, before increasing again in the mid P_{2a} zone where several values exceed 80 ppm (Fig. 3.8). The U concentrations at DH broadly follow those of Mo, with the lowest values in the early P_{2a} zone (the lowpoint is 2.46 ppm) and highest values of 23.1 ppm occur towards the top of the P_{2c} zone (Fig. 3.8). Generally U/Mo values are less than 2 throughout the Brigantian at DH, only in the early P_{2a} zone, do some values exceed this (Fig. 3.8). A thick development of the P_{2c} zone is seen at the LC section where it has elevated Mo_{EF} values and low U/Mo ratios comparable to the same level at DH (Fig. 3.10).

The early Brigantian saw onlap of the Bowland Shales onto carbonate facies at the basin margin, a transition recorded at FL where coarse calciturbidites dominate the section and black shales occur as thin interbeds (Fig. 3.9). The latter begin in the P_{1b} zone where there is a rapid rise in Mo concentrations from 4.92 ± 1.15 ppm (7 samples) to a peak of 38.4 ppm at the top of the zone, before values decline again to around 7.75 ppm in the P_{1c} zone (Fig. 3.9). Uranium concentrations are also generally higher in the P_{1b} zone (with a peak of 44.7 ppm at the top of the zone) relative to the P_{1c} zone (8.65 ± 3.52 ppm, 15 samples). The U/Mo ratios at SC rapidly decline in the P_{1b} zone to below 2 before increasing and fluctuating in the P_{1c} zone.

Pendleian (E_1 zones)

Within the basinal DH and LC sections, the transition to E zones initially sees little change in trace metal concentrations in the earliest E_{1a} zone, but in the younger part of the zone there is substantial enrichment, with Mo and U reaching 107.4 and 40.1 ppm, respectively (Fig. 3.8). This is followed by a temporary decline in trace metal concentrations in the overlaying E_{1b} zone of the DH section (Fig. 3.8), a trend also seen on the basin margin (see below). The U/Mo ratios in the Pendleian are consistently below 2 until the E_{1b} zone where the overall decline of trace metal enrichment sees a major increase of values peaking at 26.5 (Fig. 3.8).

The early Pendleian saw the transition to the early post-rift stage of basin development when black shale deposition extended for a few kilometres beyond the northern margin of the Bowland Basin, onto the Askrigg Block. Trace metal concentrations in the marginal locations are generally as high as those seen in the basin. Both the CC and SS sections occur at the northern limit of the Upper Bowland Shale outcrop and initially, in the early part of the E_{1b} zone, trace metals have low values at these locations before increasing dramatically in the later part of the zone (e.g. at CC, Mo is initially <10 ppm, before increasing to >50 ppm, although U trends are less clear and the U/Mo ratios vary; Fig. 3.11). The youngest levels of the Bowland Shale were only sampled at the basin margin locations of CC and MC. At the former, late E_{1b} to early E_{1c} zone shales show a prolonged decline in trace metal concentrations, culminating in Mo and U levels in the MC section of 2.35 and 6.08 ppm, respectively (Fig. 3.11).

3.5.4 Pyrite petrography

Framboids are generally present in most samples from the Pendleside Limestone, and consistently show mean diameters of 6-12 µm and maximum values greater than 30 µm (Figs. 3.4, 3.12). In a Wilkins diagram these populations plot in the dysoxic- oxic field, with some straying into the euxinic field (Fig. 3.12; cf. Wilkin et al., 1996). The latter framboid populations are from the B_1 (early Asbian) interval of the TLC section (Fig. 3.5).

Framboids become common within the mudrocks of the lower Lower Bowland Shales and generally have smaller mean diameters (between 6-8 µm) compared to those from the underlying Pendleside Limestone, although both intervals have similar standard deviations. As a result, in the Wilkins Plot, framboid populations mostly occur in the lower dysoxic fields, with only two samples in the euxinic field (Fig. 3.12). Framboids remain common in the younger part of the Lower Bowland Shale and populations generally have mean sizes around 6 µm, whilst maximum framboid sizes gradually decline from around 25 µm to 10 µm (Fig. 3.8). In the Wilkin Plot, these populations straddle the lower dysoxic to euxinic fields (Fig. 3.12).

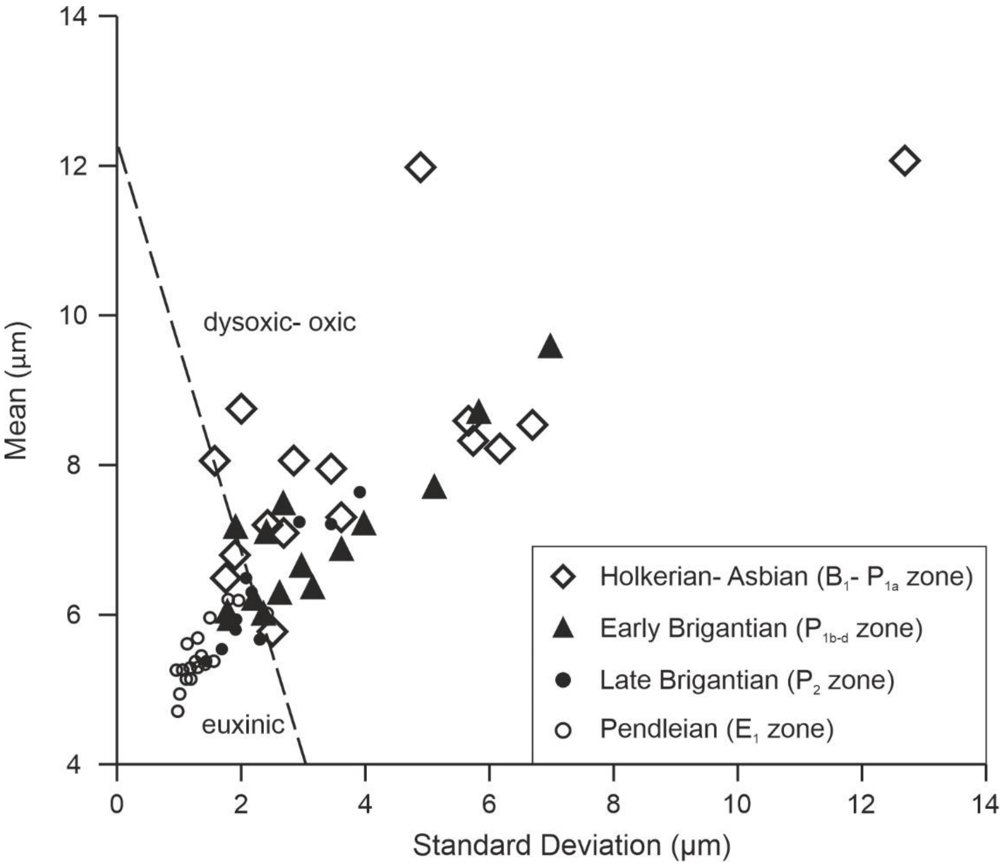

Fig. 3.12 Wilkin Plot (mean framboid diameter against standard deviation) of framboid populations from the late Holkerian to early Pendleian of the Bowland Basin. Dashed line indicates the euxinic/oxic-dysoxic threshold, as determined in modern environments (Wilkin et al., 1996).

The Upper Bowland Shale contains abundant small framboids with little size variation. These populations plot consistently in the euxinic field of the Wilkin Plot (Fig. 3.12), with the exception of the youngest sample (P_{1b} zone), which has a greater size range typical of the dysoxic field (Figs. 3.8, 3.12). Thus, the overall history of the Bowland Basin from Pendleside Limestone to Upper Bowland Shale deposition, recorded by framboid populations, is one of gradually increasing oxygen restriction culminating in prolonged euxinia.

3.6 Discussion

3.6.1 Redox proxy threshold calibrations

Defining redox thresholds is critical for redox proxy application, and various studies have investigated the cut-off values for individual proxies. Scott and Lyons (2012) summarized sediment Mo concentrations observed in different redox settings in the modern ocean, suggesting that values of <25 ppm, 25-100 ppm, and >100 ppm can potentially indicate non-euxinic, intermittently euxinic or restricted (which may be persistently euxinic), and persistently euxinic conditions with limited restriction, respectively. In our case, we note below that basinal restriction was likely fairly constant, and hence Mo concentrations can be considered to provide a reasonable first order approximation of the relative intensity of euxinia. Algeo and Tribovillard (2009), on the other hand, suggest using enrichments factors of trace metal and Mo-U covariation to distinguish dysoxic, anoxic and euxinic conditions. Furthermore, based on modern data, redox-sensitive metals expressed as ratios of elements over Al, can provide thresholds to differentiate various conditions (Bennett and Canfield, 2020). However, such values can be basin-specific and so, where possible, redox thresholds should be refined for each individual basin (Algeo and Li, 2020; Poulton, 2021). Here, we calibrate redox thresholds for the Bowland Basin based on the covarying patterns observed between the different redox proxies we have applied.

Cross plots of U_{EF} vs. Fe_{HR}/Fe_T have recently been used to assess water column redox conditions (He et al., 2022), since both parameters respond to the development of anoxia (i.e. higher U_{EF} values during anoxic deposition should correspond to elevated (>0.38) Fe_{HR}/Fe_T ratios), because both have similar redox potentials (Zheng et al., 2002). Here, we find a close degree of consistency between U_{EF} values and Fe_{HR}/Fe_T ratios (Fig. 3.13A). Thus, samples plotting in the oxic field based on Fe_{HR}/Fe_T ratios, generally have U_{EF} values <1, whereas samples in the possibly anoxic Fe_{HR}/Fe_T field have U_{EF} values that straddle a U_{EF} value of 1, suggesting fluctuating redox conditions. By contrast, almost all samples that have Fe_{HR}/Fe_T ratios consistent with anoxia (i.e. >0.38) also have elevated U_{EF} values (U_{EF} >2), supporting anoxic depositional conditions. These observations from two independent

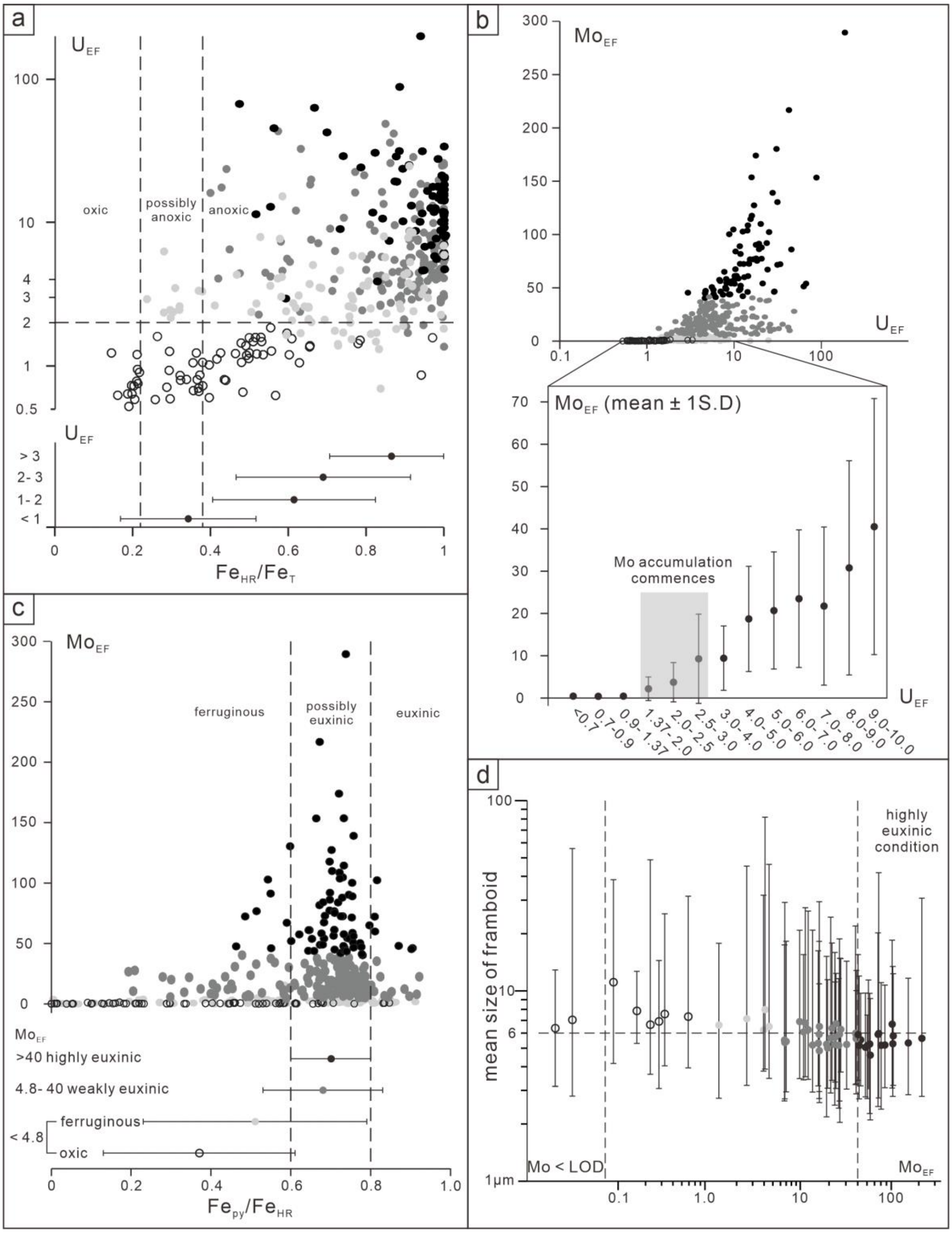

Fig. 3.13 Redox threshold calibrations based on proxy covariation; open, light grey, dark grey and black circles illustrate oxic, ferruginous, weakly euxinic and highly euxinic samples. (a) U_{EF} and Fe_{HR}/Fe_T cross plot, upper part showing data points and lower part showing statistical analysis in which Fe_{HR}/Fe_T data are displayed as mean values (± 1 S.D), where U_{EF} is <1, 1-2, 2-3 and >3. (b) Mo_{EF} and U_{EF} cross plot and its corresponding statistical analysis showing there is no Mo accumulation with U_{EF} <1.37, but that Mo enrichment increases rapidly as U_{EF} increases above 3.0. (c) Mo_{EF} and Fe_{py}/Fe_{HR} cross plot showing scattered Fe_{py}/Fe_{HR} ratios for oxic and ferruginous samples, but with Fe_{py}/Fe_{HR} ratios dominantly falling in and above the possibly euxinic zone when Mo_{EF} is > 4.8. (d)

framboid size distribution (points refer to mean value, and upper and lower limits represent the maximum and minimum framboid diameters) and Mo_{EF} cross plot showing a broad decline in framboid size as Mo_{EF} increases. Large framboids (mean value > 6 µm) occur when Mo_{EF} is below 10, while framboid mean sizes < 6 µm commonly occur with Mo_{EF} > 10. With Mo_{EF} > 40, all framboid populations are < 6 µm in mean diameter. LOD: limit of detection.

indicators of anoxia provide strong support for the robust nature of our redox interpretations, and underlines the utility of the Fe speciation proxy, when applied correctly (*contra* Pasquier et al., 2022). Consequently, for our samples, a U_{EF} threshold of >1-2, combined with Fe_{HR}/Fe_{T} ratios >0.38, provides a clear indication of anoxic depositional conditions (Fig. 3.12a. Significant molybdenum accumulation occurs only when a critical sulfide threshold is met in the water column, and thus weakly euxinic conditions may be characterized by no, or limited, Mo enrichment, whereas significant enrichments are expected under highly euxinic conditions (Helz et al., 1996). Therefore, we determine Mo enrichment thresholds attributable to euxinia based on covariation between both Mo and U, and between Mo and framboid size distributions (Fig. 3.13b, d).

In the Bowland Basin, U/Mo values are consistently <2 in samples with Fe_{py}/Fe_{HR} indicative of possibly euxinic and euxinic values (e.g. Fig. 3.8) indicating enrichment of Mo in a sulfidic water column. The U versus Mo relationship can also be examined in more detail in cross-plots of Mo_{EF} and $U_{EF.}$ In detail, Mo_{EF} values remain low when U_{EF} values are <1.37, albeit with variation as each binned U_{EF} range increases (Fig. 3.13b). These fluctuations in Mo_{EF} may reflect fluctuations in the sulfide content of the water column under weakly euxinic conditions, thus limiting extensive Mo drawdown (Emerson and Huested, 1991; Helz et al., 1996; Wegwerth et al., 2018), or may potentially reflect fluctuations between euxinic and non-euxinic anoxia (Scott and Lyons, 2012). Thus, U_{EF} values in the range 1.37-3.0 co-occur with a mean Mo_{EF} value of 4.8, and this defines our lower limit for weakly euxinic conditions in the Bowland Basin.

It has previously been suggested, based on modern euxinic settings, that Mo concentrations >100 ppm indicate stable, highly euxinic conditions where Mo supply is not limited (e.g. in unrestricted basins; Scott and Lyons, 2012), but such levels are seldom evident in the Bowland Basin data. However, Mo-determined redox thresholds are likely basin-specific. Our pyrite framboid data provide independent support for permanently euxinic conditions in some intervals (Fig. 3.12). Small populations of framboids, around 6 µm in diameter, form at the sulfidic chemocline in the water column of modern euxinic basins (Wilkin et al., 1996; Dubinin et al., 2022) and are preserved in the underlying sediments (e.g. Wignall et al., 2010). In the Bowland Basin, framboid populations with a relatively large (>6 µm) mean size occur in sediments with Mo_{EF} values of around 10 (Fig. 3.13d). For samples with average framboid sizes of 6 µm or less, associated Mo_{EF} values are >40 (Fig. 3.13d), and we consider such values to be diagnostic of Black Sea-like euxinic conditions, where there is a substantial volume of deep, highly sulfidic water (e.g. Wilkin et al., 1996).

We also consider a Mo_{EF}-Fe_{py}/Fe_{HR} cross-plot to further examine this refined threshold (Fig. 3.13C). Oxic samples have a range of Fe_{py}/Fe_{HR} ratios but very low Mo_{EF} values, reflecting pyrite formation during diagenesis. Nevertheless, most oxic samples plot below 0.6 (0.37 ± 0.24). Similarly, while anoxic ferruginous samples have low Mo_{EF} values, and Fe_{py}/Fe_{HR} ratios are higher than oxic samples on average (0.51 ± 0.28), most plot below the 0.8 threshold for robust identification of euxinia. By contrast, both weakly and highly euxinic samples have elevated Mo_{EF} values and higher Fe_{py}/Fe_{HR} ratios, with most samples falling in the possibly euxinic field. Some of these euxinic samples (as determined by Mo_{EF} enrichments) have relatively low Fe_{py}/Fe_{HR} ratios (<0.6), which could potentially be due to relatively low sulfide concentrations during diagenesis. In this scenario, enhanced sulfide generation in the euxinic water column may limit sulfate availability (and hence additional sulfide production) during diagenesis, thus preventing the additional sulfidation of Fe_{HR} phases, which is a general requirement to produce high Fe_{py}/Fe_{HR} ratios (Xiong et al., 2019; Poulton, 2021). Overall, our approach highlights the value of combining independent redox proxies to assess palaeoredox conditions and confirms the general agreement and robust nature of the different proxies we have applied, as well as providing a more nuanced interpretation of the data.

3.6.2 Evolving redox trends during Bowland Basin development

Holkerian-Asbian (B_1-P_{1a} zone)

The oldest interval examined comprises the deep-water pelagic strata of the Holkerian-age Hodderense Limestone. Only sampled at the RH section, Fe_{HR}/Fe_T and Fe_{py}/Fe_{HR} ratios indicate ferruginous deposition, which is supported by the slight U enrichments and limited Mo accumulation (Figs. 3.4, 3.14). The Hodderense Limestone is thought to be the product of a major transgressive episode/basin deepening (Riley, 1990), and the anoxic conditions may have been widespread in Bowland Basin bottom waters at this time, but a detailed appraisal awaits a more widespread study.

The transition to carbonates and mudstones of the succeeding Pendleside Limestone Formation (Gawthorpe, 1986) is marked by a decline in Fe proxy and trace metal values, indicating improved oxygenation at this (early-mid Asbian) stage in the basin history (Figs. 3.4, 3.5 and 3.14). The oldest Pendleside Limestone Formation, seen at RH, has Fe_{HR}/Fe_T ratios falling in the equivocal oxic/anoxic zone which accords with the limited U_{EF} values (Fig. 3.4). The succeeding interval is recorded at TLC, where similarly, U and Mo exhibit limited

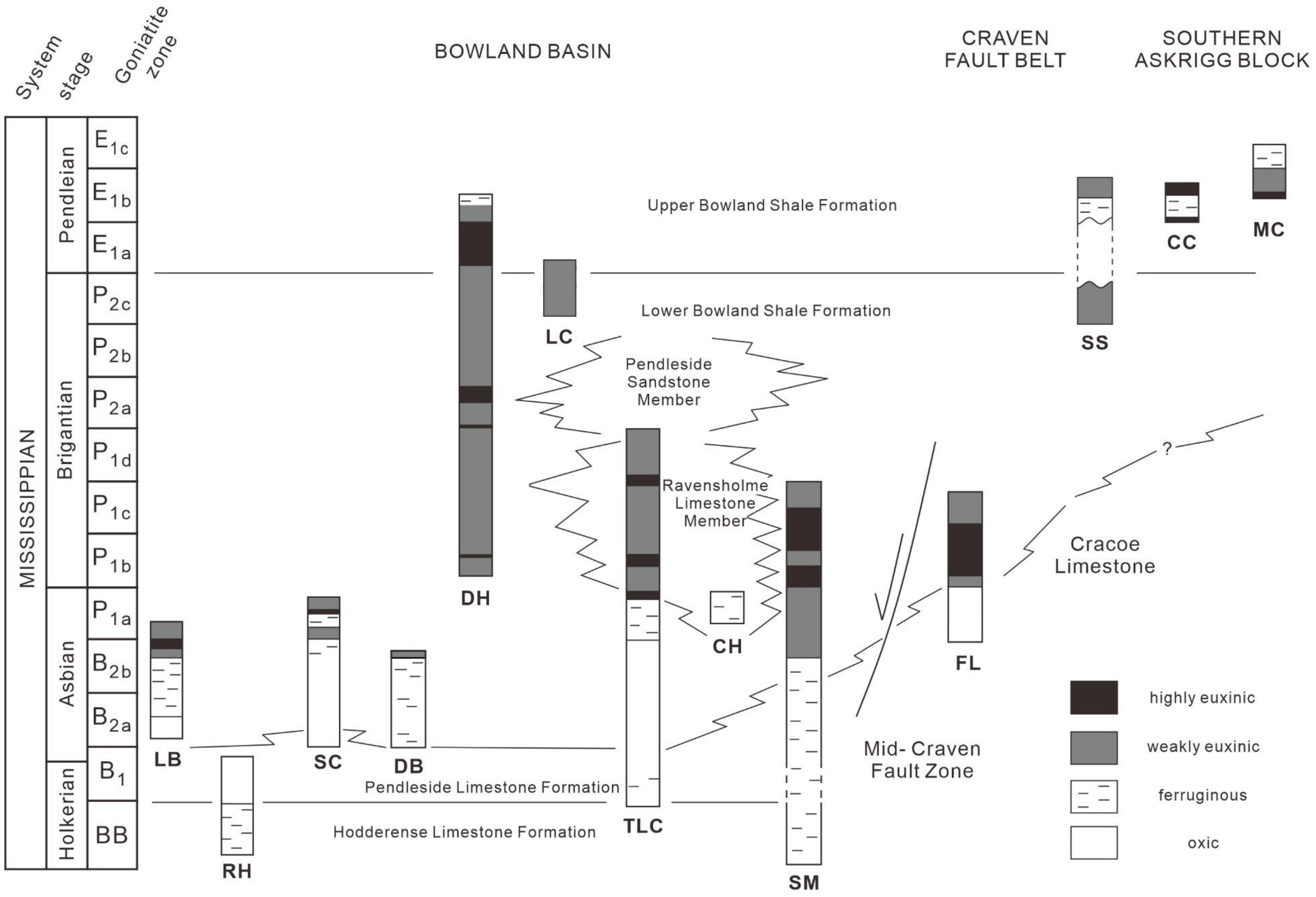

Fig. 3.14 Summary of the redox history of the Bowland Basin study sites showing a gradual increase in the extent and intensity of anoxia from the Asbian to the early Pendleian. The extent of Bowland Shale deposition also increases with onlap of the marginal Craven Fault Belt beginning in the Brigantian and extending onto the Askrigg Block in the late Brigantian- Pendleian.

enrichment (Fig. 3.5), but fluctuating Fe_{HR}/Fe_T ratios occur, with a few samples suggesting anoxia (Fig. 3.5). These signals are consistent with overall oxygenated conditions at this site, potentially with periodic development of weak dysoxia to anoxia. The medium-high Fe_{py}/Fe_{HR} ratios, combined with the presence of large-sized framboid populations, indicates formation in sulfidic pore waters (Fig. 3.14).

The onset of dark grey shale-dominated deposition defines the base of the Lower Bowland Shale Formation (Fig. 3.14) and initially there is only local evidence for anoxic depositional conditions. Thus, the TLC section records low organic C contents, with no apparent enrichment of trace metals or elevated Fe_{HR}/Fe_T ratios in the B_2 zone (Fig. 3.5). This level also lacks framboids and Fe_{py}/Fe_{HR} ratios are low (Fig. 3.5). By contrast, for the DB and LB sections in the NW of the basin (Fig. 3.7), the Fe speciation and trace metal proxies indicate ferruginous to borderline euxinic conditions, especially in the B_{2b} zone (Fig. 3.6).

Evidence for widespread anoxic conditions in the Bowland Basin does not occur until the end of the Asbian (P_{1a} zone), when TOC levels rapidly increase (locally reaching nearly 10 wt%; Fig. 3.5), as do trace metal enrichments and Fe speciation ratios, whilst pyrite framboid populations decrease dramatically in size. The P_{1a} level also marks a transition in the Fe pool to one almost entirely dominated by Fe(II) in form of Fe_{carb} and Fe_{py}, showing near-complete reduction of Fe_{HR} phases and the onset of stable ferruginous conditions (Figs. 3.4, 3.7). Elevated Mo_{EF} and Fe_{py}/Fe_{HR} ratios, combined with a rapid decline of U/Mo ratios and small pyrite framboid size distributions, all provide evidence to suggest that the basin had tipped into a weakly euxinic state by the end of the Asbian (Fig. 3.14).

The exception to these changes is seen in the CH section, where the dark grey Bowland Shales are replaced with allochthonous carbonates of the locally-developed Ravensholme Limestone Formation (Fig. 3.2). The interbedded shales show only slight U enrichments (close to our defined threshold), limited Mo enrichments, and highly variable Fe_{HR}/Fe_{T} ratios, likely indicating variable redox conditions between dysoxic-ferruginous (Figs. 3.7, 3.14). It is possible that the Ravensholme Limestone records a carbonate debris fan that was somewhat elevated above the more intensely anoxic condition of the deeper basin floor.

Early Brigantian (P_{1b} — P_{1d} zones)

During the early Brigantian organic-rich shales (TOC ranges from 4-10 wt%) accumulated over the entire Bowland Basin and most U/Mo values are below 2, Fe_{py}/Fe_{HR} ratios are, with few exceptions, within the 0.6-0.8 range, indicating conditions were likely ferruginous to weakly euxinic (Figs. 3.4, 3.5, 3.8 and 3.9). Framboid populations show considerable variation and support this redox interpretation, and plot in the euxinic to weakly dysoxic fields (Fig. 3.12). The expanded TLC section records particularly variable redox levels, ranging from ferruginous to highly euxinic, based on fluctuations in Fe speciation systematics, trace metal enrichments, U/Mo ratios and framboid size distributions (Fig. 3.5). The Lower Bowland Shale at this location is replaced by the Ravensholme Limestone, a mix of interbedded limestones and dark grey shales. Like the development of this unit at the CH section, the development of the Ravensholme Limestone at TLC records an overall weaker intensity of anoxia than the surrounding basinal shales (Fig. 3.14), which may relate to a slightly more elevated depositional site within the basin compared to the shale-dominated sections.

Active faulting in the early Brigantian saw the expansion of Lower Bowland Shale deposition to the north of the bounding South Craven Fault system (Fig. 3.3). Here, the FL section initially displays high Fe_{HR}/Fe_{T} ratios and U enrichments, suggesting ferruginous conditions early in the P_{1b} zone. This is quickly followed by a sharp increase in Fe_{py}/Fe_{HR} ratios and Mo_{EF} values, and a decline in U/Mo ratios later in the zone, indicating the onset of highly euxinic conditions in the late P_{1b} zone, before the development of weak euxinia in mid-P_{1c} times (Fig. 3.9). Through the rest of the FL section, Mo enrichments and Fe_{py}/Fe_{HR} ratios decline, indicating a shift back to ferruginous conditions. Thus, for a period during the late P_{1b} zone, the basin margin FL location was recording more intense euxinia than seen in the centre of the Bowland Basin, whilst for the remaining early Brigantian, redox levels were comparable to those in the basin centre (Fig. 3.14); a change that is discussed below.

Late Brigantian (P_2 zone)

The late Brigantian continued to see weakly euxinic conditions prevailing in the Bowland Basin (Fig. 3.14). An especially thick development of P_{2c} shales is seen at the LC section, which shows a low degree of variability in redox proxies at this level near the top of the Lower Bowland Shale Formation (Fig. 3.10). At the DH section, for the most part, Fe phase partitioning, trace metal enrichment levels and U/Mo values indicate euxinic conditions, with occasional development of ferruginous conditions. Fe_{HR}/Fe_T and Fe_{py}/Fe_{HR} ratios gradually decrease during the early P_{2a} zone, along with a decline in U and Mo (Fig. 3.8), whilst framboids increase in size and TOC falls to around 2 wt%. These trends independently suggest a transition from euxinic to ferruginous conditions, with sulfidic pore waters (Helz et al., 1996; Poulton and Canfield, 2011; Poulton, 2021). The first influx of terrigenous sand into the basin occurs at this time: the Pendleside Sandstone Member, a small turbiditic body, as seen at the top of TLC section (Figs. 3.2, 3.5). The role of turbidity currents and basin oxygenation is discussed below.

Pendleian (E_1 zones)

There was no change in depositional regime with the onset of Upper Bowland Shale deposition; organic-rich shale deposition continued to prevail throughout the basin beneath a euxinic water column (Fig. 3.14). Thus, E_{1a} zone black shales have pronounced U and Mo enrichments (U/Mo is <2), persistently high Fe proxy ratios, and very small framboid populations (Fig. 3.12). Black shale deposition continued its gradual onlap of the Craven Fault Belt marginal zone, and this region also saw euxinia developed (Fig. 3.14), whilst well-ventilated, shallow-water deposition occurred only a few kilometres to the north on the Askrigg Block (Arthurton et al., 1988).

Oxygenation levels improved in the early E_{1b} zone, both in the Basin and on its margin (Fig. 3.14). In the basinal DH section, Fe_{py}/Fe_{HR} values fall rapidly from >0.8 to 0.2 whilst Mo declines, U remains steady in concentration (therefore U/Mo increases), and framboids increase in size (Fig. 3.8). These trends suggest a transition from intensive euxinia to ferruginous conditions. This improved ventilation is also recorded in the SS and CC sections on the southern margin of Askrigg Block, where there is a major decline in Mo_{EF} values and Fe speciation ratios, as well as an increase in U/Mo ratios (Figs. 3.10, 3.11). Following the improved redox conditions in the early E_{1b} zone there was a rapid return of euxinia, indicated by increased Fe_{HR}/Fe_{T} and Fe_{py}/Fe_{HR} ratios and enrichment of trace metals (Figs. 3.10, 3.11). As with the transient improvement in oxygenation during the early P_{2a} zone, the short-lived improved ventilation in the early E_{1b} zone also coincides with the local appearance of thin turbidite sandstones (e.g. at DH; Fig. 3.8). These have a thicker development in the NW of the basin where they are called the Hind Sandstone (Kane, 2010).

The youngest levels of the Upper Bowland Shale (basal E_{1c} zone) were only sampled at the MC section, where declining trace metal enrichments and Fe_{HR}/Fe_{T} and Fe_{py}/Fe_{HR} ratios from the mid E_{1b} zone record a gradual transition from intensely euxinic to weakly euxinic conditions in the final stages of Upper Bowland Shale deposition (Figs. 3.11, 3.14). Emmings et al. (2020) studied drill core from the topmost levels of the Upper Bowland Shale (E_{1c} zone) from the northern edge of the outcrop belt (close to the FL section). Their data record a rapid improvement in oxygenation level to oxic conditions in the 20 m of mudstone occurring beneath the sharp transition to the coarse, turbiditic sandstones of the succeeding Pendle Grit Formation.

3.6.3 Controls on oxygenation in the Bowland Basin

Broadly speaking, oxygenation in marine settings is a balance between oxygen supply and oxygen consumption. The former is achieved by both vertical advection and lateral mixing and is therefore dependent on water depth and the connectivity of the deeper waters (Algeo et al., 2008). The Bowland Basin evolved from a carbonate ramp setting to a fault-bounded graben surrounded by shallower areas of carbonate deposition (Gawthorpe, 1987; Fig. 3.1B). The transition occurred around the Asbian/Brigantian boundary and coincides closely with the onset of Bowland Shale deposition, suggesting that basin isolation was a major player in the development of oxygen restriction in the basin, although anoxic deposition initially occurred only locally within the basin (Fig. 3.14).

Oxygen consumption is controlled by the abundance of decaying organic matter, which is dependent on primary productivity, and thus the nutrient supply to surface waters. Modern zones of high productivity are either fed by upwelling of nutrient-rich, deep water or from nutrient-rich riverine influx. Upwelling is primarily a phenomenon of ocean-facing continental margins and is unlikely in the Bowland Basin, which lay a long distance from the nearest ocean (Fig. 3.1A); there was no feasible route for nutrient-laden, deep waters to reach the basin without passing through shallow-water areas en route (Fig. 3.1B). Terrestrial nutrient influx is a more viable alternative and high levels have been favored as a cause of organic enrichment in a previous Bowland Shale study (Emmings et al., 2020). However, for

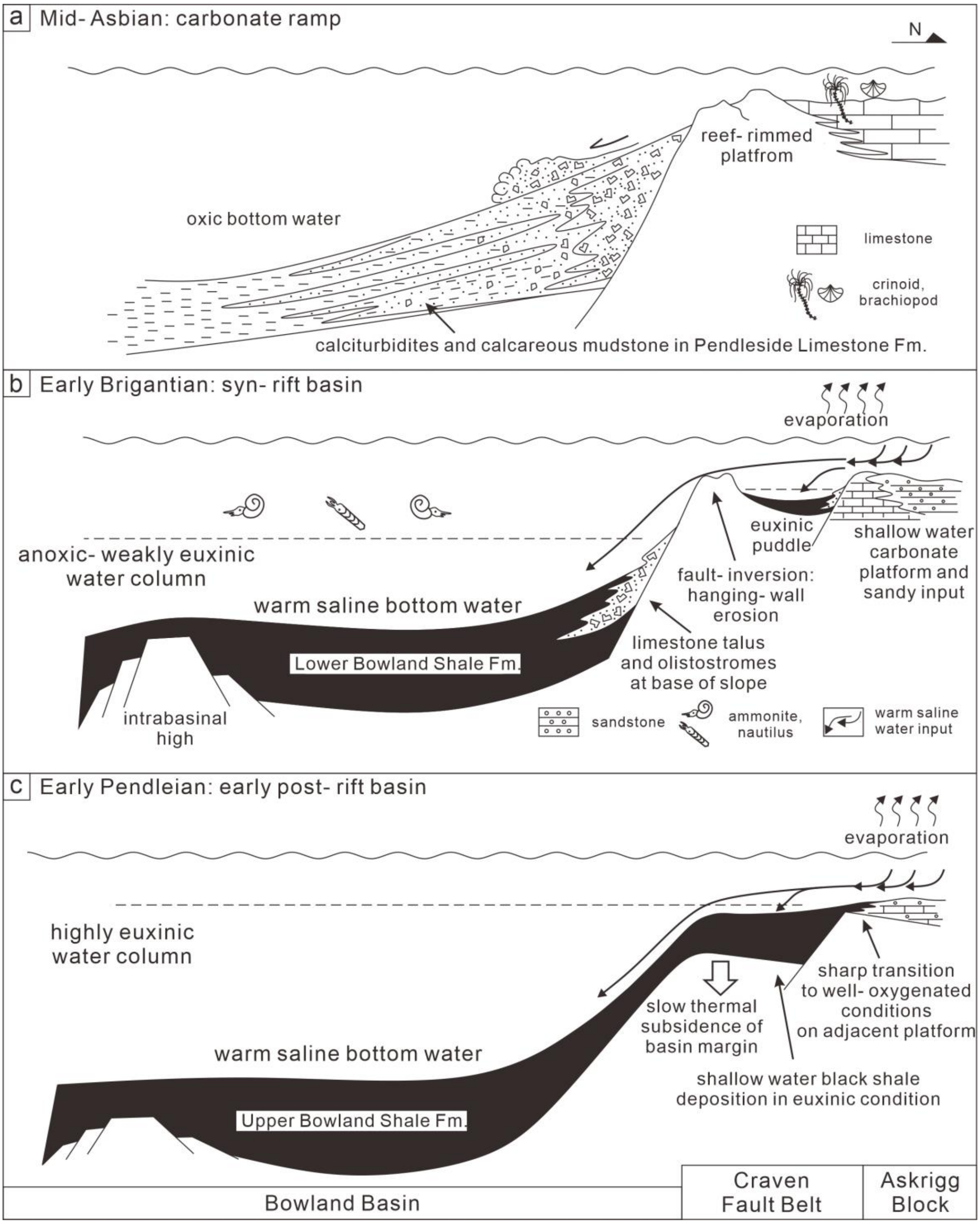

Fig. 3.15 Depositional model for the development of the Bowland Shale Formation from a carbonate ramp experiencing little oxygen restriction in the mid Asbian, to a fault-bounded syn-rift basin in the Brigantian with ferruginous-euxinic bottom waters, to a post-rift basin experiencing flank collapse and onlap of black shales onto the basin margin in the early Pendleian. Euxinic waters are envisaged to have been maintained beneath a salinity stratified water column in which warm saline bottom waters, generated on adjacent carbonate shelves, supplied the deep water.

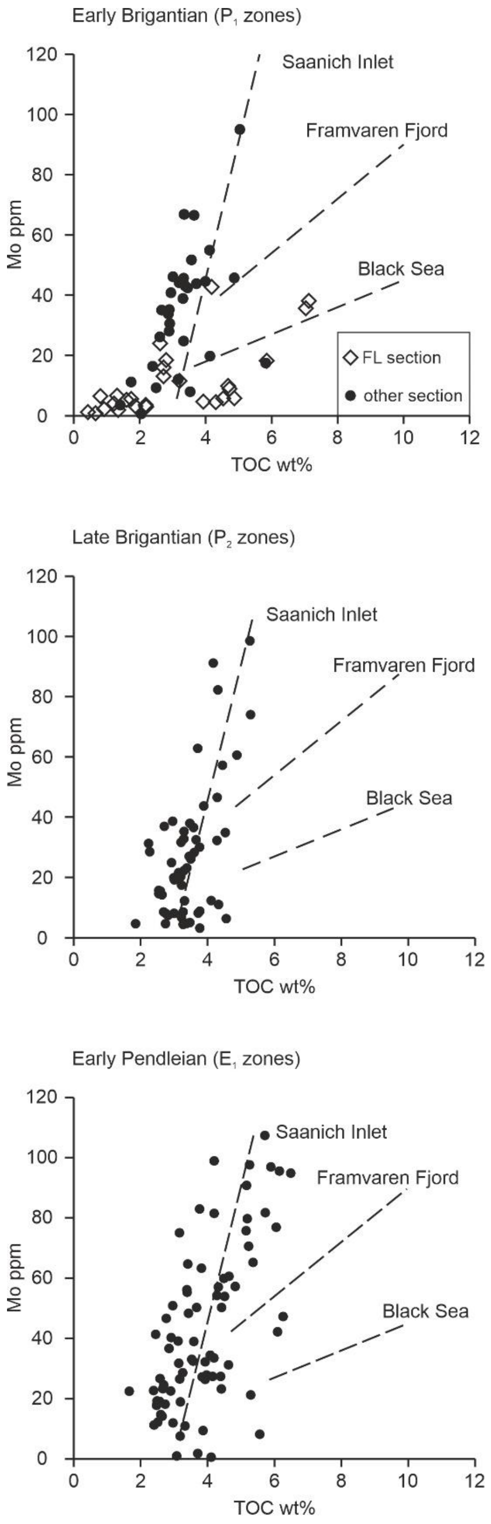

Fig. 3.16 Mo/TOC plots from the Brigantian to Early Pendleian in the Bowland Basin (dashed lines depict gradients from three modern, silled anoxic basins; Algeo and Lyons, 2006).

much of its depositional history, the Bowland Basin was surrounded by carbonate platforms and shelves (Fig. 3.1B). It is therefore unlikely that the basin received abundant terrestrial nutrients because carbonate productivity on adjacent platforms would have been affected.

This places the onus on depositional models that invoke restricted oxygen supply. Potential factors controlling the redox conditions are discussed below.

Connectivity versus isolation

Values of Mo/TOC have been used to evaluate the connectivity and degree of bottom water replenishment in silled basins (Algeo and Lyons, 2006; Algeo et al., 2007). Cross-plots generally show a positive correlation, but the gradient is controlled by the availability of aqueous Mo. In euxinic environments, rapid Mo drawdown into the sediment can result in water column concentrations that become severely depleted. Thus, in strongly restricted euxinic basins with weak deep-water renewal (such as the modern Black Sea), the enrichment of Mo relative to TOC is reduced and the gradient of Mo/TOC is low (~4). By contrast, less restricted basins, such as the modern Saanich Inlet, have gradients up to ten times steeper (Algeo and Lyons, 2006).

During the depositional history of the Bowland Shale, regression lines for Mo-TOC covariation (Fig. 3.16) have slope (*m*) values of ~44 in the early Brigantian, ~38 in the late Brigantian, and 40 in the early Pendleian, which are all typical of weakly restricted, silled basins (as also found in Emmings et al., 2020). However, the thermal maturity of the Bowland Shale is sufficiently high to have experienced hydrocarbon maturation and decreased TOC values. Vitrinite reflectance values in the region average 1.1 (Andrews, 2013), indicating a maturity on the threshold of gas generation within the basin, whilst shales from the NW margin of the basin are oil mature (Emmings et al., 2020). Calculating the original TOC values requires a suite of organic geochemical data that is not available for our study sites, but Emmings et al. (2020) report hydrogen indices (HIs) of ~180 from the Upper Bowland Shale in the NW of the basin. Assuming original HIs of >400 for the type II/III kerogens, and using the approach of Hart and Hofmann (2022), suggests original TOC values that were ca. 30% higher. Thus, the original Mo/TOC gradients within the Bowland Basin would plot between modern Framvaren Fjord and Black Sea data, indicating deep water renewal times approaching 1000 years and poor Mo replenishment (Algeo and Lyons, 2006). Interestingly, the lowest Mo/TOC gradients are seen in the marginal sub-basin developments of the Bowland Shale, where "puddles" of black shale developed in the newly subsiding Craven Fault Belt, especially in the early stages of their history (Fig. 3.15B). For example, the late P_{1a} black shales at FL has a Mo/TOC *m* of only 3.8, which is amongst the lowest encountered at any point in the basin's history (Fig. 3.16). We suggest that such settings were initially rather isolated from the main deep-water mass of the adjacent Bowland Basin, perhaps because they were perched above the main volume of bottom waters, and so developed even stronger Mo-depletion beneath highly euxinic bottom waters (Fig. 3.15b).

The degree of isolation of the Bowland Basin has been suggested to be controlled by sea-level variations (Gross et al., 2015; Emmings et al., 2020). A major phase of glacioeustasy is thought to have begun around the Asbian/Brigantian and had a clear influence in shallow marine areas (Manifold et al., 2021). For example, to the north of the Bowland Basin, eustasy is considered to have been a major control on the development of heterolithic, shallow-water cycles (Yoredale cycles) of the Brigantian-early Pendleian interval (Wright and Vanstone, 2001). Contemporaneously, in the Bowland Basin, it has been argued that transgressive phases improved connectivity, allowing fully marine goniatite and bivalve faunas to invade (Gross et al., 2015; Emmings et al., 2020; Waters et al., 2020). However, such fossils are present throughout Bowland Shale deposition and no cyclicity is manifest in either the sedimentology or the redox proxies (e.g. Fig. 3.6). Therefore, it is unlikely that eustatic fluctuations influenced Bowland Shale deposition or basin connectivity. The

Bowland Basin was probably sufficiently deep that eustatic oscillations, which may have been only a few tens of meters (Tucker et al., 2009), had little impact on deposition.

Stratification: salinity versus temperature

Whilst most Bowland Shale deposition likely occurred beneath a water column several hundred meters deep, organic-rich deposition also extended to the fault-bounded margin where depths were shallower. The transition to a post-rift phase in the Pendleian saw the Craven Fault Belt region subside and euxinic shales onlap the margin of the adjacent platform (Fig. 3.15c). It is likely that black shale deposition at marginal locations was at shallow water depths because the shales pass laterally into well oxygenated platform facies of the Yoredale cycles, which contain a diverse and abundant benthic fauna, over a distance of ca. 1 km (Rayner, 1953). For example, at FL, large limestone boulders and calciturbidites are interbedded with euxinic shales (Fig. 3.9), indicating the close proximity of shallow, well-ventilated conditions. This abrupt lateral transition is likely only possible in a strongly stratified water column where a sharp pycnocline separates a sulfidic lower water column from an oxygenated upper water column (Fig. 3.15B, C). The most intense and persistent euxinia coincides with Upper Bowland Shale deposition (Fig. 3.15C) when we infer that the thickness of sub-pycnocline waters were at their greatest. This may well have favoured their stability because re-oxygenating such a large volume of the lower water column would require major mixing.

Salinity stratification provides a highly effective mechanism to isolate the lower water column from surface waters, due to the strong density variations of water with different salinities. Models for black shale accumulation in silled basins frequently invoke an "estuarine circulation model" in which the basin has a positive water balance (like an estuary), with more water exported via low salinity surface waters than are replaced by influx of deeper, more saline waters (Tyson and Pearson, 1991; Algeo et al., 2008). This model is especially popular for the Jurassic black shales of western Europe (e.g. van de Schootbrugge et al., 2005; McArthur et al., 2008), and has also been invoked for the Bowland Shale (Gross et al., 2015; Emmings et al., 2020). However, the link between the intensity of oxygen depletion and run-off into the Bowland Basin is the opposite of that which would occur if a freshwater-fed halocline was isolating basin bottom waters. This is especially clear in the Upper Bowland Shale, where intervals of sandy turbidity flow, fed from deltas prograding from the northeast (Waters et al., 2020), coincide with improvements in basinal oxygenation. For example, a substantial turbidite system (the Pendle Grits) succeeds the Bowland Shales, and the youngest (E_{1c} zone) shales immediately below the sand influx show a rapid improvement of oxygenation from euxinic to oxic conditions (Emmings et al., 2020, Fig 2B). More minor phases of turbidity influx are seen before this, and these also coincide with improved ventilation. Thus, in the E_{1b} Zone a thin, turbidite sandbody is developed at a level where redox proxies indicate a short period of improved (ferruginous) conditions, interspersed within a euxinic interval (Fig. 3.14).

Temperature-driven stratification can also isolate bottom waters in modern shelf seas, when warmer, lower density surface waters cap colder, deep water. The strength of such stratification is weaker than salinity-drive stratification, and thermoclines are often transient or seasonal (Tyson and Pearson, 1991; Tomašovỳch et al., 2017). The sharp, lateral transition between euxinic and oxic deposition on the Bowland Basin margin and long-term stability of euxinic deep waters argues for strong stratification. Therefore, thermocline development in the Bowland Basin is unlikely. Instead, the basin may have been salinity stratified, but with the bottom waters being both warm and saline. Warm saline bottom water development is frequently invoked for periods of oceanic anoxia whereby extensive low-latitude, shelf seas in warm, arid settings are subject to evaporation that elevates salinity (e.g. Railsback, 1990; Wenzel and Joachimski, 1996; Friedrich et al., 2008). This increases water density and over-compensates for the density decline caused by warming, resulting in waters that sink into deeper waters of adjacent oceans, which thus become stratified (e.g. Brass et al., 1982; Friedrich et al., 2008; MacLeod et al., 2011; Dummann et al., 2021). We propose that this model may also operate on a smaller, epicontinental-basin scale. The Bowland Basin lay in warm, tropical latitudes and was surrounded by extensive carbonate platforms (Fig. 3.1). Therefore, we envisage an anti-estuarine depositional model for the Bowland Basin, in which WSBW generated on adjacent carbonate shelves was the source of deep basin waters. Euxinic waters developed below the resultant strong pycnocline for several million years (Fig. 3.15). Such a scenario explains why delta progradation from the north coincided with improved oxygenation of the Bowland Basin: WSBW generation declined, and dense, sediment-laden gravity currents flushed out and diluted the basinal waters, thereby improving ventilation.

An anti-estuarine basin model for black shale generation contrasts with the widely preferred estuarine, silled basin model proposed for many epicontinental black shales. However, our WSBW model may be widely applicable because many black shale occurrences occur in basins adjacent to broad carbonate shelves which are unlikely to have experienced estuarine circulation. For example, the Ravnefjeld Formation is a regionally important Permian source rock of East Greenland (Christiansen et al., 1993). The black shales were deposited in a series of narrow, laterally-linked syn-rift basins developed adjacent to carbonate platforms (Piasecki and Stemmerik, 1991), a situation closely comparable to the Bowland Shale. Organic biomarkers in the Ravnefjeld black shales indicate high salinities (Christiansen et al., 1993), and it is possible that their accumulation occurred beneath a halocline in which bottom waters were fed by highly saline surface waters. Furthermore, the Ravnefjeld shales show a remarkable persistence of organic richness along the length of their outcrop, despite considerable thickness variations (Christiansen et al., 1993), an attribute that is also similar to the Bowland Shales, especially in the Upper Bowland Shale Formation. This may be because WSBWs generate a strong, persistent halocline, with the result that sub-pycnocline conditions in the isolated bottom waters are remarkably uniform. Similarly, the Richardson Trough (Northern Yukon, Canada) was surrounded by the Great American Carbonate Bank during much of the Paleozoic, and records a prolonged history of anoxic deposition (Sperling et al. 2021). This is likely to be another example where the WSBW model is appropriate.

3.7 Conclusions

The Bowland Shales are an important regional hydrocarbon resource in UK stratigraphy; the general geochemistry, redox conditions, and depositional environments from the best-exposed sections in the Bowland Basin have been studied here. Dark grey shale and minor calciturbidite and sandy turbidites accumulated in a rift basin surrounded by carbonate platforms and shelves during 10 million years of the late Mississippian. Independent proxies have been applied and calibrated to assess the evolving redox conditions during Bowland Shale deposition. The oxic/anoxic threshold is diagnosed by U_{EF} > 1-2 and Fe_{HR}/Fe_T > 0.38, whilst Mo_{EF} > 4.8 indicates weakly euxinic conditions and values > 40 denote highly euxinic environments. U/Mo ratios are also useful in distinguishing the transition to euxinic conditions where its value declines below 2. The redox boundaries are also corroborated by pyrite framboid size analysis: Mo_{EF} > 40 is consistently associated with mean framboid populations < 6 µm in diameter, whilst weakly euxinic Mo_{EF} values occur in samples with framboids > 6 µm (Fig. 3.13). These geochemical threshold values differ in detail from those encountered in other basins and reinforces the point made by Algeo and Li (2020) that, wherever possible, redox proxies should be calibrated separately for each basin.

Bowland Shale deposition began during a phase of rifting that saw ramp collapse and establishment of block-and-basin topography. Organic-rich shale deposition was initially localised and laterally variable, but by the late Asbian TOC-rich sediments (typically 4 wt% and reaching 10 wt%) were more extensive. The transition from syn- to post-rift conditions in the Brigantian saw continued expansion of black shale deposition onto the shoulders of the basin when highly euxinic waters were present throughout the basin (Fig. 3.15C). By this stage, black shale deposition had expanded into "perched sub-basins" on the basin margin which, at their initiation, were more intensely reducing than in the main basin, suggesting they had a strong degree of isolation (Fig. 3.15B). This is corroborated by low Mo/TOC gradients in the perched sub-basins compared with the main basin. Sediment-gravity flows introduced minor turbidite sandbodies into the basin in the later stage of Bowland Shale deposition. These coincide with improvements in basin oxygenation, suggesting the gravity currents flushed out and improved basin oxygenation. The re-oxygenation effect is minor for the thin turbidites, but the massive turbidite sand influx that terminated Bowland Shale deposition was preceded by a major improvement from euxinic to oxic deposition.

A warm saline bottom water model is developed for Bowland Shale deposition, in which basinal waters were generated by evaporation in the shallow waters of the adjacent carbonate platforms. The resultant halocline was strongly developed and accounts for the stability of sub-pycnocline conditions and the rapid lateral transition from euxinia into fully oxygenated shallow water facies at the basin margin. This anti-estuarine silled basin model contrasts with "typical" positive water balance circulation models proposed for many black shales. The inverse relationship between anoxia and clastic influx to the basin argues against the latter. Thus, the estuarine circulation model for black shale deposition is not a ubiquitous shibboleth. WSBW models may be common especially for black shales that formed in basins surrounded by extensive carbonate platforms.

Acknowledgements

We thanks the following people for their valuable help: Professor Jeff Peakall, Dr. Kaixuan Ji, PGR Yuxuan Wang, Dr. Yafang Song and Dr. Zhen Xu for fieldwork assistance. Gratitude also goes to Stephen Reid for major and trace elements analysis and Dr. Richard Walshaw for SEM guidance.

References

Aitkenhead, N., 1992, *Geology of the country around Garstang*: Memoir for 1: 50,000 Geological Sheet 67 (England and Wales): HM Stationery Office.

Alcott, L.J., Krause, A.J., Hammarlund, E.U., Bjerrum, C.J., Scholz, F., Xiong, Y., Hobson, A.J., Neve, L., Mills, B.J.W., März, C., Schnetger, B., Bekker, A., & Poulton, S.W., 2020. Development of Iron Speciation Reference Materials for Palaeoredox Analysis: *Geostandards and Geoanalytical Research*, **44**, 581–591, https://doi.org/10.1111/ggr.12342.

Algeo, T.J., & Li, C., 2020, Redox classification and calibration of redox thresholds in sedimentary systems: *Geochimica et Cosmochimica Acta*, **287**, 8–26, https://doi.org/10.1016/j.gca.2020.01.055.

Algeo, T.J., & Lyons, T.W., 2006, Mo-total organic carbon covariation in modern anoxic marine environments: Implications for analysis of paleoredox and paleohydrographic conditions. *Paleoceanography*, **21**, 204–230, https://doi.org/10.1029/2004PA001112.

Algeo, T.J., Heckel, P.H., Maynard, J.B., Blakey, R.C., & Rowe, H., 2008, Modern and ancient epeiric seas and the super-estuarine circulation model of marine anoxia: *Special Paper - Geological Association of Canada*, 7–38.

Algeo, T.J., Lyons, T.W., Ronald, B., & Over, D.J., 2007, Hydrographic conditions of the Devono–Carboniferous North American Seaway inferred from sedimentary Mo–TOC relationships, *Palaeogeography, Palaeoclimatology, Palaeoecology*, **256**, 204–230, https://doi.org/10.1016/j.palaeo.2007.02.035.

Algeo, T.J., & Tribovillard, N., 2009, Environmental analysis of paleoceanographic systems based on molybdenum-uranium covariation, *Chemical Geology*, **268**, 211–225, https://doi.org/10.1016/j.chemgeo.2009.09.001.

Anderson, R.F., Lehuray, A.P., Fleisher, M.Q., & Murray, J.W., 1989, Uranium deposition in Saanich Inlet sediments, Vancouver Island, *Geochimica et Cosmochimica Acta*, **53**, 2205–2213, https://doi.org/10.1016/0016-7037(89)90344-X.

Andrews, I.J. 2013. The Carboniferous Bowland Shale gas study: geology and resource estimation: British Geological Survey for Department of Energy and Climate Change, London, UK. 56 pp open file report.

Arthur, M., and Sageman, B.B., 1994, Marine shales: depositional mechanisms and environments of ancient deposits, *Annual Review of Earth and Planetary Sciences*, **22**, 499–551, https://doi.org/10.1146/annurev.earth.22.1.499.

Arthurton, R.S., Johnson, E.W., & Mundy, D.J.C., 1988, *Geology of the country around Settle*. Memoir for 1: 50,000 Geological Sheet 67 (England and Wales): HM Stationery Office.

Benkovitz, A., Matthews, A., Teutsch, N., Poulton, S.W., Bar-Matthews, M., & Almogi-Labin, A., 2020, Tracing water column euxinia in Eastern Mediterranean Sapropels S5 and S7: *Chemical Geology*, **545**, 119627, https://doi.org/10.1016/j.chemgeo.2020.119627.

Bennett, W.W., & Canfield, D.E., 2020, Redox-sensitive trace metals as paleoredox proxies: A review and analysis of data from modern sediments, *Earth-Science Reviews*, **204**, 103175, https://doi.org/10.1016/j.earscirev.2020.103175.

Bertine, K.K., & Turekian, K.K., 1973, Molybdenum in marine deposits, *Geochimica et Cosmochimica Acta*, **37**, 1415–1434, https://doi.org/10.1016/0016-7037(73)90080-X.

Boucot, A.J., Xu, C., Scotese, C.R., & Morley, R.J., 2013, *Phanerozoic paleoclimate: an atlas of lithologic indicators of climate*, *Society for Sedimentary Geology*, **11**.

Brass, G.W., Southam, J.R., & Peterson, W.H., 1982, Warm saline bottom water in the ancient ocean, *Nature*, **296**, 620–623, https://doi.org/10.1038/296620a0.

Canfield, D.E., Raiswell, R., Westrich, J.T., Reaves, C.M., & Berner, R.A., 1986, The use of chromium reduction in the analysis of reduced inorganic sulfur in sediments and shales: *Chemical Geology*, **54**, 149–155, https://doi.org/10.1016/0009-2541(86)90078-1.

Christiansen, F.G., Piasecki, S., Stemmerik, L., & Telnaes, N., 1993, Depositional environment and organic geochemistry of the Upper Permian Ravnefjeld Formation source rock in East Greenland, *AAPG Bulletin*, **9**, 1519–1537, https://doi.org/ 10.1306/BDFF8EDE-1718-11D7-8645000102C1865D.

Clarkson, M.O., Poulton, S.W., Guilbaud, R., & Wood, R.A., 2014, Assessing the utility of Fe/Al and Fe-speciation to record water column redox conditions in carbonate-rich sediments, *Chemical Geology*, **382**, 111–122, https://doi.org/10.1016/j.chemgeo.2014.05.031.

Cope, J.C.W., Guion, P.D., Sevastopulo, G.D., & Swan, A.R.H., 1992, Carboniferous: Geological Society, London, Memoirs, **13**, 67–86.

de Jonge-Anderson, I., & Underhill, J.R., 2020, Structural constraints on Lower Carboniferous shale gas exploration in the Craven Basin, NW England, *Petroleum Geoscience*, **26**, 303–324, https://doi.org/10.1144/PETGEO2019-125.

Demaison, G.J., & Moore, G.T., 1980, Anoxic environments and oil source bed genesis, *AAPG Bulletin*, 64, 1179–1209, https://doi.org/10.1306/2F91945E-16CE-11D7-8645000102C1865D.

Dubinin, A. V, Demidova, T.P., Dubinina, E.O., Rimskaya-korsakova, M.N., Semilova, L.S., Berezhnaya, E.D., Klyuvitkin, A.A., Kravchishina, M.D., & Belyaev, N.A., 2022, Sinking particles in the Black Sea waters : vertical fluxes of elements and pyrite to the bottom , isotopic composition of pyrite sulfur, and hydrogen sulfide production, *Chemical Geology*, **606,** 120996, https://doi.org/10.1016/j.chemgeo.2022.120996.

Dummann, W., 2021, Driving mechanisms of organic carbon burial in the Early Cretaceous South Atlantic Cape Basin (DSDP Site 361), *Climate of the Past*, **17**, 469–490, https://doi.org/10.5194/cp-17-469-2021.

Earp, J.R., Poole, E.G., & Whiteman, A.J., 1961, *Geology of the country around Clitheroe and Nelson*: Memoir for 1: 50,000 Geological Sheet 68 (England and Wales): HM Stationery Office

Ebdon, C.C., Fraser, A.J., Higgins, A.C., Mitchener, B.C., & Strank, A.R.E., 1990, The Dinantian stratigraphy of the East Midlands: a seismostratigraphic approach, *Journal of the Geological Society*, 147, 519–536, https://doi.org/10.1144/gsjgs.147.3.0519.

Emerson, S.R., & Huested, S.S., 1991, Ocean anoxia and the concentrations of molybdenum and vanadium in seawater, *Marine Chemistry,* **34**, 177–196, https://doi.org/10.1016/0304-4203(91)90002-E.

Emmings, J.F., Poulton, S.W., Vane, C.H., Davies, S.J., Jenkin, G.R.T., Stephenson, M.H., Leng, M.J., Lamb, A.L., & Moss-Hayes, V., 2020, A Mississippian black shale record of redox oscillation in the Craven Basin, UK, *Palaeogeography, Palaeoclimatology, Palaeoecology*, **538**, 109423, https://doi.org/10.1016/j.palaeo.2019.109423.

Erickson, B.E., & Helz, G.R., 2000, Molybdenum(VI) speciation in sulfidic waters, *Geochimica et Cosmochimica Acta*, **64**, 1149–1158, https://doi.org/10.1016/s0016-7037(99)00423-8.

Fauchille, A.L., Ma, L., Rutter, E., Chandler, M., Lee, P.D., & Taylor, K.G., 2017, An enhanced understanding of the Basinal Bowland shale in Lancashire (UK), through microtextural and mineralogical observations, *Marine and Petroleum Geology*, **86**, 1374–1390, https://doi.org/10.1016/j.marpetgeo.2017.07.030.

Fraser, A.J., & Gawthorpe, R.L., 1990, Tectono-stratigraphic development and hydrocarbon habitat of the Carboniferous in northern England, *Geological Society Special Publication*, **55**, 49– 86, https://doi.org/10.1144/GSL.SP.1990.055.01.03.

Friedrich, O., Erbacher, J., Moriya, K., Wilson, P.A., & Kuhnert, H., 2008, Warm saline intermediate waters in the Cretaceous tropical Atlantic ocean, *Nature Geoscience*, **1**, 453– 457, https://doi.org/10.1038/ngeo217.

Gawthorpe, R.L., 1986, Sedimentation during carbonate ramp-to-slope evolution in a tectonically active area: Bowland Basin (Dinantian), northern England, *Sedimentology*, **33**, 185–206, https://doi.org/10.1002/9781444304473.ch31.

Gawthorpe, R.L., 1987, Burial dolomitization and porosity development in a mixed carbonate-clastic sequence: an example from the Bowland Basin, northern England, *Sedimentology*, 34, 533–558, https://doi.org/10.1111/j.1365-3091.1987.tb00785.x.

Gross, D., Sachsenhofer, R.F., Bechtel, A., Pytlak, L., Rupprecht, B., & Wegerer, E., 2015, Organic geochemistry of Mississippian shales (Bowland Shale Formation) in central Britain: Implications for depositional environment, source rock and gas shale potential: *Marine and Petroleum Geology*, **59**, 1–21, https://doi.org/10.1016/j.marpetgeo.2014.07.022.

Hart, B.S., & Hofmann, M.H., 2022, Revisiting paleoenvironmental analyses and interpretations of organic-rich deposits: The importance of TOC corrections, *Organic Geochemistry*, **170**, 104434, https://doi:10.1016/j.orggeochem.2022.104434.

He, T.C., Wignall, P.B., Newton, R.J., Atkinson, J.W., Keeling, J.F.J., Xiong, Y., & Poulton, S.W., 2022, Extensive marine anoxia in the European epicontinental sea during the end-Triassic mass extinction, *Global and Planetary Change*, 210, 103771, https://doi.org/10.1016/j.gloplacha.2022.103771.

Helz, G.R., Miller, C. V., Charnock, J.M., Mosselmans, J.F.W., Pattrick, R.A.D., Garner, C.D., & Vaughan, D.J., 1996, Mechanism of molybdenum removal from the sea and its concentration in black shales: EXAFS evidence, *Geochimica et Cosmochimica Acta*, **60**, 3631–3642, https://doi.org/10.1016/0016-7037(96)00195-0.

Hennissen, J.A.I., Hough, E., Vane, C.H., Leng, M.J., Kemp, S.J., & Stephenson, M.H., 2017, The prospectivity of a potential shale gas play: An example from the southern Pennine Basin (central England, UK), *Marine and Petroleum Geology*, **86**, 1047–1066, https://doi.org/10.1016/j.marpetgeo.2017.06.033.

Jenkyns, H.C., 2010, Geochemistry of oceanic anoxic events, *Geochemistry, Geophysics, Geosystems*, **11**, 1–30, https://doi.org/10.1029/2009GC002788.

Kane, I.A., 2010, Development and flow structures of sand injectites, The Hind Sandstone Member injectite complex, Carboniferous, UK, *Marine and Petroleum Geology*, **27**, 1200–1215, https://doi.org/10.1016/j.marpetgeo.2010.02.009.

Kirby, G.A., 2000, *The structure and evolution of the Craven Basin and adjacent areas: subsurface memoir*: HM Stationery Office.

Klinkhammer, G.P., & Palmer, M.R., 1991, Uranium in the oceans: Where it goes and why: *Geochimica et Cosmochimica Acta*, **55**, 1799–1806, https://doi.org/10.1016/0016-7037(91)90024-Y.

Li, S., Wignall, P.B., Poulton, S.W., Hedhli, M., & Grasby, S.E., 2022, Carbonate shutdown, phosphogenesis and the variable style of marine anoxia in the late Famennian (Late Devonian) in western Laurentia, *Palaeogeography, Palaeoclimatology, Palaeoecology*, **589**, 110835, https://doi.org/10.1016/j.palaeo.2022.110835.

MacLeod, K.G., Isaza Londoño, C., Martin, E.E., Jiménez Berrocoso, Á., & Basak, C., 2011, Changes in North Atlantic circulation at the end of the Cretaceous greenhouse interval: *Nature Geoscience*, **4**, 779–782, https://doi.org/10.1038/ngeo1284.

Manifold, L., Strother, P. Del, Gold, D.P., Burgess, P., & Hollis, C., 2021, Unravelling evidence for global climate change in Mississippian carbonate strata from the Derbyshire and North Wales platforms, UK, *Journal of the Geological Society*, **178**, jgs2020–106, https://doi.org/10.1144/jgs2020-106.

McArthur, J.M., Algeo, T.J., Van De Schootbrugge, B., Li, Q., & Howarth, R.J., 2008, Basinal restriction, black shales, Re-Os dating, and the Early Toarcian (Jurassic) oceanic anoxic event, *Paleoceanography*, **23**, 1–22, https://doi.org/10.1029/2008PA001607.

McLennan, S.M., 2001, Relationships between the trace element composition of sedimentary rocks and upper continental crust, *Geochemistry, Geophysics, Geosystems*, **2**, https://doi.org/10.1029/2000GC000109.

Munnecke, A., Samtleben, C., & Bickert, T., 2003, The Ireviken Event in the lower Silurian of Gotland, Sweden – relation to similar Palaeozoic and Proterozoic events, *Palaeogeography, Palaeoclimatology, Palaeoecology*, **195**, 99–124, https://doi.org/10.1016/S0031-0182(03)00304-3.

Newport, S.M., Jerrett, R.M., Taylor, K.G., Hough, E., & Worden, R.H., 2018, Sedimentology and microfacies of a mud-rich slope succession: In the Carboniferous Bowland Basin, NW England (UK), *Journal of the Geological Society*, **175**, 247–262, https://doi.org/10.1144/jgs2017-036.

Pasquier, V., Fike, D.A., Révillon, S., & Halevy, I., 2022, A global reassessment of the controls on iron speciation in modern sediments and sedimentary rocks: A dominant role for diagenesis, *Geochimica et Cosmochimica Acta*, **335**, 211–230, https://doi.org/10.1016/j.gca.2022.08.037.

Piasecki, S., & Stemmerik, L., 1991, Late Permian anoxia in central East Greenland: *Geological Society Special Publication*, **58**, 275–290, https://doi.org/10.1144/GSL.SP.1991.058.01.18.

Pickard, N.A.H., Rees, J.G., Strogen, P., Somerville, I.D., & Jones, G.L.I., 1994, Controls on the evolution and demise of Lower Carboniferous carbonate platforms, northern margin of the Dublin Basin, Ireland, *Geological Journal*, **29**, 93–117, https://doi.org/10.1002/gj.3350290202.

Poulton, S.W., 2021, *The Iron Speciation Paleoredox Proxy*: Elements in Geochemical, Tracers in Earth System Science. Cambridge University Press, https://doi.org/10.1017/9781108847148.

Poulton, S.W., & Canfield, D.E., 2005, Development of a sequential extraction procedure for iron: Implications for iron partitioning in continentally derived particulates, *Chemical Geology*, **214**, 209–221, https://doi.org/10.1016/j.chemgeo.2004.09.003.

Poulton, S.W., & Canfield, D.E., 2011, Ferruginous conditions: a dominant feature of the ocean through Earth's history, *Elements*, **7**, 107–112, https://doi.org/10.2113/gselements.7.2.107.

Poulton, S.W., Fralick, P.W., & Canfield, D.E., 2004, The transition to a sulphidic ocean ~1.84 billion years ago, *Nature*, **431**, 173–177, https://doi.org/10.1038/nature02912.

Railsback, L.B., 1990, Influence of changing deep ocean circulation on the Phanerozoic oxygen isotopic record, *Geochimica et Cosmochimica Acta*, **54**, 1501–1509, https://doi.org/10.1016/0016-7037(90)90175-K.

Raiswell, R., & Canfield, D.E., 1998, Sources of iron for pyrite formation in marine sediments: *American Journal of Science*, 298, 219–245, https://doi.org/10.2475/ajs.298.3.219.

Raiswell, R., Hardisty, D.S., Lyons, T.W., Canfield, D.E., Owens, J.D., Planavsky, N.J., Poulton, S.W., & Reinhard, C.T., 2018, The iron paleoredox proxies: A guide to the pitfalls, problems and proper practice: American Journal of Science, v. 318, p. 491–526, https://doi.org/10.2475/05.2018.03.

Rayner, D.H., 1953, The Lower Carboniferous rocks in the north of England: A review, *Proceedings of the Yorkshire Geological Society*, **28**, 231–235, https://doi.org/10.1144/pygs.28.4.231.

Riley, N.J., 1990, Stratigraphy of the Worston Shale Group (Dinantian), Craven Basin, north-west England, *Proceedings of the Yorkshire Geological Society*, 48, 163–187, https://doi.org/10.1144/pygs.48.2.163.

Scott, C., & Lyons, T.W., 2012, Contrasting molybdenum cycling and isotopic properties in euxinic versus non-euxinic sediments and sedimentary rocks: Refining the paleoproxies: *Chemical Geology*, **324–325**, 19–27, https://doi.org/10.1016/j.chemgeo.2012.05.012.

Sperling, E.A., Melchin, M.J., Fraser, T., Stockey, R.G., Farrell, U.C., Bhajan, L., Brunoir, T.N.,Cole, D.B., Gill, B.C., Lenz, A., Loydell, D.K., Malinowski, J., Miller, A.J., Plaza-Torres, S., Bock, B., Rooney, A.D., Tecklenberg, S.A., Vogel, J.M., Planavsky, N.J., & Strauss, J.V., 2021, A long-term record of early to mid-Paleozoic marine redox change, *Science Advances*, **7**, eabf4382, https://doi.org/10.1126/sciadv.abf4382

Tomašovỳch, A., Gallmetzer, I., Haselmair, A., Kaufman, D.S., Vidović, J., & Zuschin, M., 2017, Stratigraphic unmixing reveals repeated hypoxia events over the past 500 yr in the northern Adriatic Sea, *Geology*, 45, 363–366, https://doi.org/10.1130/G38676.1.

Tribovillard, N., Algeo, T.J., Baudin, F., & Riboulleau, A., 2012, Analysis of marine environmental conditions based on molybdenum-uranium covariation – Applications to Mesozoic paleoceanography, *Chemical Geology*, **324–325**, 46–58, https://doi.org/10.1016/j.chemgeo.2011.09.009.

Tucker, M.E., Gallagher, J., and Leng, M.J., 2009, Are beds in shelf carbonates millennial-scale cycles? An example from the mid-Carboniferous of northern England, *Sedimentary Geology*, **214**, 19–34, https://doi.org/10.1016/j.sedgeo.2008.03.011.

Tyson, R.V., & Pearson, T.H. 1991. Modern and ancient continental shelf anoxia: an overview, *Geological Society, London, Special Publications*, **58(1)**, 1-24, https://doi.org/10.2307/3515153.

van de Schootbrugge, B., McArthur, J.M., Bailey, T.R., Rosenthal, Y., Wright, J.D., & Miller, K.G., 2005, Toarcian oceanic anoxic event: An assessment of global causes using belemnite C isotope records, *Paleoceanography*, **20**, 1–10, https://doi.org/10.1029/2004PA001102.

Waters, C.N., & Condon, D.J. 2012. Nature and timing of Late Mississippian to Mid-Pennsylvanian glacio-eustatic sea-level changes of the Pennine Basin, UK, *Journal of the Geological Society*, **169**, 37-51, https://doi.org/10.1144/0016-76492011-047

Waters, C.N., Haslam, R.B., Cózar, P., Somerville, I.D., Millward, D., & Woods, M., 2017, Mississippian reef development in the Cracoe Limestone Formation of the southern Askrigg Block, North Yorkshire, UK, *Proceedings of the Yorkshire Geological Society*, **61**, 179–196, https://doi.org/10.1144/pygs2016-374.

Waters, C.N., Vane, C.H., Kemp, S.J., Haslam, R.B., Hough, E., & Moss-Hayes, V.L., 2020, Lithological and chemostratigraphic discrimination of facies within the Bowland Shale Formation within the Craven and Edale basins, UK, *Petroleum Geoscience*, **26**, 325–345, https://doi.org/10.1144/PETGEO2018-039.

Waters, C.N., Waters, R.A., Barclay, W.J., & Davies, J.R., 2009, A lithostratigraphical framework for the Carboniferous successions of northern Great Britain (onshore). British Geological Survey.

Wegwerth, A. et al., 2018, Redox evolution during Eemian and Holocene sapropel formation in the Black Sea, *Palaeogeography, Palaeoclimatology, Palaeoecology*, 489, 249–260, https://doi.org/10.1016/j.palaeo.2017.10.014.

Wei, G., Chen, T., Poulton, S.W., Lin, Y., He, T., Shi, X., Chen, J., Li, H., Qiao, S., Liu, J., Li, D., & Ling, H.F., 2021. A chemical weathering control on the delivery of particulate iron to the continental shelf, *Geochimica et Cosmochimica Acta*, **308**, 204-216, https://doi.org/10.1016/j.gca.2021.05.058.

Wenzel, B., & Joachimski, M.M., 1996, Carbon and oxygen isotopic composition of Silurian brachiopods (Gotland/Sweden): palaeoceanographic implications, *Palaeogeography, Palaeoclimatology, Palaeoecology*, **122**, 143–166, https://doi.org/10.1016/0031-0182(95)00094-1.

Wignall, P.B., 1994, Black shales: Oxford University Press, Oxford.

Wignall, P.B., & Newton, R., 1998, Pyrite framboid diameter as a measure of oxygen deficiency in ancient mudrocks, *American Journal of Science*, **298**, 537–552, https://doi.org/10.2475/ajs.298.7.537.

Wignall, P.B., Bond, D.P.G., Kuwahara, K., Kakuwa, Y., Newton, R.J., & Poulton, S.W., 2010, An 80 million year oceanic redox history from Permian to Jurassic pelagic sediments of the Mino-Tamba terrane, SW Japan, and the origin of four mass extinctions, *Global and Planetary Change*, **71**, 109–123, https://doi.org/10.1016/j.gloplacha.2010.01.022.

Wilkin, R.T., & Arthur, M.A., 2001, Variations in pyrite texture, sulfur isotope composition, and iron systematics in the black sea: Evidence for late Pleistocene to Holocene excursions of the O_2-H_2S redox transition, *Geochimica et Cosmochimica Acta*, **65**, 1399–1416, https://doi.org/10.1016/S0016-7037(01)00552-X.

Wilkin, R.T., & Barnes, H.L., 1997, Formation processes of framboidal pyrite, *Geochimica et Cosmochimica Acta*, **61**, 323–339, https://doi.org/10.1016/S0016-7037(96)00320-1.

Wilkin, R.T., Barnes, H.L., & Brantley, S.L., 1996, The size distribution of framboidal pyrite in modern sediments, *Geochimica et Cosmochimica Acta*, **60**, 3897–3912, https://doi.org/10.1016/0016-7037(96)00209-8.

Wright, V.P., & Vanstone, S.D., 2001, Onset of Late Palaeozoic glacio-eustasy and the evolving climates of low latitude areas: a synthesis of current understanding, *Journal of the Geological Society*, **158**, 579–582, https://doi.org/10.1080/00167616608728616.

Xiong, Y., Guilbaud, R., Peacock, C.L., Cox, R.P., Canfield, D.E., Krom, M.D., & Poulton, S.W., 2019, Phosphorus cycling in Lake Cadagno, Switzerland: A low sulfate euxinic ocean analogue, *Geochimica et Cosmochimica Acta*, **251**, 116–135, https://doi.org/10.1016/j.gca.2019.02.011.

Zegeye, A., Bonneville, S., Benning, L.G., Sturm, A., Fowle, D.A., Jones, C.A., Canfield, D.E., Ruby, C., MacLean, L.C., Nomosatryo, S., Crowe, S.A., & Poulton, S.W., 2012. Green rust formation controls nutrient availability in a ferruginous water column, *Geology*, **40**, 599–602, https://doi.org/10.1130/G32959.1

Zheng, Y., Anderson, R.F., van Geen, A., & Fleisher, M.Q., 2002, Remobilization of authigenic uranium in marine sediments by bioturbation, *Geochimica et Cosmochimica Acta*, **66**, 1759–1772, https://doi.org/10.1016/S0016-037(01)00886-9.

Chapter 4: Contrasting sediment sources and depositional processes in a black shale basin: the Mississippian Bowland Basin of northern England

Submitted to Sedimentology

Contrasting sediment sources and depositional processes in a black shale basin: the Mississippian Bowland Basin of northern England

Sen Li[1], Paul B. Wignall[1], Jeff Peakall[1], Jingwei Cui[1,2]

1. School of Earth and Environment, University of Leeds, Leeds LS2 9JT, UK

2. PetroChina Research Institute of Petroleum Exploration & Development, Beijing, 100083, China

4.1 Abstract

Organic-rich shale accumulation is controlled by numerous factors, ranging from diverse sedimentary processes to the source of the fine-grained sediment. This is especially the case when black shales accumulate in basins that are surrounded by shallow-water carbonate areas. The Bowland Shale is a succession of late Mississippian organic-rich mudrocks that record a range of transport processes in the anoxic Bowland Basin. Interbedded amongst the basinal mudrocks are several elongate, calciturbidite fans ~ 10 km in length, sourced from a small carbonate platform to the SE of the basin, whilst a turbidite sandstone body entered the basin from the east. An intrabasinal high in the NW of the basin deflected the progradation of the turbidite sandstones and was likely also responsible for reflection of the carbonate-carrying sediment gravity flows generating combined flow structures. Finer calcareous detritus was also sourced from the SE forming an apron of calcareous mudstone delivered by low strength debris flows. The Upper Bowland Shale is associated with the development of organic-rich shale with a fabric consisting of compacted clay lenses (0.05 – 0.4 mm in width) and hemipelagic components (including larval shells of bivalves and goniatites and tiny syngenetic framboids) and organic filaments (marine snow). The lenses are interpreted to be faecal pellets formed above the redoxcline before settling to the seabed. We consider that hemipelagic deposition is probably typical for most organic-rich shale deposition. The alternative notion, that has recently gained much traction, that they consist of transported intraclasts, is problematic because it fails to address why basinal shales have an euxinic geochemical signature rather than recording the well-oxygenated conditions of the purported source area.

Key words: faecal pellets, clay lens fabric, hemipelagic, calciturbidite fans, carbonate productivity

4.2 Introduction

The infill of sedimentary basins is controlled by numerous factors, such as tectonics, sediment source and supply, climate and eustasy which can all vary in their influence. The interaction between a basin and surrounding shelf seas provides a further important aspect of a basin's evolution, especially in settings where deep-water black shale basins are adjacent to carbonate platforms. Black shales are often seen to onlap their surrounding shallow-water carbonate platforms, a relationship that can record transgressive drowning (Schlager, 1981), the collapse of the basin margin on transition to a sag phase (e.g. Pickard et al., 1994) and/or the shutdown of the carbonate factory caused by multiple potential factors such as ocean acidification, cooling, and expansion of eutrophic basinal waters into shallower settings (e.g. Hallock & Schlager, 1986; Krencker et al., 2014; Petrash et al., 2016; Reijmer, 2021; Li et al., 2022; Andrieu et al., 2022). The relationship of these processes to the depositional conditions responsible for organic-rich sediment accumulation is a complex one that has been the subject of much recent discussion particularly for the source rocks developed in the late Mississippian basins of the British Isles. These record a prolonged history of black shale-dominated deposition, spanning ca. 10 myrs, in a series of basins surrounded by platform carbonates. The resultant mudrock, the Bowland Shale, is an important hydrocarbon resource and target for shale gas exploration in the region (Gross et al., 2015; Clarke et al., 2019; Hennissen & Gent, 2019; de Jonge-Anderson et al., 2020).

Basinal black shale deposition has traditionally been ascribed to hemipelagic processes with planktonic organic matter settling through the water column along with fine-grained clays and wind-blown fine silt (e.g. Wignall, 1994; Gorsline et al., 1996). The Bowland Shale is still occasionally referred to as a hemipelagic mudstone (Waters et al., 2009, 2020; de Jonge-Anderson et al., 2020), but the past decade has seen these ideas supplanted with the notion that mudrocks generally (and the Bowland Shale in particular) predominantly record deposition from a range of sediment gravity flows including debris flows, low concentration turbidity currents and hybrid flows transporting mud intraclasts/rip-up clasts from upper slope and shelf settings (Könitzer et al., 2014; Gross et al., 2015; Newport et al., 2018, 2020; Emmings et al., 2020a; Li et al., 2021; Peng, 2021; Wei & Swennen, 2022). The Bowland Shale also contains coarser-grained units, including the Pendleside Sandstone and several calcarenite horizons (see below), that undoubtedly record sediment transport from shallower water areas, but to ascribe a similar origin to the mudrocks challenges the assumption that basinal shales provide a reliable record of basinal geochemistry. If the shale consists of clasts supposedly derived from upslope oxic shelf settings then what redox signal do they record?

Here we examine the depositional processes responsible for Bowland Shale deposition and the latest depositional models for mudrocks, and evaluate sediment provenance, how basinal conditions interacted with the surrounding shallow-water carbonates, and the role of eustasy. Our analysis has broader implications for the depositional mechanisms of black shales and their veracity as a repository for redox conditions within basins. We also examine the reasons behind the persistence of carbonate productivity on adjacent shelves and platforms even when euxinic conditions extended to the basin margin.

4.3 Regional History

Bowland Shale deposition began in the late Asbian Stage of northern England during a phase of active tectonism that transformed ramp carbonate systems (of the Pendleside Limestone Formation) into a series of laterally-linked, fault-bounded basins flanked by carbonate platforms and shelf seas (Gawthorpe, 1986; Kirby et al., 2000; Fraser & Gawthorpe, 1990; Fig. 4.1). The Bowland Basin was the western-most of the onshore basins and is the focus of this study (Fig. 4.2). Following active rifting around the Asbian/Brigantian boundary, the basins had transitioned into a sag phase by the end Brigantian (Gawthorpe, 1986; Leeder, 1988; Hennissen & Gent, 2019), although local active tectonism was intermittently developed as late as the Pendleian Stage (Dunham & Wilson, 1985; Kirby et al., 2000; Kane 2010). Carbonate slope deposits of the Pendleside Limestone Formation were replaced by the mudrocks of the Lower Bowland Shale which developed diachronously in the late Asbian to Brigantian. The Lower Bowland Shale Formation also includes limestone (e.g. Park Style Limestone Member and Ravensholme Limestone Member) and sandstone units (e.g. Pendleside Sandstone Member) (Fig. 4.1c). Deposition was oxygen-restricted with ferruginous or weakly euxinic waters developed in the Basin (Li et al., 2023). The following Pendleian-aged black shale succession belongs to the Upper Bowland Shale Formation (Waters et al., 2009), although there is no lithological change at the Lower/Upper boundary (Waters et al., 2020). Strongly euxinic conditions became widespread (Li et al., 2023), until terminated by influx of a major turbidite sandbody (Pendle Grit Formation).

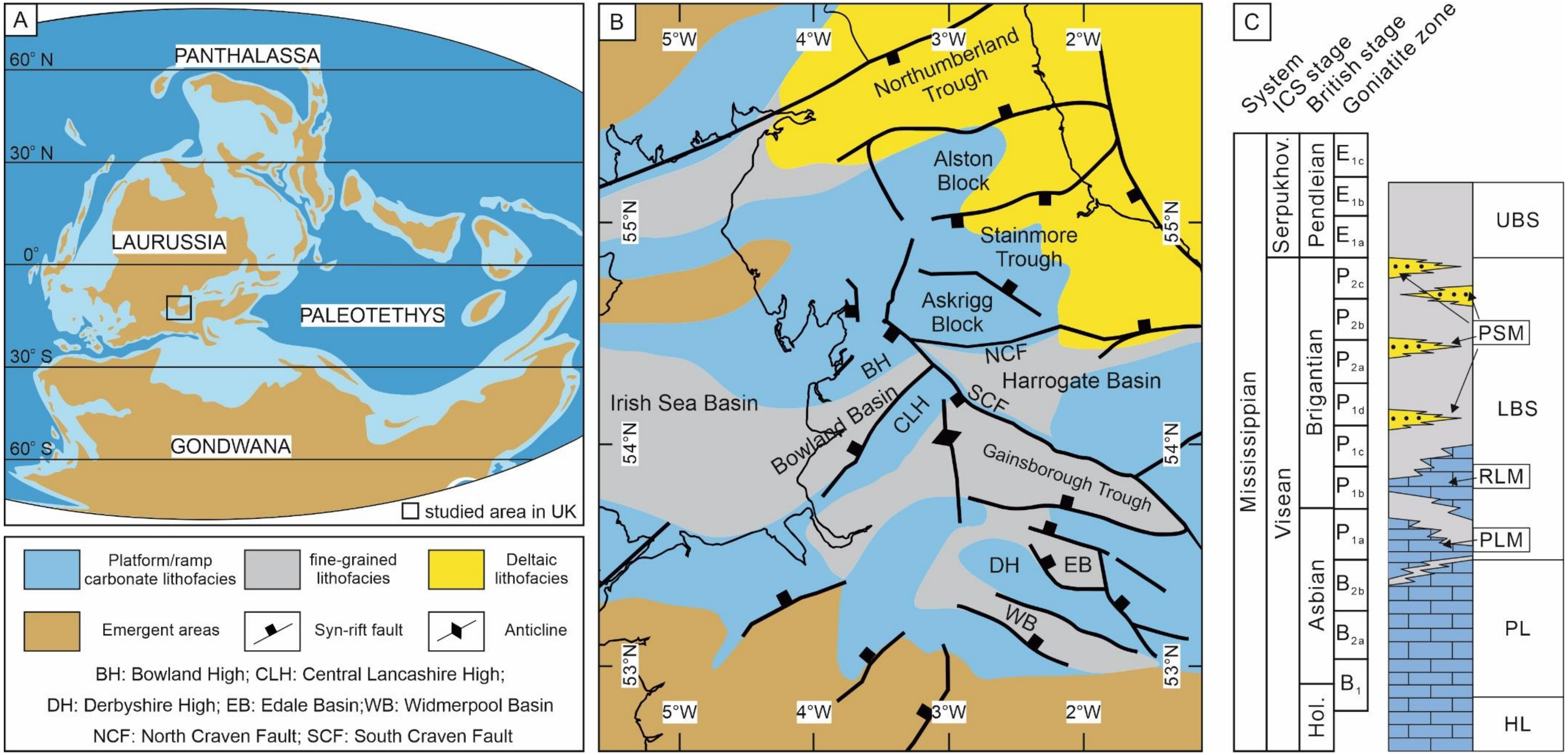

Fig. 4.1 (a) Global palaeogeography during the Mississippian showing location of the study region. (b) Regional palaeogeography showing location of the Bowland Basin amongst a series of fault-bounded block-and-basins. (c) Stratigraphy of the Bowland Basin. UBS Upper Bowland Shale Formation; LBS Lower Bowland Shale Formation; PL Pendleside Limestone Formation; HL Hodderense Limestone Formation; PSM Pendleside Sandstone Member; RLM Ravensholme Limestone Member; PLM Park Style Limestone Member. After Earp et al. (1961), Aitkenhead et al. (1992) and Waters et al. (2009). Abbreviated stages are Serpukhovian (Serpukhov.) and Holkerian (Hol.).

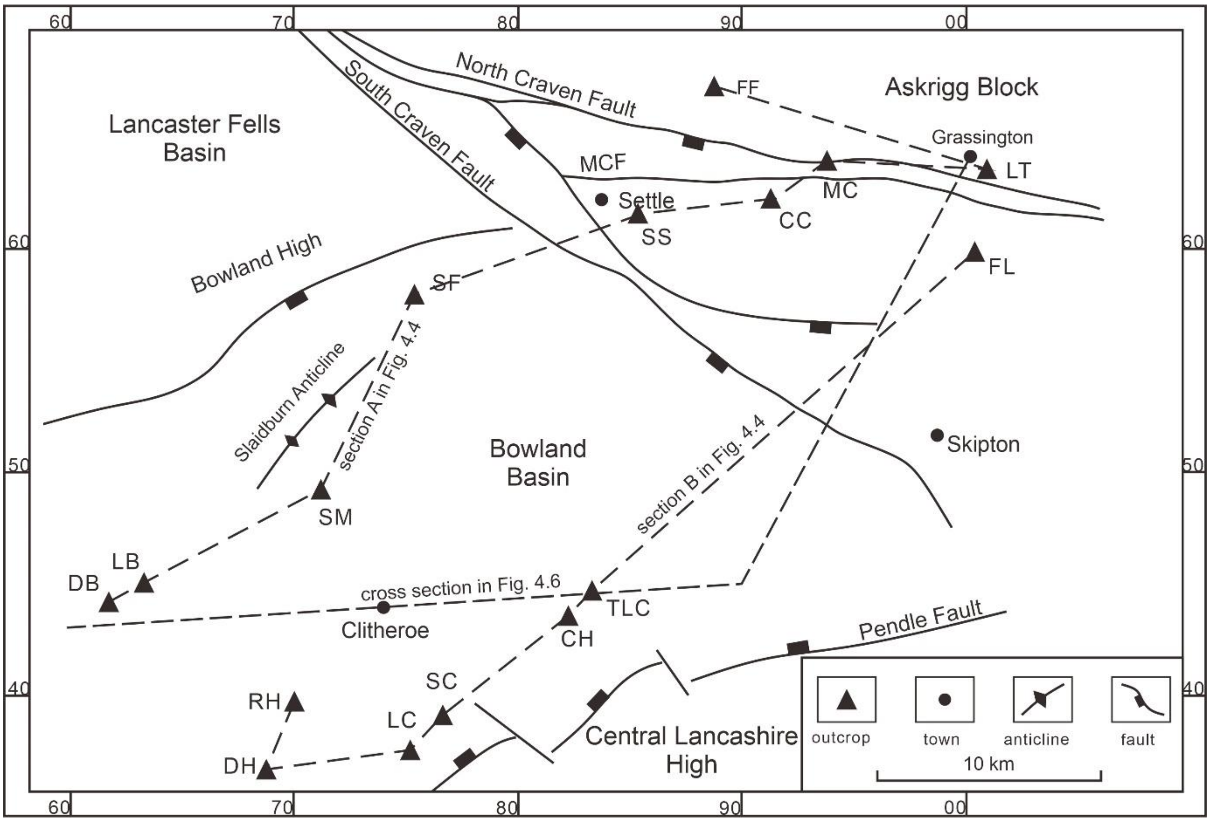

Fig. 4.2 Study area in the Bowland Basin, Craven Fault Belt (between the South and North Craven Faults), and the southern Askrigg Block and location of study sections (see Appendix A). MCF - Mid Craven Fault.

Variations in basinal accommodation space was controlled by subsidence and sediment supply and, for much of the depositional history considered here, the former outpaced the latter because at no point were shallow-water conditions developed. Water depths during Bowland Shale deposition are considered to have been at least several hundred metres (Black, 1940; Kirby et al., 2000; Emmings et al., 2020a). Even after the influx of major sandbodies, such as the 450 m-thick Pendle Grit, basinal conditions persisted. Nonetheless, base-level variations driven by glacioeustasy are also thought to have influenced deposition (Pharaoh et al., 2019).

The Bowland Shale subcrop is extensive over large areas of central northern England, where the formation is of economic interest as a hydrocarbon source (e.g. Clark et al., 2019; de Jonge-Anderson et al., 2020). Deposition occurred in several linked basins but only the Bowland Basin of central Lancashire has experienced later basin inversion (Pharaoh et al., 2019). Consequently, this area provides the best-available exposures of the Bowland Shale which have been the focus of much recent study. The Bowland Basin trends NE-SW, is around 25 km in width and at least 40 km in length although it may have extended for up to twice this distance to the SW in subcrop (Kirby et al., 2000; Waters et al., 2009; Figs. 4.1b & 4.2). The northern margin was bounded by the Askrigg Block, a structurally stable area that saw shallow-water carbonates accumulating concurrently with the Bowland Shales. The transition between basin and platform occurred in the Craven Fault Belt, an area bordered by the North and South Craven faults which diverged to the south east forming a structurally complex area over 15 km wide to the north-east of the Bowland Basin (Fig. 4.2). These faults were active during Bowland Shale deposition, strongly controlling thickness variations (see below) and local uplift and erosion in hanging wall sites (Hudson, 1930; Waters et al., 2017b). The transition from active rifting to a thermal sag phase in the early Brigantian did little to affect the northern extent of Bowland Shale which was marked by the line of the North Craven Fault throughout its depositional history.

During the Asbian and early Brigantian fringing reefs (carbonate mudmounds) of the Cracoe Limestone Formation developed along the narrow belt between Mid Craven and North Craven faults (Kirby et al., 2000; Waters et al., 2017a). The subsequent demise of the reefs, perhaps due to uplift and emergence, was followed by onlap of the Bowland Shale. On the Askrigg Block mudmound demise coincides with a change from limestones to the more heterolithic facies of the Yoredale Group, although carbonates continued to dominate deposition until the Pendleian when siltstone and minor sandstones become more prevalent (Arthurton et al., 1988). The lateral transition between the Bowland Shale formations and the Yoredale Group is remarkably abrupt, occurring over a distance of a few hundred metres (Black, 1950) with there being no transition zone (Li et al., 2023). Minor conglomeratic debris flows are suggested to have transported Askrigg Block carbonates into the Bowland Basin (Brandon & Brandon, 1998; Clarke et al., 2019) and Emmings et al. (2020a) consider that most of the mud in the Bowland Basin was sourced from deltas on the Askrigg Block.

The southeast margin of the Bowland Basin was also delineated by a series of faults that are today associated with the Pendle monocline structure (Kirby et al., 2000; Clarke et al., 2019; Pharaoh et al., 2019). To the SE of this structure lay the NE-SW trending Central Lancashire High, an isolated carbonate platform. This was not connected with the Askrigg Block carbonate platform because Bowland Shale deposition occupies the Craven Fault Belt region in the intervening area (Fig. 4.2). The Central Lancashire High is unexposed but borehole evidence indicates that (unlike the Askrigg Block), it foundered during the Pendleian and was onlapped by the Upper Bowland Shales (Kirby et al., 2000). The north-west margin of the Bowland Basin is marked by the Bowland High, which separates it from the Lancaster Fells Basin where Bowland Shales also accumulated (Kirby et al., 2000). Black shale deposition is continuous between these two basins and the Bowland High is best considered as an intrabasinal high; shallow-water conditions did not develop on this margin (Arthurton et al., 1988). Around 5 km to the southeast of the Bowland Line and parallel with it, the Slaidburn Anticline formed another intrabasinal high with a remarkably condensed Bowland Shale record (Fig. 4.2; Earp et al., 1961). These NE-SW trending anticlinal structures were probably generated by contemporaneous, dextral, strike-slip movement of the Craven Fault Belt (Arthurton, 1984; Kirby et al., 2000; Clarke et al., 2019). To the south west, the Bowland Basin broadens and passes into the Irish Sea Basin where the Bowland Shale has sourced the gas fields of the region (Fig. 4.1; Clarke et al., 2019).

4.4 Methods and Approach

Fieldwork investigations (sedimentary logging and sample collection) have been undertaken at 16 locations primarily in the Bowland Basin and Craven Reef Belt but also on the basin margin and Askrigg Block (see supplementary appendix A and D). High-resolution correlation in the Bowland Shale is accomplished using a goniatite fauna that is detailed in a literature that dates back a century, and in the memoirs of the British Geological Survey. This literature has also been used, together with our field measurements, to construct isopach maps and correlation panels for the Bowland Shale and its non-shale members.

Facies analysis was undertaken based on field and petrographic observations. Over 180 samples were thin sectioned and petrographically examined using a polarizing microscope. In addition, 96 selected samples were polished, carbon-coated and analysed on a TESCAN VEGA3 Scanning Electron Microscope (SEM) in backscatter mode to allow the pyrite component of the sediment to be examined. The components of the calcarenite lithologies were quantified by point counting in order to assess evolution on the adjacent carbonate platform source area. The sandstones of the Pendleside Sandstone Member are not studied in detail here, but are more thoroughly described elsewhere (Clarke et al., 2019; Emmings et al., 2020a).

4.5 Results

4.5.1 Regional development of Bowland Shales

The Lower Bowland Shale shows substantial thickness changes ranging from ~50 m to > 300 m within the Bowland Basin and Craven Fault Belt area to the north (Fig. 4.3). The variation is strongly controlled by faulting with an elongate depocentre developed in the hanging wall to the south of the South Craven Fault whilst a more localised depocentre occurs to the south of the Mid Craven Fault (Fig. 4.3). Peak thickness of the Lower Bowland Shale is however developed in the centre of the Bowland Basin (Fig. 4.3). This is principally caused by the development of the Pendleside Sandstone Member (see below). Rapid lateral thickness variations in the mudrocks of the Lower Bowland Shale are also seen at the zonal scale (e.g. the P_{1a} shales and early P_2 shales show rapid lateral thickness change (Fig. 4.4)) suggesting active faulting within the Basin. The thinnest Lower Bowland Shale deposits are adjacent to the Slaidburn Anticline, although they are still stratigraphically complete on this intrabasinal high (e.g. SM section in figure 4 section A). Following the demise of the fringing reef belt in the P_{1a} zone (Waters et al., 2017b), the Lower Bowland Shale onlapped the carbonate mudmounds of the Craven reef belt as seen in the FL section, where black shales are interbedded with carbonate boulder beds and coarse crinoidal calcarenites (Fig. 4.5).

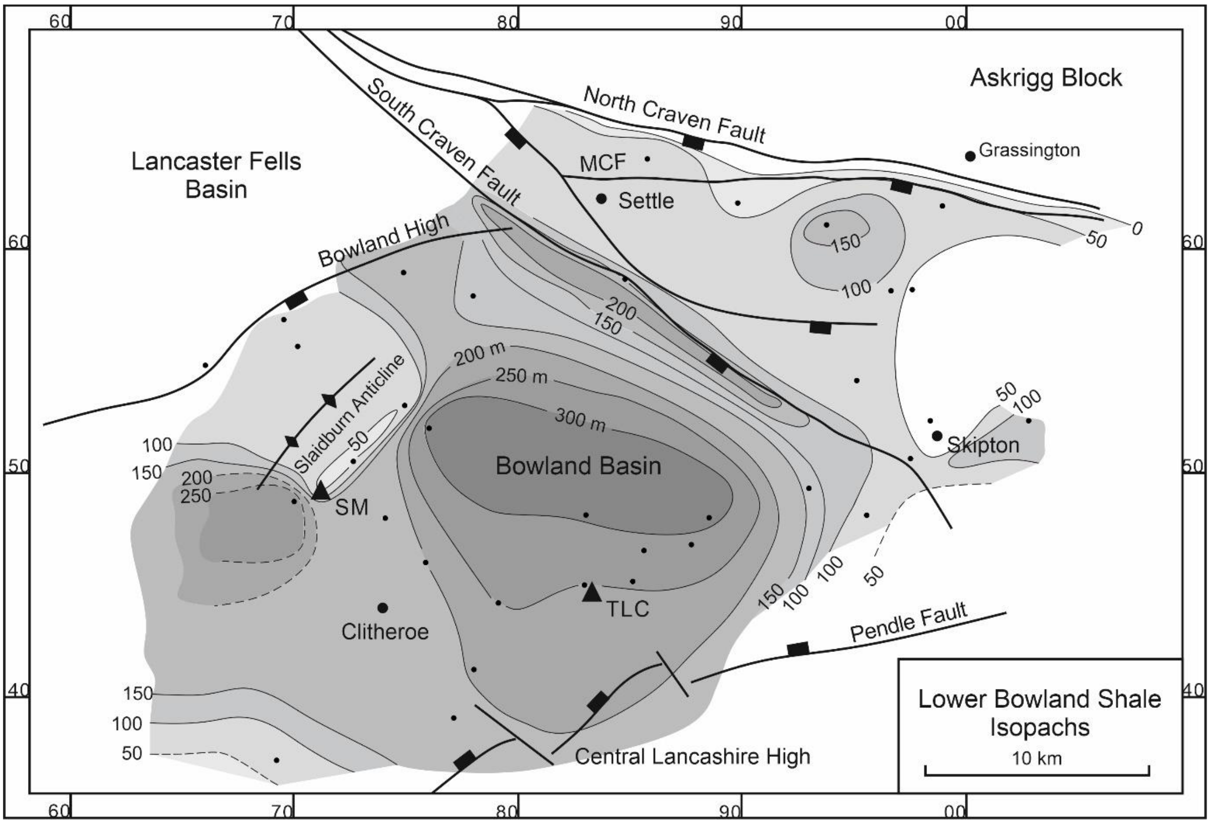

Fig. 4.3 Isopach map of the Lower Bowland Shale Formation showing the influence of structural features (Craven faults and the Slaidburn Anticline) on sediment thickness. Dots represent locations of thickness data, primarily derived from the records of Geological Survey memoirs.

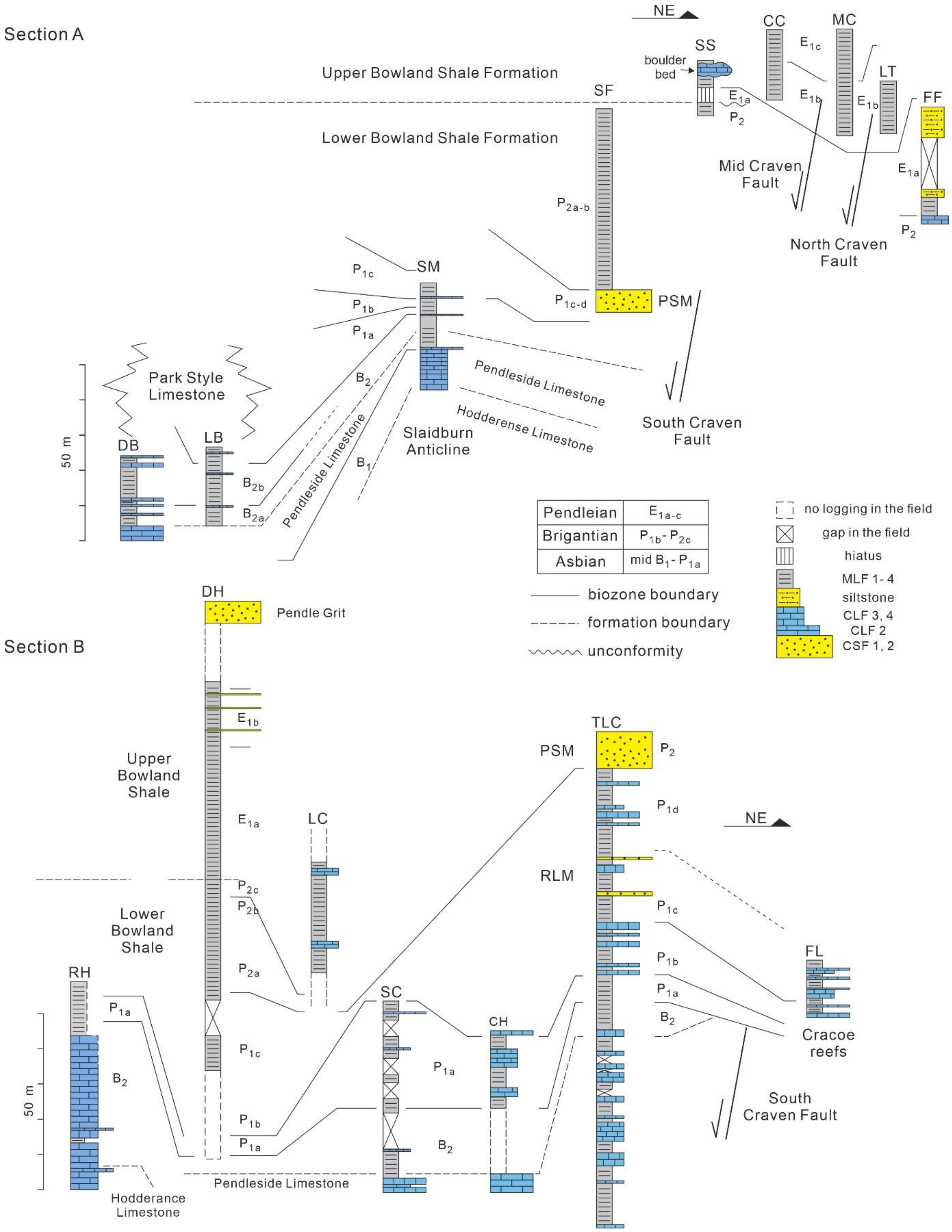

Fig. 4.4 Correlation panels for Bowland Shale sections along two NE-SW transects from the margins to the centre of the Bowland Basin (see Fig. 4.2 and appendix A for outcrop details). RSM Ravensholme Limestone Member; PSM Pendleside Sandstone Member; MLF mudstone lithofacies; CLF carbonate lithofacies; CSF clastic sandstone lithofacies (see lithofacies section in main text).

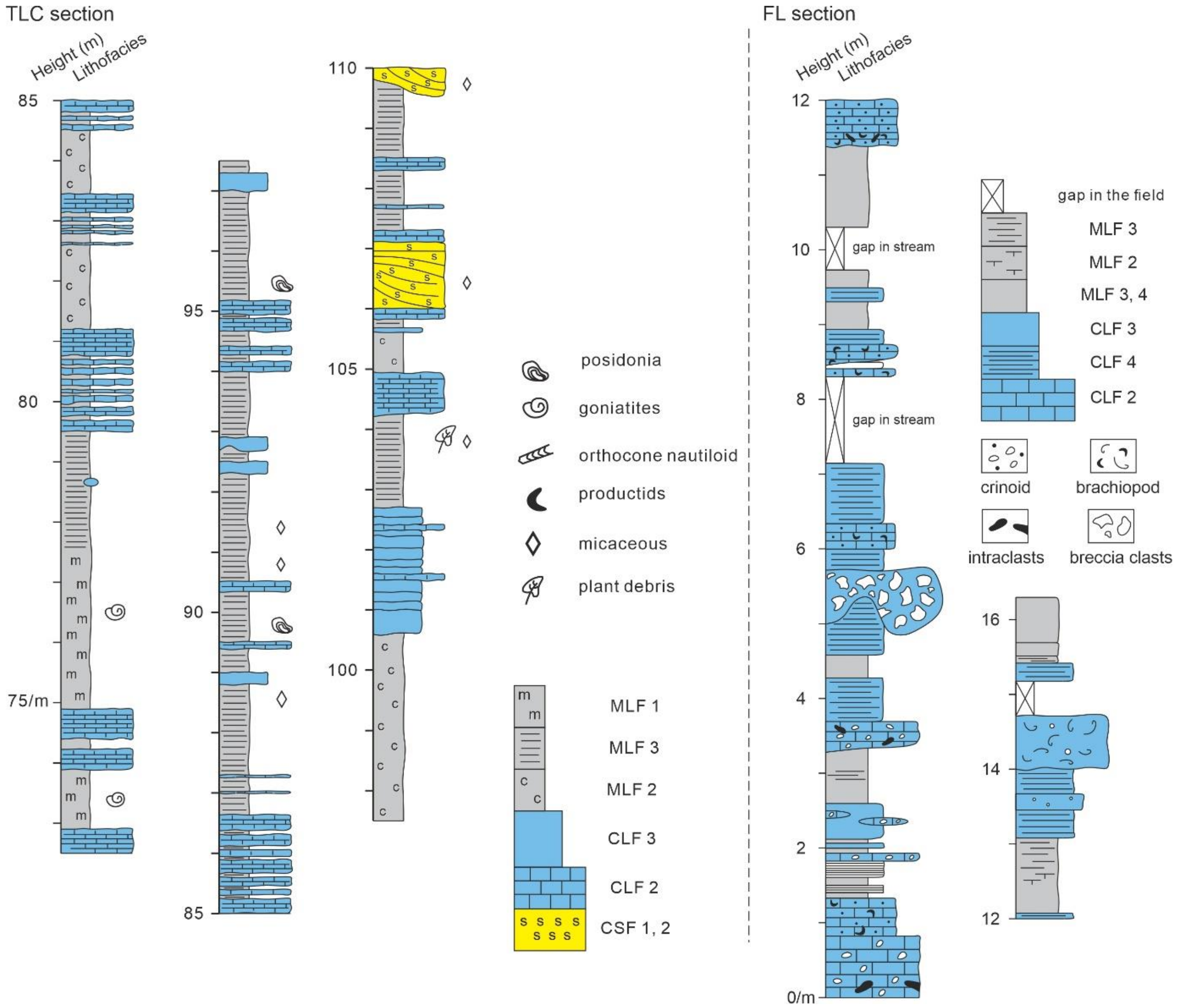

Fig. 4.5 (a) Sedimentary log of the Lower Bowland Shale at Tory Log Clough (TLC), showing numerous limestone interbeds of the Ravensholme Limestone Member. The strata below 73 m height (not shown) belongs to the underlying Pendleside Limestone Formation; topmost bed at 110 m height marks the erosive-base base of the Pendleside Sandstone. (b) Sedimentary log of the basal Lower Bowland Shale developed at Fell Lane section showing interbeds of allochthonous limestones.

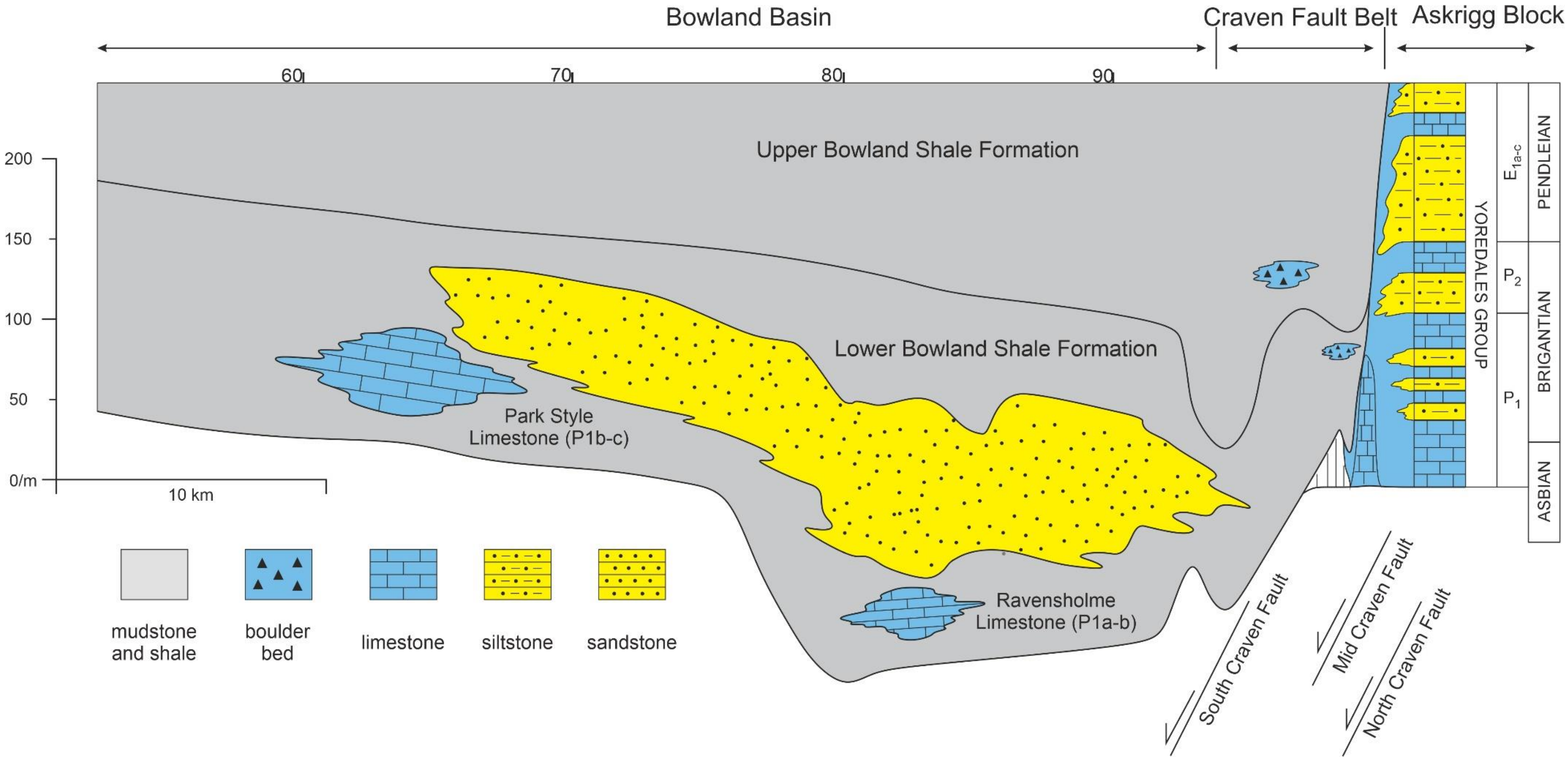

Fig. 4.6 Cross section from the southern margin of the Askrigg Block to the southern-most outcrops of the Bowland Basin, showing the thick development of the Pendleside Sandstone in the Lower Bowland Shale, and levels of main limestone units and the laterally equivalent lithologies of the Yoredale Group. See figure 4.2 for line of section. MLF for Mudstone Lithofacies, CLF is carbonate lithofacies and CSF is clastic sandstone lithofacies (see section of lithofacies in main text).

The Lower Bowland Shale Formation contains the Pendleside Sandstone Member, a substantial turbidite sandstone body (cf. Clarke et al., 2019) developed in the middle of the Formation around the P_1 – P_2 boundary (Fig. 4.6). Several shale breaks occur within the Pendleside Sandstone (recorded by Earp et al. (1961) and Clarke et al. (2019)), and it is possible that more detailed investigation could resolve this unit into individual, stacked sandbodies. The Pendleside Sandstone isopachs show peak thickness (> 200 m) in the centre of the Bowland Basin and an abrupt termination of its western development against the Slaidburn Anticline structure (Fig. 4.7), where it thins from 200 m to 0 m in a distance of only ca. 2 km (Earp et al., 1961, p.81). This indicates that the Slaidburn Anticline was a topographic barrier to turbidite progradation, whilst the expansion of the Pendleside Sandstone's area to the south and (to a lesser extent) to the north of this structure indicates the high was only ~ 10 km in length. This allowed the sands to continue prograding around the margins (Fig. 4.7). The western-most outcrops of the Pendleside Sandstone extend across the Bowland High suggesting the relief of this feature (and its ability to stop the progress of turbidity currents) was substantially less than that of the Slaidburn Anticline.

To the northeast of its development, the area of Pendleside Sandstone rapidly contracts but a narrow outcrop of contemporaneous sandstone occurs to the east of Skipton (Fig. 4.7). This sandstone body is ~50 m thick and has been locally named the Nettleber Sandstone (Hudson & Mitchell, 1937). It probably passes eastwards into the Harlow Hill Sandstone which occurs within the Lower Bowland Shale of the adjacent Harrogate Basin (Fig. 4.1). A core in this Basin showed 49 m of Harlow Hill Sandstone developed below black shales with P_{2a} goniatites (Cooper & Burgess, 1993).

The Lower Bowland Shale also contains frequent beds of limestone, either as isolated, decimetric to metre-scale tabular sheets but also as more substantial, mappable

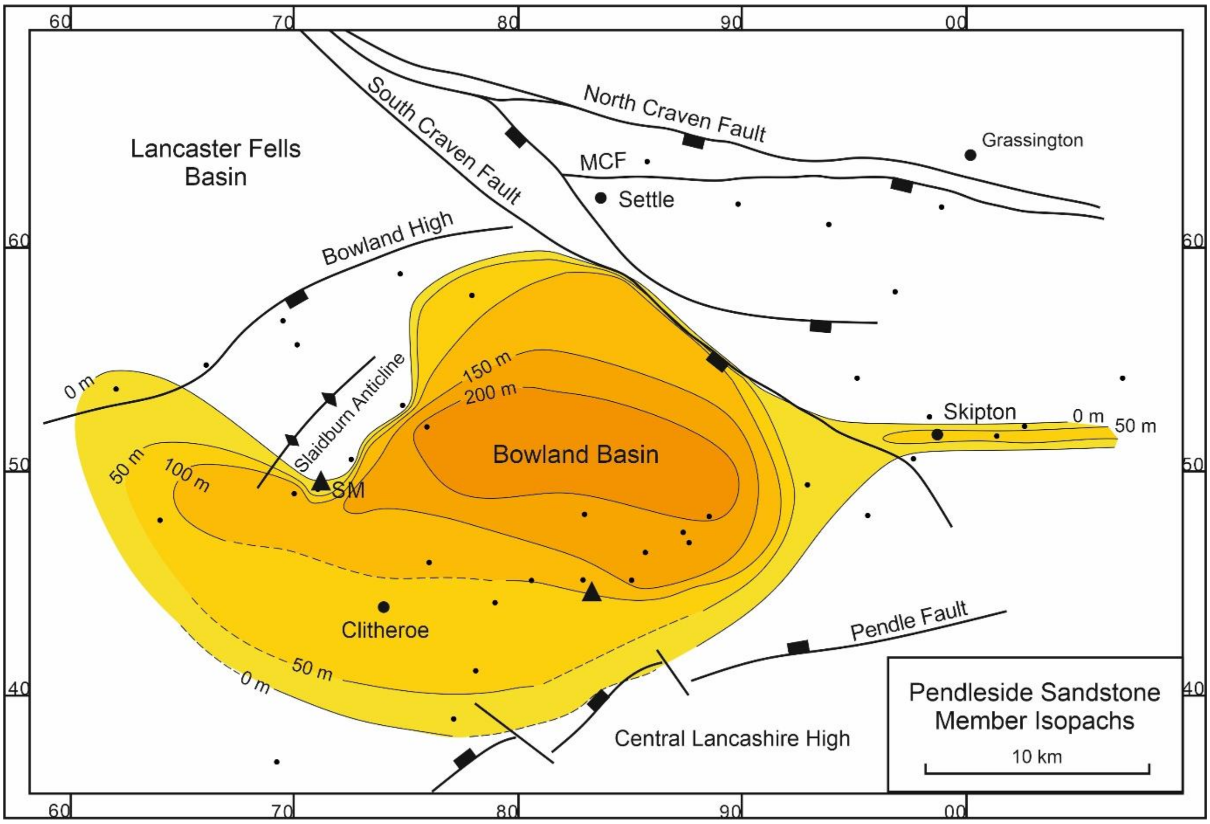

Fig. 4.7 Thickness variations in Pendleside Sandstone in the Bowland Basin. Isopachs are dashed where data density is low.

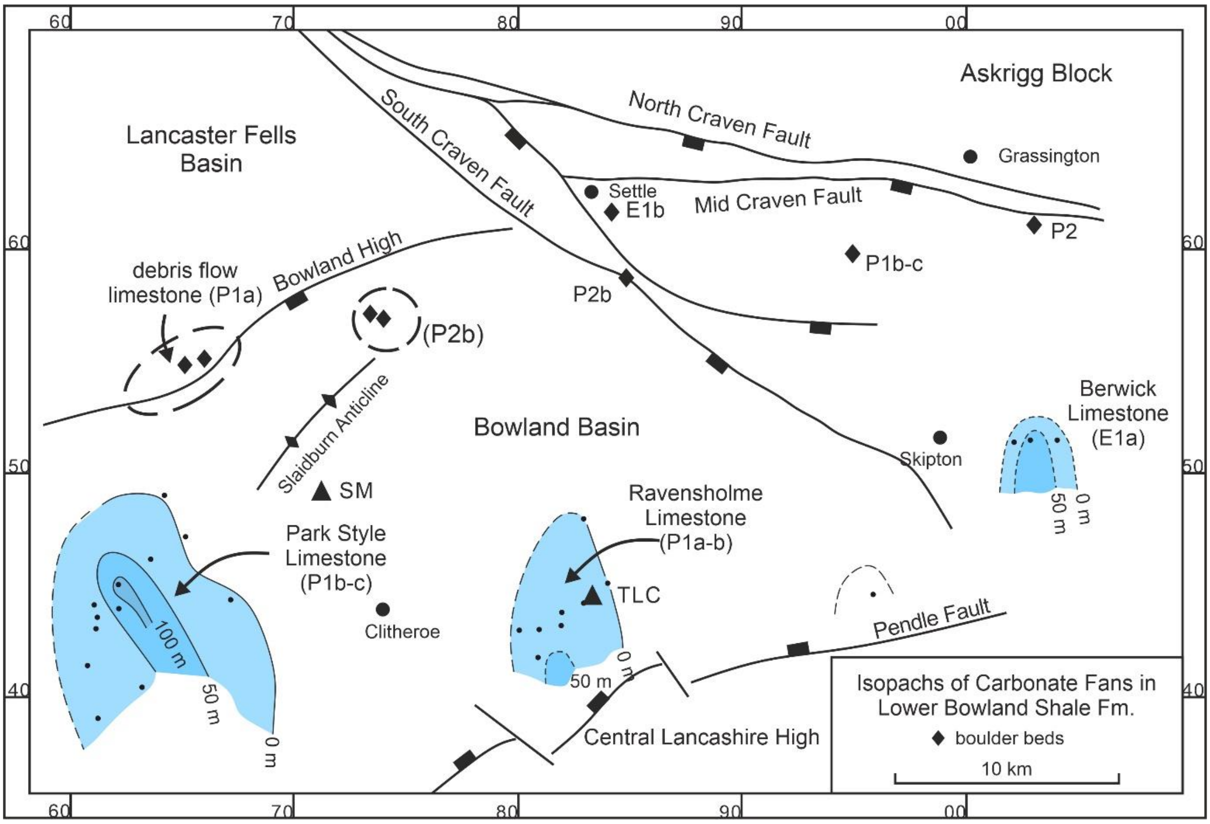

Fig. 4.8 Isopachs for carbonate bodies developed in the Bowland Shales and location of localised, limestone boulder beds.

limestone-dominated intervals (Fig. 4.8). These latter strata have been named the Park Style Limestone Member and the Ravensholme Limestone Member. Isopach maps show that the limestone bodies are of much more restricted extent than the Pendleside Sandstone. Based on their outcrop distribution both have a broadly north-south alignment and have widths (of ca. 5 km) which were probably considerably less than their length, giving them a linear outline (Fig. 4.8). Their occurrence, restricted to the southern part of the Bowland Basin strongly suggests that they were sourced from the carbonate platform on the Central Lancashire High to the south east and not the northern Askrigg Block as previously suggested (e.g. Clarke et al., 2019). At outcrop the limestone lithologies consist of both calcarenite and calcisiltite lithologies described below. Both the Park Style and Ravensholme limestones consist of amalgamated beds of carbonate in their thickest, axial development, but they pass into interbedded mudrock and limestone off axis (e.g. TLC section, Fig. 4.4). Geochemical analysis of the shales interbedded with the carbonates indicates weak anoxia during deposition (Li et al., 2023). This contrasts with the euxinic signature from contemporaneous basinal shales, a finding that suggests the limestones likely formed carbonate fans that were somewhat elevated above the more reducing, deepest waters of the basin.

Thickness trends of the Upper Bowland Shale show more subdued variations especially within the Bowland Basin, with the Slaidburn Anticline no longer affecting deposition (Fig. 4.9). This may be partly because there are no major sandstone or limestone units within the Formation (Figs. 4.6 & 4.9). However, the Hind Sandstone, a thin, turbidite sandstone body in the Lancaster Fells Basin to the NW, may have just reached the margins of the Bowland Basin but its distribution and lateral extent is rather limited, leaving an unknown orientation (Aitkenhead et al., 1992). To the east of Skipton limited outcrops of a crinoidal limestone indicate the presence of a carbonate fan of comparable thickness (~50 m thick) to those in the Lower Bowland Shale (Fig. 4.8). This is the E_{1a} age Berwick Limestone (Hudson & Mitchell, 1937), and its rapid pinching out, to both the east and west suggests the outcrop is a cross section of a north-south orientated fan like those seen in the Lower Bowland Shale.

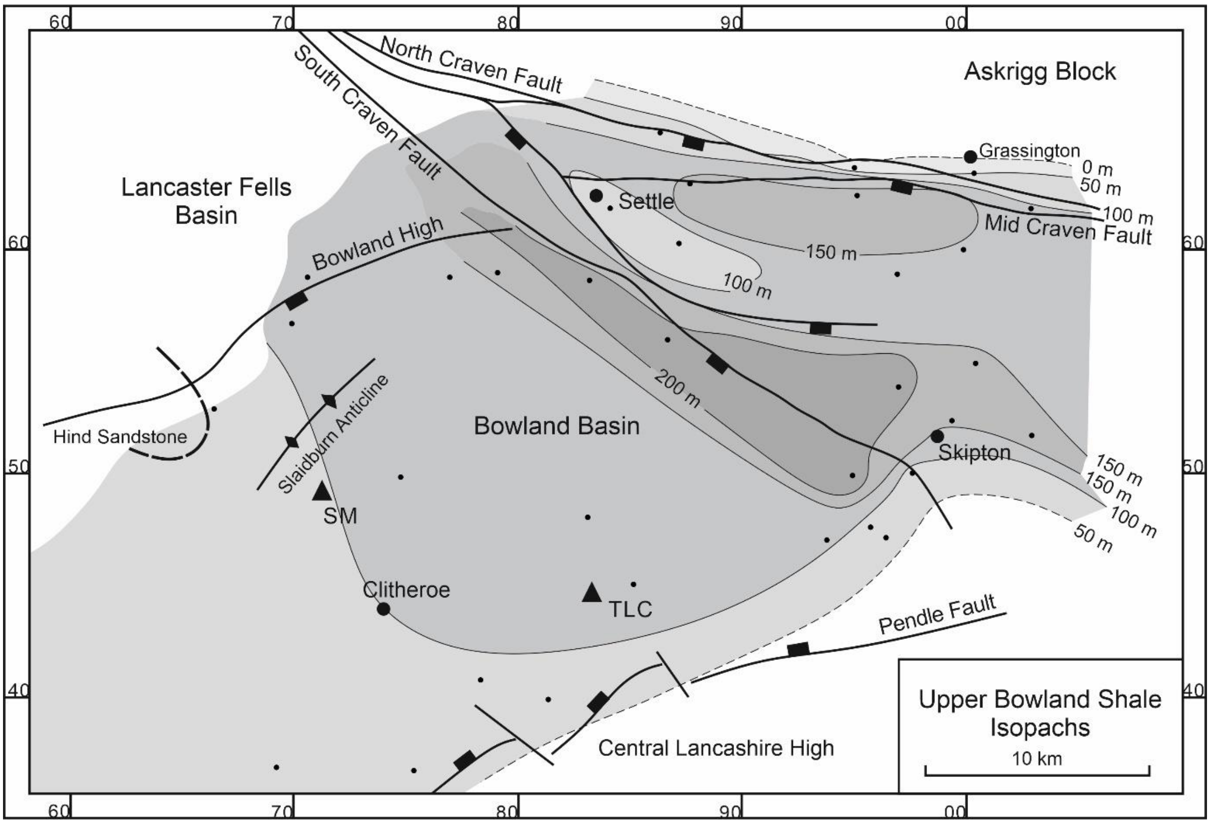

Fig. 4.9 Isopach map of the Upper Bowland Shale Formation in the Bowland Basin and Craven Fault Belt area showing principal depocentres adjacent to bounding faults.

Peak thicknesses of the Upper Bowland Shale occur in hanging wall settings adjacent to the South and Mid Craven faults (Figs. 4.6 & 4.9) indicating tectonic-controlled depocentres. The transition between the Lower and Upper Bowland Shale saw reactivation and uplift of the South Craven Fault resulting in a locally unconformable contact between the two formations (Dixon & Hudson, 1931; Arthurton et al., 1988). Thus, at the SS location P_2 shales are truncated and onlapped by E_{1b} shales (Fig. 4.4). Higher in this section irregular bodies composed of angular limestone boulders (up to 3 m in dimension) occur within the shale. These are sourced from Brigantian limestones immediately to the north (Hudson, 1930; Dixon & Hudson, 1931). Carbonate boulder beds, typically only a metre or so thick, also occur locally in the Bowland Basin (Fig. 4.8), and have been suggested to be debris flow deposits sourced from the Askrigg Block (Aitkenhead et al., 1992).

In its northern-most development, the Upper Bowland Shale passes over a short distance into the more heterolithic strata of the Yoredale Group (Fig. 4.6). No outcrop displays the transition, but field mapping around Grassington shows that it occurs over a distance of only ~200 m (Black, 1950). This boundary closely approximates with the line of the North Craven Fault although the most northerly Bowland Shale outcrops occur to the north of this structure. It is unlikely that a steep palaeoslope, between deep-water black shales and shallow-water heterolithics, occurred in the 200 m-wide transition zone (no evidence of slope failure is seen) suggesting that the basin margin black shales were deposited in a similar water depth to the Yoredale strata which are generally regarded as shallow-marine facies.

4.5.2 Carbonate Lithofacies (CLF)

CLF 1: Coarse calcirudites

Coarse calcirudites show scattered distribution close to the northern boundary faults (SS and FL locations, figures 4.4 & 4.5). They have limited lateral extent and at SS they form an irregular breccia 10 m thick and 15 m wide embedded in shales. The breccia is clast supported and clasts can be at high angles to the horizontal. The limestone boulders range from centimetre up to metre-sized and have been sourced from nearby, in situ carbonates at the margin of the Askrigg Black (Hudson, 1930; Dixon & Hudson, 1931). At FL, developments of CLF 1 occur in erosive-based beds with large, flat pebbles of reworked Bowland Shale, a few centimetres thick and up to 50 cm in width, developed in their upper part (Fig. 4.10a). The matrix of this facies is diverse, and includes micritic mudstone and skeletal components (including large crinoidal columnals) and patches of coarse, sparry cement (Fig. 4.11a, b).

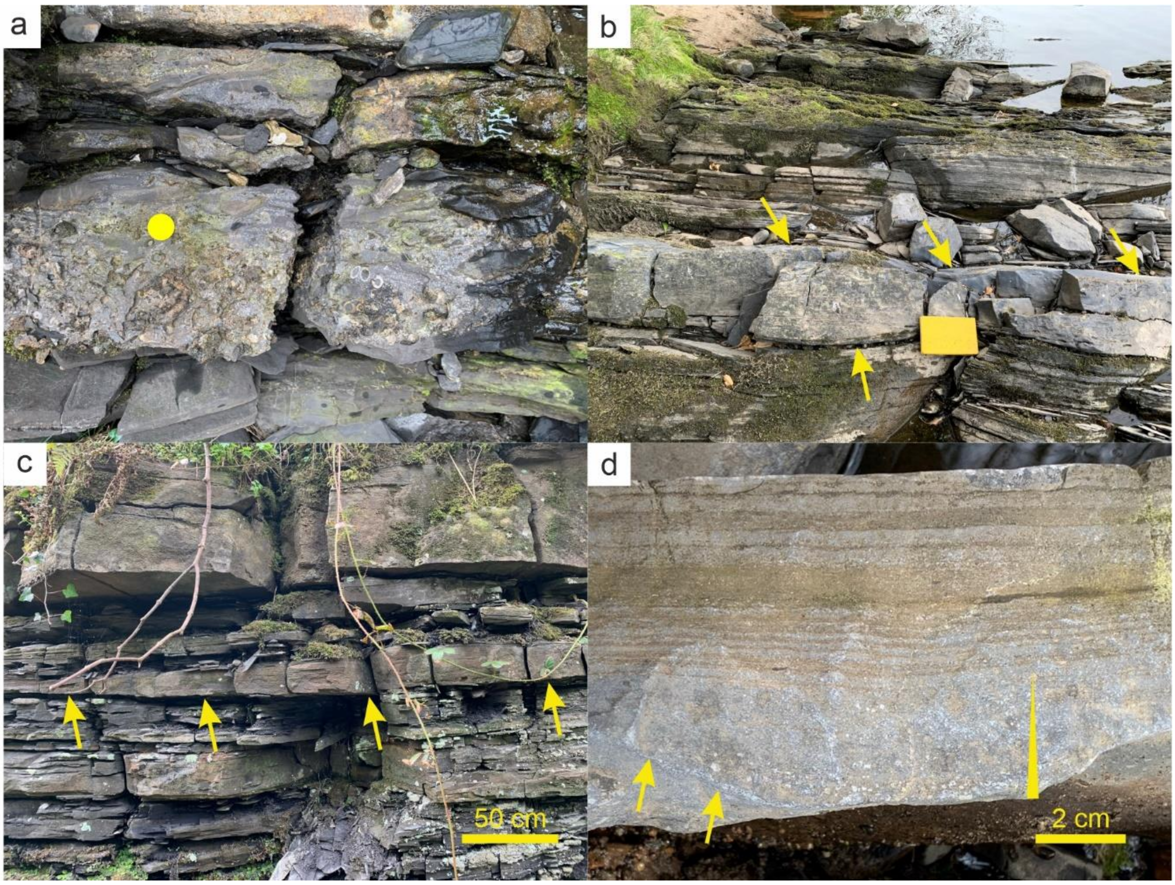

Fig. 4.10 Field photographs of carbonate beds in the Bowland Shale. (a) coarse calcirudite bed (CLF 1), dominantly composed of crinoid columnals, P_{1b} zone, Fell Lane section. (b) limestone bed (CLF 4) displaying hummocky topography, E_{1b} zone, Dinckley Hall section. Yellow notebook is 20 cm in length. (c) CLF 2 bed displaying broad hummock (yellow arrows denote base), whilst topmost bed is graded, and nearly 1 m thick, B_{2b} zone, Dobson's Brook section. (d) Loose block of CLF 2 bed showing massive, graded lower part (Ta division) grading upwards into laminated strata (Tb division), B_{2b} zone, Dobson's Brook section.

CLF 2 Calcarenite (peloid-foram-crinoid pack-grainstone)

Packstone and grainstone beds are a common component of the limestone bodies throughout the Lower Bowland Shale (Fig. 4.5). Beds are sharp based, sometimes with groove marks, and have a thickness which is typically 10 – 30 cm. Internally they can be massive to

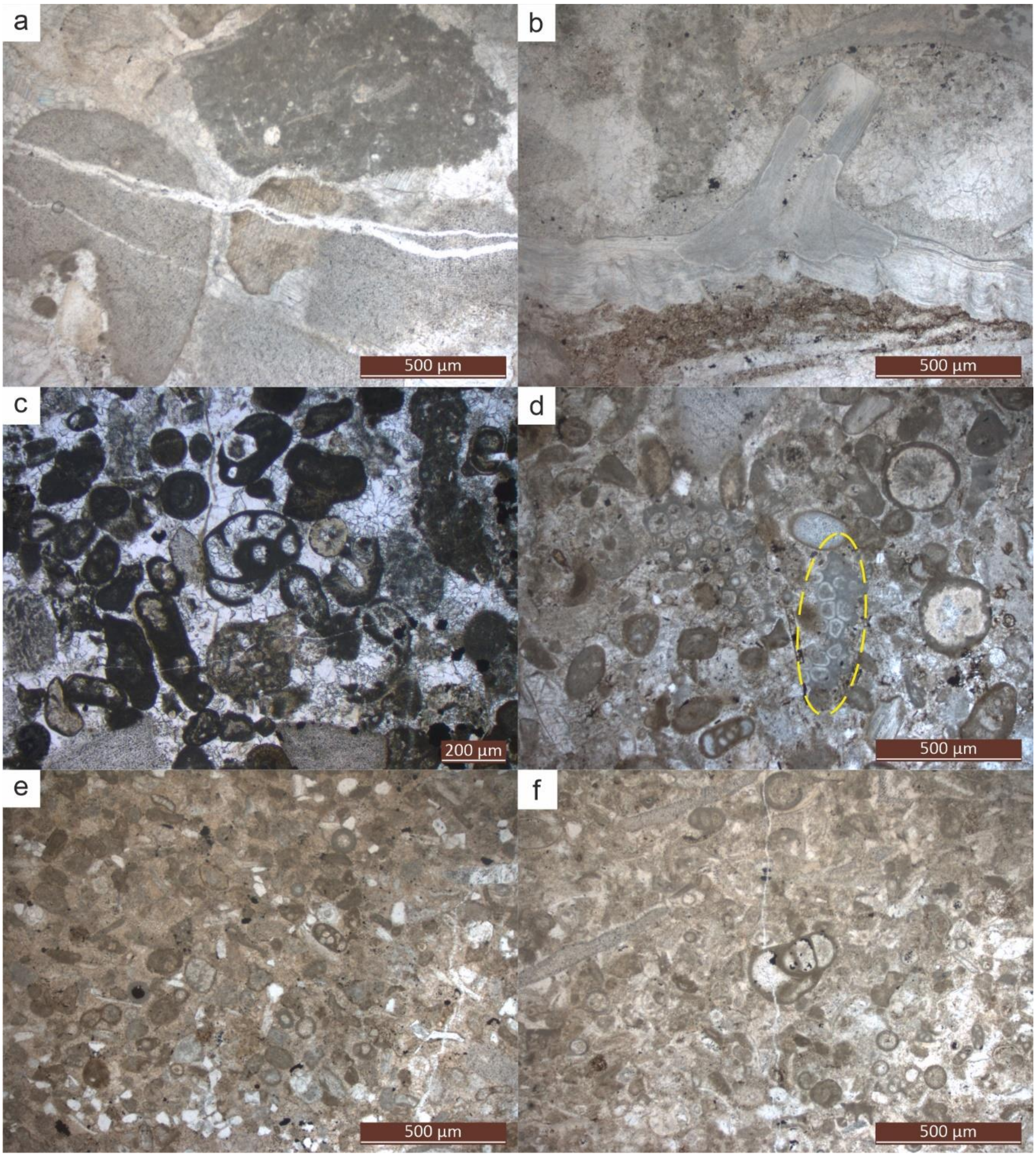

Fig. 4.11 Thin section photographs of limestone facies from the Bowland Shale. (a) CLF 1 coarse calcirudite with crinoid bioclasts and wackestone intraclast, P_{1b} zone, Fell Lane section. (b) CLF 1 coarse calcirudite with large brachiopod shell with broken spine attached. The matrix shows a mix of micrite and sparry patches, P_{1b} zone, Fell Lane section. (c) CLF 2 coarse calcarenite/grainstone composed dominated by peloids, with foram and crinoid bioclasts, basal P_{1a} zone, Tory Log Clough section. (d) CLF 2 coarse calcarenite composed of peloids, crinoid columnals (showing micrite envelopes), calcareous algae (Koninckopora, outlined) and forams. B_{2a} zone, basal Lower Bowland Shales, Dobson's Brook. (e) CLF 2 calcarenite dominated by peloids, intraclasts with micrite envelopes and rarer quartz grains, B_2 zone, basal-most Lower Bowland Shale, Swardean Clough. (f) CLF 2 fine calcarenite/ pack-grainstone with peloids, coated grains, forams and possible micritised brachiopod shells, B_2 zone topmost bed of the Pendleside Limestone, immediately below base of LBS, Swardean Clough.

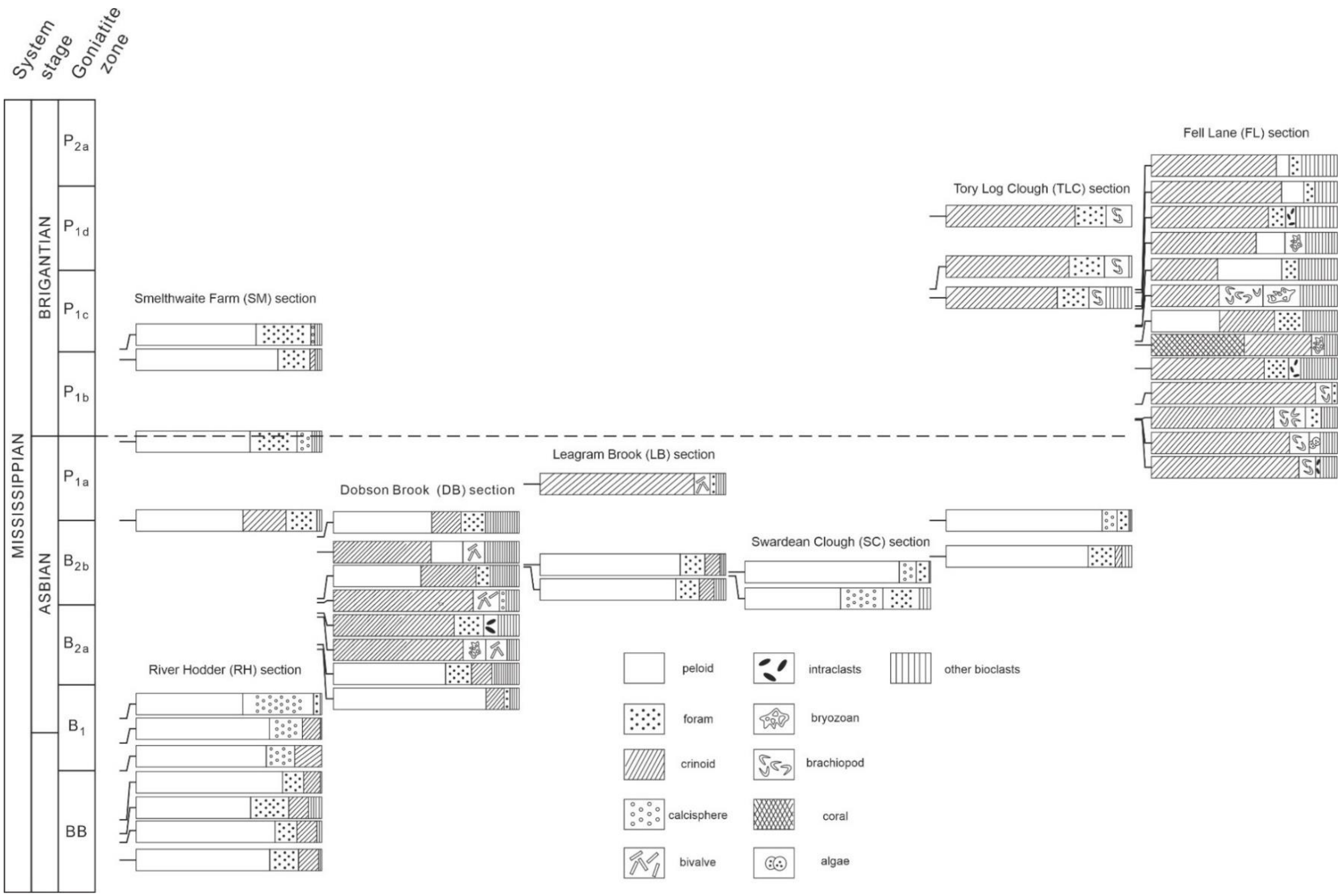
System
stage
Goniatite zone
MISSISSIPPIAN
BRIGANTIAN
ASBIAN
P_{2a}
P_{1d}
P_{1c}
P_{1b}
P_{1a}
B_{2b}
B_{2a}
B_1
BB
Smelthwaite Farm (SM) section
River Hodder (RH) section
Dobson Brook (DB) section
Leagram Brook (LB) section
Swardean Clough (SC) section
Tory Log Clough (TLC) section
Fell Lane (FL) section
peloid
foram
crinoid
calcisphere
bivalve
intraclasts
bryozoan
brachiopod
coral
algae
other bioclasts

Fig. 4.12 Evolving composition of allochthonous carbonates (CLF 2) found within the Asbian- Brigantian in the Bowland Basin. River Hodder data are from the Pendleside Limestone, all other data from the Lower Bowland Shale. The three most abundant clast types are displayed whilst others are included as 'other bioclasts'.

weakly graded, planar laminated or show internal scours and hummocky lamination (Fig. 4.10 b-d). The last structures are typically a few centimetres in height and a metre across, but the larger examples reach 20 cm thickness and 2 m in width (Fig. 4.10c). At the condensed SM location (Fig. 4.4, section A), CLF 2 grainstones infill broad, erosive hollows ranging from 5 – 30 cm deep and up to 2 m wide.

The CLF 2 beds are well sorted with an average grain size of 0.4 mm although in some beds they can be coarser (Fig. 4.11c-f). In some horizons the peloids deviate from a normally well-rounded appearance and can be somewhat angular, which may indicate that they are tiny intraclasts or bioclasts rather than peloids sensu stricto. Peloids (sensu lato) and foraminifera are the major components of CLF 2 but there is also a diversity of bioclastsincluding brachiopods, calcispheres, crinoids and bryozoans. Well-developed micritic coatings are common, especially on crinoid grains (Fig. 4.11d).

The clast content of CLF 2 beds varies throughout the history of the Bowland Basin. The ramp carbonates of the preceding Pendleside Limestone Formation are primarily composed of peloids and microspheres but there is a transition to crinoid-dominated grainstones in the Bowland Shale (Fig. 4.12). Greater diversity is seen at the FL section, developed immediately adjacent to a carbonate mudmound (~1 km distant) which was shedding fragments of corals and bryozoans as well as crinoids, during Lower Bowland Shale deposition. The Berwick Limestone in the Upper Bowland Shale was not sampled during this study, but Hudson and Mitchell (1937) report it to be composed of crinoid detritus like other Bowland Shale carbonates. The exception to this crinoid-dominated detritus are the thin CLF

2 beds, developed on the condensed intrabasinal high at SM, where peloids and small foraminifera are the main constituents (Fig. 4.11).

CLF 3 Calcisiltites

Beds of calcisiltite are common in the Lower Bowland Shale where they occur as sharp-based, tabular beds a few centimetres thick and occasionally as decimetre-thick beds displaying swaley cross lamination (e.g. in the lowermost Park Style Limestone outcrop at DB, Fig. 4.4 section A). Grains are well sorted, but can vary in size between beds in the range 0.02 mm – 0.05 mm (Fig. 4.13a, b). Occasionally coarser beds occur (e.g. in the latest Brigantian at SC, Fig. 4.4 section B) where the grain size reaches ~0.1 mm indicating a gradation into CLF 2. Sponge spicules and small calcispheres are present but most grains are typically angular and of indeterminate origin, possibly finely comminuted shell material?

CLF 4 Laminated microspar

Limestone beds displaying swaley cross-stratification and isolated hummocks, 10-15 cm thick, are seen in Upper Bowland Shale at DH (Fig. 4.4 section B and Fig. 4.10b). In thin section the facies show fine lamination with wavy bedding consisting of alternations of micrite and fine microspar (Fig. 4.13c). Based on the similarity of their sedimentary structures, it is possible that the DH beds were originally CLF 2 beds that have undergone both recrystallisation and micritization, but curiously no bioclasts remain. Laminated microspar is also seen in the Lower Bowland Shale at the SM and FL locations where the fabric is dominated by laths of calcite 0.2 mm by 0.05 mm in dimension, with their long axis developed orthogonal to bedding, that sometimes show a slightly radiating or fan-like arrangement (Fig. 4.13d). Vestiges of clay lamination occur between the crystalline layers.

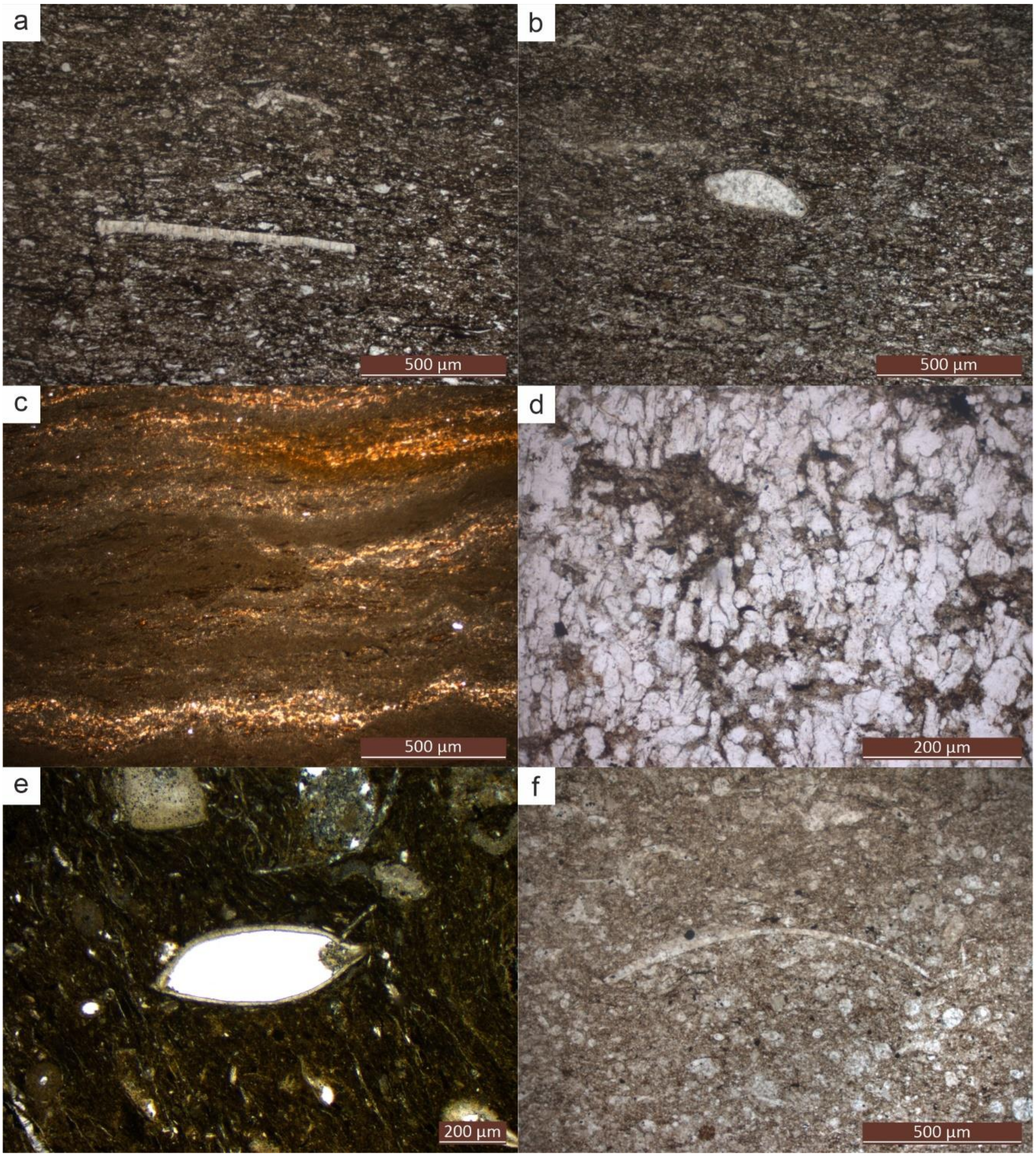

Fig. 4.13 Thin section photographs of limestone facies from the Bowland Shale. (a) CLF 3, calcisiltite with a fragment of bivalve shell showing prismatic structure, P_{1b} zone, Fell Lane (b) CLF 3 calcisiltite with spar-filled ostracod, P_{1b} zone, Fell Lane, (c) CLF 4 micritic limestone displaying wavy lamination partially recrystallised to microspar, uppermost E_{1a} zone, Dinckley Hall. (d) CLF 4 Microspar consisting of laths/stumpy prisms orientated vertically and showing a weak radial or fan-like arrangement, basal P_{1c} zone, Smelthwaite Farm (e) CLF 5, ostracod and crinoids in wackestone, basal P1a zone, Smelthwaite Farm. (f) CLF 3 bioclastic wackestone bearing calcispheres and a thin-shelled bivalve, B_{2b} zone, Dobson's Brook.

CLF 5 Bioclastic wackestone-mudstone

This is rare facies in the Lower Bowland Shales, although it is more common in the underlying Pendleside Limestone. It is composed of dark micrite that sometimes shows aggrading neomorphism to fine microspar, together with bioclasts including small crinoid columnals, sponge spicules and ostracods (Fig.4.13e). In some examples, the bioclasts are predominantly calcispheres and small, thin-shelled bivalves (Fig. 4.13f). CLF 5 beds are homogenous, with bioclasts scattered throughout, and range in thickness from 20 – 50 cm.

4.5.3 Clastic Sandstones Lithofacies (CSF)

CSF 1 Fine to coarse grained sandstone

Tabular beds of sandstone ranging from a few centimetres up to one metre thick are developed in the middle of the Lower Bowland Shale where they form the Pendleside Sandstone Member (see above). At the TLC section stacked beds of CSF 1, belonging to this Member occur at the base of the P_2 zones, but isolated sandstone beds of CSF 1 (and CSF 2 – see below) also occur up to 16 m below the base of this level in the P_{1d} zone (Fig. 4.5). Here the thickest bed reaches 1.5 m and shows an internal erosion surface overlain by CSF 1 sandstone with low angle cross beds. Thin sandstone beds are also seen in the Upper Bowland Shales, appearing ~20 m below the base of the coarse sandstones of the Pendle Grit Formation (Fig. 4.4), where they can show frondescent marks on their base.

The CSF 1 sandstones are mainly composed of grains of quartz, polycrystalline quartz and feldspar that show considerable variation in their degree of rounding and sorting (Fig. 4.14a and d). The Pendleside Sandstone beds at TLC show considerable inter-grain suturing and good sorting (grain size is around 0.1 – 0.2 mm; Fig. 4.14a). In contrast, the sub-Pendle Grit sandstones at DH are poorly sorted (grain size varies from 0.1 – 2.0 mm) with the largest grains being well rounded, whilst the angularity increases with decreasing grain size (Fig. 4.14d).

CSF 2 Fine-grained sandstone with bioclasts

This heterolithic lithofacies consists of decimetric beds that co-occur with CSF 1 beds below the Pendleside Sandstone at TLC in the P_{1d} zone. The clastic content is the same as for CSF 1 but with the addition of bioclasts that constitute about 25% of the grains. These include crinoid columnals, foraminifers, and abraded fragments of brachiopods and bryozoans (Fig. 4.14b and c). The grain size variation is comparable to those in the interbedded CSF 1 beds with an average of 0.2 mm for both sandy grains and bioclasts.

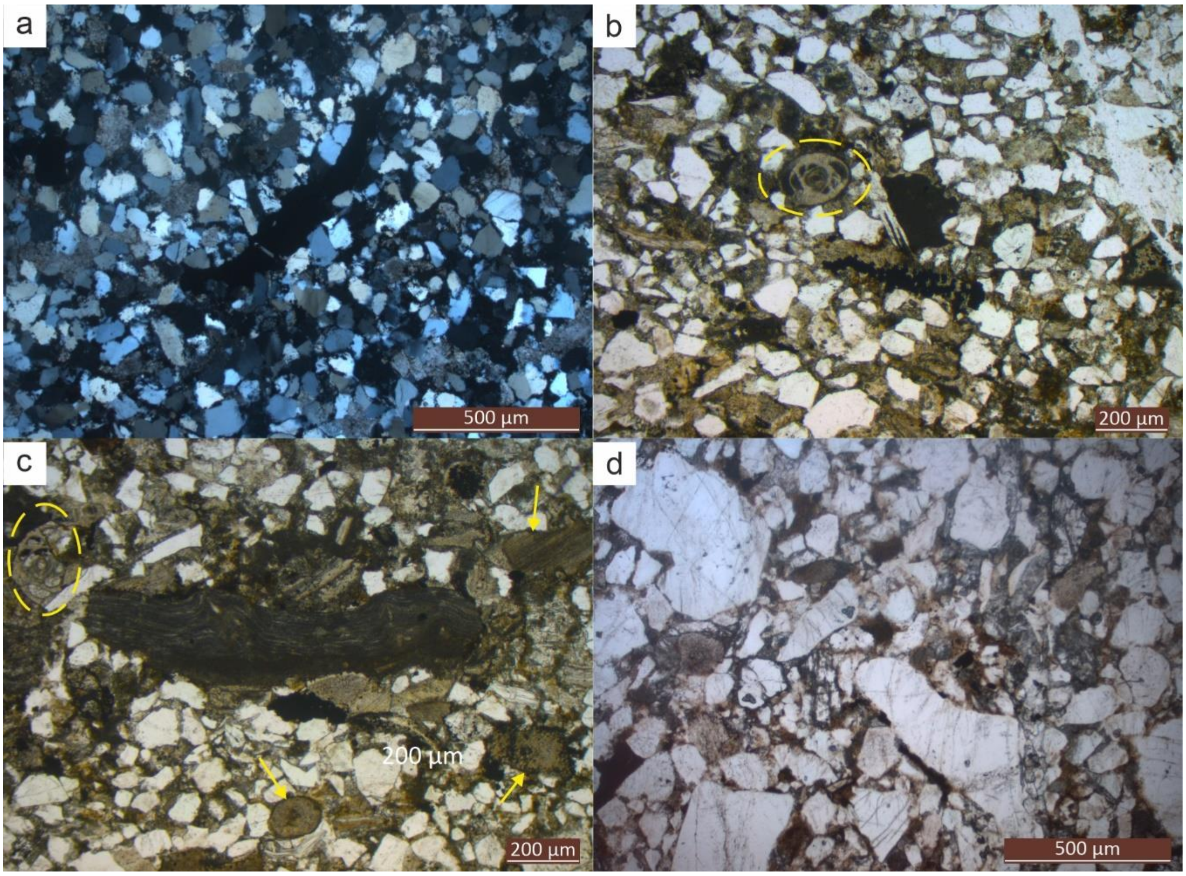

Fig. 4.14 Thin section photographs of clastic sandstone lithofacies from the Bowland Shale. (a) CSF 1 well sorted, fine sandstone seen in cross-polars, P_{1d} zone, Tory Log Clough. (b) CSF 2, bioclast-rich sandstone with forams (yellow circle, Archaediscus), basal P_{1d} zone, Tory Log Clough. (c) CSF 2, bioclast-rich sandstone containing brachiopod fragments (central), crinoid fragments (yellow arrows) and a foram (yellow circle, Archaediscus), basal P_{1d} zone, Tory Log Clough. (d) CSF 1 medium-fine grained sandstone with poor sorting, lower E_{1b} zone, Dinckley Hall.

4.5.4 Mudrock Lithofacies

MLF 1 Homogenous mudstone

Homogenous mudstones, often with wispy bioturbation structures, are common in the uppermost Pendleside Limestone and the Lower Bowland Shale where it is restricted to beds of Asbian age (Fig. 4.15). MLF 1 beds are typically a few tens of centimetres thick. Other than their clay and minor carbonate content, they contain a low density of organic filaments, pyrite and rare, silt-size calcareous and quartz grains. Fossils, including thin-shelled brachiopods, occur rarely (Fig. 4.16f).

MLF 2 Calcareous, silty mudstone

Calcareous, silty mudstone beds are common in the Lower Bowland Shale up to the mid-Brigantian, with the proportion of silt grade material varying considerably (Fig. 4.15). At outcrop the facies can be blocky or weakly fissile. Beds range from decimetres to metres in thickness and are usually massive but can show diffuse lamination defined by alternations of calcareous-rich and clay-rich laminae. The clay grade material is dispersed throughout the MLF 2 or it can occur as lenses similar to those in MLF 4 described below. The non-clay component is dominated by angular carbonate grains with a range of shapes, averaging 0.04 mm in size but with considerable variation (Fig. 4.16 a, b, e), that are distributed throughout the fabric. These are too small to attribute to bioclast types but they may be the highly fragmented detritus of the larger, identifiable bioclasts that are occasionally present. These include crinoid columnals (ranging up to 2 mm in diameter, but typically <0.5 mm), thin-shelled bivalves and calcispheres. Pyrite framboids and quartz silt grains are also present with the latter occasionally reaching up to 10 % abundance.

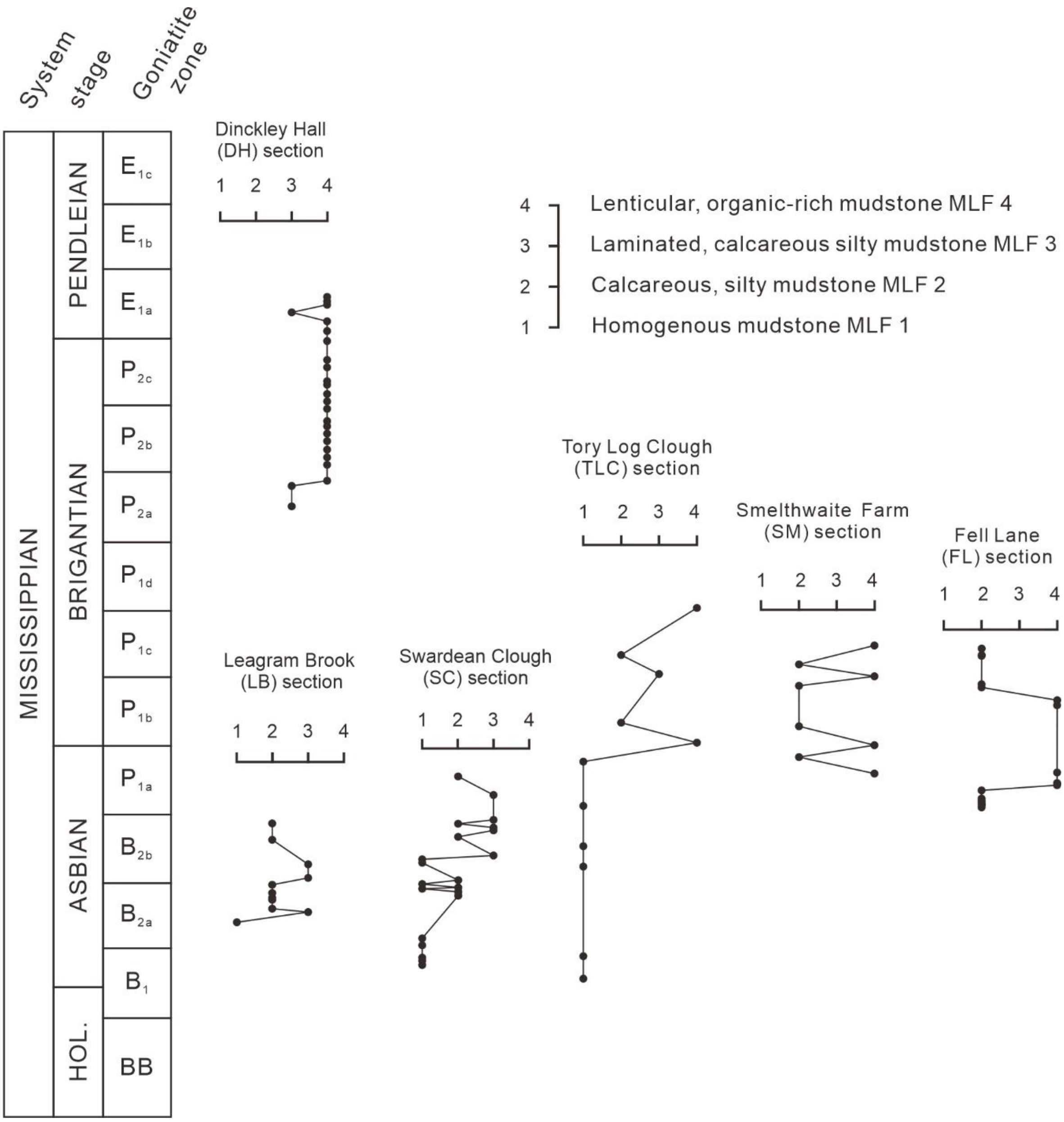

Fig. 4.15 Stratigraphic variation of mudrock facies in selected Bowland Shale outcrops showing increasing importance of MLF 4 in younger strata. HOL - Holkerian.

MLF 3 Laminated, calcareous, silty mudstone

The MLF 3 facies occurs sporadically throughout the Bowland Shale, and is a hard, platy shale at outcrop. It is most common in the sections from the SW of the Bowland Basin which

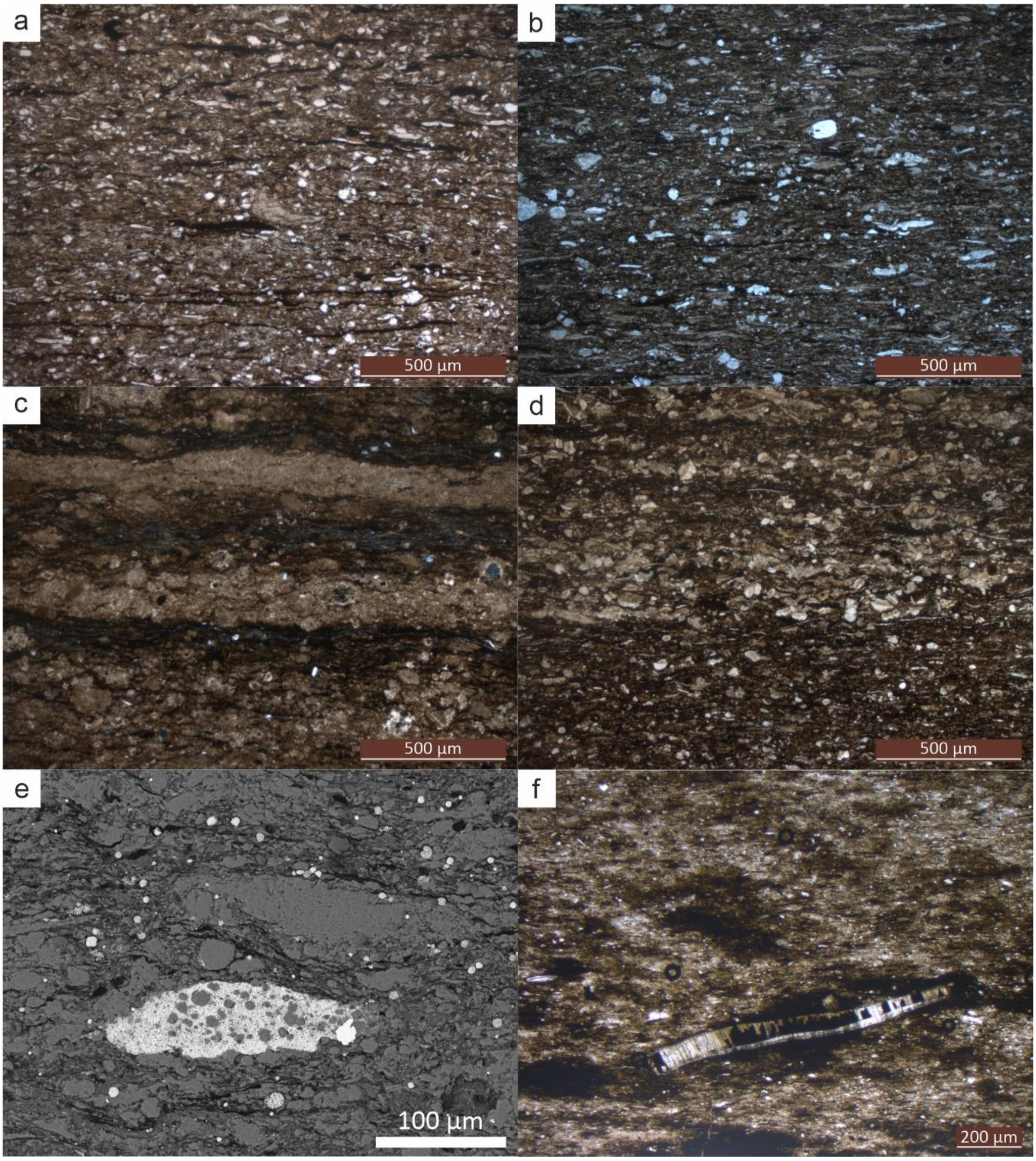

Fig. 4.16 Thin section and SEM photographs of mudrock facies from the Bowland Basin. (a) MLF 2 calcareous, silty mudstone with common organic filaments, topmost Pendleside Limestone, B zone, Swardean Clough. (b) MLF 2 calcareous, silty mudstone with common bioclast fragments, B_{2a} Zone, basal Lower Bowland Shale, Dobson's Brook. (c) MLF 3 laminated, calcareous mudstone consisting of carbonate-rich and clay rich laminae, P_{1a} Zone, Swardean Clough. (d) MLF 3 laminated, calcareous mudstone consisting of carbonate-rich laminae composed of angular calcisilt (fragmented bioclasts?) with clay and organic-rich laminae, uppermost P_{1a} zone, Swardean Clough. (e) MLF 2 SEM image showing abundant carbonate grains (light grey), clay minerals (dark grey), organic matter (black) and pyrite (bright colour) in the form of small, spherical framboids and a pyrite lens incorporating carbonate clasts, $P_{1b\text{-}P1c}$ boundary, Smelthwaite Farm. (f) MLF 1 homogenous mudstone with bivalve fragment showing prismatic structure and partial pyritic replacement, B_2 zone, basal Lower Bowland Shale, Tory Log Clough.

lie adjacent to the Central Pennine High (Fig. 4.2). Laminations consist of alternations, on a 0.5 – 2.0 mm scale, between calcareous and silty mudstone layers. The latter are identical to the MLF 2 sediments (although they can be notably organic rich) and contain a similar range of clasts. The calcareous layers are sharp based and compositionally dominated by indeterminate, angular carbonate grains, minor quartz silt grains, lenses of micrite and occasionally peloids (Fig. 4.16c, d). The thicker laminae are sometimes erosive based and develop scours infilled with calcisilt lenses, but other laminae have diffuse boundaries.

MLF 4 Lenticular, organic-rich mudstone

Dark grey to black shales of MLF 4 dominate the Upper Bowland Shale and also at several levels in the Lower Bowland Shale (Fig. 4.15). In thin section these are seen to consist of organic-rich mudstone with flattened clay lens structures that taper to a point. The clay-dominated lenses show a great size variation within individual layers, ranging from 0.05 mm to 0.4 mm in length and < 0.06 mm in width, and are embedded in a matrix of clay, organic matter, pyrite framboids and fine silt grains with occasional phosphatic nodules (Fig. 4.17a-f). Examination under SEM shows there is no difference in mineral composition between clay lenses and the clay in the matrix (Fig. 4.17e). Individual lamina ranging from 1 – 5 mm thick are occasionally present in MLF 4 and consist of homogenous, organic matter-rich clay (Fig. 4.17c). Bioclasts, derived from the pelagic realm, are common in MLF 4 and include goniatite protoconchs, bivalve larval shells (prodissoconchs) (Fig. 4.17a), spar-filled calcispheres and chert-filled radiolarian tests (Fig. 4.17b, f). Unlike the bioclasts in other Bowland Shale facies, shells are consistently well preserved in MLF 4. Even the ultra-thin shells of prodissoconchs are rarely fragmented.

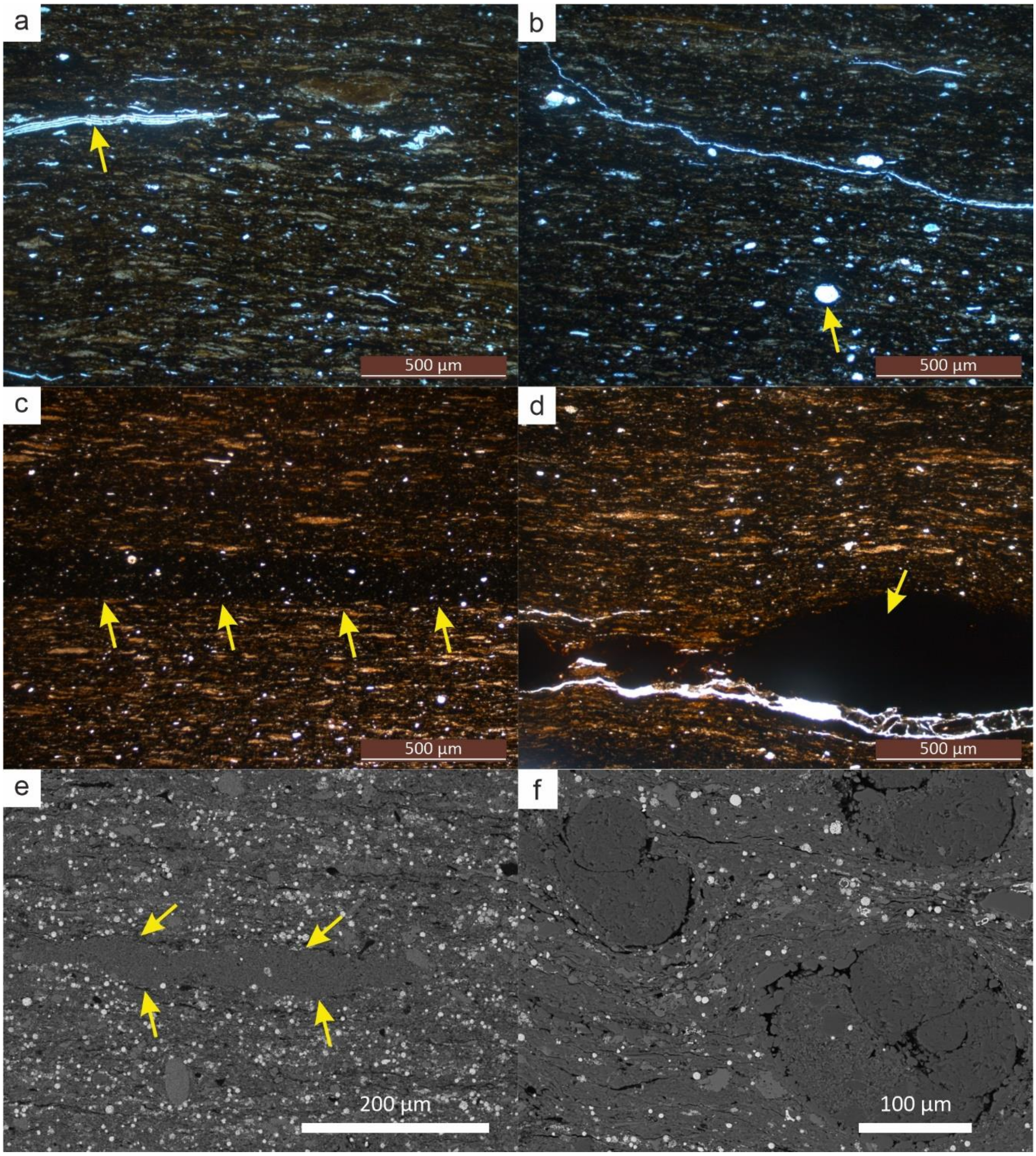

Fig. 4.17 Thin section and SEM photographs of lenticular, organic-rich mudrocks, MLF 4, from Dinckley Hall. a) example showing thin, articulated bivalve prodissoconch (yellow arrow), basal E_{1a} zone. b) example with scattered radiolarians (arrowed), P_{2b} zone. c) example showing typical clay lens-rich layer fabric and a homogenous lamina consisting of clay and organic matter (arrows denote the base), mid E_{1a} zone. d) example with phosphatic nodules (largest example arrowed), mid E_{1a} zone. (e) SEM image showing a clay lens lacking framboids (delineated by arrows) in a matrix with abundant small framboids (bright spots), lower E_{1a} zone. (f) example with several ammonitellas (larval goniatites) in a matrix rich in framboids and clay lenses, basal P_{1c} zone.

4.6 Discussion

4.6.1 Carbonate depositional processes and platform resilience

The clast-supported, coarse calcirudites of CLF 1 occur adjacent to the faults of the Craven Fault Belt and are likely to have been shed from steep slopes generated during the active faulting phases of the Craven Fault Belt. Thus, CLF 1 records rock fall/avalanche accumulations. Although not studied here, minor conglomeratic debris flows have been reported from around the Bowland (intrabasinal) High (Fig. 4.8) which are thought to have been sourced from the Askrigg Block (Brandon & Brandon, 1998). Evidence for the bypass of such debris flows (or possibly slides/slumps) but sourced from the Central Lancashire High, is provided by grooves at the base of beds of CLF 2 beds (cf. Peakall et al., 2020; Baas et al., 2021b).

The majority of carbonate beds in the Bowland Basin are well-sorted calcarenites or calcisiltites (CLF 2 and 3) that occur as sharp-based, tabular beds that were likely deposited from waning turbidity currents. Most beds are massive or planar laminated suggesting T_a and T_b divisions, but hummocks and swaley cross-stratified structures are seen in the SW of the Basin, especially in the Park Styles Limestone (Fig. 4.10c). These suggest combined flow deposition (Tinterri, 2011; Hofstra et al., 2018; Privat et al., 2021) possibly due to the interaction between source turbidity currents and currents reflected from the Slaidburn Anticline. This structure was <5 km to the NE of the Park Styles Limestone and clearly impeded the progress of the Pendleside Sandstone (cf. Fig. 4.8) suggesting it was an intrabasinal high. Thus, carbonate-laden sediment gravity flows heading north-northwest from the Central Lancashire High could have reflected off this structure. Nonetheless a few beds of CLF 2 are also found in the condensed SM section developed on this high; up to 2m wide scours on one surface indicate occasional powerful flows on this high.

The paucity of micrite in MLF 2 and 3 could reflect efficient hydrodynamic sorting during turbulent flow but there are no down-dip micrites known from the basin. More probably, it reflects a micrite-poor sediment source. It has been suggested that extensive carbonate platforms of the Askrigg Block sourced the Bowland Shale carbonates (Clarke et al., 2019), but the restriction of the main carbonate bodies to the SE of the basin suggests that they were being shed from the smaller Central Lancashire High (Fig. 4.8). The well rounded bioclasts and abundance of calcisilt suggests prolonged agitation and winnowing on this platform with much abrasion and attrition of carbonate clasts together with a long-term shift from peloid to crinoid-dominated carbonate production (Fig. 4.12). The elongate nature of the principal carbonate bodies suggests sediment was point sourced from the margin of the Central Lancashire High (Fig. 4.8). We can only speculate why this would be the case, but it might reflect a margin with a discontinuous fringe of reef mounds restricting sediment shedding to embayments between the reefs.

The failure of the Askrigg Block to supply carbonate detritus to the Bowland Basin is somewhat enigmatic. The development of a marginal reef belt along the line of the Mid Craven Fault in the Asbian may have provided a barrier to carbonate shedding (Kirby et al., 2000; Waters et al., 2017b), but reef formation ceased at the end of Asbian and the mounds were subsequently onlapped by the Lower Bowland Shale (Fig. 4.6). By the Pendleian black shales had extended a short distance on to the Askrigg Block (Fig. 4.9) where they passed laterally into the shallow-water Yoredale Group over a short distance. A more likely reason for the lack of sediment transport from the Askrigg Block may come from the thickness trend of the Yoredale Group. The Group thickens northwards from the footwall of the North Craven Fault (Waters & Lowe, 2013) suggesting there was a gradient in this direction, albeit a gentle one in this platform area, that resulted in little sediment transport to the south. In support of this idea, the minor deltaic sandbodies in the Yoredale Group that prograded onto the Askrigg Block from the north did not reach its southern margin (Waters & Lowe, 2013).

In addition to the calcarenite/calcisiltite lobes, the mudrock lithologies of the Bowland Shale also have a substantial carbonate content (MLF 2 and 3). The laminated mudstones of MLF 3 have been identified in previous studies (e.g. Fig. 16c in Clarke et al. (2019) and Facies B in Emmings et al. (2020a)) and have been reasonably interpreted as "microturbidites" deposited from low density turbidity currents (Clarke et al., 2019, p. 299; Emmings et al., 2020a, p.272). However, depositional processes responsible for the more massive facies of MLF 2 are difficult to determine. Some pelagic component may be present (e.g. the clay content and organic filaments), but the silt grade carbonate material, distributed throughout the facies, is unlikely to have settled from the water column. Potentially the massive nature of MLF 2 beds may be due to homogenization by intense bioturbation, but burrows are not seen. A bioturbated homogenization origin seems more likely for MLF 1, which shows occasional burrow mottling, and MLF 4 which both contain larger, unfragmented bioclasts which are likely to be in situ benthos.

In their study of the Bowland Shale, Emmings et al. (2020a) identified examples of MLF 2 which, based on their illustrations, were mostly assigned to their Facies B and C, and attributed to hemipelagic deposition and "small density flow events". The clay and organic content may indeed be of hemipelagic origin, but it co-occurs with fine calcareous detritus. Much of this calcareous material is less than 50 microns in size and it could have been shed into the Bowland Basin via suspension clouds of fine sediment sourced from surrounding carbonate platforms. However, a few carbonate grains are larger, up to 0.5 mm and occasionally up to 2.0 mm in size. These are likely too large to have been transported by suspension clouds, therefore we suggest beds of MLF 2 may record deposition from fine-grained, low-strength debris flows (cf. Talling et al., 2012), with their poor sorting, and ‘floating’ silt grains, being evidence of this transport process. The lack of bed contacts in MLF 2 makes the size of individual flow events difficult to ascertain.

Whatever the depositional process of MLF 2, it is likely that the carbonate platform on the Central Lancashire High supplied the calcarenites/calcisiltite bodies in the Bowland Basin and a significant proportion of the fine-grained sediment too, especially in the Lower Bowland Shale. The Berwick Limestone (E_{1a} zone) is the youngest carbonate unit in the basin probably because subsidence in the later Pendleian saw the Upper Bowland Shale onlap the Central Lancashire High thereby “killing” the carbonate factory after this time (Kirby et al., 2000; Waters et al., 2020).

Finally, there are the enigmatic CLF 4 beds, which typically occur interbedded with MLF 4. In some cases, the limestone beds appear to be diagenetically recrystallised examples of CLF 3 (Fig. 4.13f) but others resemble aragonite fans that were widespread on anoxic seafloors in the Early Triassic (e.g. Woods et al., 2007). The Bowland Shale examples are much smaller (crystals are < 1 mm height) – the fans are not visible to the naked eye – whilst many of the Early Triassic examples can reach 30 cm thickness with crystals laths of similar scale, but they show a distinctive radial structure with long axes orthogonal to bedding (Fig. 4.13d). Euxinic conditions within the Bowland Basin may have been sufficiently alkaline to occasionally allow direct carbonate precipitation on the seafloor, probably originally as aragonite laths that have converted to calcite.

The prolonged development of anoxic-euxinic waters in the Bowland Basin over a period of ~10 million years clearly did not impact carbonate productivity on the surrounding carbonate platforms. This contrasts with many examples that show the shut-down of shallow-water carbonates by onlapping black shales (e.g. Petrash et al., 2016). A clear example is close at hand in the contemporaneous Dublin Basin 250 km to the west of the Bowland Basin where progressive carbonate platform collapse in the Brigantian saw the expansion of deep-water, organic-rich shale deposition. By the Pendleian, shales of the Donore Formation covered the entire region (Pickard et al., 1994). Carbonate aggradation was presumably unable to keep pace with subsidence rates in the Dublin region. In other examples, carbonate shutdown is attributed to the poisoning by upwelling of basinal euxinic waters (Caplan & Bustin, 1999; Li et al., 2022). This did not occur during Bowland Shale deposition even though euxinic black shales developed in close proximity to the well-oxygenated facies of the Yoredale Group (Fig. 4.6). This suggests a sharp demarcation between euxinic and oxic deposition and the likelihood of a stable density interface within the upper water column that protected the shallow waters from sulphidic incursions.

4.6.2 Clastic depositional process and sediment source

The sandstone facies of the Pendleside Sandstone are considered to be a turbidite sandbody (Clarke et al., 2019), an interpretation supported by our isopach map for this Member which shows a broad outcrop occupying the central portion of the basin, and a narrow eastern development that likely records the feeder channel (Fig. 4.7). Clarke et al. (2019) suggested that sandstones with abraded bioclasts (our facies CSF 2) found in the Pendleside Sandstone could record marine reworking in a shelfal source area before sediment was transported into the basin. Alternatively, we propose that the bioclasts may have been shed off the northern end of the Central Lancashire High into the Pendleside Sandstone feeder channel and incorporated with the clastic sediment being transported westwards into the Basin.

The lenticular, organic-rich mudstone of MLF 4 dominates the Upper Bowland Shale, is also common in the Lower Bowland Shale, and in many black shales generally (Könitzer et al., 2014; Li et al., 2020; Peng, 2021). Its origin has been the subject of considerable study, especially the component clay lenses which are often considered to be intraclasts (Könitzer et al., 2014; Laycock et al., 2017; Schieber et al., 2010; Emmings et al., 2020a; Newport et al., 2020), transported either as bedload (Könitzer et al., 2014; Peng, 2021) or within low strength, cohesive debris flows (Boulesteix et al., 2019; Wei & Swennen, 2022). Emmings et al. (2020a p.272) suggested that the Bowland Shale lenses are "mud clasts sourced from upslope scour by tidal and/or wind shear and delivered [to the basin] via bedload currents". Tidal range is however predicted to have been very small for the Upper Carboniferous basins (Wells et al., 2005) ensuring tidal currents are unlikely to have been a source of erosive power. In support of their bedload transport interpretation, Emmings et al. (2020a) showed illustrations of clasts showing imbrication and climbing ripple cross sets (see also Könitzer et al., 2014, Fig. 4.5c), but their images are not compelling. Examples of 'imbrication' show incorrect orientations and stacking relationships relative to flow or consist of an isolated pair of clasts rather than a bedload layer, whilst ripples are defined by indistinct cross-cutting laminae. Transport of clay lenses by bedload, would be expected to lead to bedload layers at least several grain-diameters in thickness (Gomez, 1991) without organic material in between them. Furthermore, bedload transport should produce lenses that are much better sorted (e.g., Kuenen & Humbert, 1969; Komar et al., 1991), and, given the observed size range, the lenses should show tractional structures such as upper-stage plane beds or ripples, (e.g., Arnott & Hand, 1989; Baas et al., 2021a).

Other authors have similarly suggested an intraclast origin for Bowland Shale clay lenses but with transport in dilute density flows (Könitzer et al., 2014; Newport et al., 2020). However, Könitzer et al. (2014) also suggested a more varied origin, with some clay lenses proposed to be faecal pellets (presumably of zooplankton?) or organomineralic aggregates formed in the water column by entrapment with marine snow (cf. Macquaker et al., 2010). We consider a hemipelagic origin to be the dominant process in the accumulation of MLF 4 with the size range of lenses being typical of modern pelagic faecal pellets (Turner, 2015). A marine snow origin is unlikely because this material is organic-rich, aggregated phytodetritus (Turner, 2015), whilst the lenses of the Bowland Shale are composed of clay minerals. A marine snow origin is more likely for the organic filaments found between the lenses. More generally, key evidence for the pelagic origin of MLF 4 comes from the sediment between the clay lenses; this includes the very thin planktonic larval shells of bivalves (prodissoconchs) which are unfragmented and aligned parallel to bedding (Fig. 4.17a). Transport and deposition from gravity currents would fragment such shells and leave some at higher angles in the sediment, neither is observed in MLF 4.

Pyrite framboids are abundant in the Upper Bowland Shale, especially in MLF 4, but they are very small (average size around 5 – 6 μm), suggesting they formed at the redox boundary within the water column before sinking to the seabed where no further framboids form: a situation pertaining in the modern euxinic basin of the Black Sea (Li et al., 2023). Notably, framboids are absent from within the clay lenses (Fig. 4.17e). In the interpretation of Emmings et al. (2020a) it is argued that the rip-up clast were derived from a source area of “shelfal, mud-rich successions” where the prevailing oxic conditions did not support pyrite formation. On arrival on the basin floor, a supposedly consolidated nature of the intraclasts ensured that their low permeability “limited infiltration by syngenetic and/or diagenetic (sulphidic) pore-fluids” (Emmings et al., 2020b p.284), hence the absence of framboids from within the lenses. However, the highly compacted/flattened nature of the lenses suggests they were water-rich when deposited rather than them being lithified rip-up clasts. A further problem with this scenario is that the clay clasts are the dominant component of MLF 4 and yet the geochemical signature of this facies is one of intense euxinia (Emmings et al., 2020b; Li et al., 2023) rather than the oxic deposition of the supposed shelf-mud source area. The framboid-free clay lenses are more easily explained by their formation in the upper water column as faecal pellets, above the site of framboid formation at the redox boundary. Syngenetic framboids do not form below the redox boundary (Wilkin & Barnes, 1997), hence their absence from the clay lenses that had settled to the seabed.

It is of course possible that there are multiple origins for the clay lenses, both as reworked clasts and faecal pellets, and that a range of depositional processes is responsible for mudrock accumulation. However, a key issue with the intraclast origin for black shale deposition specifically lies in its significance for many geochemical studies. Many if not most black shale facies are identical to MLF 4 and they are considered to provide a reliable record of basinal redox conditions, but if the majority of constituent clasts are transported from the shallow-water basin margin then this assumption is wrong. As we note above, the fabric of MLF 4 suggests the clay lenses settled through the water column, together with the associated clay matrix, tiny framboids, organic filaments (marine snow) and pelagic bioclasts (e.g. planktonic bivalve larval shells, goniatites, radiolarians and calcispheres). Consequently, the Bowland Shales (and black shales generally) are likely to provide an in situ record of redox conditions as assumed in geochemical studies.

4.6.3 Eustatic influence?

Deep-water carbonate systems are typically fed from adjacent carbonate platforms during highstand or transgression when productivity is high: a phenomenon known as highstand shedding (e.g. Reijmer et al., 2015). In contrast, clastic turbidite systems are traditionally formed during lowstand conditions when base level fall ensures clastic sediment is transported to the shelf break. During Bowland Shale deposition carbonate fans formed in the Bowland Basin around the Asbian/Brigantian boundary ($P_{1a\text{-}b}$), in the early Brigantian ($P_{1b\text{-}c}$) and in the early Pendleian (E_{1a}), whilst a clastic turbidite systems formed in the mid Brigantian (around the P_1/P_2 boundary) and Bowland Shale deposition was terminated in the late Pendleian (E_{1c}) when the substantial Pendle Grit turbidite system arrived. Curiously, these occurrences do not fit closely with purported base-level changes in the surrounding region. The Asbian/Brigantian boundary is marked by a major palaeokarst surface in platform carbonates in the region, which is considered to be a third-order sequence boundary and one of the few clear eustatic signatures of the interval (Manifold et al., 2021). This lowstand coincides with the formation of the Ravensholme Limestone within the Bowland Basin, indicating that base-level fall was not sufficient to expose the Central Lancashire High and shut down carbonate productivity. In contrast, the early Pendleian (E_{1a}) saw the development of black shales over large areas of Europe suggesting a major transgression (Clarke et al., 2019). This interval coincides with the final carbonate fan development in the Bowland Basin, which could indicate highstand shedding. However, the other carbonate fans in the Basin do not correlate with transgressive episodes and the E_{1a} development may be purely coincidental. The notion of an E_{1a} eustatic transgression is in any case highly questionable because there was no associated expansion of Bowland Shale deposition in the region, and neither is there evidence for back-stepping on the Askrigg Block (Fig. 4.4). Other factors, notably tectonism and development of sediment transport routes were likely to be much more important than eustasy in controlling the supply of sediment (both clastic and carbonate) to the Bowland Basin. It is noteworthy that recent studies have also challenged the received wisdom that eustasy affected deposition of the distinctly cyclic Yoredale Group on the Askrigg Block, and instead favour autogenic controls

(Manifold et al., 2020, 2021). The absence of synchrony between basinal facies development and cyclicity on surrounding shelf areas supports the contention of Manifold and colleagues.

4.7 Conclusions

Deposition within the Bowland Basin, during Bowland Shale accumulation, was influenced by a variety of factors, including tectonics, sediment supply (especially productivity on surrounding carbonate platforms) and clastic sediment access routes to the basin. There is no evidence that eustasy influenced deposition. Arenaceous clastic sediment reached the basin from the east through a narrow conduit, and it is likely that clay material also arrived via this route in suspension. Intrabasinal topography deflected turbidity currents bringing clastic detritus into the basin whilst causing reflection of carbonate-laden turbidity currents sourced from a platform to the southeast. The resulting combined flows produced calciturbidites with structures reminiscent of storm deposition (swaley and hummocky cross stratification). At no point did the extensive carbonate platform developed on the Askrigg Block to the north of the Bowland Basin supply significant sediment, probably because the prevailing sediment transport direction on this margin was northwards. Carbonate productivity was maintained on the platforms adjacent to the anoxic waters of the Bowland Basin suggesting a strong and stable pycnocline confined the sulfidic waters to the deeper water column.

The fine-grained strata of the Bowland Shale formations record a diverse range of depositional processes. During Lower Bowland Shale accumulation a significant quantity of carbonate detritus was shed from the Central Lancashire High, a small, highly-productive carbonate platform, leading to the development of elongate, carbonate fans fed by turbidity currents, and more widespread calcareous shales throughout the basin. Hemipelagic deposition during Lower Bowland Shale deposition was of lesser importance than the supply of sediment from these sediment-gravity flows. The Upper Bowland Shale, by contrast, records more uniform black shale deposition dominated by hemipelagic settling. It is argued that the dominant lenticular fabric of the shales, with their abundant clay lenses represents settling of faecal pellets formed in the water column, together with other pelagic components with which they are intimately interbedded (e.g. marine snow, syngenetic framboids and larval stages of marine organisms). The alternative, that clay lenses accumulated from transport of rip-up clasts, either as bedload or in dilute density currents, is not supported by the associated presence of the well-preserved ultra-thin shells of planktonic origin in the Bowland Shale euxinic facies. The notion that black shales are the result of traction transport of reworked mudstone intraclasts over long distances (e.g. Schieber et al., 2010; Li et al., 2021; Peng, 2021) may be correct in some cases but it challenges the accepted wisdom in geochemical studies that use black shales as a repository of the in situ redox signal within the basin.

Acknowledgements: Our gratitude goes to Dr. Kaixuan Ji, Yuxuan Wang, Dr. Yafang Song, Zhen Xu and Dr. Jed Atkinson who provided valuable help during fieldwork.

References

Aitkenhead, N. 1992 Geology of the Country Around Garstang: Memoir for 1: 50,000 Geological Sheet 67 (England and Wales).

Andrieu, S., Krencker, F.N. & Bodin, S. 2022 Anatomy of a platform margin during a carbonate factory collapse: implications for the sedimentary record and sequence stratigraphic interpretation of poisoning events. *Journal of Geological Society London*, **179**, jgs2022-005.

Arnott, R.W.C. & Hand, B.M. 1989. Bedforms, primary structures and grain fabric in the presence of suspended sediment rain. *Journal of Sedimentary Research*, **59**, 1062–1069, https://doi.org/10.1306/212F90F2-2B24-11D7-8648000102C1865D.

Arthurton, R.S. 1984. The Ribblesdale fold belt, NW England—a Dinantian-early Namurian dextral shear zone. *Geological Society of London Special Publication*, **14**, 131–138.

Arthurton, R.S., Johnson, E.W. & Mundy, D.J.C. 1988. Geology of the country around Settle.

Baas, J.H., Best, J. & Peakall, J. 2021a. Rapid gravity flow transformation revealed in a single climbing ripple. *Geology*, **49**, 493–497, https://doi.org/10.1130/G48181.1.

Baas, J.H., Tracey, N.D. & Peakall, J. 2021b. Sole marks reveal deep-marine depositional process and environment: Implications for flow transformation and hybrid-event-bed models. *Journal of Sedimentary Research*, **91**, 986–1009, https://doi.org/10.2110/jsr.2020.104.

Black, W.W. 1940. The Bowland Shales from Thorlby to Burnsall, Yorkshire. *Leeds Geological. Association*, **5**, 308–321.

Black, W.W. 1950. The Carboniferous geology of the Grassington area, Yorkshire. *Proceedings of the Yorkshire Geological Society*, **28**, 29–42.

Booker, K.M. & Hudson, R.G.S. 1926. The Carboniferous sequence of the Craven Lowlands south of the reef limestones of Cracoe. *Proceedings of the Yorkshire Geological Society*, **20**, 411–438.

Boulesteix, K., Poyatos-Moré, M., Flint, S.S., Taylor, K.G., Hodgson, D.M. & Hasiotis, S.T. 2019. Transport and deposition of mud in deep-water environments, Processes and stratigraphic implications. *Sedimentology*, **66**, 2894–2925, https://doi.org/10.1111/sed.12614.

Brandon, A. & Brandon, A. 1998. Geology of the Country Around Lancaster: Memoir for 1: 50 000 Geological Sheet 59 (England and Wales).

Caplan, M.L. & Bustin, R.M. 1999. Devonian-Carboniferous Hangenberg mass extinction event, widespread organic-rich mudrock and anoxia: Causes and consequences. Palaeogeography, Palaeoclimatology Palaeoecology, **148**, 187–207, https://doi.org/10.1016/S0031-0182(98)00218-1.

Clarke, H., Turner, P., Bustin, R.M., Riley, N. & Besly, B. 2018. Shale gas resources of the Bowland Basin, NW England - A holistic study. *Petroleum Geoscience*, **24**, 287–322, https://doi.org/10.1144/petgeo2017-066.

Cooper, A.H. & Burgess, I.C. 1993. Geology of the country around Harrogate: memoir for 1: 50, 0000 geological sheet 62 (England and Wales).

de Jonge-Anderson, I. & Underhill, J.R. 2020. Structural constraints on Lower Carboniferous shale gas exploration in the Craven Basin, NW England. *Petroleum Geoscience*, **26**, 303–324, https://doi.org/10.1144/petgeo2019-125.

Dixon, E.E.L., & Hudson, R.G.S. 1931. A mid-Carboniferous boulder-bed near Settle. *Geological Magazine*, **68**, 81-92, https://doi.org/10.1017/S001675680009539X.

Dunham, K.C. & Wilson, A.A. 1985. Geology of the Northern Penine Orefield, Volume 2. Stainmore to Craven. Economic Memoir.

Earp, J.R., Poole, E.G. & Whiteman, A.J. 1961. Geology of the country around Clitheroe and Nelson. HM Stationery Office.

Emmings, J.F., Davies, S.J., Vane, C.H., Moss-Hayes, V. & Stephenson, M.H. 2020a. From marine bands to hybrid flows: Sedimentology of a Mississippian black shale. *Sedimentology*, **67**, 261–304, https://doi.org/10.1111/sed.12642.

Emmings, J.F., Poulton, S.W., Vane, C.H., Davies, S.J., Jenkin, G.R.T., Stephenson, M.H., Leng, M.J., Lamb, A.L. & Moss-Hayes, V. 2020b. A Mississippian black shale record of redox oscillation in the Craven Basin, UK. *Palaeogeography Palaeoclimatology Palaeoecology*, **538**, 109423, https://doi.org/10.1016/j.palaeo.2019.109423.

Fraser, A.J. & Gawthorpe, R.L. 1990. Tectono-stratigraphic development and hydrocarbon habitat of the Carboniferous in northern England. *Geological Society Special Publication*, **55**, 49–86.

Gawthorpe, R.L. 1986. Sedimentation during carbonate ramp-to-slope evolution in a tectonically active area: Bowland Basin (Dinantian), northern England. *Sedimentology*, **33**, 185–206, https://doi.org/10.1111/j.1365-3091.1986.tb00531.x

Gomez, B. 1991. Bedload transport. *Earth Science Review*, **31**, 89–132, https://doi.org/10.1016/0012-8252(91)90017-A.

Gorsline, D.S., Nava-Sanchez, E. & de Nava, J.M. 1996. A survey of occurrences of Holocene laminated sediments in California Borderland Basins: products of a variety of depositional processes. *Geological Society London Special pulication*, **116**, 93–110.

Gross, D., Sachsenhofer, R.F., Bechtel, A., Pytlak, L., Rupprecht, B. & Wegerer, E. 2015. Organic geochemistry of Mississippian shales (Bowland Shale Formation) in central Britain: Implications for depositional environment, source rock and gas shale potential. *Marine Petroleum Geology*, **59**, 1–21, https://doi.org/10.1016/j.marpetgeo.2014.07.022.

Hallock, P. & Schlager, W. 1986. Nutrient excess and the demise of coral reefs and carbonate platforms. Palaios, 389–398, https://doi.org/10.2307/3514476.

Hennissen, J.A.I. & Gent, C.M.A. 2019. Total organic carbon in the Bowland-Hodder Unit of the southern Widmerpool Gulf: a discussion. *Journal of Petroleum Science Engineering*, **178**, 1194–1202, https://doi.org/10.1016/j.petrol.2019.01.097.

Hofstra, M., Peakall, J., Hodgson, D.M. & Stevenson, C.J. 2018. Architecture and morphodynamics of subcritical sediment waves in an ancient channel–lobe transition zone. *Sedimentology*, **65**, 2339–2367, https://doi.org/10.1111/sed.12468.

Hudson, R.G.S. 1930. The carboniferous of the Craven Reef Belt: The Namurian Uncomformity at Scaleber, Near Settle. *Proceedings of the Geologists' Association*, **41**, 290-IN8, https://doi.org/10.1016/S0016-7878(30)80021-X.

Hudson, R.G.S. 1940. The mirk fell beds (Namurian, E2) of tan hill, Yorkshire. *Proceedings of the Yorkshire Geological Society*, **24**, 259–289.

Hudson, R.G.S. & Mitchell, G.H. 1937. The Carboniferous geology of the Skipton anticline. Summary of Progress of the Geological Survey for 1935, 1–45.

Kane, I.A. 2010. Development and flow structures of sand injectites: The Hind Sandstone Member injectite complex, Carboniferous, UK. *Marine Petroleum Geology*, **27**, 1200–1215, https://doi.org/10.1016/j.marpetgeo.2010.02.009.

Kirby, G.A. 2000. The structure and evolution of the Craven Basin and adjacent areas: subsurface memoir. Stationery Office.

Komar, P.D. 1991. The hydraulic interpretation of turbidites from their grain sizes and sedimentary structures. Deep-Water Turbidite Systems, 41–53, https://doi.org/10.1002/9781444304473.ch3.

Könitzer, S.F., Davies, S.J., Stephenson, M.H. & Leng, M.J. 2014. Depositional controls on mudstone lithofacies in a basinal setting: implications for the delivery of sedimentary organic matter. *Journal of Sedimentary Research*, **84**, 198–214, https://doi.org/10.2110/jsr.2014.18.

Krencker, F.N., Bodin, S., Hoffmann, R., Suan, G., Mattioli, E., Kabiri, L., Föllmi, K.B. & Immenhauser, A. 2014. The middle Toarcian cold snap: Trigger of mass extinction and carbonate factory demise. Global Planetary Change, 117, 64–78, https://doi.org/10.1016/j.gloplacha.2014.03.008.

Kuenen, P.H. & Humbert, F.L. 1969. Grain size of turbidite ripples. *Sedimentology*, **13**, 253–261, https://doi.org/10.1111/j.1365-3091.1969.tb00172.x.

Laycock, D.P., Pedersen, P.K., Montgomery, B.C. & Spencer, R.J. 2017. Identification, characterization, and statistical analysis of mudstone aggregate clasts, Cretaceous Carlile Formation, Central Alberta, Canada. *Marine Petroleum Geology*, **84**, 49–63, https://doi.org/10.1016/j.marpetgeo.2017.03.012.

Leeder, M.R. 1988. Recent developments in Carboniferous geology: a critical review with implications for the British Isles and N.W. Europe. *Proceedings of the Geologists' Association*, **99**, 73–100, https://doi.org/10.1016/S0016-7878(88)80001-4.

Li, S., Wignall, P.B., Poulton, S.W., Hedhli, M. & Grasby, S.E. 2022. Carbonate shutdown, phosphogenesis and the variable style of marine anoxia in the late Famennian (Late Devonian) in western Laurentia. *Palaeogeography Palaeoclimatology Palaeoecology*, **589**, 110835, https://doi.org/10.1016/j.palaeo.2022.110835.

Li, S., Wignall, P.B., Xiong, Y. & Poulton, S. 2023. Calibration of redox thresholds in black shale: Insight from a stratified Mississippian basin with warm saline bottom waters. *GSA Bulletin*, https://doi.org/10.1130/B36915.1.

Li, S., Zhu, R.K., Cui, J.W., Luo, Z., Jiao, H., & Liu, H. 2020. Sedimentary characteristics of fine-grained sedimentary rock and paleo-environment of Chang 7 member in the Ordos Basin: A case study from Well Yaoye 1 in Tongchuan. *Acta Sedimentol Sinca*, **38**, 554-570 (In Chinese with English abstract), https://doi.org/10.14027/j.issn.1000-0550.2019.062.

Li, Z., Schieber, J., & Pedersen, P.K. 2021. On the origin and significance of composite particles in mudstones: Examples from the Cenomanian Dunvegan Formation. *Sedimentology*, **68**, 737-754, https://doi.org/10.1111/sed.12801.

Macquaker, J.H.S., Keller, M.A. & Davies, S.J. 2010. Algal blooms and “marine snow”: Mechanisms that enhance preservation of organic carbon in ancient fine-grained sediments. *Journal of Sedimentary Research*, **80**, 934–942, https://doi.org/10.2110/jsr.2010.085.

Manifold, L., Hollis, C. & Burgess, P. 2020. The Anatomy of a Mississippian (Viséan) carbonate platform interior, UK: depositional cycles, glacioeustasy and facies mosaics. Sedimentary Geology, **401**, 105633, https://doi.org/10.1016/j.sedgeo.2020.105633.

Manifold, L., del Strother, P., Gold, D.P., Burgess, P. & Hollis, C. 2021. Unravelling evidence for global climate change in mississippian carbonate strata from the derbyshire and north wales platforms, UK. Journal of Geological Society London, **178(5)**, https://doi.org/doi: 10.1144/jgs2020-106.

Newport, S.M., Hennissen, J.A.I., Armstrong, J.P., Taylor, K.G., Newport, L.P. & Hough, E. 2020. Can One-Run-Fixed-Arrhenius Kerogen Analysis Provide Comparable Organofacies Results to Detailed Palynological Analysis? A Case Study from a Prospective Mississippian Source Rock Reservoir (Bowland Shale, UK). *Natural Resources Research*, **29**, 2011–2031, https://doi.org/10.1007/s11053-019-09543-z.

Newport, S.M., Jerrett, R.M., Taylor, K.G., Hough, E. & Worden, R.H. 2018. Sedimentology and microfacies of a mud-rich slope succession: In the Carboniferous Bowland Basin, NW England (UK). *Journal of Geological Society London*, **175**, 247–262, https://doi.org/10.1144/jgs2017-036.

Peakall, J., Best, J., Baas, J.H., Hodgson, D.M., Clare, M.A., Talling, P.J., Dorrell, R.M. and Lee, D.R. 2020. An integrated process-based model of flutes and tool marks in deep-water environments: Implications for palaeohydraulics, the Bouma sequence and hybrid event beds. *Sedimentology*, **67**, 1601–1666, https://doi.org/10.1111/sed.12727.

Peng, J. 2021. Sedimentology of the Upper Pennsylvanian organic-rich Cline Shale, Midland Basin: From gravity flows to pelagic suspension fallout. *Sedimentology*, **68**, 805–833, https://doi.org/10.1111/sed.12811.

Petrash, D.A., Gueneli, N., Brocks, J.J., Méndez-Dot, J.A., González-Arismendi, G., Poulton, S.W. & Konhauser, K.O. 2016. Black shale deposition and early diagenetic dolomite cementation during Oceanic Anoxic Event 1: The mid-Cretaceous Maracaibo Platform, northwestern South America. *American Journal of Science*, **316**, 669–711, https://doi.org/10.2475/07.2016.03.

Pharaoh, T., Haslam, R., Hough, E., Kirk, K., Leslie, G., Schofield, D. & Heafford, A. 2020. The Môn–Deemster–Ribblesdale fold–thrust belt, central UK: a concealed Variscan inversion belt located on weak Caledonian crust. *Geological Society London Specical Publication*, **490**, 153–176.

Pickard, N.A.H., Rees, J.G., Strogen, P., Somerville, I.D. & Jones, G.L.I. 1994. Controls on the evolution and demise of Lower Carboniferous carbonate platforms, northern margin of the Dublin Basin, Ireland. *Geological Journal,* **29**, 93–117, https://doi.org/10.1002/gj.3350290202.

Privat, A.M., Hodgson, D.M., Jackson, C.A., Schwarz, E. and Peakall, J. 2021. Evolution from syn-rift carbonates to early post-rift deep-marine intraslope lobes: The role of rift basin physiography on sedimentation patterns. *Sedimentology*, **68**, 2563–2605, https://doi.org/10.1111/sed.12864.

Reijmer, J.J.G., Palmieri, P., Groen, R., & Floquet, M. 2015. Calciturbidites and calcidebrites: Sea-level variations or tectonic processes? *Sedimentary Geology*, **317**, 53-70, https://doi.org/10.1016/j.sedgeo.2014.10.013.

Reijmer, J.J.G. 2021. Marine carbonate factories: Review and update. *Sedimentology*, **68**, 1729–1796, https://doi.org/10.1111/sed.12878.

Schieber, J., Southard, J.B. & Schimmelmann, A. 2010. Lenticular shale fabrics resulting from intermittent erosion of water-rich muds—interpreting the rock record in the light of recent flume experiments. *Journal of Sedimentary Research*, **80**, 119–128, https://doi.org/10.2110/jsr.2010.005.

Schlager, W. 1981. The paradox of drowned reefs and carbonate platforms. *Geological Society of American Bulletin*, **92**, 197–211, https://doi.org/10.1130/0016-7606(1981)92<197:TPODRA>2.0.CO;2.

Talling, P.J., Masson, D.G., Sumner, E.J. & Malgesini, G. 2012. Subaqueous sediment density flows: Depositional processes and deposit types. *Sedimentology*, **59**, 1937–2003, https://doi.org/10.1111/j.1365-3091.2012.01353.x.

Tinterri, R. 2011. Combined flow sedimentary structures and the genetic link between sigmoidal-and hummocky-cross stratification. *GeoActa*, **10**, 1–43.

Turner, J.T. 2015. Zooplankton fecal pellets, marine snow, phytodetritus and the ocean's biological pump. *Progress in Oceanography*, **130**, 205–248, https://doi.org/10.1016/j.pocean.2014.08.005.

Waters, C.N., & Lowe, D. 2013. Chapter 2: geology of the limestones, in Waltham. Caves and Karst of the Yorkshire Dales, Volume 1: Great Hucklow, UK, British Cave Research Association, 11–28.

Waters, C.N., Cózar, P., Somerville, I.D., Haslam, R.B., Millward, D. & Woods, M. 2017a Lithostratigraphy and biostratigraphy of the Lower Carboniferous (Mississippian) carbonates of the southern Askrigg Block, North Yorkshire, UK. *Geological Magazine*, **154**, 305–333, https://doi.org/10.1017/S0016756815000989.

Waters, C.N., Haslam, R.B., Cózar, P., Somerville, I.D., Millward, D. & Woods, M. 2017b. Mississippian reef development in the Cracoe Limestone Formation of the southern Askrigg Block, North Yorkshire, UK. *Proceedings of the Yorkshire Geological Society*, **61**, 179–196, https://doi.org/10.1144/pygs2016-374.

Waters, C.N., Vane, C.H., Kemp, S.J., Haslam, R.B., Hough, E. & Moss-Hayes, V.L. 2020. Lithological and chemostratigraphic discrimination of facies within the Bowland Shale Formation within the Craven and Edale basins, UK. *Petroleum Geoscience*, **26**, 325–345, https://doi.org/10.1144/petgeo2018-039.

Waters, C.N., Waters, R.A., Barclay, W.J. & Davies, J.R. 2009. A lithostratigraphical framework for the Carboniferous successions of northern Great Britain (onshore). 174 pp.

Wei, W. & Swennen, R. 2022. Sedimentology and lithofacies of organic-rich Namurian Shale, Namur Synclinorium and Campine Basin (Belgium and S-Netherlands). *Marine Petroleum Geology*, **138**, 105553, https://doi.org/10.1016/j.marpetgeo.2022.105553.

Wells, M.R., Allison, P.A., Hampson, G.J., Piggott, M.D., & Pain, C.C. 2005. Modelling ancient tides: the Upper Carboniferous epi-continental seaway of Northwest Europe. *Sedimentology*, **52**, 715-735, https://doi.org/10.1111/j.1365-3091.2005.00718.x.

Wignall, P.B. 1994. Black shales. Oxford University Press, USA.

Wilkin, R.T. & Barnes, H.L. 1997. Formation processes of framboidal pyrite. *Geochimica et Cosmochimica Acta*, **61**, 323–339, https://doi.org/10.1016/S0016-7037(96)00320-1.

Woods, A.D., Bottjer, D.J. & Corsetti, F.A. 2007. Calcium carbonate seafloor precipitates from the outer shelf to slope facies of the Lower Triassic (Smithian-Spathian) Union Wash Formation, California, USA: Sedimentology and palaeobiologic significance. *Palaeogeography Palaeoclimatology Palaeoecology*, **252**, 281–290, https://doi.org/10.1016/j.palaeo.2006.11.053.

Chapter 5: Conclusions and future work

5.1 Conclusions

Two carbonate shutdown events have been investigated which show distinct sedimentary evolution. A ramp setting cannot effectively prevent the spread of anoxic waters into the zone of carbonate production causing carbonate demise followed by black shale deposition. In a block-and-basin type setting, the anoxic bottom waters can be isolated in the basin whilst carbonate production can still thrive long after the adjacent basin becomes anoxic (Fig. 5.1).

In the first case study, based on the Devonian-Carboniferous Jura Creek section, expansion of anoxic bottom water onto the carbonate ramp shows coincident carbonate demise and black shale deposition (Fig. 5.1). Thus, healthy carbonate ramp deposition was stopped by declining seafloor oxygen levels, followed by phosphogenesis of the youngest carbonates. The topmost limestone is a hard ground that was reworked, possibly by internal wave action along a pycnocline, producing a lag of phosphatic clasts and pyrite grains including giant framboids (reaching 100 μm diameter) and polyframboids. The following lower Exshaw Formation archives a complex redox history. Initially, the occurrence of small framboids, and elevated Fe_{HR}/Fe_T and Fe_{py}/Fe_{HR} values, combined with enhanced trace metal (U, Mo and Re) accumulation all suggest intense euxinia. These conditions were replaced by ferruginous anoxic conditions recorded in radiolarian-rich, black shales that have moderate concentrations of trace metals, low pyrite content and, remarkably for a black shale, no framboids. The Mo-U covariation trends suggest that elevated Mo enrichment under ferruginous conditions was promoted by a particulate shuttle mechanism (Fe cycling in ferruginous condition). The return of better ventilated conditions (dysoxic bottom water and sulfidic pore waters) around the Devonian/Carboniferous boundary is marked by a decrease in trace metal concentration and the absence of syngenetic pyrite but reappearance of diagenetic framboids. Constrained by conodont biostratigraphy and Re-Os dating, it is found that the timing of carbonate shutdown in western Laurentia started prior to the Hangenberg Crisis while this crisis is coincided with an improvement in ventilation, from euxinic to ferruginous conditions in our study. Evidence from other basins in western North America suggests an even greater increase in oxygenation at this time. The link between the Hangenberg extinction crisis and oceanic anoxia likely needs re-evaluating.

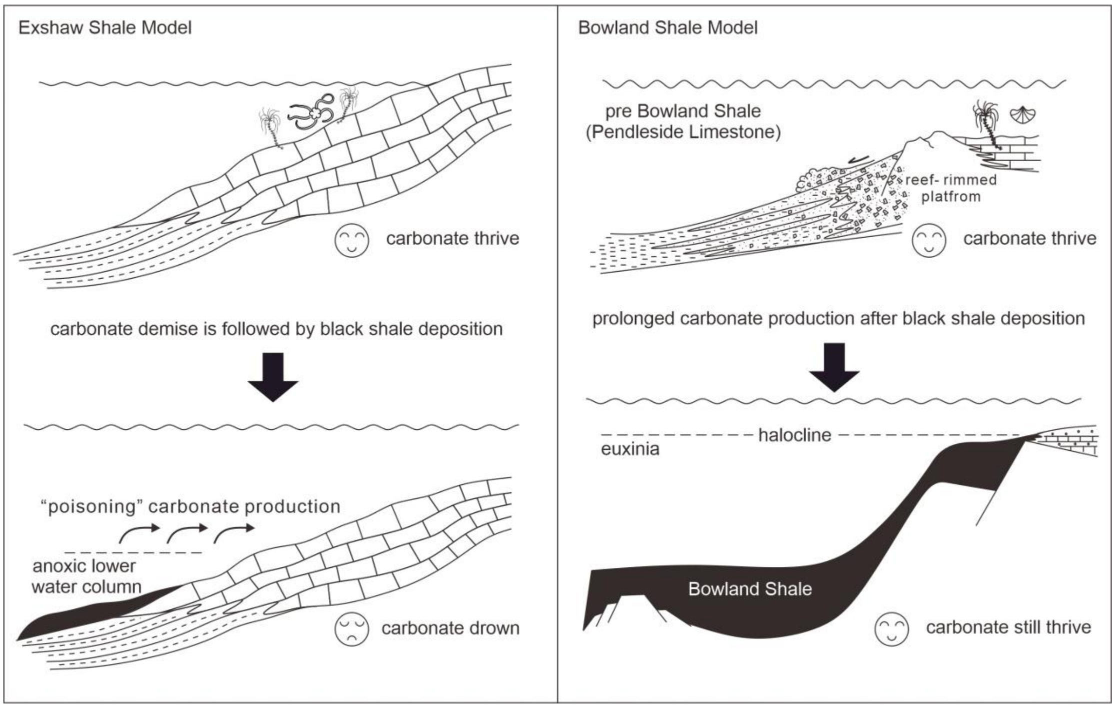

Fig 5.1 Conceptual model for black shale and carbonate production on different tectonic settings (Exshaw Shale Model and Bowland Shale Model). Anoxic conditions can transgress up a carbonate ramp unhindered, causing shutdown of

carbonate production. Syn-rift topography of the Bowland Shale combined with development of a strongly stratified water column isolates the bottom waters from the adjacent carbonate platforms allowing them to persist.

In the second, combined sedimentology and geochemistry investigation on the Bowland Basin, it is found that the relationship between black shale deposition and carbonate production is more complicated.

Firstly, the redox evolution of the Bowland Basin is again assessed using multiple redox proxies (Mo and U systematics, Fe phase partitioning and pyrite morphology). Trace metal enrichment can be subject to multiple factors, and thus basin-specific redox thresholds for Mo and U proxies are devised. The mutual corroboration of independent (Mo and U systematics, Fe phase partitioning and pyrite morphology) also validates Fe phase partitioning as a robust redox proxy. The Bowland Basin was initially oxic before anoxic conditions began to expand from basin centre locations. By the end of Bowland Shale deposition, black shale deposition extended from the basin centre into marginal settings where they transitioned over a short distance into carbonates. Weakly euxinic conditions were widespread during Lower Bowland Shale deposition and basin waters evolved to became highly euxinic in the Upper Bowland Shale deposition (Fig. 5.2).

On the other hand, detailed field investigation and petrographic study combined with previous research prove that there are several calciturbidite fans sourced from a small carbonate platform to the SE of the Basin. These occur in the Lower Bowland Shale along with a substantial turbidite fan composed of sand sourced from the NE of the Basin. The turbidite deposition could dilute the high salinity bottom water and therefore stimulate the vertical circulation. This could explain the episodic ventilation

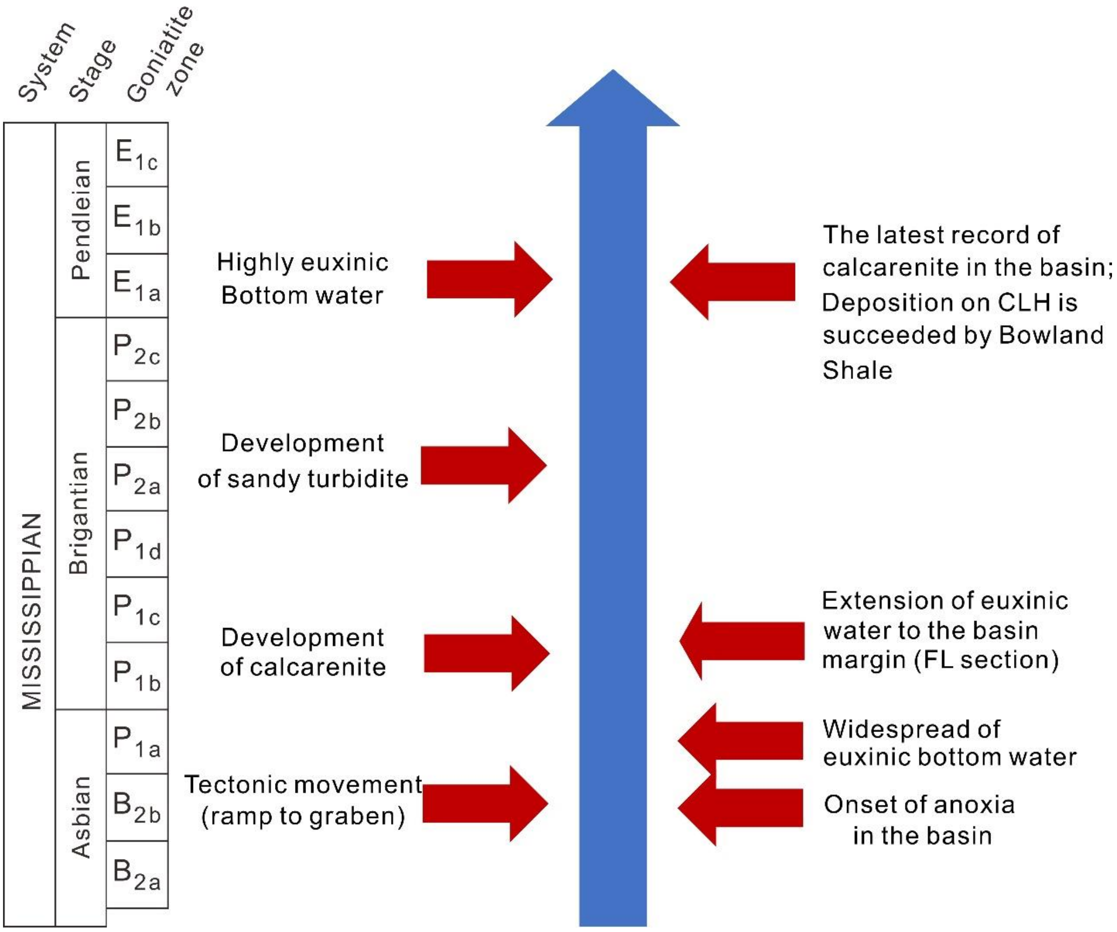

Fig. 5.2 Depositional history in Bowland Basin spanning from Asbian to early Pendleian.

in local areas including TLC, CH and DH section (Fig. 3.14). However, combined with redox history in Bowland Basin, the occurrence of calciturbidite also indicate that the carbonate platforms remained healthy after the deoxygenation in the basin (Fig. 5.2). The basin maintained stable anoxic conditions through Brigantian. However, it is highly likely that the oxygen depletion water body was constrained in the basin with little link to the block margin. Only when the Pendleian witnessed the onset of highly euxinic condition, did the black shale deposition extend to the south margin of Askrigg Block and drown carbonate on the Central Lancashire High. The onset of highly euxinic water column coincided with the last occurrence of calcarenite in the basin and Upper Bowland Shale deposition on the Central Lancashire High (Fig. 5.3). Since then, no more calcarenite deposition is found in the basin, suggesting a termination of carbonate production on surrounding blocks. In contrast to the carbonate demise in the Canadian study, a prolonged carbonate production is displayed in Bowland Basin (Fig. 5.1). It is speculated that anoxia developed in many basins throughout the northern England region whilst productive carbonate platforms thrived in shallow waters during Brigantian. Anoxic bottom water is constrained in the basin for long time before its final intrusion to the shallow area in Pendleian when carbonate production shut down.

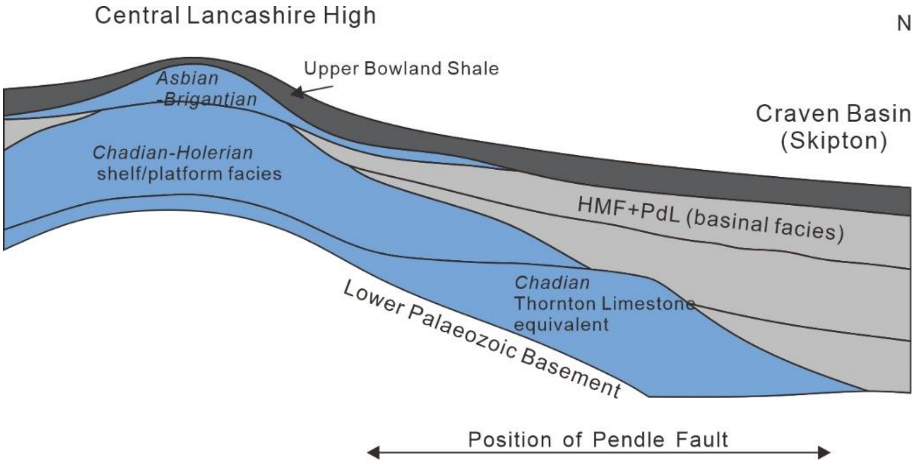

Fig. 5.3 Model demonstrating the development of carbonate production and its termination on Central Lancashire High, which is succeeded by Upper Bowland Shale (modified from Evans & Kirby 1999); HMF: Hodderence Mudstone Formation; PdL: Pendleside Limestone Formation.

A model of WSBW is introduced to explain the onset of anoxia in the Bowland basin. Field logging shows that there is a sharp transition to fully oxygenated facies at the basin margin, suggesting that there was a well-developed water column pycnocline. Previous studies on the Bowland Shale have suggested conditions of eutrophication and an estuarine circulation regime, due to freshwater influx from distant deltas, was responsible for Bowland Basin anoxia (e.g. Emmings et al., 2020b). However, freshwater influence in the Basin is unlikely given the surrounding carbonate platforms and terrestrial input is still far away from the basin. Consequently, the WSBW model reconciles all the contention. Due to evaporation on the adjacent carbonate platforms, warmer but denser saline waters infilled the Basin generating a halocline in the water column (Fig. 3.15, Fig. 5.4). Limited connectivity of the basinal waters restricted water circulation leading to deoxygenation. It is worth noting that WSBW could have persisted for long time. But anoxic condition can only be found since mid-Asbian, which coincided with the tectonic movement in Asbian- Brigantian (Fig. 5.2). In contrast to a ramp setting, topography of a graben presents a stronger constraint on the water circulation between basins and blocks, leading to gradual silled condition in the basin.

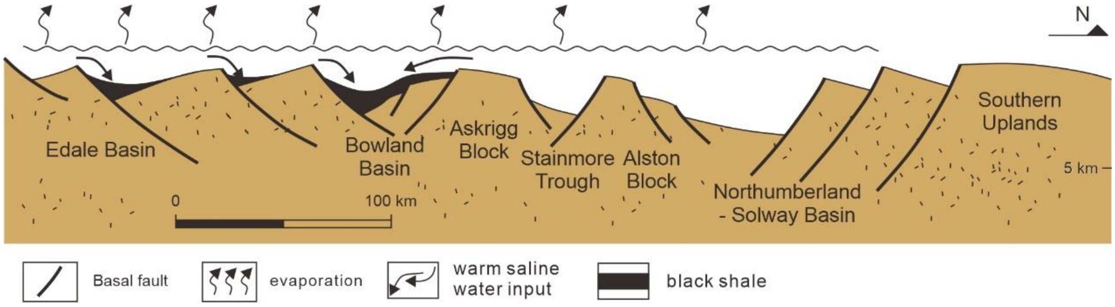

Fig. 5.4 WSBW circulation in block-and-basin in Northern England; with the progradation of deltaic sand coming from the North, black shale deposition is mainly found in the basins on the south (Fraser & Gawthorpe 1990 with modification).

Furthermore, considering the block-and-basin topography in northern England, similar conditions could also be expected in the basins on the south including Bowland Basin, Edale Basin and Widmerpool Basin. This is supported by the onset of black shale deposition in each basin being about the same time, which is driven by

Asbian- Brigantian tectonic movement (Fig. 5.4). This also indicates that WSBW model is promising to explain black shale deposition in basin-and-block settings in lower latitude.

The depositional processes for mudstone/shale are highlighted. Particularly, MLF-4, lenticular organic-rich mudstone is a record of faecal pellet and mainly in-situ deposition bearing solid geochemical information. Recently studies have emphasised diverse processes for mudstone deposition, including long-distance traction transport of clay intraclasts for the lens-rich facies (Schieber et al., 2010; Emmings et al., 2020a). However, evidence suggests its origin is dominated by in-situ depositional processes. Firstly, thin section analysis and SEM observations suggest that clay lens-rich shale deposition is a record of faecal pellet accumulation, probably derived from zooplankton, instead of intraclasts. Therefore, hemipelagic deposition is probably predominant for most organic-rich shale deposition in Bowland basin. This is supported by the geochemical analysis of the mudrocks; transport of reworked clasts of mudstone into a basin from surrounding shelf seas (which in any case do not have a record of mudstone deposition) is unlikely to record such anoxic/euxinic signatures. Additionally, there is a general upward transition of mudstone lithofaceis shifting from calcareous mudstone to clay lens-rich organic-rich shales in the Bowland Shale Formation. This suggests that the deposition of lenticular mudstone relates to environmental change showing elevated productivity and/or enhanced preservation (high TOC) while deposition of reworked intraclast cannot explain this.

5.2 Future work

1. Are ramp carbonate more prone to demise by intrusion of anoxia water body than platform carbonates?

Black shale deposition is both recorded in West Canada Sedimentary Basin and Bowland Basin. However, whilst black shale deposition is responsible for the carbonate demise in the first one this is not the case in the Bowland, at least for the adjacent platform carbonate on the Askrigg Block. However, west of the Bowland Basin, in the Dublin Basin, a carbonate platform is onlapped by black shales suggesting such settings are not immune to basinal anoxia. The Central Lancashire High adjacent to the Bowland Basin was a small but productive platform onlapped by the Upper Bowland Shale indicating another likely example of platform demise due to incursion of anoxic waters. Further examples are needed of integrated redox histories of basins and platforms to evaluate the causes of carbonate productivity persistence.

2. Is the warm saline bottom water (WSBW) model more widely applicable to basins surrounded by carbonate platform?

A warm saline bottom water model is proposed to foster anoxia in the Bowland Basin, because of the unlikelihood of developing a positive water balance basin when surrounding areas are carbonate platforms. However, direct evidence of elevated salinity is not available. Potentially this notion could be tested by organic biomarker or other salinity proxies to see if there is any salinity change with the onset of black shale (e.g. Christiansen et al., 1993; Wei & Algeo 2020).

3. What mechanism controls redox variation in Bowland Shale?

In Chapter 3, it is proposed that deoxygenation in Bowland Basin is associated with influx of warm saline bottom water from surrounding platforms but the reasons for the redox evolution in the basin is unclear. Although the input of calciturbidite and sandy turbidite episodically marginally improves oxygenation, the redox analysis overall reveals a trend from oxic, ferruginous, weakly euxinic to highly euxinic conditions. A control on this long-term trend could be changes in the phosphorus cycle. Phosphorus cycling in Bowland Basin is limited in early Asbian as the water column is fully oxygenated and much P is likely sequestered with iron oxides. It is hypothesized that the onset of anoxia may trigger the phosphate cycling in this basin, promoting elevated primary productivity in the surface water which could again enhance organic matter influx to the seafloor. Considering the absence of upwelling, the phosphate flux via recycling could play a dominant role in controlling the supply of nutrient and redox variation in the basin. Evaluation of phosphorus speciation (ratios of C_{org}/P_{org} and C_{org}/P_{reac}) could be applied to quantify P recycling in different redox settings.

4. Can Re/Mo and Re/U be reliable redox proxies?

Re becomes an increasingly important proxy in evaluating transitional redox conditions due to its unique redox potential. In contrast to accumulation of U and Mo, Re drawdown begins in shallow dysoxic sediments even when bottom waters are oxygenated, indicating a sensitivity to the subtle redox variation. In addition, Re accumulation is not associated with a particulate shuttle and not adsorbed by any oxide minerals. However, in the presence of H_2S, reprecipitation may occur with complexes of Mo-Fe-S which are enriched in euxinic condition (Helz 2022). To explore the variation of Re/Mo and Re/U in diverse redox settings, a compilation of U, Mo and Re data from modern environment is envisaged. Combined with the data in Chapter 3, and data from other basins, a study on application of Re/Mo and Re/U could help develop more sophisticated and subtle redox proxies.

References

Christiansen, F.G., Piasecki, S., Stemmerik, L., & Telaes, N. 1993. Depositional environment and organic geochemistry of the Upper Permian Ravnefjeld Formation source rock in East Greenland. *AAPG bulletin*,**77(9)**, 1519-1537.

Emmings, J.F., Davies, S.J., Vane, C.H., Moss-Hayes, V. & Stephenson, M.H. 2020a. From marine bands to hybrid flows: Sedimentology of a Mississippian black shale. *Sedimentolog*y, **67**, 261–304, https://doi.org/10.1111/sed.12642.

Emmings, J.F., Poulton, S.W., Vane, C.H., Davies, S.J., Jenkin, G.R., Stephenson, M.H., & Moss-Hayes, V. 2020b. A Mississippian black shale record of redox oscillation in the Craven Basin, UK. *Palaeogeography, Palaeoclimatology, Palaeoecology*, **538**, 109423.

Evans, D.J., & Kirby, G.A. 1999. The architecture of concealed Dinantian carbonate sequences over the Central Lancashire and Holme highs, northern England. *Proceedings of the Yorkshire Geological Society*, **52(3)**, 297-312.

Fraser, A.J., & Gawthorpe, R.L. 1990. Tectono-stratigraphic development and hydrocarbon habitat of the Carboniferous in northern England. *Geological Society, London, Special Publications*, **55(1)**, 49-86.

Helz, G.R. 2022. The Re/Mo redox proxy reconsidered. *Geochimica et Cosmochimica Acta*, **317**, 507-522.

Schieber, J., Southard, J.B. & Schimmelmann, A. 2010. Lenticular shale fabrics resulting from intermittent erosion of water-rich muds—interpreting the rock record in the light of recent flume experiments. *Journal of Sedimentary Research*, **80**, 119–128, https://doi.org/10.2110/jsr.2010.005.

Wei, W., & Algeo, T.J. 2020. Elemental proxies for paleosalinity analysis of ancient shales and mudrocks. *Geochimica et Cosmochimica Acta*, **287**, 341-366.

Appendix A Field locations in Bowland Basin and on Craven Fault Belt. Locations are given with six figure national grid references.

No.	Location Name /national grid ref	Description of the site	Lithology	Biostratigraphy	Setting
1	Cow Close (CC) SD 908 622	A 19 m-thick section of Upper Bowland Shale, stream section	Dark grey shales with horizons of large, ovoid concretions.	E_{1b} zone (Arthurton *et al.*, 1988)	Craven Fault Belt
2	Clough Head Beck (CH) SD 822 438	An 18.5 m-thick stream section of the Ravensholme Limestone Member	Alternating calcareous shales and laminated or massive limestones	P_{1a-b} zone (Earp *et al.*, 1961)	Bowland Basin
3	Dinckley Hall (DH) SD 688 366 to SD 685 366	Left bank of River Hodder, 106 m-thick section including both the Lower and Upper Bowland Shale	Mainly dark grey shale and calcareous shale with a few thin calcarenite lenses and sandstone interbeds	P_{1a}- E_{1b} zone (Earp *et al.*, 1961)	Bowland Basin
4	Dob Dale Beck (SF) SD 752 596 to SD 754 596	A 60 m-thick section in the Pendleside Sandstone and Lower Bowland Shale	Sandstone and massive siltstone in the lowest 6 m, overlain by mudstone and shale	P_{1d}- P_{2b} zone (Earp *et al.*, 1961)	Bowland Basin
5	Dobson’s Brook (DB) SD 619 441	A 15.7 m- thick stream section in the Lower Bowland Shale	Dominantly dark grey mudstones with interbeds of calcarenite and a calcirudite	B_{2a}- B_{2b} zone (Aitkenhead *et al.*, 1992)	Bowland Basin
6	Fountain Fell (FF) SD 873 718	A 32 m-thick gully section in the Yoredale Group	2 m sandy limestone bearing shell fragments succeeded by a 30 m succession consisting of medium-grey mudstone, silty mudstone and siltstone with plant fragments, burrows and diverse brachiopods	E_{1a} zone (Hudson, 1940)	South margin of Askrigg Block
7	Fell Lane (FL) SD 987 598	Section in the walls of a sinkhole that exposes the contact between the Pendleside Limestone and ~15 m of the overlying Lower Bowland Shale	Coarse-grained, crinoidal grainstone, overlain by 15 m of interbedded black shales, coarse calcarenites and calcirudites.	P_{1b}- P_{1c} zone (Booker & Hudson, 1926; Black, 1940)	Craven Fault Belt
8	Linton Church (LT) SD 005 633	Left bank of River Wharfe displaying 14 m-thick section of Upper Bowland Shale	Dark grey shale with abundant *Posidonia* and goniatites, large elongate concretions	E_{1b} zone (Black, 1950)	Margin of Askrigg Block
9	Leagram Brook (LB) SD 630 452 to SD 629 451	A 22 m-thick stream section of Lower Bowland Shale	Dominated by mudstones but with thin limestones	B_{2a}- P_{1a} zone (Aitkenhead *et al.*, 1992)	Bowland Basin

10	Light Clough (LC) SD 752 377	A 31 m-thick section in a small stream, straddling the Lower/Upper Bowland Shale boundary	Mainly dark grey shale with several, thin calcisiltite beds	P_{2c} – E_{1a} zone (Earp *et al*., 1961)	Bowland Basin
11	Moor Close Gill (MC) SD 933 639 to SD 935 640	An 18 m-thick stream section of Upper Bowland Shale	Mainly dark grey shale with abundant *Posidonia* and goniatites throughout	E_{1c} zone (Arthurton *et al*., 1988)	Craven Fault Belt
12	River Hodder (RH) SD 702399	A 35m thick river section beginning in the Hodderense Limestone (~2 m thick)	Mainly tabular beds of limestone of calcarenite and bioclastic wackestones with minor beds of grey shale, and small-scale slumping.	B_1 zone (Earp *et al*., 1961)	Bowland Basin
13	School Share (SS) SD 846 623	A 10 m thick section of Upper Bowland Shale in a tributary of Scaleber Beck	Dominated by dark grey shales with irregular masses of limestone boulder beds in the upper 5 m	P_2- E_{1b} (hiatus in E_{1a} zone) (Dixon & Hudson, 1931)	Craven Fault Belt
14	Smelthwaite Farm (SM) SD 711 494	A highly condensed (~ 23 m thick) stream section, ranging from the Hodderense Limestone to the Lower Bowland Shale	Pale micritic limestone in the first 8 m, succeeded by 12 m- thick dark grey shale with calcarenite lenses	B_2- P_{1c} zone (Earp *et al*., 1961)	Slaidburn Anticline (intrabasinal high)
15	Swardean Clough (SC) SD 765 391	A 53 m–thick stream section from the top of Pendleside Limestone into the Lower Bowland Shale	Mainly limestone beds in first 4 m section, followed by ~50 m-thick dark grey shale with gaps	B_2- P_{1a} zone (Earp *et al.,* 1961)	Bowland Basin
16	Tory Log Clough (TLC) SD 833 447	A 135 m-thick stream section from the top of the Pendleside Limestone to the Lower Bowland Shale with the Pendleside Sandstone Member at the top	Alternating beds of micritic limestone and mudstone followed by, at height of 56 m, dark grey shale with thin beds of calcarenite and micrite; sandstone beds appear at 106 m height	B_2- P_{1d} zone (Earp *et al.,* 1961)	Bowland Basin

References

Aitkenhead, N., McC Bridge, D., Riley, N.J., and Kimbell, S.F., 1992, Geology of the country around Garstang. Memoir for 1:50 000 sheet 67 (England and Wales). British Geological Survey.

Arthurton, R.S., Johnson, E.W., and Mundy, D.J.C., 1988, Geology of the country around Settle. Memoir for 1:50 000 sheet 60 (England and Wales). British Geological Survey.

Black, W.W. 1950. The Carboniferous geology of the Grassington area, Yorkshire. *Proceeding of Yorkshire Geological Society*, **28**, 29–42.

Black, W.W. 1940. The Bowland Shales from Thorlby to Burnsall, Yorkshire. Transactions of the Leeds Geological Association, **5**, 308-321.

Booker, K.M. and Hudson, R.G.S. 1926, The Carboniferous sequence of the Craven Lowlands south of the reef limestones of Cracoe. *Proceedings of the Yorkshire Geological Society*, **20**, 411-438.

Dixon, E.E.L. and Hudson, R.G.S. 1931, A Mid-Carboniferous boulder-bed near Settle. *Geological Magazine*, **68**, 81-92.

Earp, J.R., Magraw, D., Poole, E.G., Land, D.H., and Whiteman, A.J. 1961, Geology of the country around Clitheroe and Nelson. Explanation of one-inch geological sheet 68, new series. Institute of Geological Sciences.

Hudson, R.G.S. 1940. The mirk fell beds (Namurian, E2) of tan hill, Yorkshire. *Proceedings of the Yorkshire Geological Society*, **24**, 259–289.

Appendix B Framboidal pyrite date set on TLC, SM, RH and DH section

Sample ID	pyrite diameter in µm										
TLC-2	5.29	6.93	8.62	6.42	5.35	5.22	3.59	6.30	5.12	5.04	3.50
	4.18	4.27	6.15	5.70	7.12	5.86	5.10	4.37	4.02	5.13	5.56
	2.80	2.87	7.76	12.27	4.74	9.30	5.40	6.04	6.71	5.10	6.17
	5.35	5.90	3.83	3.73	6.65	7.20	6.76	6.98	6.67	6.19	6.82
	12.89	7.68	5.91	4.71	6.13	9.69	9.12	5.94	7.46	7.86	7.21
	7.62	6.10	6.36	6.88	7.40	6.29	6.00	4.56	6.39	6.70	4.70
	5.99	7.47	9.09	7.02	7.33	8.08	5.97	6.94	7.17	7.89	8.51
	5.85	5.48	8.69	6.93	7.06	7.59	7.78	4.66	6.60	4.52	6.34
	8.99	8.29	10.33	7.12	6.65	7.95					
TLC-30	6.40	8.53	9.02	7.41	6.80	6.16	5.81	6.74	8.39	5.01	5.38
	9.78	5.75	6.64	9.66	9.23	6.90	10.16	4.43	4.67	7.86	7.55
	8.12	7.90	12.14	10.11	4.90	5.85	7.43	7.17	7.55	10.58	7.96
	18.61	6.83	7.30	4.28	8.69	7.72	4.18	8.75	10.18	8.55	6.03
	6.75	5.92	6.64	12.73	5.60	12.88	7.27	7.48	5.97	5.22	6.22
	5.17	7.59	5.73	4.04	7.83	6.89	7.91	6.01	5.27	6.24	10.01
	7.84	5.60	5.54	8.55	6.89	10.18	8.33	4.81	8.89	7.54	9.26
	6.30	5.56	6.95	8.81	7.56	8.22	16.14	7.38	10.11	6.45	10.85
	5.42	7.25	6.33	8.68	7.04	7.36	7.44	10.93	11.26	10.85	6.78
	16.17	8.35	7.56	13.79	7.91	7.97	7.36	7.71	6.00	8.38	7.75
	5.17	9.38	12.62	8.92	10.93	7.48	8.90	8.11	7.60	9.34	8.07
	8.51	7.22	9.22	25.41							
TLC-74	6.49	7.91	8.08	8.48	11.29	11.76	11.82	11.85	12.06	12.71	3.95
	14.09	16.34	45.27	8.11	6.29	17.40	6.41	4.86	8.74	5.28	5.23
	6.20	3.19	7.71	5.54	5.97	14.45	4.46	8.74	5.70	10.67	6.05
	7.78	13.48	15.16	7.25	4.71	7.42	8.92	6.72	5.72	10.85	33.17
	5.19	4.31	6.11	4.88	5.39	6.78	7.52	7.35	6.41	9.98	9.44
	8.33	5.10	5.59	8.33	4.98	5.79	8.12	5.12	9.24	12.13	4.79
	3.66	4.14	5.72	6.81	7.41	7.87	7.72	4.58	9.19	4.85	4.56
	5.14	5.93	10.98	15.72	7.29	7.60	4.95	6.72	5.15	7.31	5.32
	6.87	6.09	11.72	7.19	6.20	7.84	9.56	11.06	18.83	5.42	5.96
	6.77	8.66	5.18	7.52	8.06	11.32	10.33	6.17	5.19	8.33	7.49
	6.11	8.10	3.64	8.66	6.03	6.38	5.41	5.49	6.06	6.41	6.78
	6.33	10.37	26.85	6.52	10.19	7.71	7.38	5.05	5.33	5.46	4.59
	11.73	5.91	7.84	5.29	6.14	6.79	5.80	7.12	7.13	13.58	5.97
	6.74	6.97	7.12	29.51	4.60	6.20	6.99	9.35	10.07	7.37	7.43

	7.95	11.46	8.50	9.57	4.72	6.82	18.02	4.44	5.53	8.05	8.58
	6.12	4.68	14.16	9.38	7.28	9.67	6.65	43.96	27.62	10.33	20.30
	5.38	6.21	7.14								
TLC-45	7.23	8.57	4.35	4.71	4.54	4.84	17.03	7.75	6.22	5.88	5.88
	7.57	5.76	4.31	7.72	4.40	5.04	12.01	4.28	4.73	5.27	4.28
	4.72	8.70	6.93	12.30	4.30	6.88	11.45	15.85	12.94	5.97	3.65
	4.90	4.22	7.23	7.58	6.16	6.61	4.45	4.18	4.16	8.73	6.14
	6.99	3.88	10.41	5.99	8.04	21.44	6.31	8.41	6.57	7.12	5.07
	6.28	4.14	7.68	5.36	5.78	6.50	4.73	6.22	7.10	17.77	9.38
	7.17	8.83	8.46	7.19	6.06	48.82	4.08	7.39	8.26	7.89	5.43
	5.32	5.59	6.17	6.47	6.61	17.02	17.44	7.69	12.32	7.42	13.12
	42.72	5.37	8.66	5.49	5.20	4.81	7.37	7.82	10.95	8.23	9.06
	5.96	14.91	14.84	5.31	9.08	6.55	7.16	7.09	8.61	6.03	4.67
	6.70	13.43	10.22	5.90	20.81	7.95	4.27	13.42	3.70	5.72	
TLC-48	No framboid observed										
TLC-28	11.17	8.65	9.09	6.35	8.91	10.74	11.80	6.38	7.26	8.56	6.98
	7.45	6.48	8.78	4.59	8.46	9.61	9.98	7.81	7.09	6.36	6.94
	6.74	8.01	11.18	8.92	12.98	8.02	5.77	5.72	9.77	4.94	13.45
	8.48	7.05	5.29	5.89	8.32	6.51	56.00	4.54	7.25	5.95	7.66
	6.71	4.91	4.27	6.39	7.53	8.16	8.26	7.47	3.45	4.66	17.23
	7.29	4.90	6.46	5.65	8.97	5.89	6.27	5.67	10.29	12.78	5.39
	6.75	7.82	9.25	9.81	8.08	4.45	6.21	5.77	6.73	5.52	4.62
	6.61	11.17	6.17	5.40	13.36	7.62	5.20	8.82	7.10	6.89	5.90
	7.05	3.15	5.35	6.54	10.07	6.53	9.62	5.10	5.77	6.43	5.42
	10.44	7.01	9.68	7.83	4.41	8.64	6.90	7.01	4.34	5.85	5.96
	3.66	3.98	4.67	7.95	8.65	9.21	9.49	7.48	9.87	7.57	5.89
	12.69	6.54	53.69	14.13	12.92	10.81	6.57	12.60	5.96	7.14	7.48
	4.65	3.39	5.80	8.57	11.86	6.53					
TLC-56	8.48	7.52	8.38	6.11	3.36	4.49	6.41	6.95	4.41	5.35	4.25
	5.15	7.04	4.35	6.24	5.87	4.51	4.40	18.86	6.68	4.24	4.24
	4.23	5.73	6.75	4.52	4.84	5.20	3.16	7.02	3.72	3.70	4.64
	5.60	5.64	5.68	6.18	3.72	5.00	6.86	6.51	6.05	6.63	6.24
	5.74	5.03	4.16	5.82	6.33	8.72	5.88	5.26	4.35	6.31	5.75
	4.39	6.29	5.92	7.97	4.18	6.58	5.95	4.89	4.71	5.88	5.64
	4.22	5.24	4.89	3.97	3.46	3.65	4.56	5.52	4.45	5.41	5.40
	9.49	29.19	5.70	6.10	5.74	3.77	3.95	5.13	9.31	5.44	5.28
	5.87	9.19	4.12	4.68	5.47	4.46	3.85	8.77	6.62	6.77	6.39
	5.32	5.33	4.41	6.20	4.87	7.52	8.18	3.88	5.95	6.23	4.96
	2.89	4.36	3.76	4.97	5.14	5.28	4.81	5.79	5.76	4.47	4.96
	8.46	16.95	3.93	5.95	5.45	5.33	6.80	6.22	5.04	6.32	5.06
	5.54	4.70	6.45	15.60	4.89	4.93	8.13	6.28	8.48	8.04	6.97
	4.41	4.18	5.54	6.68	4.02	4.23	4.45	3.28	3.49	4.18	6.04
	5.39	6.65	5.87	4.92	5.98	5.64	7.26	6.96	17.70	4.92	4.80
	5.54	6.68	4.02	4.23	4.45	3.28	3.49	4.18	6.04	5.39	3.49
	5.63	6.05	3.82	3.43	4.32	5.18	5.73	4.96	4.88	5.13	5.87
	4.86	6.33	5.58	5.73	4.79	5.13	5.57	4.85	4.20	5.99	6.37
	4.95	16.78	4.11	5.32	6.48	5.86	4.60	6.98	7.24	3.94	4.22

	5.99	4.51	4.90	6.75	5.96	5.23	5.04	8.83	5.84	5.05	2.99
	4.30	6.47	4.96	3.04	5.37	6.02	4.02	5.90	4.60	6.35	3.80
	4.70	3.25	4.32	7.65	2.86	4.49	3.60	4.62	4.67	5.84	3.34
	6.34	5.29	3.93	4.00	7.86	4.53	10.31	5.70	5.98	4.94	6.00
	5.74	6.76	5.18	5.45	5.87	4.67	4.78	5.74	4.58	3.57	6.25
	3.50	5.22	6.17	5.80	8.10	5.35	10.20	4.64	5.19	5.14	13.76
	6.29	6.53	4.54	7.11	7.78	6.80	6.34	5.03	7.91	7.12	2.71
	4.57	3.50	5.07	4.98	13.82	4.42	5.86	5.26	4.06	5.48	7.28
	5.46	5.72	6.16	8.16	3.61	4.29	8.50				
TLC-86	No framboid observed										
TLC-57	4.79	7.07	5.15	4.60	8.13	10.61	4.07	4.37	12.01	4.15	6.95
	5.79	5.19	4.52	4.80	5.85	6.85	7.09	6.95	9.62	5.92	6.17
	4.20	4.87	5.14	8.13	4.72	3.80	5.72	5.61	18.61	8.22	5.91
	6.33	6.41	6.83	5.92	5.20	4.59	4.15	5.66	5.09	5.69	8.02
	5.48	6.68	11.16	6.82	14.48	6.66	11.74	5.71	8.86	6.33	5.12
	4.87	3.87	3.88	8.17	8.72	5.59	4.66	4.79	19.17	4.41	8.25
	5.75	15.23	4.94	6.12	5.49	4.10	4.18	4.04	8.74	16.41	7.00
	11.08	6.24	5.88	10.27	4.16	4.88	8.67	6.45	3.04	5.75	8.74
	5.54	4.89	4.78	5.43	11.31	7.65	20.58	5.10	7.24	3.34	4.51
	5.02	5.35	5.32	3.58	3.81	5.56	5.63	5.56	5.30	4.85	8.94
	6.53	4.91	5.22	5.89	7.60	5.58	9.46	6.18	3.68	4.86	7.32
	5.64	5.17	5.95	5.03	3.33	6.50	6.48	5.96	7.47	6.24	6.48
	5.96	6.17	4.73	8.40	8.03	3.84	8.86	4.66	9.66	4.23	6.47
	5.12	4.75	5.52	16.44	29.88	6.46	8.66	8.84	5.17	7.88	4.57
	4.68	4.81	5.04	5.50	6.68	6.83					
TLC-19	7.41	5.57	6.69	4.50	4.79	3.98	14.44	7.81	5.99	9.19	8.06
	13.75	7.73	5.44	7.69	6.32	6.61	7.49	5.25	4.40	4.88	5.57
	6.36	8.80	8.25	8.20	5.32	7.81	10.22	5.93	7.16	7.44	9.59
	7.85	5.68	6.73	7.66	5.69	9.18	9.01	4.82	7.03	6.60	8.15
	8.91	9.24	6.53	7.31	7.93	6.68	6.57	5.03	3.07	9.60	6.94
	5.75	5.53	8.64	9.07	8.12	5.76	5.35	5.97	7.12	10.16	6.90
	5.13	9.34	4.61	6.13	6.76	6.88	7.17	8.26	5.57	6.67	6.80
	10.15	6.52	4.64	6.78	9.60	5.27	7.37	7.91	5.67	6.14	3.92
	6.19	7.78	7.39	11.65	5.72	6.55	6.80	5.89	6.34	10.02	6.94
	5.98	8.07	4.30	5.18	5.29	5.32	5.54	7.11	7.29	6.13	7.56
	6.70	11.30	7.57	8.46	10.98	6.35	7.93	6.98	7.09	5.32	9.71
	10.19	7.19	7.06	9.84	11.32						
TLC-100	29.47	22.57	21.53	20.87	19.24	17.39	17.29	16.85	15.35	14.67	4.16
	14.09	13.61	11.60	9.14	7.38	6.27	5.99	5.59	5.32	5.00	5.54
	6.38	6.76	7.08	13.22	14.82	17.81	23.17	55.85	66.86	21.23	4.50
	28.44	49.88	5.71	5.94	6.78	7.44	16.80	18.47	5.28	6.16	13.42
	15.32	18.00	4.61	5.21	5.28	6.94	10.12	11.55	17.26	18.49	9.86
	4.57	6.23	6.74	6.92	7.15	13.93	21.64	23.97	4.61	5.13	5.24
	5.56	5.98	7.07	10.55	17.08	17.98	19.79	25.22	2.60	3.10	3.47
	3.63	3.94	4.33	4.45	4.87	5.29	5.63	6.02	7.56	9.05	9.70
	5.51										
TLC-85	4.57	7.32	29.80	4.15	4.47	5.28	7.86	28.44	5.37	5.39	7.19

	4.80	14.23	19.26	5.56	4.39	5.31	6.23	6.27	9.05	5.71	4.73
	6.11	5.12	4.21	5.28	6.86	6.43	10.96	4.04	6.07	6.21	6.27
	6.51	6.75	6.68	6.98	7.87	30.95	5.64	5.12	6.36	6.61	7.21
	7.57	7.62	9.36	9.95	13.99	8.00	5.73	4.04	4.46	4.46	4.70
	7.33	4.42	4.53	11.45	5.42	7.41	8.00	4.40	4.46	5.61	5.80
	8.96	12.08	5.76	6.09	6.18	4.74	4.74	4.89	5.03	5.03	5.16
	5.47	9.50	11.07	5.90	9.40	7.25	9.66	19.54			
TLC-80	8.83	6.74	6.15	8.12	8.63	6.67	7.62	8.09	7.31	8.25	6.53
	7.57	11.90	6.08	5.24	7.44	8.54	5.25	8.17	10.78	2.73	6.13
	6.13	6.30	6.36	6.62	7.76	6.13	3.65	3.66	4.23	14.02	8.01
	7.91	6.38	5.53	12.94	8.70	5.45	9.92	14.52	7.07	8.31	8.74
	4.89	7.59	6.97	7.96	17.79	4.27	4.31	4.41	6.79	6.82	5.50
	3.97	5.95	6.59	3.79	4.17	6.98	6.52	5.34	9.21	7.47	7.70
	6.57	6.15	8.78	5.43	5.67	6.54	8.18	7.70	6.45	4.73	5.14
	16.17	5.50	5.55	6.34	7.74	8.14	9.01	4.00	6.43	8.83	4.53
	10.38	5.48	5.74	5.11	5.40	6.13	7.45	7.54	5.84	6.82	4.38
	5.49	6.79	5.76	6.85	5.59	6.02	7.92	9.73	10.81	5.28	5.47
	5.94	5.97	3.96	4.21	5.45	9.05	8.01	6.21	7.19	7.94	5.81
	9.66	9.00	6.33	13.72	8.10	4.36	5.37	6.73	6.74	9.39	8.89
	9.15	10.37									
TLC-2	6.66	6.74	6.94	7.89	5.03	4.98	9.82	32.56	7.37	5.70	5.32
	6.46	6.72	15.22	7.90	5.42	8.60	7.73	4.43	8.64	5.81	9.07
	12.57										
TLC-39	8.14	8.68	7.72	8.21	10.63	5.98	6.10	8.98	7.27	9.98	8.23
	9.19	4.18	6.72	10.37	12.34	8.10	12.18	6.92	9.83	9.89	8.80
	7.24	8.74	9.84	8.04	7.53	11.65	4.34	9.38	6.99	7.72	8.25
	6.04	8.99	8.19	8.69	9.20	12.15	8.09	10.16	9.01	10.10	9.25
	10.70	14.95	6.05	8.99	10.15						
TLC-15	8.34	9.18	9.78	11.48	11.71	11.83	13.20	13.46	15.29	7.25	18.16
	7.96	5.73	5.78	6.99	7.28	7.36	7.52	7.55	9.44	6.72	13.41
	5.74	9.87	19.25	28.65	5.91	8.94	9.62	11.00	14.01	21.39	4.96
	19.36	13.54	57.32	8.58	27.50	8.38	11.20	13.80	14.74	15.45	6.01
	6.60	9.19	10.46	6.95	6.81	28.25	9.94	57.32			
TLC-35	11.40	8.31	8.62	7.30	8.17	6.07	7.06	7.09	9.03	7.31	5.30
	9.77	11.09	7.67	7.90	8.87	7.86	12.67	9.13	9.73	6.35	6.51
	7.17	9.34	7.54	7.89	7.92	8.83	10.34	9.26	12.30	9.62	10.30
	8.02	7.86	7.07	7.67	9.31	11.54	11.09	8.32	7.82	7.08	7.43
	8.73	10.30	6.57	6.36	7.72	8.25	6.80	6.65	8.40	5.80	7.21
	7.63	5.85	7.92	6.25	5.91	7.52	5.61	6.58	9.23	5.81	7.88
	6.21	6.87	7.31	6.86	6.72	8.59	8.18	7.02	6.58	6.76	7.97
	6.10	7.74	9.36	8.68	10.44	10.06	8.39	9.20			
TLC-8	10.29	10.19	7.44	7.47	8.32	10.91	13.45	7.82	13.23	16.06	8.40
	19.48	7.55	9.87	8.66	10.01	6.11	8.38	10.96	13.62	7.92	13.32
	16.10	10.33	20.72	10.27	13.04	10.11	7.77	7.80	9.25	12.67	13.71
	9.56	13.57	16.16	12.42	5.32	7.71	9.04	10.12	6.53	7.56	14.14
	13.77	10.52	13.95	16.40	14.28	8.25	5.09	7.44	8.07	7.47	13.76
	14.47	13.78	11.05	14.61	16.55	14.37	18.58	10.08	9.14	10.79	4.16

	5.74 9.01 13.87 11.60 14.84 17.89 16.63 6.65 8.55 6.26 7.38 20.85 7.19 10.84 15.00 11.18 14.93 18.76 16.77 5.36 6.16 9.93 7.35 8.03 12.34 11.26 15.97 11.93 15.20 23.18 17.28 7.31 11.94 12.63 13.29 5.76 11.32 12.15 16.52 12.34 15.27 23.32 17.57 5.58 8.15 7.06 9.80 11.03 10.49 13.41 17.37 12.91 15.50 26.31 7.75 8.82
TLC-103	35.13 25.24 9.41 19.53 11.86 25.91 27.88 24.11 21.78 22.06 9.01 6.35 8.47 10.49 8.07 8.65 13.65 18.85 20.51 6.36 7.05 7.59 7.75 8.68 8.98 9.47 10.09 5.43 6.02 6.10 6.13 6.26 6.42 6.89 11.71 16.35 19.06 52.01
TLC-92	5.73 6.20 6.59 5.97 2.63 4.00 8.50 5.54 5.80 7.68 4.33 6.34 7.78 7.62 6.41 6.52 4.52 6.09 6.10 5.69 11.72 4.62 5.34 7.39 9.21 4.69 7.62 7.80 4.01 4.11 6.34 6.11 3.60 6.04 6.45 7.92 8.97 7.58 8.67 12.29 3.67 5.54 5.95 3.69 4.55 4.04 6.27 3.18 3.94 4.17 5.94 4.34 6.60 8.75 4.85 5.70 4.48 4.73 4.97 7.22 5.18 6.53 5.76 4.69 5.23 4.58 4.51 4.73 6.20 5.34 6.38 6.37 10.45 7.00 3.17 4.45 7.83 2.97 7.68 7.18 7.62 3.51 7.83 4.07 5.64 4.64 4.16 12.51 4.46 4.77 7.94 6.70 6.85 3.64 3.76 2.04 3.16 4.32 7.35 7.10 7.35 9.95 4.96 6.35 3.34 3.38 3.52 3.66 4.16 6.93 6.33 6.54 4.39 6.56 5.39 10.62 6.87 8.61 4.71 7.88 6.18 10.87 8.82 9.61 4.90 3.03 6.69 5.99 6.84 8.99 13.35 4.01 8.27 4.28 4.82 3.61 5.84 4.74 10.56 5.57 4.82 6.87 3.90 5.60 9.40 6.65 4.93 9.53 4.24 10.12 4.38 7.98 8.47 3.51 8.84 3.60 4.76 2.50 13.00 3.59 3.71 6.37 7.20 3.87 5.83 4.06 4.44 6.74 8.75 5.51 6.12 5.88 6.20 5.26 14.85 5.64 4.55 9.54 6.40 10.34 6.54 5.40 7.19 6.25 6.26 6.31 9.92 7.65 6.32 6.49 8.83 5.32 6.63 6.00 8.27 7.39 4.87
TLC-25	6.27 11.19 10.34 6.10 10.87 6.27 16.87 4.91 5.67 7.47 14.08 6.19 6.59 6.72 6.88 6.86 7.04 6.69 5.41 6.34 5.01 3.94 6.31 8.99 3.12 6.98 7.01 7.17 5.59 5.71 6.96 7.38 6.45 7.87 8.13 9.58 4.67 6.45 8.96 5.91 7.65 7.92 6.36 8.10 5.16 7.10 28.81 6.06 6.35 6.88 6.41 8.23 6.32 7.21 5.80 10.05 7.02 4.84 39.38 7.20 6.72 7.72 7.60 7.04 5.88 17.70 6.37 7.49 5.10 4.93 7.47 7.65 6.60 7.32 9.09 6.03 7.88 9.92 19.02 6.24 7.51 8.36 7.83 6.36 8.42 7.27 6.67 6.38 11.49 14.38 6.29 5.61 5.82 6.28 6.77 11.14 9.71 6.70 12.79 7.15 7.63 4.92 6.89 5.48 3.83 6.42 5.80 8.01 6.50 12.22 7.16 46.97
TLC-98	8.71 8.08 6.79 3.81 8.28 5.03 7.96 5.98 5.82 5.77 5.44 22.16 18.67 9.46 6.12 4.53 4.29 8.35 7.80 7.41 7.00 6.96 6.90 9.54 6.02 8.84 7.64 9.26 7.91 7.25 8.37 7.61 7.19 7.13 7.10 6.31 9.13 8.17 5.28 7.91 15.92 4.80 8.00 7.66 7.43 7.09 6.98 6.75 6.74 5.38 7.08 16.03 8.41 8.32 8.09 8.07 7.86 7.79 7.69 7.69 7.66 7.49 7.33 7.20 7.04 7.03 6.99 6.98 6.93 6.92 6.89 6.54 4.89 15.18 12.39 6.81 19.63 7.08 6.17 8.77 7.34 5.60 10.96 32.23 9.71 8.61 8.11 8.07

	6.47	5.54	58.70	29.96	9.47	8.22	7.17	6.10	19.77	11.32	
	10.05	27.87	13.09	12.46	20.44	18.00					
SM-1	5.51	5.28	7.97	8.13	9.13	5.08	4.41	4.07	12.85	10.15	9.62
	7.94	4.72	4.44	4.43	3.29	9.61	9.21	7.95	6.18	6.16	5.03
	8.93	8.04	5.63	4.96	8.99	6.86	6.56	4.23	2.72	7.46	5.42
	4.58	4.28	3.96	6.90	6.20	5.33	7.23	5.66	16.41	6.86	5.85
	3.37	10.71	6.07	5.22	2.99	7.42	6.43	5.49	5.26	5.18	8.68
	6.50	5.73	5.30	5.17	4.17	6.01	5.77	9.29	8.07	7.51	7.24
	7.22	6.93	9.98	7.42	7.38	7.34	5.50	4.97	4.80	3.82	2.73
	7.31	6.98	5.72	5.68	4.71	4.66	4.54	13.44	10.05	8.13	7.51
	6.74	12.03	5.33	4.74	18.35	10.68	8.38	5.76	5.73	5.01	6.39
	4.52	4.40	6.25	6.15	15.99	29.43	17.01	5.51	5.05	5.00	4.93
	4.66	4.05	9.13	8.41	8.06	7.33	5.47	4.01	3.56	8.64	8.00
	6.23	6.04	4.40	4.00	3.91	2.59	9.96	7.59	6.80	6.74	4.87
	11.98	9.56	9.31	9.04	7.73	7.46	6.35	10.23	8.72	7.39	15.01
	9.53	6.95	5.25	24.06	13.50	13.03	8.80	7.75	7.66	14.68	
	11.86	8.15	7.92	5.17	3.66	7.61	5.92	4.90			
SM-2	No framboid observed										
SM-3	8.99	11.47	10.78	9.12	8.92	8.81	8.76	8.70	8.55	8.33	7.65
	7.44	7.08	6.80	6.54	6.29	6.16	12.37	10.55	8.07	6.70	6.67
	5.36	4.13	3.07	6.86	6.68	6.49	5.42	4.78	4.02	4.01	4.00
	3.89	3.88	3.74	3.58	3.49	3.33	9.71	8.78	8.72	8.66	7.86
	7.77	7.32	6.40	6.39	6.28	5.96	5.59	5.57	5.47	5.39	5.09
	5.08	4.91	4.70	4.66	4.38	3.97	3.25	7.91	5.08	10.19	8.81
	8.17	7.68	7.54	7.45	7.30	7.14	7.01	6.74	5.84	5.82	5.01
	3.88	10.02	8.91	7.56	6.96	6.19	6.12	5.98	5.31	4.82	4.72
	3.84	3.64	8.47	7.69	6.59	9.14	6.60	6.27	6.23	6.18	5.73
	11.17	7.83	4.43	8.96	5.91	4.11	7.33	8.44	9.19	9.85	9.09
	7.09	6.95	6.30	9.58	6.47	6.15	6.25	9.13	6.62	6.98	5.14
	6.58	5.74	5.68	5.55	4.81	8.47	7.88	7.65	7.51	7.54	6.96
	6.94	6.93	6.85	11.03	8.01	7.96	7.35	7.20	6.75	6.72	
SM-4	8.71	8.77	5.18	8.19	5.83	7.45	6.50	5.39	4.49	14.64	7.15
	14.43	5.59	5.67	4.82	11.67	5.08	4.98	9.01	9.34	5.17	8.92
	15.35	8.24	3.82	4.33	6.67	8.34	7.96	7.31	8.91	8.04	7.91
	7.77	6.98	6.90	6.63	5.65	5.60	5.56	5.08	8.89	6.44	7.92
	7.45	7.03	6.72	6.45	5.86	5.60	5.33	4.76	3.94	8.14	7.88
	6.10	7.48	6.73	6.87	6.66	5.92	5.18	4.43	7.28	6.76	7.00
	10.53	7.00	6.79	4.65	27.37	6.98	5.79	14.03	7.11	8.56	8.60
	8.41	7.92	6.72	5.24	4.92	15.37	9.84	7.33	6.76	6.64	6.15
	5.51	6.05	9.28	5.68	7.56	6.87	8.92	6.00	3.92	6.28	4.61
	6.78	8.18	5.84	7.25	7.08	6.31	4.85	3.54	7.02	6.82	5.07
	6.58	8.06	7.81	5.78	5.31	4.81	10.52	7.66	7.15	6.48	7.42
	5.85	5.56	5.31	4.32	6.02	5.04	3.94	6.83	6.56	6.27	5.69
	5.33	8.36	7.39	6.94	7.00	6.92	8.90	8.05	8.32	7.12	5.21
	4.10	7.03									
SM-5	9.73	6.97	8.56	7.89	5.96	5.21	7.97	6.92	7.53	5.04	7.73
	8.26	6.11	5.84	5.39	11.50	7.37	6.98	9.38	6.80	8.42	8.16

	5.79	6.18	9.16	6.64	3.97	7.59	6.16	11.89	8.75	7.56	7.37
	6.61	5.72	7.00	6.52	10.14	4.89	3.94	9.42	6.40	5.91	6.45
	6.90	5.41	8.61	7.57	7.31	6.21	6.88	5.90	9.36	6.24	8.79
	8.05	6.71	6.37	5.08	7.14	10.24	6.78	7.65	7.23	7.31	4.38
	9.27	9.82	7.29	7.16	10.05	7.35	7.29	20.84	8.14	8.29	9.85
	8.45	7.20	7.05	5.37	5.17	6.78	4.56	5.90	5.32	5.59	12.28
	11.14	7.98	7.26	6.92	4.60	4.29	4.03	6.46	10.24	5.69	6.11
	7.87	6.50	12.61	5.39	4.72	5.01	6.60	6.31	3.46	7.27	6.21
	7.44	3.58	4.27	7.11	4.57	5.25	8.14	6.14	5.49	4.68	4.40
	4.90	4.86	14.47	15.27	7.27	6.93	4.71	6.84	3.65	6.41	5.30
	8.59	8.73	5.80	14.35	9.03	6.67	6.09				
SM-6	No framboid observed										
SM-7	16.51	9.63	5.74	4.12	3.46	7.04	5.13	4.41	7.45	8.77	6.26
	5.11	5.00	4.84	4.83	5.80	15.77	7.85	6.50	6.65	5.64	8.25
	8.43	4.43	4.63	4.54	5.52	4.21	7.22	4.87	5.28	6.03	5.97
	4.39	3.33	30.72	5.76	5.64	4.11	9.37	8.13	8.57	5.47	8.88
	4.70	4.63	6.77	5.73	4.70	15.34	7.74	7.60	15.54	8.65	8.02
	10.14	6.36	12.91	11.07	4.79	4.82	3.22	4.01	6.11	4.74	5.31
	4.12	5.31	4.20	4.13	6.81	3.96	7.87	6.35	6.52	7.29	6.45
	7.34	6.59	4.69	6.27	5.60	9.51	8.70	6.69	8.17	5.20	10.44
	3.81	11.41	8.21	5.19	4.06	6.67	7.31	5.69	7.17	5.36	4.84
	6.55	7.32	9.30	5.61	4.96	4.01	3.88	5.57	4.21	6.02	4.89
	3.89	3.62	3.57	3.34	4.02	3.00	5.59	8.89	7.50	3.59	5.14
	4.72	4.64	2.79	3.49	6.24	5.72	5.45	4.26	3.24	6.46	5.02
	4.70	4.10	5.84	5.03	10.69	5.75	4.79	6.39	5.45	6.31	6.14
	5.82	5.77	5.91	5.65	4.79	4.47	14.62	6.71	5.76	5.25	5.01
	4.93	4.86	4.76	4.14							
SM-8	6.14	4.29	5.97	7.97	6.78	8.06	5.79	10.09	8.77	5.34	6.54
	5.31	7.82	11.88	6.50	8.25	5.68	10.98	7.58	5.66	5.95	5.55
	8.54	7.81	6.44	4.67	5.12	7.82	7.73	5.12	5.04	7.33	6.87
	7.01	18.92	4.37	7.83	7.22	6.56	11.15	7.13	6.28	5.84	6.61
	9.06	8.12	7.37	6.92	5.14	5.65	6.83	7.86	7.28	4.15	3.66
	6.15	4.85	4.88	6.39	6.13	5.47	9.69	5.25	9.43	7.51	6.24
	5.73	6.48	9.62	7.15	6.18	5.26	8.10	5.89	7.65	5.20	9.02
	7.58	5.72	5.66	6.49	3.61	6.55	6.50	7.83	6.20	6.47	10.17
	5.77	7.73	7.54	5.15	3.47	10.96	7.84	7.02	5.38	6.79	7.67
	5.54	8.71	8.97	7.64	5.54	20.66	17.20	10.92	7.55	10.73	8.95
	5.25	4.83	8.28	7.75	7.64	7.43	9.01	5.48	4.52	5.25	4.89
	5.64	6.17	6.50	5.20	5.48	6.89	4.49	5.18	5.97	5.22	3.86
	4.79	4.24	5.50	7.48	8.26	6.50	4.13	6.26	5.92	5.63	6.99
	6.43	6.88	46.25	8.20	6.59	7.93	5.49	5.93			
SM-10	12.38	9.55	8.92	6.85	5.36	3.09	7.09	5.07	4.66	7.15	7.13
	5.65	4.73	5.45	7.10	4.17	11.68	7.78	10.73	5.89	5.61	8.29
	9.64	8.51	7.65	5.05	4.20	8.81	7.61	6.20	5.90	4.34	5.70
	8.12	14.20	9.10	5.88	5.74	8.44	6.16	10.40	8.37	6.09	7.42
	6.04	11.13	7.58	4.99	8.37	7.40	6.55	5.66	5.32	3.95	18.48
	17.68	5.30	11.82	8.47	10.73	6.55	8.61	8.50	5.61	8.00	6.14

	13.95	9.05	8.71	15.74	12.14	9.11	7.71	6.97	6.92	10.56	5.24
	5.21	8.11	6.36	12.37	8.40	7.03	8.10	6.06	5.54	4.55	4.23
	11.86	7.51	6.31	6.22	5.57	4.64	4.32	5.10	10.07	7.24	9.42
	7.73	5.93	4.42	11.76	7.45	9.87	4.51	4.34	8.91	8.36	7.15
	9.20	8.83	5.43	5.41	6.81	12.62	5.94	3.67	6.99	10.69	9.34
	6.36	6.23	6.79	6.37	8.56	9.55	5.21	6.64	6.81	5.43	4.02
	5.56	8.77	4.93	7.31	5.73	8.07	6.62	13.40	16.10	6.67	6.26
	5.22	6.48	5.97	4.57	4.30	10.26	10.18	5.79	5.81	5.50	4.83
	10.48	5.52	6.49	8.66	6.26	15.28	6.65	4.03	6.64	6.53	6.15
	5.75	4.82	5.71	5.44	8.42	7.45	6.45	7.74	6.71	12.19	7.90
	9.40	8.09	6.72	6.04	9.57	6.54	6.55	6.36	6.43	15.55	5.26
	11.02	6.33	8.50	6.58	6.30	8.10	6.04	5.79	8.89	4.02	9.16
	6.12	5.95									
SM-12	6.03	6.00	5.78	7.95	6.61	6.10	5.98	5.85	5.05	5.10	4.15
	4.00	3.57	3.34	3.11	7.29	5.15	4.71	15.55	5.98	4.07	7.81
	5.05	4.91	3.40	14.46	5.00	4.91	4.76	7.28	6.56	4.83	4.48
	4.36	4.31	4.04	5.66	6.46	4.73	5.25	2.74	4.88	11.03	4.51
	5.76	4.35	3.98	5.95	5.67	5.48	5.00	4.64	4.01	7.46	6.07
	5.06	9.72	6.66	6.56	5.01	8.57	6.79	7.93	6.68	5.68	4.08
	3.63	6.19	5.40	4.80	4.08	6.48	6.37	5.98	5.79	5.59	4.73
	10.00	3.90	5.93	16.94	13.71	6.71	3.91	6.32	6.17	4.74	5.91
	9.53	6.77	5.20	7.00	6.86	5.67	8.87	7.86	7.35	4.97	4.96
	4.50	3.59	10.27	10.20	6.83	5.43	4.89	4.84	10.36	11.78	5.11
	10.62	6.70	5.24	4.54	3.94	3.18	6.37	5.41	4.48	7.71	4.11
	13.07	6.87	10.90	7.47	7.45	6.45	5.97	5.76	5.53	4.16	11.66
	5.28	8.77	6.69	6.35	6.25	5.24	4.85	6.10	11.70	8.08	7.98
	7.60	7.05	9.59	6.00	5.43	5.30	11.25	4.74	7.25	5.13	15.98
	8.31	6.23	4.99	7.74	7.74	5.32	5.05	4.25	8.19	8.17	7.90
	5.90	5.88	11.97	5.78	7.33	5.22	4.53	3.15	16.38	12.94	6.96
	5.81	5.61	6.65	5.72	5.24	4.18	4.10	8.67	6.23	5.68	5.12
	5.02	3.50	5.05	6.34	5.01	12.16	9.54	9.49	8.64	7.49	13.87
	14.90	8.90	8.24	6.51	6.26	5.38	4.25	4.09	6.72	4.44	9.79
	8.91	5.53	5.32	5.01	4.63	4.63	4.32	4.07	11.10	7.70	41.82
	15.08	18.21	6.73	12.23	9.62	8.53	7.91	6.59	6.39	8.25	
SM-13	10.80	4.97	8.83	10.06	10.24	7.04	7.58	7.46	7.18	4.89	8.84
	6.93	2.92	12.24	17.21	8.08	6.46	5.00	6.77	4.92	17.13	8.57
	5.38	15.79									
SM-14	7.81	6.87	6.46	5.65	4.82	4.55	9.88	4.00	9.68	5.41	9.31
	8.34	7.99	7.72	5.70	5.29	7.12	16.53	9.75	9.68	6.31	2.85
	2.47	7.10	6.62	3.37	9.88	7.47	7.11	7.03	5.17	4.69	4.72
	7.96	6.48	4.17	2.84	5.51	5.41	8.69	6.12	10.88	4.78	5.83
	6.79	4.25	18.67	6.84	5.68	5.26	8.12	7.13	12.61	7.57	6.96
	6.17	4.29	5.16	11.09	9.83	5.91	4.65	4.32	8.02	6.36	5.90
	4.10	8.81	6.67	4.95	5.21	5.18	4.25	4.17	7.94	4.83	6.80
	4.52	7.94	7.59	5.05	6.03	4.79	4.19	3.66	8.09	5.47	5.22
	4.33	8.50	4.15	7.86	6.77	5.57	5.40	5.12	4.92	7.76	7.05
	5.75	11.45	10.12	8.40	8.38	8.32	12.12	4.55	20.18	5.55	5.41

	4.66 7.59 7.53 4.13 3.21 3.06 8.50 5.12 5.01 5.00 4.93 4.78 4.64 4.56 4.41 3.06 5.54 7.73 7.22 4.21 3.29 10.86 6.08 5.96 10.42 5.48 3.79 5.61 6.95 9.25 5.63 7.82 5.70 3.34 18.35 9.04 7.50 7.50 6.78 6.49 6.43 5.97 5.27 5.08 4.48 4.43 4.01 3.62 3.49 2.70 19.56 12.03 7.05 4.44 4.4211.34 6.01 5.40
RH-1	11.92 24.63 11.20 6.93 14.88 6.34 8.13 16.62 12.06 19.25 4.30 5.19 7.63 7.21
RH-16	No framboid observed
RH-5	No framboid observed
RH-15	24.71 8.24 6.71 5.21 10.37 7.46 11.98 9.14 10.16 6.08 7.12 11.10 6.16 7.46 9.04 5.12 7.88 4.63 7.48 5.86 6.24 6.74 6.21 10.69 8.94 8.11 7.69 6.59 6.05 5.79 7.26 7.18 8.24 6.50 9.34 6.26 7.72 11.59 8.93 10.20 7.86 5.09 7.74 7.69 31.46 8.72 8.30 9.54 7.13 4.63 8.17 6.64 6.43 8.27 8.15 6.34 10.55 7.29 6.53 5.44 5.86 8.97 9.56 7.16 5.98 4.59 8.73 6.70 6.35 6.29 4.70 10.24 9.28 7.21 5.35 5.14 4.22 3.94 9.49 6.84 7.61 6.60 5.34 6.41 14.20 8.30 7.51 7.38 7.70 6.75 6.66 7.97 12.05 6.83 6.70 6.62 8.98 6.60 7.78 9.94
RH-12	No framboid observed
RH-7	17.85 8.36 6.33 4.87 24.81 10.92 10.56 8.46
RH-10	No framboid observed
RH-11	No framboid observed
RH-14	6.67 10.83 7.55 7.04
RH-12	12.22 8.47 8.63 9.41 8.24
RH-17	No framboid observed
RH-8	No framboid observed
RH-2	7.29 5.06 4.11 4.92 8.83 6.95 8.88 7.33 10.48 7.15 6.57 7.52 7.53 22.68 7.96 7.70 5.73 4.86 5.64 12.88 5.46 15.53 8.04 9.26 5.68 10.35 7.45 7.04 6.28 8.48 75.49 4.93 6.95 11.52 6.30 5.27 5.71 8.10 54.34 16.91 5.59 5.99 4.59 6.48 8.45 9.31 37.90 15.20 6.09 5.55 6.57 4.73 6.40 15.71 81.90 8.98 4.27 7.98 23.36 16.11 6.57 6.86 29.82 5.98 15.28 6.33 14.20 9.54 3.88 8.13 15.61 16.61 6.58 12.02 17.11 10.33 19.97 7.98 5.68 24.71 11.50 7.17 10.20 11.77 9.45 13.10 11.80 24.01
DH-41	8.16 8.84 4.52 4.83 5.29 5.80 4.66 5.82 7.80 4.47 5.19 6.06 6.83 6.32 4.42 4.45 5.93 6.27 6.64 7.12 4.47 5.75 5.87 6.98 7.15 5.54 5.62 4.32 6.28 10.66 2.72 4.41 5.97 6.09 8.20 5.20 7.83 7.18 7.34 6.96 3.89 4.14 5.76 6.87 6.11 6.56 18.22 5.14 18.22 6.16 6.47 8.13 6.64 6.52 7.15 5.62 5.03 4.55 5.64 9.77 6.80 4.33 7.00 3.74 4.64 5.98 5.94 4.21 4.12 10.94 6.25 4.14 4.99 7.98 5.87 5.90 7.89 4.76 5.18 7.45 4.28 3.93 5.97 6.26 5.08 5.17 4.19 5.73 5.76 13.97 3.90 6.10 6.13 6.17 7.95 6.03 9.76 10.74 5.01 5.27 4.46 5.42 7.34 5.87 10.63 4.65 6.51 5.41 5.87 7.35

	8.40	7.29	4.72	4.76	6.82	4.69	5.46	7.44	8.67	7.50	6.55
	5.23	3.29	5.59	7.23	8.70	3.44	5.18	7.29	5.84	13.51	3.97
	4.13	9.68	5.31	6.04	9.82	6.71	4.38	4.88	4.97	5.57	6.55
	6.27	3.17	7.10	6.80	7.38	5.00	5.92	5.69	5.26	4.81	7.64
	5.51	6.61	7.24	6.65	8.56	5.76	5.88	7.86	5.13	5.60	7.12
	3.45	6.01	7.33	7.42	4.12	5.09	5.68	5.64	7.47	3.79	
DH-7	13.37	2.61	3.51	3.61	4.94	8.94	7.54	5.28	6.47	5.23	4.80
	4.97	7.69	3.43	4.14	4.16	4.41	5.57	7.89	4.35	5.72	6.17
	7.82	10.58	7.43	5.54	5.94	7.22	4.36	6.30	9.46	5.78	5.85
	3.01	3.74	4.30	6.07	7.88	5.29	5.38	13.89	7.16	4.35	5.70
	5.51	6.11	7.72	8.62	7.15	3.46	8.58	4.97	6.48	6.75	7.06
	7.74	7.90	4.66	6.80	7.23	7.84	3.90	10.80	6.08	5.82	5.80
	4.81	4.41	6.77	3.72	7.36	5.54	3.55	4.77	5.23	6.60	6.75
	6.38	5.95	6.10	3.85	4.03	5.21	4.00	4.15	5.15	5.25	7.27
	4.51	4.58	6.10	4.00	5.00	5.74	5.81	3.88	4.77	5.58	5.85
	6.74	4.50	7.11	4.32	3.71	4.95	6.51	4.43	5.27	5.54	6.11
	6.06	7.34	6.40	12.52	6.21	6.32	4.20	4.28	5.70	5.54	6.59
	3.53	6.88	5.19	6.32	6.38	4.88	8.58	4.41	5.92	5.95	4.32
	7.66	8.08	6.15	7.85	3.65	5.41	6.81	8.89	3.49	7.28	4.60
	7.06	5.17	7.15	4.45	4.72	4.93	5.34	6.37	4.48	7.14	5.55
	4.59	5.27	9.94	6.14	7.10	3.96	4.62	4.65	5.73	6.87	7.58
	7.87	5.68									
DH-19	4.39	4.57	4.64	4.74	4.96	4.97	5.08	5.15	5.17	5.21	6.44
	4.58	5.66	6.48	5.22	5.24	5.37	5.48	5.50	5.57	5.60	5.68
	5.69	5.70	6.46	4.65	5.69	6.49	5.81	5.82	5.97	6.11	6.12
	6.27	6.27	6.33	6.34	6.47	6.68	4.71	5.76	6.68	6.78	7.17
	7.23	7.82	12.47	3.82	4.16	4.64	4.72	4.81	6.76	4.75	5.78
	6.74	5.03	5.10	5.15	5.18	5.34	5.87	5.97	6.05	6.16	6.18
	7.25	4.87	5.80	6.88	6.40	6.55	6.70	6.91	8.25	10.71	
	10.84	3.49	3.80	7.52	4.93	5.81	2.30	3.95	4.28	4.31	4.44
	4.47	4.61	4.66	4.72	4.90	4.91	7.63	4.96	5.86	2.84	4.92
	5.10	5.29	5.29	5.32	5.34	5.41	5.56	5.60	5.71	8.51	5.14
	5.88	3.30	5.75	5.92	6.04	6.17	6.61	6.72	6.93	7.12	8.06
	8.58	10.59	5.15	6.03	3.70	2.94	3.38	3.64	3.96	4.00	4.11
	4.12	4.17	4.33	4.35	3.32	5.20	6.17	3.74	4.37	4.38	4.45
	4.52	4.60	4.90	5.20	5.24	5.36	5.40	4.36	5.38	6.19	4.19
	5.46	5.54	5.56	5.57	5.68	6.00	6.02	6.11	6.25	6.26	4.42
	5.63	6.19	4.19	4.25	5.40	3.95	5.23	3.08	3.63	5.14	3.40
	4.42	6.21	4.27	5.46	4.09	5.29	3.67	3.80	5.22	3.45	4.71
	6.41	4.28	5.71	4.33	5.36	4.34	3.80	5.51	3.47	4.74	7.32
	4.30	5.75	4.41	5.58	4.50	4.16	5.72	3.49	4.75	4.33	5.78
	4.45	5.82	4.52	4.23	6.14	3.53	5.25	4.56	6.13	4.58	5.91
	4.65	4.60	6.34	3.65	5.27	4.98	6.22	4.77	5.98	4.66	4.37
	6.40	3.70	5.41	5.05	6.32	4.89	6.23	5.21	4.62	6.47	3.82
	5.50	5.10	6.78	5.19	6.60	5.43	4.91	7.12	4.11	5.80	5.32
	3.02	5.20	6.77	5.63	4.96	7.41	4.19	5.96	5.40	3.52	5.21
	2.18	15.19	5.07	3.39	4.40	6.09					

DH-36	3.95	4.16	4.56	4.65	4.72	4.75	5.21	5.83	5.95	6.20	4.08
	5.08	8.62	6.58	6.15	6.38	7.14	7.89	9.08	9.45	4.19	4.40
	4.74	4.79	5.24	4.75	5.47	9.93	7.27	7.72	5.28	6.10	6.97
	3.28	4.21	4.44	4.72	4.79	5.15	5.96	5.48	7.85	3.25	4.65
	6.13	6.35	8.56	17.45	4.62	5.66	6.91	7.59	8.99	9.95	6.38
	4.07	4.10	6.13	6.36	7.47	9.43	4.64	4.76	4.88	4.93	4.95
	5.59	6.10	4.20	6.79	4.66	7.65	7.33	3.59	4.25	4.77	5.62
	6.25	6.32	7.73	5.95	6.27	5.13	7.19	5.73	8.36	6.90	8.50
	10.96	4.29	5.10	8.22	4.40	4.86	5.25	5.53	5.91	4.73	6.63
	4.32	9.97	4.47	5.23	5.85	7.07	8.15	3.73	4.54	5.02	4.75
	6.62	3.55	7.85	5.09	5.79	6.90	7.29	4.98	5.78	5.47	5.98
	6.00	5.90	4.27	11.03	4.32	5.31	5.15	4.52	4.60	4.98	4.57
	8.35	4.43	4.58	4.75	5.21	6.86	11.21	4.33	5.65	5.52	4.97
	5.97	6.30	4.96	6.09	8.21	2.66	2.98	3.86	7.66	4.54	5.20
	6.00	5.90									
DH-3	3.25	5.80	6.99	7.35	4.50	5.21	7.11	10.76	3.94	4.63	5.22
	7.36	3.65	6.20	7.91	6.09	7.24	4.98	5.17	5.24	6.16	6.38
	7.02	4.95	5.23	5.26	5.54	5.83	7.24	4.46	6.72	4.59	6.62
	4.78	5.55	7.18	3.54	4.24	5.58	6.21	4.18	4.85	7.38	6.75
	7.35	6.45	6.10	7.35	5.16	12.53	4.79	8.30	6.15	6.68	7.11
	7.83	8.45	3.82	4.99	5.67	5.81	8.15	3.44	6.81	5.87	5.68
	3.37	8.48	6.79	12.72	3.54	4.03	6.40	7.19	3.86	4.13	4.25
	4.41	8.64	4.52	6.94	6.26	8.21	3.89	4.34	4.65	4.80	5.55
	7.22	7.08	7.96	6.18	6.59	6.96	7.02	4.63	4.65	7.11	3.90
	8.46	4.78	4.82	7.38	7.79	9.35	4.15	4.49	5.55	6.43	4.73
	5.21	6.02	5.06	6.53	5.84	5.31	3.31	5.65	5.30	4.92	5.16
	3.79	4.30	4.40	4.97	5.59	4.55	6.14	6.17	5.17	6.65	6.77
	6.31	3.87	6.38	6.05	6.37	5.72	3.30	3.85	5.78	5.78	4.19
	4.99	12.81	6.88	7.05	6.79	7.88	4.65	4.61	6.78	6.91	4.02
	7.85	10.85	7.75	7.82	7.90	5.01	6.37	11.69	4.71	7.73	8.30
	4.26	5.42	4.62	8.84	7.68	4.74	4.83	4.91	5.12	6.59	8.55
	4.32	4.46	3.57	5.09	10.17	8.36	5.28	6.83	4.74	5.83	8.50
DH-11	3.88	4.41	4.74	4.80	5.02	5.48	6.42	6.96	7.05	7.24	8.43
	17.06	4.40	4.67	4.79	4.82	5.08	5.34	5.61	5.84	6.53	6.86
	3.77	4.01	5.23	6.31	6.83	3.07	5.44	5.65	6.89	3.37	4.19
	4.56	5.35	5.40	5.58	5.91	6.17	6.74	6.81	7.40	3.96	4.77
	5.34	5.53	6.22	6.31	6.43	7.41	7.59	3.94	4.75	4.82	6.40
	6.43	6.75	7.00	4.53	8.35	4.78	5.31	5.65	5.76	6.16	6.52
	8.84	4.70	4.86	5.40	6.41	6.44	8.15	3.91	5.42	5.92	6.64
	6.71	3.30	5.24	5.90	6.09	6.22	6.36	7.09	6.28	8.26	9.73
	18.78	5.14	5.29	5.58	5.80	5.88	6.31	6.53	5.78	6.02	7.11
	7.12	3.15	4.21	4.26	5.89	7.27	7.28	7.51	8.11	5.21	5.26
	5.48	5.58	6.88	6.91	6.97	7.71	4.50	4.78	4.91	5.18	5.30
	6.67	6.72	6.76	6.96	8.00	8.66	9.78	4.56	4.91	5.81	6.79
	7.03	3.83	3.94	4.16	4.39	5.11	5.53	5.72	3.90	6.23	6.39
	9.43	4.67	5.86	6.17	4.40	6.48	8.04	4.28	4.49	4.50	6.39
	4.61	6.99	7.80	7.96	5.42	5.70	5.79	4.72	5.91	6.17	7.07

	7.39	8.26	4.57	4.88	4.78	5.27	6.01	6.70	7.57	7.79	5.63
	2.64	3.87	5.51	5.71	6.01	6.55	6.37	7.66	7.69	9.56	12.64
	6.33	6.87	6.84	5.05	6.51	6.52	7.09	7.81	8.87	7.05	8.89
	5.67	5.86	5.97	6.64	8.22						
DH-14	3.78	4.24	4.45	4.76	4.95	6.19	6.26	6.66	4.86	5.04	6.44
	6.11	6.48	2.91	4.16	5.59	5.94	5.19	5.67	5.87	6.29	7.67
	24.40	4.12	4.32	4.48	4.49	7.28	6.52	6.92	5.35	4.45	5.96
	6.40	4.59	5.10	5.41	5.58	6.04	6.09	6.18	3.82	4.52	4.63
	13.20	7.11	7.42	5.85	5.07	5.98	8.72	4.73	4.83	5.47	5.66
	5.93	6.01	8.38	9.36	3.24	4.82	3.33	7.29	8.13	5.94	5.18
	6.31	6.19	4.32	4.53	4.99	5.13	5.60	5.62	5.99	6.24	4.28
	5.76	3.29	4.42	6.00	5.18	6.55	4.58	5.09	5.16	5.75	5.77
	6.45	6.59	6.78	4.09	4.28	6.50	3.94	5.53	6.04	5.45	7.04
	4.46	4.84	5.22	5.47	5.58	6.16	6.35	7.59	8.42	10.56	7.17
	4.52	5.72	6.15	5.55	7.07	4.17	4.92	5.08	5.74	6.06	7.59
	8.31	8.42	3.24	3.63	7.71	4.74	5.83	6.52	7.14	7.39	3.77
	5.04	5.21	5.62	5.71	5.80	6.11	7.14	4.06	4.40	15.01	4.88
	5.91	7.17	5.01	7.82	5.55	6.41	7.71	17.63	3.59	4.95	5.29
	5.62	6.31	7.94	3.81	4.91	6.03	7.51	5.14	3.69	4.46	5.06
	5.17	5.84	6.62	6.99	15.47	3.61	4.70	6.29	4.27	5.06	6.86
	7.79	5.22	5.27	8.53	5.50	5.66					
DH-57	15.11	13.23	6.10	6.48	4.62	7.49	4.32	4.35	9.12	5.21	5.64
	6.58	6.88	5.12	5.20	11.24	12.46	8.51	7.56	8.89	5.06	5.36
	5.75	6.72	15.51	5.58	12.31	6.54	6.88	5.40	8.12	8.34	4.23
	4.56	7.67	7.87	5.60	5.23	5.59	7.91	5.63	6.37	4.83	5.24
	10.49	10.08	11.15	6.31	8.44	4.45	5.34	4.63	6.90	3.39	4.20
	3.59	6.36	7.58	5.59	6.26	5.11	9.08	11.06	12.48	6.25	7.16
	4.96	9.53	8.46	11.60	8.57	6.23	12.92	9.14	5.76	15.42	
	17.85	8.51	5.17	5.25	6.02	6.10	17.64	7.63	6.53	7.70	5.29
	4.96	8.04	7.93	7.60	6.45	6.47	3.70	5.15	13.10	3.84	4.76
	6.14	5.61	4.31	5.39	5.50	6.81	4.12	4.43	5.94	7.44	5.23
	7.08	5.19	7.08	8.08	7.37	6.24					
DH-27	4.22	4.34	4.56	4.94	5.29	5.31	5.51	5.54	6.06	6.31	5.02
	4.30	5.86	7.11	7.73	4.73	4.76	4.90	5.05	5.17	5.24	5.29
	5.61	5.69	5.16	4.37	6.07	3.23	5.73	5.75	5.86	5.90	6.65
	6.79	14.17	5.49	5.64	6.13	5.26	4.67	6.21	3.64	12.13	4.57
	5.84	5.87	5.92	6.12	6.49	6.61	7.34	3.49	5.33	4.71	6.22
	4.12	3.52	3.52	3.77	4.54	4.77	4.93	4.96	5.22	5.95	6.03
	5.43	4.88	6.91	4.53	6.13	7.13	4.22	5.34	5.43	5.46	5.76
	5.92	5.94	6.38	6.32	5.03	7.16	4.63	6.52	6.58	6.69	6.81
	6.96	7.25	7.25	9.68	4.75	4.75	6.65	5.12	7.37	5.96	4.81
	4.92	5.30	5.31	5.38	5.81	5.91	6.06	6.11	6.56	6.90	5.28
	7.98	7.23	6.69	4.63	4.96	5.09	5.92	6.23	6.27	8.36	14.97
	18.25	11.23	5.36	10.85	8.21	3.97	4.21	4.24	4.42	4.62	4.70
	4.83	5.23	5.29	5.40	3.23	5.71	5.19	3.77	5.43	5.64	5.65
	5.72	5.92	6.13	6.31	6.36	6.37	6.55	3.96	5.77	5.41	4.87
	6.73	6.98	2.95	3.69	3.78	3.96	4.25	4.35	4.68	4.72	3.99

	5.78 6.76 5.11 5.81 8.70 4.55 5.94 3.68 5.34 7.38 4.21 5.41 3.78 4.22 5.89 3.86 4.25 7.18 4.29 4.37 7.42 4.36 4.41 7.81 4.99 5.37 12.73 4.99 5.42 5.31 7.34 5.36 8.28
DH-25	4.60 8.10 5.50 5.97 7.45 10.77 11.46 18.27 4.00 4.49 5.10 4.91 7.07 5.26 3.53 5.72 6.14 21.78 3.86 3.95 6.95 8.03 5.40 6.54 3.43 4.47 4.80 5.54 5.91 6.18 6.23 6.43 5.21 5.93 6.80 16.18 6.00 8.79 5.55 7.10 6.25 5.86 7.19 5.46 5.59 5.62 6.22 6.35 6.73 14.13 6.84 3.57 4.77 6.22 4.61 5.12 5.12 7.12 7.52 7.66 7.69 11.42 3.73 4.23 4.37 4.30 8.38 9.14 5.29 6.64 7.69 5.76 4.80 4.98 7.76 7.64 10.24 12.68 13.13 6.43 26.27 11.24 6.64 5.17 5.17 6.11 8.22 5.31 11.17 6.23 6.13 6.63 7.71 3.60 3.87 4.83 5.68 5.99 7.91 7.64 17.40 6.36 15.50 4.14 6.34 7.55 8.21 5.25 6.63 15.67 7.80 8.97 6.18 7.11 8.16 7.12 11.62
DH-145	24.67 26.90 8.45 13.08 21.46 19.79 16.99 22.05 6.30 27.92 5.52 7.20 9.07 9.83 9.87 11.78 10.48 10.49 11.83 12.69 12.49 13.42 17.21 15.94 19.03 20.07 22.03 22.09 23.36 16.36 18.52 24.70 12.46 17.38 20.46 23.84 30.63 21.44 24.63 27.86 28.32 28.26 32.89 28.60 18.30 9.09 12.77 16.38 16.48 15.48 11.58 13.45 14.34 7.96
DH-140	5.80 7.66 10.39 6.91 10.35 7.69 12.70 7.34 8.54 11.31 6.66 7.40 7.75 7.82 8.60 8.95 7.48 6.90 6.98 7.10 7.90 5.44 6.33 8.83 5.49 6.76 5.53 6.48 6.89 5.35 3.86 5.42 6.00 7.65 7.41 6.17 7.92 5.71 8.07 7.35 4.01 6.32 6.87 5.16 5.91 6.08 6.25 7.00 5.86 12.49 7.22 5.84 5.86 7.09 5.23 4.88 5.52 6.37 5.34 5.09 6.06 4.91 5.07 5.11 6.12 5.54 5.87 6.06 7.37 8.34 6.58 6.41 5.54 10.34 5.59 6.05 7.09 3.80 6.32 5.00 6.46 7.28 10.14 5.89 5.28 8.51 6.04 5.95 11.64 7.52 14.80 8.33 4.64 6.97 8.03 8.31 5.49 4.90 6.27 4.44 5.09 6.26 5.36 4.15 4.74 6.97 5.53 7.62 6.89 5.40 6.28 8.15 6.10 6.63 5.63 5.81 5.02 4.71 4.46 4.18 5.87 6.40 4.17 4.89 5.37 8.39 3.75 5.88 6.30 6.73 7.15 7.71 6.53 4.30 4.78 5.27 6.05 9.40 6.67
DH-147	17.20 13.59 10.99 13.63 13.74 9.30 8.19 9.13 9.90 8.53 10.68 12.97 8.93 12.59 7.23 14.49 16.38 11.39 13.56 9.97 13.47 14.13 5.95 9.11 10.55 21.52 7.77 12.78 10.93 12.79 12.69 13.97 10.36 7.98 8.77 9.63 10.83 27.76 24.65 27.87 8.93 20.48 16.58 10.55 5.74 15.51 17.55 19.00
DH-138	4.49 5.26 5.70 3.61 3.80 3.97 4.06 4.28 4.37 4.91 4.41 4.71 4.78 6.05 4.63 6.03 5.28 3.59 4.12 4.20 5.93 3.69 4.08 5.00 5.92 5.06 4.62 4.97 6.04 6.28 6.42 3.85 5.91 6.63 4.43 4.55 3.77 6.18 5.21 3.36 4.95 5.80 5.02 4.21 4.53 4.63 3.26 3.79 4.30 3.91 3.97 10.90 4.44 4.64 4.66 4.90 5.24 5.40 5.86 4.73 5.86 5.10 5.26 5.04 4.17 3.81 5.30 6.50 4.42 5.09 5.12 5.31 5.67 5.74 4.24 4.49 4.62 5.51 4.91 4.12 4.89 5.99 6.52 3.87 4.00 4.10 4.74 5.52

	6.01	5.34	5.64	5.21	4.29	5.39	8.00	8.23	4.29	5.06	6.25
	7.19	3.83	4.15	4.31	5.34	5.65	5.62	4.59	5.78	2.96	3.65
	3.98	4.03	4.69	4.73	5.32	3.11	3.20	3.50	3.18	5.78	5.00
	4.19	4.68	4.77	4.87	3.98	4.07	4.56	4.72	4.88	4.99	5.20
	3.74	5.79	5.14	5.31	5.32	5.87	4.51	4.86	5.24	6.29	3.94
	4.33	4.52	3.76	6.99	5.28	4.88	5.16	5.35	6.01	4.20	4.89
	4.96	5.42	5.64	5.66	4.15	3.59	5.67	6.38	3.53	3.95	3.98
	4.27	4.55	4.78	5.93	6.36	7.35	5.15	3.96	3.88	4.17	4.95
	5.09	5.47	6.27	3.61	4.00	4.85	4.32	6.04	3.97	4.35	4.44
	4.50	4.53	5.34	5.98	6.66	4.71	4.74	6.12	6.28	4.64	
	4.62										
DH-147-2	30.29	10.40	31.49	20.99	21.09	14.43	18.29				
DH-35	8.99	8.43	5.78	3.86	4.32	5.05	5.46	5.19	5.35	4.77	6.51
	7.34	7.52	13.96	5.90	8.02	5.57	6.73	5.49	8.60	3.92	5.55
	5.62	6.64	7.48	7.48	5.17	5.08	3.48	4.65	5.89	3.70	7.94
	6.48	15.75	3.61	4.07	4.27	4.34	5.27	12.66	4.35	5.66	7.33
	3.40	4.39	5.46	8.20	7.31	6.57	6.57	11.65	5.69	5.41	6.53
	4.20	6.61	17.50	4.92	4.82	5.03	5.37	8.36	6.59	6.27	5.32
	8.30	6.64	6.90	7.21	6.23	11.51	4.78	7.13	13.43	4.36	4.79
	4.83	5.89	8.30	13.47	6.89	4.23	4.23	6.16	4.13	3.84	4.02
	9.90	9.87	5.52	9.42	4.86	5.24	3.45	4.04	6.01	7.70	7.06
	13.50	6.12	3.77	5.78	3.99	6.47	16.44	6.47	7.59	4.86	6.44
	5.03	12.23	6.10	5.86	6.27						
DH-144	4.29	4.41	5.37	8.62	21.94	4.67	5.10	6.30	7.06	5.11	5.24
	5.66	4.49	4.99	5.65	6.28	5.11	6.49	6.76	6.80	7.73	6.53
	5.59	6.84	6.09	5.11	5.31	6.22	4.89	7.07	6.83	7.80	6.02
	6.86	8.83	11.25	4.64	6.55	9.02	4.98	5.18	6.17	5.69	6.39
	4.99	7.17	6.89	7.32	9.81	5.01	5.76	6.22	6.39	4.87	5.85
	8.89	7.42	5.76	6.56	6.16	7.79	7.11	7.95	4.58	6.33	7.44
	10.14	7.22	7.41	5.08	5.10	5.68	6.20	4.31	4.64	6.28	8.27
	6.18	5.33	5.44	6.31	7.03	4.79	5.25	5.27	5.82	7.11	3.45
	4.64	5.52	6.33	8.41	7.98	5.73	6.31	6.73	7.19	4.27	5.27
	6.55	7.19	6.39	3.77	4.88	5.52	7.67	4.14	6.54	7.29	6.43
	6.46	6.83	7.05	6.14	6.96	5.81	7.17	4.53	5.22	5.56	6.02
	4.42	6.65	6.23	6.94	7.02	11.54	4.36	4.58	5.00	6.04	5.04
	5.57	5.61	5.85	6.03	4.47	5.26	5.36	6.07	9.90	5.76	12.96
	5.19	5.68	6.40	7.10	4.64	5.62	7.05	5.43	5.20	7.67	5.49
	5.77	5.99	6.34	6.92	5.43	7.19	4.55	6.01	5.14	5.73	10.71
	5.54	5.71	6.87	4.95	4.98	6.18	6.42	6.43	6.69	5.33	5.58
	8.04	5.25	6.14	4.31	6.38	6.43	9.17	3.79	5.35	5.51	6.20
	4.35	4.55	5.21	5.68	5.77	5.48	7.43	4.37	4.78	9.69	6.06
	4.62	5.86	6.05	6.51	7.32	8.66	4.20	5.02	5.05	6.56	3.22
	4.85	4.82	5.25	7.23	4.29	4.87	5.46	5.70			
DH-139	6.83	7.17	6.01	4.39	5.16	5.41	5.83	4.07	4.09	6.85	6.18
	6.41	5.64	5.97	6.95	13.32	5.75	5.90	9.37	6.53	4.34	15.52
	4.00	6.73	4.89	6.05	3.81	10.63	6.38	5.18	5.59	5.76	5.94
	5.97	5.96	5.29	8.33	3.39	4.51	4.66	5.43	4.68	4.84	7.38

	5.51	6.80	4.82	7.11	5.90	6.28	6.61	7.35	13.23	5.62	8.13
	8.39	5.29	6.04	6.60	5.77	6.51	6.76	7.17	7.52	5.76	6.70
	5.75	6.14	6.27	5.65	4.75	5.41	6.92	5.30	6.83	9.92	11.85
	12.93	5.61	6.30	5.59	5.49	5.17	7.55	5.45	3.80	5.67	4.92
	3.90	5.75	8.05	6.25	5.60	3.98	4.82	4.64	4.99	5.66	5.47
	7.96	3.91	4.34	5.02	6.06	6.53	8.08	5.83	6.62	5.92	6.31
	4.54	6.54	8.84	5.86	5.20	5.58	6.14	4.02	6.33	5.70	4.78
	5.37	7.04	6.70	5.88	6.21	7.43	5.17	6.02	7.92	9.03	4.56
	6.44	3.95	5.49	6.28	11.62	3.53	4.39	5.00			
DH-123	7.47	3.66	4.83	5.18	5.44	3.87	4.25	4.83	4.93	5.46	4.98
	3.75	4.06	4.15	4.78	6.86	5.81	5.81	5.07	3.65	4.31	5.16
	4.33	4.51	4.57	4.64	4.82	5.50	5.58	5.72	5.99	6.28	5.53
	6.39	6.56	5.10	6.61	5.18	5.18	5.51	5.41	7.03	4.22	5.58
	5.03	5.13	5.71	6.50	4.98	4.29	4.34	4.45	5.29	5.28	5.71
	6.49	7.42	6.24	6.39	5.22	5.32	5.36	5.54	5.57	4.72	5.72
	4.84	5.68	4.31	4.82	5.16	5.55	7.07	4.23	5.14	6.25	5.90
	5.62	6.01	5.09	5.57	5.69	6.12	4.60	6.03	6.66	4.04	5.79
	4.16	4.67	6.21	6.64	4.01	4.66	4.83	5.04	5.07	4.70	6.10
	4.98	5.28	5.55	5.27	5.61	4.18	7.26	4.74	4.96	4.75	6.27
	3.64	5.01	5.36	6.37	6.26	4.79	5.43	6.82	6.89	4.32	7.05
	5.02	4.39	3.50	4.38	5.61	5.79	6.71	4.87	3.91	4.66	7.12
	5.68	3.59	4.91	5.45	6.28	2.94	4.37	4.58	5.04	5.64	7.44
	5.80	2.72	3.59	3.87	3.96	4.57	4.58	4.81	4.91	4.93	7.46
DH-69	3.21	3.82	4.85	5.12	5.17	5.39	6.20	6.21	6.24	4.51	5.56
	7.48	3.04	3.22	7.64	4.05	5.04	5.47	4.89	5.14	3.58	4.50
	6.95	4.82	4.98	4.64	5.02	6.91	3.80	4.06	4.50	5.15	4.50
	4.59	5.16	4.73	4.73	5.39	5.48	5.78	4.03	5.60	5.98	6.44
	5.26	4.69	3.35	4.71	4.82	6.16	3.91	5.67	5.70	5.23	4.02
	4.86	5.81	4.44	5.01	5.36	6.07	6.53	4.43	6.00	4.07	6.00
	3.81	3.90	5.13	5.86	6.47	5.33	5.99	3.84	7.06	4.71	5.15
	5.67	4.43	5.39	5.65	4.61	4.77	6.38	6.12	6.47	3.32	4.17
	4.55	4.94	6.39	11.41	6.85	3.91	4.52	6.56	4.79	4.99	5.54
	3.77	4.36	4.52	6.10	6.35	5.28	5.41	5.57	5.97	4.54	5.46
	3.36	4.39	4.65	4.95	7.15	4.66	5.60	5.63	4.32	3.35	6.08
	5.55	4.68	3.71	3.48	3.34	3.88	5.92	6.33	5.62	4.71	5.76
	6.42	5.36	5.16	4.69	4.53	4.02	4.34	6.39	6.10	6.82	6.91
	6.66	5.82	5.77	4.42	5.55	5.68	3.46	4.25	4.61	5.55	5.47
	3.69	4.45	5.47	7.87							
DH-47	5.59	6.62	7.57	6.57	5.01	6.99	5.69	5.71	4.01	4.45	6.17
	12.72	7.47	5.35	9.30	4.72	7.06	7.26	3.96	4.72	5.71	7.22
	5.57	6.30	6.91	7.55	6.99	7.57	8.32	5.65	5.43	11.90	5.57
	4.84	7.07	4.97	5.46	4.57	6.29	8.29	3.38	4.06	5.13	4.47
	6.94	11.86	3.70	5.55	7.34	9.48	10.17	4.46	8.33	7.43	8.17
	4.56	5.13	5.55	7.72	3.52	4.52	5.29	5.96	7.43	4.68	5.88
	7.31	7.49	5.44	5.25	10.75	5.17	6.49	9.90	4.96	6.96	8.58
	10.28	5.49	5.17	5.30	6.23	5.82	4.13	4.96	7.84	8.14	8.70
	4.63	4.74	5.47	5.81	5.87	6.02	4.16	4.21	5.30	5.88	4.07

	5.39	5.68	6.98	5.82	6.83	4.72	3.96	4.41	5.23	5.08	5.08
	4.50	7.40	5.84	6.51	8.77	6.59	3.61	4.51	5.56	6.34	7.95
	5.01	15.92	3.92	5.59	4.41	6.97	6.02	7.00	6.28	6.34	6.94
	11.99	5.64	6.05	7.94	7.94	6.50	3.58	4.64	5.33	6.34	3.32
	4.80	4.13	4.20	4.07	4.68	4.75	4.49	6.02	7.68	9.22	10.29
	7.89	5.09	3.92	4.18	8.48	3.64	4.91	4.66	5.97	7.23	6.07
	5.18	6.46	5.66								
DH-54	5.58	5.55	11.46	15.52	4.51	6.66	7.14	5.50	7.36	11.90	5.09
	5.53	5.76	6.60	6.00	6.22	6.26	7.83	7.49	3.41	5.07	5.42
	7.47	5.45	6.32	6.87	6.26	6.52	5.11	6.13	6.18	5.26	5.83
	6.20	5.10	5.32	5.39	5.49	5.62	6.35	6.37	15.03	3.90	4.45
	5.33	5.74	3.79	5.32	6.38	8.42	12.10	8.20	5.16	4.82	4.97
	6.28	4.50	5.72	5.73	8.53	5.01	5.46	5.57	6.98	5.13	6.54
	7.15	5.45	6.32	6.61	8.08	8.80	5.24	5.87	6.68	4.53	4.47
	5.39	5.55	8.81	6.60	6.95	7.58	7.95	5.67	3.74	4.81	5.41
	5.98	7.56	3.93	5.36	6.84	6.94	7.80	13.90	5.29	6.62	8.11
	6.08	6.14	7.13	6.63	6.94	7.16	5.61	4.13	8.68	8.85	6.30
	6.55	4.69	5.64	6.95	8.72	12.36	5.08	5.11	5.99	7.12	14.12
	6.54	7.30	8.79	5.21	5.94	4.74	5.32	5.64	5.90	6.30	6.44
	6.89	7.31	10.45	4.82	4.06	5.26	6.68	6.86	13.91	4.00	4.89
	5.31	6.62	6.62	7.65	8.48	3.99	4.54	5.13	6.10	6.49	5.54
	5.70	7.57	4.77	5.16	5.35	5.37	7.97	14.13	4.23	4.29	5.20
	6.30	8.24	4.43	7.80	6.10	6.56	5.51	6.63	3.97	5.91	7.40
	9.37	3.93	5.10	5.42	5.67	5.72	5.82	6.01	6.97	6.95	7.30
	6.84										
DH-82	3.93	4.04	4.53	4.55	4.65	4.74	5.05	5.10	5.14	5.35	5.79
	5.79	6.30	7.14	4.58	5.24	5.96	6.00	7.12	4.78	4.94	5.17
	5.40	5.82	5.87	6.08	6.10	6.20	6.21	6.43	6.95	8.28	6.09
	4.69	4.75	5.86	4.40	4.29	4.99	5.66	4.51	3.90	7.35	6.05
	7.76	5.25	5.46	6.67	6.16	7.35	4.78	6.13	4.96	5.31	4.27
	7.29	6.18	5.44	5.48	5.96	4.72	4.23	7.99	6.47	5.85	6.12
	4.44	4.28	6.57	7.16	5.41	5.42	4.08	5.62	4.85	5.47	4.61
	3.43	6.87	6.32	5.42	6.21	5.22	5.21	5.59	7.61	8.14	8.28
	4.46	6.70	7.31	2.88	3.20	3.62	3.88	4.64	6.15	6.39	7.40
	8.74	4.89	5.61	5.61	6.69	7.43	7.46	8.18	3.33	3.88	4.29
	4.46	5.00	5.88	6.11	6.35	6.72	6.90	7.56	3.79	4.74	4.98
	5.30	5.68	5.83	6.27	6.62	10.00	3.68	3.68	4.39	5.43	5.74
	6.04	6.24	7.31	3.87	4.50	4.77	5.13	5.38	5.46	5.75	5.95
	6.55	7.01	7.42	3.27	4.51	4.78	4.81	6.86	7.35	4.40	5.05
	5.50	6.59	6.83	7.03	7.98	8.78	4.05	5.11	5.18	5.59	5.60
	6.07	6.52	6.85	9.07	3.77	4.13	4.58	4.59	4.67	4.79	5.59
	6.45	6.49	8.89								
DH-85	6.79	4.85	5.69	4.71	5.67	8.14	5.23	6.16	6.89	6.22	6.46
	13.71	5.76	7.13	7.25	5.66	6.04	6.13	6.66	5.74	6.78	7.63
	4.88	5.93	4.80	6.18	7.79	6.63	8.50	5.12	8.15	6.64	11.82
	7.32	6.81	6.66	4.97	5.30	4.49	5.36	7.03	7.24	8.77	10.32
	5.55	5.37	4.85	11.22	5.27	6.36	5.51	9.20	6.58	7.76	9.07

	5.20	6.78	10.92	5.33	7.27	4.77	8.05	8.00	11.38	11.27	6.65
	5.27	8.49	5.02	7.78	4.58	6.15	8.36	10.35	7.97	10.29	8.60
	10.47	6.56	4.93	5.61	7.31	7.32	4.58	4.60	9.29	6.00	20.19
	6.14	6.01	8.72	6.89	10.41	7.69	9.00	6.46	5.17	6.53	5.87
	5.87	9.72	6.96	4.09	5.01	6.94	7.38	4.70	5.64	6.30	6.11
	6.07										
DH-73	9.76	7.05	9.31	6.74	7.87	6.95					
DH-61	6.22	5.55	6.26	5.40	4.47	7.65	4.97	4.18	3.75	6.20	7.81
	5.60	6.47	5.11	3.67	3.33	4.57	3.70	4.06	4.59	7.36	4.43
	4.79	4.80	5.26	6.10	4.25	5.15	4.14	8.50	5.36	6.18	6.25
	5.52	3.74	5.39	4.36	4.71	5.89	4.76	5.25	6.23	3.53	20.87
	5.36	6.30	4.76	14.02	4.42	5.43	5.17	5.99	5.34	13.35	4.14
	5.87	10.23	4.14	5.06	4.64	4.2	4.33	3.72	4.27	5.72	3.48
	4.55	3.35	5.85	7.17	5.67	5.06	6.59	4.83	4.53	7.37	5.51
	5.74	10.78	7.49	5.78	5.28	4.91	6.3	5.94	5.95	3.86	3.99
	13.16	5.28	6.47	4.97	5.15	4.35	3.3	4.26	5.46	4.3	4.86
	4.57	14.57	5.33	6.49	6.46	6.4	4.17	4.4	4.84	5.34	5.93
	5.2	4.33	6.61	6.54	4.67	3.33	3.81	4.71	7.16	7.02	5.37
	7.19	11.9	5.44	8.02	3.98	4.62	4.36	7.58	5.69	4.05	3.72
	3.91	7.24	7.61	4.18	4.24	7.38	5.89	4.27	5.26	4.82	6.58
	5.83	5.25	6.82	3.45	8.95	5.83	6.82	5.04	4.08	6.09	4.34
	5.96	4.78	5.98	5.59	5.35	3.81	3.28	4.42	5.21	3.87	12.74
	3.23	5.7	5.19	3.06	5.61	5.02	5.17	5.45	6.32	5.17	4.9
	5.63	7.78	5.46	4.65	4.59	15.4	4.18	2.94	4.98	5.62	4.73
	4.01	3.96	9.91	4.23	4.33	7.49	4.84	5.35	4.77	6.08	5.04
	5.47	3.28	4.18	4.81	3.62	4.28	12.17	7.10	4.4		
DH-44	5.1	4.23	3.48	4.18	5.21	4.23	5.46	7.14	3.26	5.84	6.35
	4.6	7.36	6.04	6.42	6.52	5.67	5.3	6.99	4.5	6.87	5.61
	4.53	6.76	5.31	5.8	3.24	5.66	4.7	5.14	5.64	4.75	3.04
	3.56	4.08	5.64	7.26	6.21	5.55	6.84	3.73	5.13	5.47	6.36
	4.72	5.46	5.59	4.43	4.08	4.99	5.61	5.54	8.76	4.63	3.11
	3.46	5.71	4.47	5.63	6.75	3.95	6.15	5.95	5.37	4.99	5.61
	3.91	5.51	6.15	5.33	5.14	6.75	6.59	5.52	7.63	6.5	4.62
	5.42	4.01	4.71	5.49	5.16	5.05	4.9	8.96	5.64	4.56	7.75
	6.7	4.67	3.27	5.87	11.66	5.22	5.53	4.3	6.38	5.16	5.33
	3.55	7.1	7.41	6.11	6.07	6.97	4.91	6.53	6.28	6.98	5.45
	5.41	5.14	5.83	6.38	6.45	5.17	6.68	5.09	3.62	4.15	6.09
	4.29	4.23	4.75	4.63	4.39	4.12	5.98	6.66	3.69	5.25	6.95
	6.67	2.85	5.35	4.82	6.27	4.21	5.34	3.06	3.05	4.27	11.01
	5.33	5.86	7.35	5.96	5.41	6.09	4.62	3.28	4.43	3.88	4.51
	6.49	5.52	5.76	4.29	4.08	4.03	5.96	4.7	3.84	4.09	4.48
	3.85	5.19	3.38	3.3	3.54	5.55	6.06	5.31	6.05	4.23	5.8
	6.55	4.5	6.88	6.63	4.3	4.72					
DH-52	3.99	5.14	4.81	3.72	3.69	4.56	4.96	4.96	11.97	3.25	4.13
	4.31	4.81	4.79	5.53	4.28	5.68	3.83	4.16	4.56	5.14	4.91
	7.51	5.87	4.99	3.7	4.19	4.39	3.01	5.35	5.16	6.74	7.2
	5.19	6.16	5.6	3.58	5.44	5.78	4.31	9.16	4.19	3.22	5.54

	6.94	5.36	6.32	7.96	4.55	5.94	8.29	5.37	5.13	7.82	5.47
	6.32	4.05	10.99	5.25	3.83	6.02	10.79	3.17	7.82	5.38	5.00
	3.99	3.8	4.7	5.61	5.43	4.26	7.24	6.78	4.00	7.52	6.77
	9.53	4.7	6.13	4.7	5.61	5.96	4.99	4.28	4.98	5.38	11.37
	8.41	6.03	4.51	6.43	4.09	3.76	4.36	5.5	3.52	2.71	7.53
	4.07	4.01	3.61	5.6	9.29	5.67	4.14	4.19	3.92	5.42	9.13
	5.43	3.7	5.2	3.77	4.4	6.89	4.89	4.84	8.42	9.29	4.57
	4.81	5.05	5.45	7.86	5.86	10.44	4.91	3.38	4.96	6.07	6.31
	5.77	4.58	5.58	5.89	6.67	6.37	4.02	5.16	6.3	4.23	7.24
	5.87	4.13	7.9	6.99	4.8	4.14	4.52	5.85	4.14	4.52	5.85
	8.27	5.96	3.59	4.34	5.58	3.16	4.29	7.51	7.34	4.97	8.42
	6.77	6.51	6.26	4.38	6.28	5.01	4.44	5.04	4.76	4.95	5.58
	6.32	3.1	5.98	7.00							
DH-78	7.93	3.29	5.13	8.07	7.53	9.23	4.46	4.23	3.43	3.14	6.57
	3.96	5.19	5.13	5.55	6.82	4.92	3.53	3.61	3.08	4.93	5.31
	4.15	4.79	5.10	7.02	4.24	4.89	4.91	4.30	4.72	5.50	3.59
	3.72	4.37	5.08	5.61	6.89	8.89	5.02	4.26	4.46	5.79	4.39
	5.19	4.80	4.96	4.57	10.35	4.56	5.56	3.78	5.56	4.86	5.47
	4.45	3.87	4.55	11.46	4.07	3.59	4.39	5.47	8.44	5.53	3.68
	5.06	4.17	3.96	5.04	3.99	4.88	8.37	3.58	3.81	5.24	7.28
	5.36	8.21	4.15	7.49	4.83	6.79	8.22	4.94	4.22	3.78	6.26
	5.38	3.55	6.11	4.92	5.69	4.12	6.68	4.81	6.32	6.48	5.35
	7.99	4.55	6.50	5.26	6.02	5.00	5.11	3.30	4.72	3.89	3.58
	5.36	6.14	6.38	9.06	4.78	5.06	5.02	4.95	8.51	5.43	5.06
	4.97	4.46	7.07	3.23	6.15	3.09	6.77	5.14	10.68	4.42	7.52
	3.69	5.08	4.46	4.92	4.66	4.71	3.77	5.13	7.25	6.49	4.91
	7.74	5.58	6.11	5.88	6.47	3.85	7.87	5.49	8.34	5.00	3.27
	5.02	4.76	4.76	5.93	5.65	4.30	5.56	5.01			
DH-65	4.54	5.29	3.72	3.62	5.48	5.87	4.31	4.75	4.56	5.11	4.56
	6.64	6.30	4.63	5.91	3.75	3.53	5.95	4.37	4.98	3.83	4.05
	4.60	4.25	4.19	4.13	4.45	3.95	4.56	4.58	4.87	4.13	5.07
	4.31	4.10	3.29	4.76	4.88	4.92	4.36	5.04	4.47	5.77	4.27
	4.13	3.68	4.78	5.72	4.61	4.29	5.41	4.59	3.56	4.45	5.17
	5.37	4.57	3.83	4.07	4.39	3.07	5.21	5.21	3.63	2.71	3.29
	4.86	4.02	3.46	4.04	5.31	4.77	5.00	4.49	5.47	5.13	3.34
	3.54	6.00	3.98	3.24	5.93	3.96	3.76	3.82	4.09	4.60	5.50
	3.72	9.12	4.57	4.66	4.30	4.11	5.67	5.77	5.42	4.25	4.21
	4.19	4.64	5.89	4.38	4.34	5.73	4.78	4.12	3.93	5.75	5.27
	4.08	3.47	4.05	4.89	3.21	5.84	4.64	6.14	4.85	5.60	4.34
	4.86	5.37	6.10	5.37	4.31	5.49	4.03	3.00	2.76	4.65	4.32
	3.99	5.79	6.84	4.05	6.19	4.58	4.59	5.67	3.25	4.72	6.74
	4.65	6.05	4.86	4.23	3.51	4.21	4.79	5.35	5.56	3.44	3.34
	5.47	5.11	3.87	6.51	4.41	5.98	5.44	3.06	3.32	5.31	4.63
	4.36	5.20	4.47	3.91	3.26	4.16	4.88	3.76	4.59	2.63	5.47
	3.94	4.12	4.79	6.10	6.91	5.42	4.76	5.38	5.91	3.94	4.11
	7.30	4.93	4.56	4.82	6.19	6.15	4.47	5.14	5.24	6.23	6.40
	6.94	4.46	4.77	4.33	5.48	4.35	4.56	4.58	3.95	4.45	5.93

	5.13	6.21	6.02	5.37	4.70	4.67	7.34	4.04	4.64	7.14	4.96
	4.38	3.66	3.79	4.63	4.51	4.26	5.54	4.44	4.06	5.35	4.14
	3.81	5.03	3.73	4.20	4.39	4.48	6.14	5.31	5.35	5.06	3.82
	5.98	3.94	4.39	5.19	3.24	4.76	5.81	4.15	4.79	5.31	4.21
	3.50	6.47	6.82	5.46	3.29	3.86	5.37	3.83	5.17	4.52	4.03
	4.67	5.10	4.63	5.56	3.22	4.07	4.67	3.58	5.14	3.50	5.44
	2.45	4.11	4.61	5.36	5.18	6.14	7.61	4.44	4.44	5.72	3.57
	4.27	5.22	3.29	3.52	5.34	6.27	4.13	2.10	5.56	3.86	3.90
	3.19	4.18	5.34	5.86	2.96	4.93	4.69	4.99	3.62	5.22	5.88
	6.22	5.57	2.91	4.54	3.50	2.91	3.82	4.81	6.51	3.90	5.98
	5.86	5.70	4.19	3.80	3.48	5.67	4.32	4.75	4.84	6.61	3.10
	4.41	3.57	4.64	3.96	6.19	4.65	4.58	5.96	4.92	3.00	3.99
	5.07										
DH-91	4.11	5.17	8.95	3.96	7.65	8.95	3.71	5.90	3.71	5.24	8.72
	5.88	4.60	5.30	4.05	4.12	10.35	6.85	7.69	4.48	5.41	6.26
	6.93	4.90	6.03	5.98	7.62	7.72	7.36	4.43	5.69	5.18	5.71
	5.77	4.93	12.32	8.24	4.12	8.99	6.85	8.49	6.18	6.73	5.61
	6.08	6.01	7.20	4.78	7.60	6.24	8.17	4.15	5.53	6.23	5.67
	4.99	3.39	5.24	4.22	4.39	7.78	7.45	4.48	3.19	5.84	4.19
	4.94	6.61	5.60	5.94	4.38	6.42	4.63	3.55	4.88	4.40	4.52
	4.70	5.67	4.80	7.69	3.79	6.62	6.24	8.63	6.02	4.63	5.87
	6.68	5.78	5.72	5.37	3.95	6.51	6.55	7.74	6.50	5.19	3.57
	6.37	6.64	7.08	7.60	5.83	6.19	7.92	5.98	5.31	7.22	5.48
	6.48	4.87	4.34	6.07	7.34	5.69	6.39	8.15	5.67	6.70	6.68
	5.25	4.71	9.61	3.93	6.18	5.65	5.52	7.63	4.17	5.19	6.84
	4.94	7.30	7.63	7.44	4.92	3.58	5.79	6.04	6.92	5.28	8.10
	6.09	5.26	5.30	7.55	4.79	4.64	4.92	5.59	5.19	6.21	7.37
	7.39	6.91	3.40	4.15	8.03	6.73	5.03	3.84			
DH-31	6.05	7.64	12.38	4.46	4.73	5.84	5.91	14.78	8.27	6.53	5.33
	5.49	6.60	19.17	10.19	5.01	6.10	5.40	6.56	5.59	6.00	6.59
	11.22	7.14	4.23	9.55	8.76	5.37	4.68	5.68	5.33	6.45	5.55
	4.12	6.72	19.18	5.92	6.56	13.61	8.00	6.51	8.00	6.23	5.36
	3.85	10.14	4.43	31.82	5.00	5.96	4.83	4.77	14.81	7.67	5.52
	9.39	7.31	5.76	7.39	7.35	7.12	5.26	11.77	6.43	6.35	5.94
	5.22	9.66	6.12	5.35	5.71	6.09	5.21	5.92	6.40	4.42	4.88
	5.38	7.64	6.59	4.43	5.99	6.32	7.33	5.06	3.79	7.05	6.35
	7.16	6.08	6.49	7.52	6.59	8.11	5.56	5.01	6.81	5.87	4.68
	11.34	6.85	6.39	5.04	8.31	7.59	6.97	5.17	7.22	7.03	7.84
	6.63	7.28	5.28	7.96	5.45	5.18	7.87	4.85	4.97	8.98	6.70
	9.09	13.07	6.78	6.50	5.29	17.18	5.76	6.79	12.43	4.83	8.89
	5.87	12.07	7.18	5.11	16.60	8.76	5.55	5.44	5.51	15.60	7.12
	6.21	4.89	5.13	5.81	5.03	5.41	10.96	6.42	6.37	4.52	9.12
	6.24	8.37	8.27	5.98	11.27	7.43	8.76	11.29	11.03	4.16	4.74
	5.09	5.57	9.59	17.59	8.83	6.48	13.39	4.57	4.38	6.54	20.03
	4.62	5.21	6.60	5.64	4.46	5.59	23.77	6.03	5.47	6.20	9.80
	7.61	5.21	6.75	14.84	4.90	6.38	8.13	6.14	6.76	4.47	5.91
	3.90	4.68	5.61	6.49	4.43	14.61	4.29	5.78	6.61	11.22	8.00

	5.07	4.27	6.04	6.07	6.45	10.41	7.43	6.99	6.22	5.90	6.46
	5.14	5.45	5.99	7.84	4.28	3.90	5.15	6.53	10.09	5.98	3.97
	3.93	4.96	4.48	4.39	7.86	7.09	5.29	8.73	5.28	6.01	7.29
	5.75	12.39	4.86	4.39							
DH-107	5.89	6.24	4.71	4.54	5.12	5.59	5.88	7.02	8.31	3.94	6.25
	5.58	5.52	5.10	6.51	3.57	3.72	4.98	5.20	3.40	4.36	5.06
	3.71	8.63	8.53	6.11	4.51	6.69	4.62	4.76	3.80	6.70	3.10
	3.95	4.24	6.26	3.54	4.26	5.79	4.09	4.31	8.61	4.23	4.74
	5.99	3.72	4.64	4.80	5.82	5.17	4.99	6.04	4.21	6.18	3.57
	5.71	6.25	3.24	3.80	4.58	4.71	7.50	5.27	5.00	5.88	4.43
	4.74	4.63	6.22	6.26	5.24	5.26	4.93	4.93	7.49	5.36	5.03
	6.68	4.13	4.42	4.19	4.50	5.27	3.31	4.05	4.13	4.41	5.04
	5.47	5.87	4.35	6.50	6.88	3.55	4.07	4.49	4.81	5.38	5.43
	5.77	4.67	5.47	3.66	4.51	4.69	4.83	4.51	5.29	5.03	6.54
	4.45	4.73	5.70	4.46	6.27	3.75	4.88	4.62	4.23	5.55	6.41
	4.10	5.24	10.73	5.48	5.26	4.63	4.98	5.22	3.59	3.62	3.77
	4.10	4.69	5.32	5.81	8.58	5.84	5.56	4.76	5.05	5.96	6.56
	4.18	4.65	4.80	4.95	6.44	6.64	7.67	5.65	5.72	5.06	5.24
	6.42	5.23	4.59	5.43	5.36	5.18	6.14	5.42	5.80	6.40	5.84
	5.81	6.85	5.52	5.85	6.53	6.02	6.60	6.10	5.36	6.91	6.32
	6.93										
DH-103	4.30	4.48	5.20	5.33	4.34	5.20	3.52	5.47	5.49	4.23	5.51
	3.94	5.32	9.71	6.81	3.83	4.99	5.92	3.54	4.46	5.82	5.28
	5.40	6.61	2.77	3.46	4.79	5.57	5.62	5.82	4.69	5.81	4.66
	6.68	4.11	3.66	4.70	4.58	6.15	5.28	5.03	6.14	4.17	4.50
	4.83	5.59	3.23	4.60	6.30	2.27	3.58	3.69	3.27	4.96	5.02
	5.64	4.01	5.11	5.81	4.35	5.42	4.09	6.68	4.10	5.25	5.77
	6.01	4.61	4.67	4.90	5.43	6.13	5.16	3.54	5.68	5.25	9.71
	4.23	5.14	6.30	4.54	5.48	4.13	5.89	7.10	5.43	5.91	5.27
	5.17	5.50	5.94	6.59	4.50	4.02	5.79	5.26	4.59	4.44	5.68
	4.65	4.59	5.56	4.46	5.45	6.10	6.26	6.88	5.32	5.89	3.75
	5.02	5.10	5.14	6.25	6.09	5.44	4.84	5.82	5.81	5.11	4.99
	5.42	5.47	3.68	5.21	5.37	6.99	7.32	4.23	4.69	6.35	3.93
	4.19	7.09	6.17	4.41	5.28	6.33	6.55	5.42	5.52	5.89	6.56
	4.75	5.41	5.36	5.89	4.68	4.90	6.07	4.91	5.11	4.17	4.40
	6.50	4.55	5.64	4.73	7.11	5.43	6.78	4.21	7.00	4.20	4.76
	5.45	5.59	5.73	3.96	3.96	4.41	5.14	5.38	5.30	6.75	4.56
	5.21	4.75	4.17	5.58	4.27	4.29	6.30	5.39	5.39	5.59	5.99
	6.01	4.31	4.64	6.67	7.31	7.84	5.92	4.03	4.96	6.06	7.00
	5.65	6.95	4.60	4.71	3.77	2.99	4.28	4.62	4.77	4.89	5.06
	5.61	6.70	4.71	4.77	6.26	4.44	6.48	6.09	5.40	5.72	4.81
	4.61	6.50	4.70	5.47	4.09	4.15	4.80	4.89	4.61	5.52	5.64
	5.76	5.77	9.68	4.45	7.23	6.25	5.48	6.28	5.91	5.15	3.95
	4.81										
DH-95	4.44	4.93	6.95	5.09	5.45	4.44	4.59	6.87	4.49	4.59	6.68
	3.84	4.71	4.50	5.47	8.11	4.04	5.04	4.60	4.96	5.64	6.92
	4.29	4.30	4.02	4.11	4.50	5.21	7.33	5.79	8.53	5.14	8.08

	3.13	6.85	5.22	5.25	5.41	6.11	4.76	5.10	6.61	4.76	5.10
	6.61	5.56	6.93	5.82	5.87	5.41	7.02	5.53	4.25	5.80	6.32
	4.85	6.21	4.93	5.91	7.92	4.56	5.90	4.68	4.18	4.55	6.58
	6.96	6.17	5.04	5.70	7.38	7.14	4.27	4.69	4.71	4.55	5.42
	6.41	6.61	7.14	8.50	5.38	3.70	7.91	4.75	6.79	4.24	5.47
	5.94	5.69	4.61	3.31	4.01	4.83	6.33	3.12	3.65	3.86	4.57
	7.07	6.15	4.81	7.39	4.26	6.00	7.21	5.63	5.27	5.65	3.79
	4.11	6.87	3.23	3.90	3.97	4.13	3.82	4.26	6.75	4.86	4.96
	7.84	7.53	5.47	6.59	5.28	4.84	4.59	6.77	7.00	2.90	3.72
	4.14	6.01	5.45	7.04	5.23	5.14	4.78	3.74	8.39	4.01	5.77
	6.78	6.71	13.43	5.18	5.45	7.28	3.22	4.64	5.13	4.11	2.99
	6.28	7.16	5.06	4.15	5.83	6.80	3.59	5.27	5.40	5.86	4.93
	5.66	6.54	4.19	6.78	5.53	3.94	3.26	6.57	5.65	7.02	4.93
	6.39	7.59	5.74	7.31	7.59	4.16	4.35	5.75	3.85	4.27	5.61
	5.11	3.47	5.69	3.73	5.44	6.89	4.85	5.39	6.03	6.32	7.04
	4.83	5.21	5.49	3.61	4.34	6.29	5.28	6.33	5.69	7.50	4.71
	2.79	2.92	4.14	4.61	4.63	6.53	4.68	5.11	6.23	4.47	5.83
	5.94	6.59	7.11								
DH-131	2.78	3.25	4.33	4.47	4.71	4.77	5.00	6.03	6.17	6.23	3.17
	5.26	6.50	4.72	3.47	5.41	4.82	4.30	6.50	11.61	6.17	6.55
	3.38	3.54	3.58	5.00	4.04	4.55	5.77	6.38	6.88	6.68	7.24
	3.16	5.31	4.38	6.38	6.45	7.46	3.24	5.39	8.00	4.99	5.76
	6.83	3.54	5.86	6.61	5.46	3.46	5.68	4.04	6.91	3.92	4.60
	6.81	5.05	6.89	4.42	6.09	5.62	6.62	6.23	4.48	4.67	4.68
	5.80	6.99	3.00	6.02	5.68	3.49	4.04	4.15	5.31	4.74	4.99
	5.21	4.87	7.31	5.37	7.67	5.67	6.78	5.68	4.82	6.52	3.48
	6.28	2.82	4.12	6.94	3.12	4.34	4.21	5.78	4.78	8.42	6.20
	5.00	4.60	3.47	5.05	4.19	7.14	6.50	6.69	5.19	5.48	4.07
	4.47	4.71	5.48	3.30	5.73	4.39	4.68	4.81	4.31	7.56	5.55
	4.72	5.68	5.20	5.40	7.16	2.42	3.43	4.11	2.83	3.64	3.88
	5.17	6.45	6.29	4.71	6.73	4.83	4.39	4.97	4.27	5.96	5.45
	7.27	4.37	7.05	4.27	4.30	4.69	4.81	5.13	7.68	3.51	4.67
	6.50	5.15	4.88	5.06	5.06	3.37	5.48	5.17	6.35	7.32	4.44
	3.56	4.26	4.56	4.43	4.63	4.66	4.79	5.01	5.69	6.63	8.85
	3.86	6.48	5.99	3.41	7.38	4.35	5.44	7.16	5.88	8.30	6.32
	5.51	5.20	6.15	6.23	4.19	5.65	4.46	5.24	7.60	4.87	3.98
	6.26	4.02	6.31	4.96	4.45	7.85	9.74	3.93	4.08	4.53	6.78
	5.60	7.29	4.05	4.41	4.82	5.22	8.07	3.71	5.28	4.81	4.14
	5.77	5.68	4.31	6.70	3.24	5.62	5.48	5.68	6.26	5.67	6.89
	3.64	6.17	6.17	3.17	6.68	5.05	5.26	3.40	5.63	5.32	8.38
	11.51	4.46	7.88	4.53							
DH-119	3.05	3.82	3.87	4.50	5.37	3.62	4.22	5.92	4.36	5.45	6.29
	4.09	4.19	4.80	3.08	3.41	5.58	6.37	3.40	4.37	5.90	4.56
	4.54	4.73	5.13	5.99	7.58	4.62	4.87	5.16	4.36	3.55	3.91
	4.86	4.87	5.24	4.95	6.43	6.44	5.31	3.11	5.59	5.98	3.32
	4.10	5.02	5.99	3.10	5.14	6.74	5.66	4.67	3.28	3.59	5.66
	4.64	4.64	4.86	5.06	5.32	4.58	5.00	6.55	3.98	5.17	6.20

	6.65	7.76	5.57	5.49	7.35	5.20	6.22	5.90	5.38	5.08	4.50
	6.77	4.02	5.67	5.93	4.56	5.21	6.19	6.72	4.50	4.35	6.15
	5.51	4.11	5.98	5.28	4.10	4.54	5.77	5.82	4.02	4.19	5.10
	5.42	3.14	3.63	4.56	6.15	5.47	5.77	4.96	3.85	5.66	4.72
	4.83	5.45	5.59	3.12	3.77	3.89	5.01	6.24	3.94	5.29	5.07
	5.30	5.95	4.98	4.82	4.46	5.10	5.47	5.68	5.33	8.40	3.67
	5.77	6.06	5.07	5.64	6.19	4.39	4.20	5.46	4.13	5.28	6.65
	4.10	4.39	4.57	5.08	10.97	5.39	6.01	6.05	6.86	4.34	8.30
	5.67	5.67	5.29	6.26	5.22	11.48	4.47	5.02	5.13	5.63	6.62
	4.20	4.85	4.78	5.33	5.69	6.49	6.70	5.40	6.36	5.86	5.98
	6.01	7.78	5.70	6.39	5.88	4.20	4.75	4.03	4.49	6.45	4.43
	4.38	5.30	6.79	5.12	5.27	5.53	5.94	3.26	5.42	4.71	5.13
	5.41	4.13	6.31	6.70	4.36	5.34	5.74	5.30	5.24	3.39	5.92
	6.17	8.67	4.84	5.92	4.36	5.18	4.64	5.30	4.47	4.73	5.97
	5.78	4.35	6.67	5.63	6.89	14.32	4.45	5.50	8.41	5.20	5.54
	4.85	5.87	4.57	5.19	6.66	5.75	5.59	3.49	5.53	5.93	6.47
	4.70	5.36	4.28	4.29	5.81	5.20	7.78	5.89	4.50	4.77	5.08
	5.69	3.69									
DH-137	4.29	4.60	4.58	5.71	16.25	5.83	6.67	4.58	4.34	4.94	3.48
	3.90	3.80	4.30	5.00	6.98	6.37	7.96	6.88	4.74	6.19	3.88
	4.38	4.60	4.82	5.08	5.59	4.22	4.71	6.20	8.73	4.44	8.68
	6.46	5.86	11.25	5.65	4.33	5.75	3.21	5.27	4.20	4.18	9.34
	3.48	4.30	5.30	4.24	4.76	4.95	5.54	7.54	4.13	7.99	3.66
	4.89	5.18	7.75	5.71	5.46	9.23	4.26	4.92	6.21	5.10	6.67
	4.65	7.49	4.98	5.49	6.77	6.94	4.72	5.63	8.29	4.85	5.98
	8.05	3.80	3.82	4.60	4.80	4.91	5.39	5.46	6.96	4.51	4.58
	4.16	4.31	5.96	5.14	4.28	5.42	6.91	9.27	12.87	13.74	4.67
	5.92	6.42	4.95	12.50	5.03	5.07	5.79	6.37	4.28	4.53	4.77
	6.04	5.04	5.14	4.51	4.51	12.72	10.01	15.26	15.04	10.70	3.17
	8.55	5.47	4.31	4.90	5.60	7.35	4.71	5.31	3.99	7.13	6.82
	11.43	4.65	6.60	8.29	5.10	9.10	5.93	6.96	12.43	15.07	4.87
	5.37	5.61	5.70	6.98	5.01	5.27	11.80	14.76	6.85	5.69	8.32
	7.96	5.94	7.42	5.26	3.41	3.76	3.88	3.98	3.34	4.15	6.15
	3.84	4.04	4.77	4.12	4.65	4.95	5.49	5.58	5.83	6.01	6.34
	3.58	4.16	5.77	4.55	4.70	6.25	3.84	6.09	4.18	4.26	6.59
	6.73	11.47	5.67	9.67	4.92	6.02	6.73	5.31	5.57	4.10	4.38
	5.15	4.95	6.88	4.97	3.96	5.64	4.91	4.54	8.72	3.88	6.03
	7.83	3.48	4.36	6.11	4.15	5.94					
DH-132	No framboid observed										
DH-127	5.41	3.42	4.03	4.36	5.43	4.23	5.13	3.94	4.35	4.84	3.85
	4.89	5.03	5.04	7.81	5.65	8.17	5.30	4.39	5.58	3.81	7.30
	8.88	4.80	4.96	7.58	4.49	4.47	5.84	5.67	5.90	3.51	6.11
	4.38	6.02	7.10	4.11	4.18	4.61	3.53	3.57	4.21	4.55	4.73
	4.94	5.01	5.85	3.54	3.65	5.02	4.88	5.77	5.94	3.68	3.78
	4.08	4.58	5.66	6.92	4.47	4.65	5.30	5.82	6.36	5.99	4.21
	5.23	5.25	4.90	2.51	4.34	5.39	5.90	6.12	4.39	5.66	6.83
	4.46	5.87	4.86	7.96	7.04	4.65	5.77	4.35	6.57	4.83	7.20

	6.03	7.07	7.13	7.42	5.57	5.86	5.02	5.40	3.82	9.99	7.56
	5.18	3.30	4.39	4.15	11.15	4.58	6.32	4.86	4.00	4.46	5.38
	5.91	5.93	4.75	6.82	3.68	4.30	6.09	6.11	5.61	5.98	6.32
	4.35	4.97	4.66	5.37	6.76	5.61	4.46	4.74	6.58	6.87	4.76
	4.94	6.57	6.80	5.63	4.93	3.97	5.83	6.81	3.69	6.31	5.18
	4.73	5.41	6.23	5.43	5.73	5.19	5.90	4.16	5.59	5.65	7.08
	5.44	5.72	7.12	3.94	4.09	5.25	4.86	5.13	5.76	7.01	9.29
	5.24	6.30	4.17	3.97	4.74	5.39	4.42	4.92	5.93	6.76	6.93
	7.64	5.21	6.17	6.29	3.58	4.70	5.40	4.79	4.51	4.41	5.71
	3.99	4.63	5.08	4.44	4.82	7.03	7.17	4.21	4.92	6.80	6.38
	8.01	6.03	6.40	5.34	6.12	4.84	4.22	5.56	5.63	3.99	4.61
	4.95	5.08	5.73	5.91	6.32	5.79	6.50	4.61	6.46	5.42	7.43
	5.34	5.36	5.87	5.97	6.67	4.81	7.86	5.79	6.09	6.19	5.41
	4.31	4.12	6.15	4.32	3.93	4.30	4.90	5.15	5.24	6.43	7.21
	4.79	3.42	4.38	5.70	6.69	3.83	4.83	6.61	6.49	6.64	4.51
	5.12	5.39	4.15	3.60	4.04	4.07	5.82	4.92	3.91	4.66	3.96
	4.06	3.89	5.34	3.23	4.28	4.42	5.78	5.66	4.18	4.69	7.47
	4.25	5.18									
DH-115	4.83	6.45	6.06	6.12	6.33	5.39	5.96	6.04	5.67	5.80	5.80
	6.04	7.78	2.39	2.75	3.82	4.16	4.42	4.18	7.83	4.43	4.21
	4.45	6.05	4.79	5.31	6.15	6.72	3.94	4.60	4.66	5.72	5.74
	6.71	5.08	6.60	7.89	3.64	5.22	6.28	11.06	4.53	5.40	4.66
	4.48	3.07	4.45	6.12	3.42	4.20	4.44	4.87	6.12	3.85	4.89
	6.72	3.87	4.41	7.95	4.98	5.70	3.23	3.73	3.75	3.95	3.84
	5.46	6.21	7.04	6.39	4.69	5.17	5.45	4.03	4.54	6.86	7.00
	4.29	4.86	4.04	4.14	5.28	4.61	4.82	4.83	4.15	5.30	3.67
	4.20	5.44	4.26	4.60	5.13	4.46	7.62	4.27	6.03	5.19	5.09
	5.24	5.97	6.05	6.07	7.43	3.69	5.08	4.96	5.10	5.23	5.02
	6.45	6.50	4.74	6.08	5.18	4.92	5.56	6.04	3.55	4.30	6.44
	4.84	7.38	4.10	4.64	5.58	7.97	4.80	5.20	5.33	5.48	5.70
	5.84	4.73	7.97	4.38	4.69	4.85	6.47	7.85	5.52	8.50	3.98
	6.87	4.92	6.85	6.77	4.34	5.65	5.94	5.43	6.15	4.99	6.65
	3.98	4.51	5.83	4.82	4.21	5.12	4.13	3.76	6.73	3.62	7.09
	4.18	6.37	4.30	5.15	5.26	6.06	7.05	8.17	5.96	6.24	3.69
	3.79	6.60	6.42	6.44	4.39	5.18	4.63	4.89	5.82	3.96	6.96
	6.53	5.32	5.29	7.82	5.59	5.85	4.61	4.66	5.90	8.09	4.23
	4.69	3.78	3.53	4.86	5.94	4.41	5.82	4.65	5.91	6.01	5.36
	6.43	3.77	4.76	6.70	3.77	4.26	4.64	4.92	7.71	4.12	4.56
	4.62	6.05	4.64	6.26	7.69	5.02	6.42	6.91	3.61	3.63	4.51
	6.89	3.17	4.70	7.03	6.26	4.99	6.57	5.54	4.77	5.04	5.66
	5.69	4.87	4.94	5.08	6.02	4.13	5.21	8.44	4.69	5.17	5.42
	3.85	4.31	4.73	2.87	4.63	4.69	9.85	5.03	5.61	7.69	5.60
	4.78	5.24	6.65	5.48	4.68	5.56	4.96	7.28	7.46	7.72	7.45
	4.53	8.91	3.56	5.91	6.04	3.57	4.77	4.82	2.64	5.98	4.16
	4.20	6.00	6.23	5.50	4.41	8.04	4.56	4.78	5.00	5.14	6.22
	7.18	6.29	5.37	5.20	5.43	4.70	6.94	4.32	6.48	5.27	3.46
	6.17	4.21	5.46								

DH-111	5.55	6.31	6.37	3.86	4.42	4.61	4.78	5.57	5.45	6.90	5.36
	6.39	5.93	4.71	7.20	6.39	5.84	5.65	6.53	5.92	5.65	4.15
	5.60	5.65	6.40	7.02	3.34	4.77	4.98	5.41	5.59	6.00	8.30
	5.90	5.22	5.81	6.36	7.02	5.19	4.09	7.41	6.72	5.83	4.89
	6.54	5.05	6.23	5.16	5.22	4.62	6.16	4.90	4.91	4.69	6.79
	5.74	6.06	7.72	5.92	5.61	4.75	5.05	7.45	5.47	5.89	6.37
	3.42	4.96	5.54	5.88	4.55	4.97	5.41	4.67	4.87	4.26	5.01
	4.27	5.62	7.04	5.00	5.01	6.67	5.67	5.83	5.03	5.38	5.71
	6.98	7.71	4.78	4.73	7.55	5.12	6.11	5.71	3.73	5.71	5.87
	3.46	5.84	5.23	7.21	3.84	6.70	5.85	6.45	9.72	6.16	4.94
	5.29	6.82	6.49	4.10	5.62	4.28	4.43	5.78	5.01	3.58	6.25
	5.79	4.74	4.87	5.83	5.88	4.74	4.85	4.93	5.32	5.41	6.73
	7.04	5.57	7.45	5.60	4.75	4.42	6.39	4.27	5.51	5.90	4.99
	3.47	4.32	6.30	4.59	6.57	8.28	4.79	7.07	6.27	8.58	5.56
	3.95	3.89	6.96	5.43	6.96	4.98	5.87	5.69	5.54	4.90	7.28
	5.80	7.08	4.97	7.31	5.41	6.83	4.98	4.39	5.56	4.41	4.30
	7.39	5.54	4.25	5.17	6.37	6.12	7.72	4.72	4.86	5.52	6.02
	4.45	4.75	5.85	6.62	3.51	4.05	8.00	4.62	6.77	4.07	3.66
	8.21	5.22	9.46	5.88	5.08	5.18	4.17	5.65	6.52	5.95	9.23
	4.37	3.17	4.70	4.78	3.99	5.37	4.99	4.81	5.06	4.88	7.63
	4.96	6.24	6.41	4.78	6.89	6.51	6.01	5.69	6.83	6.14	6.38
	3.75	5.96	4.31	4.44	4.61	5.48	5.14	5.48	4.25	4.91	4.95
	7.02	6.82	4.37	6.41	4.96	5.64	5.02	5.04	5.84	4.84	4.91
	4.31	5.60	7.56	5.92	5.45	8.11	5.07	5.94	5.25	7.37	
DH-99	3.58	4.68	5.07	5.33	5.43	5.54	3.24	3.88	5.58	5.90	6.05
	6.44	2.85	3.15	3.75	4.21	5.10	6.25	3.92	4.21	4.58	5.54
	4.87	5.89	6.55	7.88	3.65	3.69	4.66	5.68	4.49	4.52	4.91
	6.66	4.35	6.55	7.53	6.80	6.17	5.62	5.40	4.91	3.60	4.12
	6.41	6.42	6.48	4.39	4.50	5.10	3.97	4.32	3.40	3.57	3.58
	3.98	3.88	3.92	5.71	3.62	4.85	5.15	5.49	5.70	4.36	5.90
	4.61	3.34	3.82	4.23	4.47	4.61	5.00	5.43	5.50	6.52	6.53
	6.90	7.00	7.11	4.32	5.14	4.53	4.51	6.74	6.30	6.06	5.15
	3.75	4.58	4.15	4.77	5.22	5.41	5.45	6.28	4.73	4.87	4.31
	3.63	6.89	4.30	4.75	4.67	6.44	6.65	4.85	5.80	6.04	5.03
	4.99	7.03	6.82	3.41	5.86	5.14	4.68	6.51	6.16	2.96	3.83
	3.07	5.08	5.26	4.92	4.39	6.61	5.09	5.78	5.58	7.80	4.27
	5.30	5.80	6.01	5.30	5.32	5.11	5.48	6.69	3.54	5.90	6.94
	5.68	6.05	3.91	4.24	4.82	5.34	6.87	7.08	5.12	4.05	5.64
	6.34	4.01	4.96	5.01	5.62	3.87	7.01	3.99	5.77	7.41	3.87
	3.33	6.49	4.67	6.29	5.32	3.03	4.16	5.21	7.42	4.15	5.88
	9.75	5.89	4.33	5.84	4.55	4.64	4.21	4.42	4.44	6.34	4.77
	5.20	5.31	8.80	6.48	6.12	4.72	4.23	4.38	5.44	6.07	6.49
	6.89	4.90	6.29	4.22	4.72	3.53	5.48	5.96	5.15	4.41	3.88
	4.75	5.86	3.86	3.24	4.03	5.12	7.09	3.73	2.78	7.82	4.25
	4.89	6.28	6.30	5.04	5.07	4.08	4.53	6.45	7.17	4.42	3.37
	3.69	3.12	5.94	7.28	6.98	4.98	4.06	4.15	5.06	3.78	4.59
	4.49	3.57	3.75	5.52	4.69						

Appendix C Geochemical data in Bowland Basin

Table S1 Geochemical data on TLC section. TOC = total organic carbon, ND = not determined, LOD = limit of quantification

ID	Height m	Lithology	TOC wt%	Al wt%	Fe wt%	Fecarb wt%	Feox wt%	Femag wt%	Fepy wt%	Mo ppm	U ppm
TLC-3	1.7	calcareous shale	0.49	3.96	1.37	0.13	0.49	0.01	0.13	1.01	2.56
TLC-4	2.4	micrite	ND	0.51	1.03	0.74	0.05	0.00	0.16	0.15	0.43
TLC-5	3.2	shale	0.59	3.77	1.19	0.20	0.10	0.01	0.26	0.61	1.91
TLC-7	5.8	shale	1.16	7.59	3.55	0.39	0.06	0.07	0.83	0.26	1.93
TLC-a	6.5	shale	1.06	7.94	3.69	0.12	1.26	0.22	0.02	0.24	2.21
TLC-8	7.7	shale	1.04	7.68	3.35	0.30	0.06	0.08	0.22	0.13	1.97
TLC-10	9.3	calcareous shale	1.32	7.22	3.70	0.40	0.11	0.09	0.94	0.37	2.83
TLC-12	10.6	calcareous shale	0.77	4.52	2.42	0.56	0.19	0.03	0.18	0.26	1.61
TLC-13	12.5	micrite	0.50	2.93	2.34	1.03	0.04	0.03	0.31	0.17	1.23
TLC-14	14.8	shale	0.58	3.47	1.44	0.25	0.34	0.03	0.09	0.21	1.44
TLC-16	15.8	shale	0.87	6.12	3.40	0.41	0.05	0.08	0.61	0.22	1.73
TLC-17	16.3	micrite	0.35	2.39	3.72	2.08	0.05	0.06	0.25	0.17	1.16
TLC-19	17.7	calcareous shale	0.39	2.86	2.39	0.90	0.05	0.04	0.29	0.15	1.20
TLC-20	18.6	shale	0.69	4.49	2.09	0.25	0.13	0.04	0.34	0.20	1.94
TLC-21	19	shale	0.86	6.25	2.58	0.20	0.30	0.05	0.28	0.15	1.88
TLC-23	23.8	shale	1.20	8.39	3.80	0.48	0.07	0.09	0.17	0.33	2.22
TLC-24	26.2	micrite	1.09	3.68	1.71	0.26	0.22	0.01	0.63	0.23	1.75
TLC-27	32.6	calcareous shale	0.73	3.80	2.64	0.66	0.11	0.04	0.51	0.25	1.64
TLC-29	37.1	micrite	0.28	3.20	1.79	0.15	0.59	0.04	0.00	<LOD	0.90
TLC-30	40.2	shale	0.97	7.17	2.79	0.22	0.20	0.05	0.55	0.44	2.02
TLC-31	45.4	micrite	0.06	3.54	2.53	0.41	0.05	0.04	0.79	0.42	1.83
TLC-32	45.8	calcareous shale	0.45	5.22	1.98	0.15	0.02	0.01	0.25	0.32	1.65
TLC-33-2	48.6	calcareous shale	0.22	2.04	1.59	0.58	0.04	0.05	0.25	0.36	5.50
TLC-34	50.6	shale	0.65	10.62	3.30	0.14	0.03	0.05	1.09	0.96	2.24
TLC-35	52.1	shale	0.47	4.64	2.64	0.24	0.10	0.09	0.13	0.14	1.54
TLC-36	54	shale	0.35	3.52	2.14	0.54	0.08	0.04	0.10	<LOD	1.30

TLC-39	56.5	black shale	1.16	7.85	2.07	0.15	0.05	0.07	0.03	<LOD	3.39
TLC-40	56.95	micrite	0.32	6.78	4.00	0.38	0.06	0.15	0.25	0.28	1.86
TLC-41	58.05	black shale	0.50	7.70	3.41	0.18	0.11	0.13	0.56	0.18	1.92
TLC-47	61.2	black shale	1.61	4.91	2.87	1.68	0.17	0.03	0.30	0.27	3.44
TLC-42	63.6	black shale	4.37	9.71	2.87	0.29	0.06	0.02	1.08	2.02	8.08
TLC-44	64.2	black shale	1.66	9.73	2.85	0.52	0.14	0.05	0.13	0.41	4.30
TLC-45	65.2	black shale	2.48	10.60	2.78	0.41	0.05	0.04	0.79	0.45	4.53
TLC-46	65.9	micrite	1.54	4.94	20.71	7.76	0.34	4.57	0.82	<LOD	4.41
TLC-50	66.8	black shale	2.41	10.07	3.32	0.48	0.07	0.03	1.40	1.25	5.96
TLC-51	68	black shale	7.17	8.85	3.67	0.61	0.04	0.02	2.41	27.93	13.22
TLC-53	68.9	black shale	7.38	6.85	13.11	0.64	0.09	0.02	7.02	58.03	7.04
TLC-54	69.3	shale	4.62	9.82	2.96	0.23	0.03	0.00	1.64	2.83	8.91
TLC-55	69.8	black shale	10.54	6.53	4.76	0.40	0.03	0.01	1.56	7.15	9.27
TLC-56	70.8	black shale	4.74	7.62	3.93	0.49	0.04	0.01	2.75	9.61	7.12
TLC-58	73.1	mudstone	3.53	5.21	3.78	0.95	0.02	0.00	2.89	8.08	5.77
TLC-60	75.5	mudstone	1.60	3.52	2.88	1.29	0.03	0.00	1.54	<LOD	2.80
TLC-61	76.7	mudstone	2.04	6.10	1.93	0.38	0.04	0.00	1.34	0.60	52.67
TLC-62	77.8	shale	3.01	1.91	2.67	0.98	0.03	0.00	1.51	46.47	20.90
TLC-63	78.3	shale	4.12	5.90	5.26	1.17	0.03	0.02	4.19	55.33	16.35
TLC-66	81.8	calcaerous mudstone	2.61	4.12	1.44	0.45	0.02	0.00	0.60	26.38	15.50
TLC-67	82.6	calcarenite	ND	2.24	1.93	0.72	0.01	0.00	1.33	7.36	5.55
TLC-68	83.7	calcaerous mudstone	3.17	7.50	2.75	0.72	0.03	0.01	1.90	12.21	10.81
TLC-70	87.1	shale	2.59	8.33	2.53	0.45	0.03	0.01	1.44	1.31	8.97
TLC-71	88.1	shale	1.77	8.89	2.72	0.47	0.04	0.05	0.31	1.36	7.66
TLC-72	89.2	shale	2.51	7.66	2.59	0.55	0.03	0.02	1.26	9.70	10.79
TLC-73	89.9	shale	2.60	11.63	2.67	0.26	0.02	0.03	0.98	0.36	2.68
TLC-74	91.1	shale	1.22	5.76	2.35	0.87	0.04	0.02	1.16	2.78	5.05
TLC-75	92.1	shale	1.96	7.98	4.45	1.13	0.05	0.69	1.60	1.34	4.00
TLC-76	93.2	shale	2.34	7.27	2.28	0.47	0.03	0.05	0.78	0.62	10.62
TLC-77	94.1	calcarenite	ND	0.47	2.66	1.85	0.03	0.15	0.52	0.82	3.59
TLC-78	95.3	shale	2.90	5.39	2.93	0.55	0.05	0.02	2.08	6.66	29.66

TLC-79	96.3	shale	3.06	9.62	3.28	0.52	0.03	0.01	1.45	1.75	9.21
TLC-81	99.4	calcareous shale	1.11	3.41	2.99	1.90	0.07	0.01	0.74	0.96	4.50
TLC-83	102.6	micrite	1.45	2.77	1.50	0.92	0.03	0.01	0.42	0.64	8.27
TLC-84	103.5	shale	2.50	9.52	4.96	0.63	0.03	0.01	0.72	9.33	7.83
TLC-87	105.7	shale	3.33	10.00	2.63	0.47	0.02	0.01	1.96	24.98	11.00
TLC-90	107.8	shale	3.38	10.12	2.13	0.36	0.02	0.01	1.45	43.36	9.73
TLC-92	110.6	mudstone	2.90	7.00	2.02	0.61	0.05	0.01	1.33	35.48	11.48
TLC-93	113.6	shale	3.65	7.61	5.16	1.11	0.05	0.02	4.13	67.04	12.50
TLC-94	115.4	mudstone	3.35	4.05	6.01	1.57	0.05	0.05	5.15	67.30	16.42
TLC-95	117.2	micrite	ND	0.27	0.34	0.24	0.01	0.00	0.06	1.35	0.82
TLC-97	122	shale	2.89	7.06	2.97	0.97	0.03	0.01	1.81	28.32	13.39
TLC-99	124.8	shale	4.87	12.68	4.49	0.69	0.04	0.01	1.75	46.10	18.56
TLC-101	129	shale	2.39	9.46	5.15	1.32	0.10	0.02	3.33	16.56	11.08

Table S2 Geochemical data on LB section. TOC = total organic carbon, ND = not determined, LOD = limit of quantification

ID	Height m	Lithology	TOC	Al wt%	Fe wt%	Fecarb wt%	Feox wt%	Femag wt%	Fepy wt%	Mo ppm	U ppm
LB-2	0.2	calcareous shale	0.35	7.02	3.32	0.32	0.03	0.18	0.09	1.04	1.57
LB-3	1	calcareous shale	0.58	7.14	2.86	0.33	0.10	0.12	0.03	<LOD	1.82
LB-4	1.5	calcareous shale	0.43	6.00	2.79	0.28	0.03	0.20	0.02	<LOD	1.10
LB-5	2	calcareous shale	0.58	7.77	2.85	0.19	0.09	0.18	0.00	<LOD	1.70
LB-6	3	dark grey shale	0.88	1.89	4.96	1.92	0.12	0.12	1.67	7.94	14.85
LB-7	3.5	dark grey shale	0.62	1.71	3.84	2.03	0.04	0.00	1.42	0.42	4.69
LB-8-2	4	shale	3.95	7.84	2.25	0.32	0.01	0.01	0.33	0.61	5.94
LB-9	4.8	dark grey shale	1.73	2.52	10.55	1.72	0.05	0.00	8.98	0.69	5.23
LB-10	5.1	dark grey shale	4.36	5.97	3.03	0.84	0.01	0.00	0.59	8.51	9.22
LB-11-2	5.3	micritic limestone	ND	0.89	0.58	0.29	0.00	0.00	0.24	0.54	1.65
LB-11	5.7	micritic limestone	ND	1.35	1.19	0.70	0.00	0.00	0.43	0.76	1.64
LB-12	5.8	grey platy shale	1.76	5.00	2.79	0.97	0.05	0.00	1.35	2.00	10.00

LB-13	6	grey platy shale	3.17	9.22	3.94	0.45	0.02	0.01	2.54	1.99	9.36
LB-14	7	dark grey calcareous shale	4.66	6.32	3.70	0.90	0.03	0.04	1.15	4.32	9.00
LB-16	9	dark grey calcareous shale	4.70	9.00	3.11	0.37	0.11	0.03	1.30	2.56	9.54
LB-17	10	dark grey calcareous shale	2.55	4.33	3.93	2.00	0.06	0.03	1.68	1.55	4.53
LB-18	10.9	platy dark grey shale	1.19	1.73	5.57	4.35	0.07	0.03	0.67	0.19	2.18
LB-19	11.8	calcareous blocky mudstone	4.64	4.93	3.37	0.69	0.03	0.03	2.67	21.26	14.34
LB-20	13	calcareous blocky mudstone	3.64	4.79	1.88	0.46	0.04	0.02	0.45	42.54	19.05
LB-21	13.6	calcareous blocky mudstone	2.09	2.24	1.89	1.21	0.02	0.02	0.66	9.20	9.81
LB-22	14.1	dark grey shale	4.10	4.81	2.07	0.36	0.01	0.02	1.47	4.46	7.29
LB-25	15	dark grey shale	5.31	7.57	4.94	1.03	0.03	0.04	3.14	61.44	19.66
LB-26	16	dark grey shale	2.88	7.48	2.85	0.72	0.03	0.02	1.49	4.55	9.52
LB-27	17	dark grey shale	4.89	2.86	1.78	0.54	0.01	0.02	1.36	58.63	20.18
LB-28	18	dark grey shale	3.86	4.55	4.44	1.16	0.08	0.05	3.17	63.91	29.03
LB-30	20	dark grey shale	3.91	3.59	1.62	0.35	0.01	0.03	1.11	7.34	13.28
LB-32	21	mudstone	1.45	2.57	3.34	0.36	0.02	0.03	1.66	5.30	10.86

Table S3 Geochemical data on RH section. TOC = total organic carbon, ND = not determined, LOD = limit of quantification

ID	Height m	Lithology	TOC wt%	Al wt%	Fe wt%	Fecarb wt%	Feox wt%	Femag wt%	Fepy wt%	Mo ppm	U ppm
RH-2	0.8	mudstone	0.81	3.07	1.68	0.28	0.37	0.02	0.20	2.35	2.93
RH-3	0.9	micrite	ND	0.98	0.95	0.31	0.02	0.02	0.40	0.68	2.00
RH-6	2.5	micrite	0.31	1.81	1.24	0.33	0.04	0.02	0.26	2.88	1.44
RH-7	2.8	micrite	ND	0.82	0.84	0.38	0.09	0.02	0.06	0.11	1.07
RH-13	11.5	mudstone	0.61	7.61	5.37	0.10	0.70	0.24	0.06	0.12	1.56
RH-15	13.1	mudstone	1.23	7.21	2.19	0.23	0.30	0.04	0.24	0.79	1.68
RH-17	14.3	shale	0.76	7.97	2.87	0.06	0.64	0.15	0.00	0.19	1.65
RH-20	15.9	mudstone	0.96	7.29	1.91	0.02	0.61	0.04	0.01	0.48	1.72

Table S4 Geochemical data on FL section. TOC = total organic carbon, ND = not determined, LOD = limit of quantification

ID	Depth m	Lithology	TOC wt%	Al wt%	Fe wt%	Fecarb wt%	Feox wt%	Femag wt%	Fepy wt%	Mo ppm	U ppm
FL-4	1.09	shale	3.93	1.94	1.01	0.13	0.35	<LOD	0.40	4.68	28.27
FL-5	1.14	shale	4.31	2.10	0.87	0.13	0.10	<LOD	0.32	4.57	23.89
FL-7	1.38	shale	4.87	3.10	1.76	0.18	0.26	<LOD	0.96	5.87	23.07
FL-8	1.48	laminated micrite	ND	0.50	0.27	0.05	0.03	<LOD	0.08	2.38	13.86
FL-9	1.53	shale	4.53	1.97	0.87	0.11	0.21	<LOD	0.43	5.77	24.77
FL-10	1.70	laminated micrite	1.72	0.61	0.21	0.02	0.05	<LOD	0.07	5.84	13.40
FL-13	1.80	laminated micrite	1.60	0.53	0.19	0.03	0.00	<LOD	0.06	5.34	12.38
FL-15	1.93	shale	4.72	4.10	2.15	0.22	0.29	<LOD	1.51	9.07	17.81
FL-16	2.05	laminated micrite	2.18	1.57	0.79	0.09	0.00	<LOD	0.70	3.63	13.81
FL-17	2.30	micrite	2.20	2.04	0.71	0.05	0.00	<LOD	0.55	3.04	9.60
FL-18	2.70	shale	4.68	3.44	2.23	0.25	0.04	<LOD	1.18	9.99	23.92
FL-19	3.20	shale	5.85	4.36	2.39	0.16	0.01	<LOD	2.04	18.38	24.67
FL-20	3.30	shale	7.04	4.13	2.85	0.30	0.21	<LOD	1.60	35.93	41.78
FL-23	3.80	laminated micrite	4.18	1.28	0.45	0.09	0.02	<LOD	0.26	43.04	13.66
FL-24	4.40	shale	7.13	4.45	1.46	0.10	0.02	<LOD	1.16	38.40	44.72
FL-25	4.70	laminated micrite	0.81	0.41	0.16	0.02	0.03	<LOD	0.04	6.58	6.50
FL-27	5.90	laminated micrite	1.31	0.96	0.34	0.05	0.00	<LOD	0.10	6.74	7.89
FL-29	6.70	laminated micrite	2.72	1.20	0.53	0.09	0.01	<LOD	0.43	16.16	14.15
FL-31	8.80	laminated micrite	1.35	0.97	0.64	0.21	0.01	<LOD	0.37	1.97	9.68
FL-32	9.30	laminated micrite	0.92	1.88	0.67	0.11	0.02	<LOD	0.31	2.27	12.06
FL-33	10.40	shale	2.72	6.94	2.57	0.51	0.05	<LOD	1.60	13.23	13.97
FL-34	10.80	shale	2.80	5.85	3.03	0.62	0.02	<LOD	1.00	18.61	9.14
FL-35	11.30	shale	2.62	6.43	3.04	0.48	0.05	<LOD	1.91	24.23	12.43
FL-39	12.50	calcareous mudstone	1.87	3.16	1.48	0.30	0.01	<LOD	1.13	3.28	10.95
FL-40	12.80	calcareous shale	3.21	3.82	1.38	0.32	0.02	<LOD	0.28	11.66	8.65
FL-41	13.20	laminated micrite	0.66	0.54	0.28	0.05	0.00	<LOD	0.07	0.85	3.31
FL-44	15.30	laminated micrite	0.43	1.04	0.83	0.41	0.00	<LOD	0.39	1.23	2.93

FL-45	15.50	calcareous shale	1.22	3.31	2.76	1.33	0.07	<LOD	1.38	4.07	5.42
FL-46	15.60	shale	4.04	4.30	4.16	1.29	0.04	<LOD	2.44	2.04	6.67
FL-47	16.20	shale	4.03	5.43	4.67	1.87	0.02	<LOD	2.52	3.38	6.03

Table S5 Geochemical data on SS section. TOC = total organic carbon, ND = not determined, LOD = limit of quantification

ID	Height m	Lithology	TOC wt%	Al wt%	Fe wt%	Fecarb wt%	Feox wt%	Femag wt%	Fepy wt%	Mo ppm	U ppm
SS11	0	shale	2.54	6.32	3.37	0.74	0.18	0.09	1.51	15.68	8.74
SS12	0.1	shale	2.54	6.06	3.15	0.64	0.05	0.06	1.70	14.54	9.64
SS13	1.1	shale	2.92	6.58	3.35	0.65	0.05	0.06	2.20	24.85	12.81
SS14	1.5	shale	3.01	7.44	3.67	0.57	0.05	0.05	2.41	19.16	13.19
SS15	1.7	shale	2.84	9.30	2.90	0.28	0.04	0.02	1.73	2.22	8.18
SS16	2.7	shale	3.13	11.99	3.19	0.27	0.04	0.04	1.51	1.58	8.48
SS17	3.7	shale	3.26	12.01	2.01	0.15	0.06	0.04	0.32	1.49	10.96
SS18	4.7	shale	2.77	10.88	1.71	0.12	0.26	0.06	0.01	0.82	9.34
SS19	5.7	shale	2.60	6.79	2.82	0.59	0.04	0.05	1.79	14.67	10.23
SS20	6.7	shale	2.64	6.18	2.53	0.49	0.04	0.05	1.51	14.19	12.89
SS21	7.7	shale	2.73	6.96	2.67	0.51	0.05	0.04	1.72	18.12	11.61
SS22	8.7	shale	2.90	6.07	3.12	0.86	0.05	0.04	1.95	22.56	11.31

Table S6 Geochemical data on MC section. TOC = total organic carbon, ND = not determined, LOD = limit of quantification

ID	Height m	Lithology	TOC	Al wt%	Fe wt%	Fecarb wt%	Feox wt%	Femag wt%	Fepy wt%	Mo ppm	U ppm
MC-8	0	platy shale	2.45	3.80	2.72	0.79	0.07	0.02	1.85	41.37	10.78
MC-9	1	platy shale	2.77	3.71	2.27	0.65	0.05	0.02	1.56	46.66	13.38
MC-1	2	flaky shale	2.58	7.71	3.21	0.64	0.05	0.03	2.22	26.70	9.87
MC-2	2.3	flaky shale	2.39	7.48	3.21	0.68	0.05	0.03	2.15	22.68	8.67
MC-3	2.8	flaky shale	2.66	8.36	3.74	0.61	0.05	0.03	2.46	23.27	9.77
MC-4	3.5	flaky shale	2.69	8.19	3.98	0.63	0.05	0.03	2.63	24.53	10.02
MC-5	4.4	flaky shale	2.57	8.15	3.78	0.67	0.06	0.04	2.57	19.07	8.43
MC-6	5.3	flaky shale	3.17	7.36	3.49	0.63	0.05	0.04	2.31	26.51	11.60

MC-7	6.4	block mudstone	2.48	6.20	3.02	0.69	0.05	0.03	1.92	17.78	7.94
MC-10	10	flaky shale	2.54	13.33	3.97	0.35	0.03	0.03	2.01	8.28	9.66
MC-11	11	flaky shale	2.96	13.64	4.43	0.59	0.05	0.07	2.09	1.48	8.07
MC-12	11.9	flaky shale	2.47	14.14	4.35	0.37	0.07	0.06	2.09	1.23	8.13
MC-15	16	flaky shale	2.40	10.41	4.08	0.75	0.08	0.10	1.98	11.26	12.12
MC-16	17.2	flaky shale	2.10	11.02	1.41	0.33	0.06	0.07	0.97	2.35	6.08

Table S7 Geochemical data on DB section. TOC = total organic carbon, ND = not determined, LOD = limit of quantification

ID	Height m	Lithology	TOC	Al wt%	Fe wt%	Fecarb wt%	Feox wt%	Femag wt%	Fepy wt%	Mo ppm	U ppm
DB-8	0.1	mudstone	3.69	6.76	2.93	0.04	2.16	0.04	0.01	4.91	6.00
DB-9	0.5	micirte	1.25	1.79	2.07	1.11	0.29	0.01	0.60	1.92	4.32
DB-10	1.1	mudstone	1.26	5.37	2.09	0.09	1.33	0.02	0.01	1.71	3.95
DB-13	2.6	mudstone	3.86	5.05	3.47	0.51	0.22	0.01	1.61	6.01	12.63
DB-14	3.2	mudstone	1.46	10.36	2.04	0.23	0.30	0.01	0.22	0.33	3.13
DB-15	4.2	mudstone	2.34	3.99	2.61	1.15	0.18	0.28	0.39	1.65	8.19
DB-16	4.9	mudstone	1.28	10.86	1.84	0.20	0.09	0.01	0.24	0.22	3.54
DB-19	6.3	mudstone	2.24	7.77	2.17	0.26	0.01	<LOD	0.39	1.04	6.47
DB-20	6.8	mudstone	0.89	2.66	2.21	0.92	0.01	0.01	0.93	0.75	7.45
DB-22	7.8	mudstone	3.90	9.77	3.09	0.31	0.01	<LOD	0.95	1.13	9.02
DB-23	9.8	grey shale	3.01	9.67	2.04	0.12	0.98	<LOD	0.03	0.67	12.27
DB-1	12.1	mudstone	2.52	8.91	4.17	0.51	0.02	<LOD	2.63	1.50	6.92
DB-2	12.7	mudstone	3.03	9.53	3.59	0.36	0.02	<LOD	1.30	1.44	14.42
DB-3	13.4	micrite	1.25	1.25	0.85	0.28	0.04	<LOD	0.46	1.14	3.41
DB-5	14	mudstone	3.61	5.00	2.78	0.44	0.04	<LOD	0.30	3.52	11.01
DB-7	14.6	mudstone	5.09	4.29	1.90	0.33	0.08	<LOD	0.35	24.66	24.06

Table S8 Geochemical data on SC section. TOC = total organic carbon, ND = not determined, LOD = limit of quantification

ID	Height m	Lithology	TOC wt%	Al wt%	Fe wt%	Fecarb wt%	Feox wt%	Femag wt%	Fepy wt%	Mo ppm	U ppm
SC-2	0.6	calcarenite	0.31	ND	ND	ND	ND	ND	ND	ND	ND

SC-8	4.1	shale	2.51	7.70	5.35	0.55	0.05	0.04	3.56	1.04	4.07
SC-9	5.2	shale	2.60	8.08	2.79	0.68	0.05	0.06	0.58	0.51	3.92
SC-10	6	shale	1.41	8.92	2.48	0.48	0.17	0.06	0.48	1.04	3.31
SC-12	7.6	shale	2.33	10.58	3.50	0.56	0.05	0.09	1.50	0.99	3.90
SC-13	9.2	shale	2.32	9.77	3.25	0.79	0.05	0.14	0.83	0.92	4.35
SC-14	11	shale	1.88	10.16	3.63	0.82	0.06	0.23	0.70	0.74	4.01
SC-15	12	micrite	0.45	2.32	29.80	13.53	0.31	4.18	0.14	0.12	1.26
SC-16	22	shale	3.13	8.20	1.92	0.41	0.04	0.03	1.08	1.11	4.80
SC-17	23	shale	2.43	5.50	3.36	1.60	0.04	0.02	1.29	0.45	3.48
SC-18	23.8	shale	2.20	6.03	3.75	1.44	0.05	0.03	1.84	0.82	4.02
SC-19	24.1	micrite	0.88	1.81	13.57	7.93	0.19	3.02	0.43	0.00	1.47
SC-20	25	shale	1.96	8.74	2.49	0.31	0.04	0.03	1.10	0.58	7.37
SC-21	26	shale	1.71	8.92	2.58	0.36	0.03	0.05	0.89	0.64	4.93
SC-22	30.5	shale	3.52	6.67	3.27	0.68	0.03	0.03	2.24	25.53	10.22
SC-23	31.4	shale	3.32	7.04	3.24	0.84	0.04	0.03	2.31	25.11	7.11
SC-24	32.4	shale	2.56	6.28	3.61	0.90	0.03	0.03	2.50	30.05	7.21
SC-25	37.2	shale	3.68	5.72	4.00	0.89	0.05	0.03	3.08	30.69	9.79
SC-28	39.6	shale	1.23	2.86	2.81	1.39	0.04	0.02	1.52	<LOD	6.90
SC-29	40.6	shale	1.56	7.11	3.59	0.46	0.02	0.03	2.46	2.55	4.24
SC-30	41.6	shale	1.99	6.08	3.19	1.07	0.04	0.03	1.52	<LOD	2.79
SC-31	42.20	shale	1.90	8.38	1.75	0.25	0.04	0.03	0.61	<LOD	4.34
SC-32	42.8	micrite	0.82	1.97	20.98	12.97	0.35	3.26	0.28	<LOD	2.50
SC-33	43	mudtone	1.46	9.01	1.76	0.26	0.07	0.03	0.39	<LOD	3.89
SC-34	48	shale	3.38	3.37	3.52	1.04	0.03	0.03	2.41	45.87	17.34
SC-36	50	shale	3.49	6.09	4.53	1.20	0.05	0.04	3.17	41.75	8.68
SC-38	52	mudstone	3.76	3.57	4.59	1.35	0.05	0.04	3.04	7.98	10.54
SC-39	52.8	mudstone	2.84	4.49	2.92	0.81	0.03	0.03	1.87	18.63	9.50

Table S9 Geochemical data on LC section. TOC = total organic carbon, ND = not determined, LOD = limit of quantification

ID	Height m	Lithology	TOC wt%	Al wt%	Fe wt%	Fecarb wt%	Feox wt%	Femag wt%	Fepy wt%	Mo ppm	U ppm

LC-1	0	dark grey shale	3.30	7.59	3.35	0.80	0.02	0.00	2.30	22.23	8.82
LC-2	1	dark grey shale	3.38	9.03	5.32	1.26	0.07	0.01	3.64	23.13	9.52
LC-3	2.3	dark grey shale	3.76	8.78	5.71	1.39	0.04	0.00	4.19	29.98	13.36
LC-4	3.3	dark grey shale	3.66	9.88	5.91	1.20	0.04	0.01	4.08	32.48	16.06
LC-5	5.2	dark grey shale	3.31	11.07	3.71	0.42	0.03	0.00	2.46	12.19	12.84
LC-6	6.3	dark grey shale	3.50	9.66	5.71	1.10	0.04	0.01	4.25	26.12	16.03
LC-7	7.3	dark grey shale	2.69	2.26	3.15	2.06	0.07	0.01	0.92	8.50	10.33
LC-8	8.1	dark grey shale	3.27	3.13	2.58	1.25	0.07	0.01	1.30	4.38	8.06
LC-9	9.1	dark grey shale	3.72	5.18	2.69	0.50	0.02	0.01	2.02	8.12	3.49
LC-10	10.1	dark grey shale	2.82	3.40	2.76	0.69	0.03	0.02	1.99	7.36	6.90
LC-11	11.1	dark grey shale	3.47	4.93	6.01	1.26	0.11	0.02	4.91	37.90	10.55
LC-12	12.4	dark grey shale	3.60	5.75	5.37	1.47	0.04	0.02	2.84	28.21	12.00
LC-13	13.4	dark grey shale	3.45	6.21	2.63	0.59	0.03	0.03	1.91	26.93	11.08
LC-14	14.4	dark grey shale	3.22	9.60	3.95	0.50	0.02	0.00	3.00	17.43	9.56
LC-15	15.4	dark grey shale	4.28	7.63	2.31	0.33	0.02	0.01	1.70	32.20	10.61
LC-16	16.4	dark grey shale	4.53	8.93	4.70	1.24	0.05	0.00	3.52	34.81	19.07
LC-17	17.5	dark grey shale	5.27	6.28	4.76	1.00	0.48	0.04	3.26	98.51	22.79
LC-19	20	dark grey shale	4.11	3.22	2.63	0.50	0.07	0.01	2.10	12.30	12.11
LC-20	21	dark grey shale	4.33	2.98	2.25	0.41	0.08	0.01	1.73	10.99	7.18
LC-21	22	dark grey shale	3.47	2.86	2.19	0.49	0.02	0.02	1.68	5.00	6.19
LC-22	23	dark grey shale	1.85	1.04	1.14	0.37	0.01	0.01	0.81	4.57	5.97
LC-23	23.9	dark grey shale	3.37	3.37	1.82	0.32	0.03	0.03	1.46	4.64	8.55
LC-24	25	dark grey shale	3.22	3.41	2.67	0.33	0.14	0.03	2.13	6.64	5.42
LC-25	26	dark grey shale	4.63	3.48	3.74	0.47	0.01	0.01	3.33	31.21	7.02
LC-27	28.2	dark grey shale	3.18	6.30	5.52	0.44	0.06	0.01	4.50	7.56	3.74

Table S10 Geochemical data on CC section. TOC = total organic carbon, ND = not determined, LOD = limit of quantification

ID	Height m	Lithology	TOC wt%	Al wt%	Fe wt%	Fecarb wt%	Feox wt%	Femag wt%	Fepy wt%	Mo ppm	U ppm
CC-4	0	dark shale	3.33	10.87	5.01	0.83	0.06	0.06	3.20	10.93	14.72
CC-5	1.2	dark shale	4.22	14.08	1.69	0.11	0.03	0.03	0.23	2.22	14.41

CC-6	1.6	dark shale	4.31	12.09	1.81	0.31	0.15	0.04	0.05	2.24	13.98
CC-7	2.8	dark shale	4.76	11.93	5.55	0.32	0.06	0.01	4.09	3.95	16.27
CC-8	3.8	dark shale	3.95	10.30	3.46	0.32	0.32	0.03	1.59	3.50	7.66
CC-10	4.6	mudstone	4.92	12.31	3.35	0.25	0.06	0.02	1.95	2.11	15.14
CC-11	5.2	mudstone	2.97	4.08	1.61	0.55	0.04	0.02	0.86	11.91	12.29
CC-12	5.5	mudstone	1.66	1.22	3.72	2.59	0.07	0.01	0.44	22.42	7.04
CC-13	7	mudstone	3.39	5.50	2.59	0.81	0.06	0.02	1.68	55.30	19.34
CC-14	8	mudstone	3.38	5.23	2.59	0.80	0.11	0.02	1.53	56.14	12.36
CC-2	18.4	mudstone	3.41	5.67	2.73	0.74	0.09	0.03	1.58	64.64	20.12

Table S11 Geochemical data on CH section. TOC = total organic carbon, ND = not determined, LOD = limit of quantification

ID	Height m	Lithology	TOC wt%	Al wt%	Fe wt%	Fecarb wt%	Feox wt%	Femag wt%	Fepy wt%	Mo ppm	U ppm
CH-1	0.1	calcaerous mudstone	0.72	6.20	2.70	0.21	0.03	0.06	0.27	0.72	2.61
CH-2	0.4	micrite	ND	0.87	3.45	2.28	0.04	0.04	0.17	<LOD	1.41
CH-3	0.8	calcaerous mudstone	0.94	9.18	3.52	0.08	0.98	0.17	0.07	0.34	2.25
CH-5	2	calcaerous mudstone	0.88	7.42	2.54	0.17	0.17	0.06	0.42	0.16	2.07
CH-7	2.9	micrite	0.20	1.38	1.32	0.61	0.27	0.02	0.05	0.16	0.85
CH-9	4.8	micrite	ND	0.34	1.32	0.61	0.07	0.01	0.48	<LOD	0.32
CH-10	5.6	calcaerous mudstone	0.35	4.35	2.38	0.21	0.69	0.06	0.39	0.25	0.95
CH-12	6.5	micrite	0.31	2.41	2.96	1.49	0.09	0.03	0.32	0.28	1.77
CH-13	6.8	micrite	0.41	3.92	3.34	0.48	0.04	0.09	0.27	0.29	2.20
CH-14	8.6	calcaerous mudstone	0.56	5.77	2.22	0.15	0.17	0.04	0.08	0.28	1.29
CH-15	10.8	micrite	0.31	3.18	1.95	0.19	0.02	0.03	0.50	0.80	1.18
CH-17	14.5	micrite	0.14	1.81	2.50	1.58	0.03	0.03	0.18	<LOD	0.90
CH-18	15	calcaerous mudstone	0.37	5.04	1.94	0.15	0.22	0.05	0.08	0.45	1.03
CH-19	16.4	calcaerous mudstone	0.67	3.80	1.74	0.16	0.04	0.07	1.37	0.45	1.15

Table S12 Geochemical data on DH section. TOC = total organic carbon, ND = not determined, LOD = limit of quantification

ID	Height	Lithology	TOC	Al	Fe	Fecarb	Feox	Femag	Fepy	Mo	U

	m			wt%	wt%	wt%	wt%	wt%	wt%	ppm	ppm
DH-1	0.0	micrite	1.74	2.54	2.25	0.90	0.12	0.03	1.05	11.27	6.77
DH-2	1.0	shale	3.45	6.95	2.21	0.45	0.09	0.04	1.25	42.76	10.27
DH-3	1.5	shale	3.57	6.75	2.72	0.64	0.04	0.03	1.87	52.06	12.15
DH-4	2.0	shale	3.72	6.70	2.44	0.52	0.04	0.03	1.60	44.16	12.15
DH-5	2.5	shale	3.31	4.79	2.98	0.85	0.05	0.04	1.82	39.20	14.58
DH-6	3.0	shale	3.33	5.49	2.70	0.67	0.04	0.03	1.82	46.00	8.88
DH-8	4.0	calcareous shale	4.13	3.20	3.00	1.03	0.04	0.03	1.92	19.96	6.72
DH-9	4.5	micirte	1.41	1.80	3.74	2.65	0.12	0.02	0.72	3.56	2.32
DH-10	5.0	shale	5.82	9.25	7.14	0.91	0.09	0.04	6.08	17.59	7.08
DH-11	5.5	shale	3.99	8.94	4.56	0.97	0.05	0.05	3.40	44.89	12.50
DH-12	6.0	shale	3.20	8.23	7.38	1.47	0.08	0.06	5.79	44.46	11.75
DH-13	6.5	shale	2.67	10.04	7.77	1.70	0.14	0.06	5.81	35.30	9.73
DH-14	7.0	shale	2.87	8.44	7.29	1.68	0.09	0.06	4.91	33.98	10.82
DH-16	14.0	shale	2.91	10.90	5.08	1.16	0.06	0.06	3.67	30.84	16.23
DH-17	16.0	shale	2.95	8.66	7.97	1.83	0.16	0.07	5.86	41.10	17.57
DH-18	29.5	mudstone	5.04	7.89	10.13	1.81	0.10	0.09	7.92	95.65	21.25
DH-19	30.0	mudstone	2.71	10.17	7.03	1.70	0.08	0.06	4.19	36.92	13.42
DH-20	30.5	mudstone	2.24	10.67	6.53	1.53	0.15	0.06	4.74	31.21	10.98
DH-21	31.0	shale	2.27	7.43	3.41	0.79	0.04	0.04	2.46	28.49	17.64
DH-23	32.0	calcareous shale	4.56	2.70	3.89	2.16	0.10	0.03	1.37	6.31	17.53
DH-25	33.0	calcareous shale	3.00	3.53	2.66	1.28	0.05	0.03	1.08	8.06	6.99
DH-26	33.5	shale	4.31	8.69	4.04	0.86	0.06	0.04	3.00	82.20	16.84
DH-27	34.2	shale	2.59	11.81	5.21	1.06	0.09	0.05	3.58	15.42	11.97
DH-28	34.8	shale	2.17	11.30	4.47	0.69	0.05	0.04	2.91	7.78	5.85
DH-29	35.4	shale	2.79	10.44	4.38	0.82	0.05	0.05	1.84	14.67	8.70
DH-30	35.8	shale	3.20	11.13	5.19	1.18	0.08	0.08	3.52	20.22	13.52
DH-31	36.4	shale	2.76	10.82	4.10	0.70	0.06	0.07	2.21	7.97	6.48
DH-33	36.9	shale	3.09	10.70	4.41	0.81	0.07	0.07	1.34	1.35	4.55

DH-34	37.8	shale	2.99	11.24	4.15	0.94	0.06	0.08	2.20	19.84	9.57
DH-36	38.6	shale	2.64	11.36	4.67	0.99	0.07	0.07	3.09	14.23	7.49
DH-37	39.3	shale	1.98	11.09	3.83	0.53	0.05	0.03	2.18	4.83	5.38
DH-38	39.9	shale	2.46	11.47	3.97	0.51	0.05	0.03	2.44	6.39	6.16
DH-39	40.4	shale	1.59	10.12	5.11	1.54	0.08	0.02	2.64	0.73	2.46
DH-40	40.8	micrite		0.92	1.64	0.96	0.03	0.01	0.68	2.83	6.63
DH-41	41.0	shale	3.21	10.50	3.87	0.61	0.05	0.03	2.55	31.63	9.63
DH-42	41.5	shale	3.29	9.63	3.93	0.71	0.05	0.02	2.75	32.79	7.12
DH-43	42.3	calcareous shale	4.88	4.23	2.09	0.50	0.07	0.01	1.42	60.57	24.46
DH-44	43.0	calcareous shale	4.17	3.18	3.96	1.01	0.06	0.02	3.01	91.13	17.59
DH-45	43.5	calcareous shale	4.45	3.75	1.13	0.31	0.04	0.01	0.74	57.19	15.46
DH-46	44.0	calcareous shale	5.29	3.37	1.17	0.32	0.02	0.01	0.81	73.98	18.79
DH-47	44.7	calcareous shale	3.27	2.91	2.05	0.66	0.16	0.02	1.32	8.54	26.35
DH-48	45.7	calcareous shale	3.77	6.59	3.06	0.61	0.05	0.02	2.38	3.12	4.20
DH-49	46.2	calcareous shale	2.74	4.53	2.74	0.57	0.05	0.02	2.37	4.58	12.34
DH-50	46.8	calcareous shale	3.89	5.80	3.05	0.59	0.03	0.01	2.25	43.64	9.35
DH-51	47.8	shale	3.30	6.13	1.82	0.38	0.05	0.02	1.14	35.21	11.73
DH-52	48.5	shale	4.29	5.63	2.02	0.46	0.04	0.02	1.45	46.49	11.44
DH-53	49.2	mudstone	3.58	9.61	2.63	0.44	0.13	0.02	1.75	36.54	10.34
DH-54	49.9	calcarenite	3.14	10.62	3.50	0.75	0.05	0.03	2.56	21.56	9.34
DH-55	50.5	shale	2.96	9.74	5.34	1.34	0.07	0.03	4.12	38.61	10.37
DH-56	51.3	shale	3.71	8.93	6.47	1.53	0.12	0.04	2.07	62.76	22.90
DH-57	51.7	calcareous shale	3.77	2.10	3.43	2.22	0.08	0.02	0.90	8.76	9.81
DH-58	52.4	shale	3.23	7.48	8.30	2.39	0.75	0.05	4.70	42.38	14.35
DH-59	53.1	shale	4.29	8.65	10.03	2.30	0.21	0.04	7.24	36.71	19.26
DH-60	53.7	calcareous shale	5.43	3.69	2.11	0.41	0.04	0.02	1.55	15.25	23.14
DH-61	54.2	calcareous shale	4.50	4.47	2.88	0.56	0.07	0.02	2.05	11.36	6.20
DH-62	54.7	shale	4.92	4.94	2.89	0.55	0.03	0.02	2.17	10.26	6.77
DH-63	55.2	shale	3.87	4.28	2.72	0.62	0.03	0.03	2.13	9.44	2.04

DH-65	56.2	shale	4.49	5.47	8.88	2.07	0.11	0.04	6.86	59.93	21.41
DH-66	56.7	shale	5.29	7.66	2.23	0.42	0.25	0.01	1.36	21.23	18.22
DH-67	57.2	shale	4.15	3.80	1.55	0.43	0.02	0.01	1.07	27.35	26.19
DH-69	58.3	shale	4.64	5.80	4.57	1.08	0.05	0.02	3.60	60.62	18.62
DH-75	61.1	shale	4.41	3.52	2.32	0.39	0.01	0.01	1.82	23.26	5.97
DH-77	62.1	shale	4.08	3.28	1.49	0.39	0.02	0.01	1.02	34.46	7.93
DH-80	63.6	shale	3.12	7.43	8.08	2.31	0.56	0.04	5.39	39.09	12.37
DH-81	64.1	shale	2.85	6.13	5.14	1.24	0.04	0.02	3.90	36.69	10.46
DH-83	65.1	calcareous shale	3.84	6.16	2.15	0.42	0.03	0.01	1.50	27.20	12.20
DH-84	65.6	calcareous shale	3.19	2.92	1.33	0.41	0.02	0.01	0.89	18.96	8.48
DH-87	67.0	calcareous shale	3.14	2.79	0.96	0.32	0.01	0.01	0.62	31.74	14.06
DH-88	67.7	calcareous shale	3.57	3.55	1.30	0.39	0.03	0.01	0.89	32.41	10.07
DH-89	68.2	shale	3.93	3.89	1.95	0.52	0.03	0.01	1.37	26.39	7.58
DH-90	68.7	shale	3.97	3.90	2.26	0.52	0.03	0.02	1.68	27.79	33.91
DH-91	69.3	shale	3.16	3.84	9.12	2.27	0.23	0.04	6.91	75.05	13.15
DH-92	69.8	calcareous shale	4.39	4.44	1.32	0.42	0.09	0.01	0.55	27.33	15.01
DH-93	70.3	shale	3.82	3.86	5.83	1.56	0.06	0.03	4.46	63.27	27.80
DH-94	70.8	shale	3.76	4.09	6.30	1.65	0.11	0.03	4.67	82.91	20.48
DH-95	71.3	calcareous shale	4.20	4.21	6.83	1.77	0.16	0.04	5.17	81.48	20.84
DH-96	71.8	calcareous shale	4.20	5.29	7.58	1.69	0.11	0.04	5.67	98.93	16.25
DH-98	72.8	shale	3.67	5.49	4.54	1.41	0.05	0.02	3.16	50.23	22.57
DH-99	73.3	mudstone	5.36	6.73	5.22	1.77	0.27	0.03	3.13	65.25	27.91
DH-101	74.4	mudstone	6.09	7.11	10.01	2.35	0.19	0.05	6.91	42.15	21.16
DH-104	76.4	shale	2.91	3.99	3.22	0.95	0.05	0.01	2.19	40.30	29.55
DH-105	76.8	shale	5.26	4.57	6.12	1.43	0.21	0.04	4.63	97.64	24.63
DH-108	78.6	shale	5.17	6.71	5.97	1.37	0.17	0.04	4.30	90.77	34.60
DH-109	79.5	shale	5.89	6.19	5.47	1.39	0.07	0.03	3.82	96.91	38.28
DH-110	80.0	shale	6.49	5.63	7.11	1.64	0.08	0.05	5.22	94.84	34.94
DH-111	80.5	shale	4.51	6.27	5.19	2.02	0.26	0.03	2.84	53.92	31.25

DH-113	81.5	shale	5.23	8.13	7.18	1.77	0.11	0.05	5.36	70.58	19.87
DH-114	82.0	shale	5.71	4.52	12.98	2.21	1.59	0.13	9.32	107.38	26.69
DH-115	82.5	shale	6.05	5.33	6.05	1.71	0.15	0.04	4.40	76.91	38.37
DH-116	83.0	mudstone	6.15	5.94	7.26	1.77	0.09	0.05	4.43	95.57	40.08
DH-117	83.5	mudstone	5.73	6.05	6.72	1.72	0.15	0.04	1.81	81.70	27.14
DH-119	84.7	mudstone	6.26	7.85	9.05	1.84	0.35	0.06	6.50	47.25	20.72
DH-120	85.4	mudstone	4.83	6.40	6.00	1.40	0.08	0.03	4.15	57.24	25.82
DH-121	86.2	laminated shale	3.59	2.72	2.74	1.23	0.05	0.01	1.37	38.95	14.48
DH-122	86.9	shale	2.96	2.65	3.45	1.39	0.12	0.01	1.81	50.83	11.63
DH-123	87.6	shale	3.43	4.75	4.09	0.99	0.05	0.01	3.03	48.30	13.55
DH-125	89.1	shale	5.15	7.50	5.07	1.21	0.06	0.04	3.87	75.75	24.23
DH-127	90.3	laminated shale	3.53	7.39	5.25	1.07	0.07	0.03	3.73	33.06	19.19
DH-129	91.5	shale	4.32	6.97	4.34	1.04	0.05	0.04	2.05	57.05	21.86
DH-130	92.2	shale	4.28	6.90	5.12	1.24	0.08	0.05	3.63	54.25	30.25
DH-131	92.9	shale	4.19	6.80	4.35	1.14	0.07	0.05	2.73	33.54	19.45
DH-133	94.3	shale	3.71	13.25	4.41	0.39	0.06	0.03	2.85	1.80	12.08
DH-136	96.7	shale	5.56	12.05	5.43	0.46	0.06	0.04	3.16	8.18	14.72
DH-137	97.4	shale	3.93	10.96	9.51	1.68	0.10	0.07	7.05	32.24	17.08
DH-138	98.3	shale	3.26	9.45	5.80	1.32	0.10	0.06	4.03	28.56	18.75
DH-140	99.5	shale	2.51	2.34	4.27	2.72	0.11	0.04	0.76	12.13	39.82
DH-142	100.3	shale	5.19	7.41	5.61	1.24	0.08	0.08	3.86	79.73	26.10
DH-143	101.4	shale	4.11	13.80	2.56	0.19	0.14	0.07	0.57	0.60	15.97
DH-144	102.4	shale	4.42	6.66	6.68	2.04	0.10	0.55	2.47	50.27	37.62
DH-146	104.1	shale	3.08	14.31	3.19	0.78	0.08	0.47	0.36	0.99	7.95

Table S13 Geochemical data on SM section. TOC = total organic carbon, ND = not determined, LOD = limit of quantification

ID	Height m	Lithology	TOC	Al wt%	Fe wt%	Fecarb wt%	Feox wt%	Femag wt%	Fepy wt%	Mo ppm	U ppm
SM-15	3	micirte	ND	0.84	1.47	0.28	0.44	0.09	0.05	<LOD	4.47
SM-16	5.1	calcarenite	ND	0.54	0.84	0.40	0.08	0.02	0.02	<LOD	0.48

SM-17	7.8	crinoidal calcarenite	ND	1.99	2.65	0.72	0.04	0.08	0.14	<LOD	2.33
SM-20	9.7	dark grey mudstone	3.59	6.13	3.37	0.36	0.05	0.07	1.30	1.68	16.98
SM-22	11.7	dark grey platy shale	ND	7.41	3.83	0.37	0.05	0.05	1.93	3.26	8.03
SM-23	12.4	dark grey platy shale	7.94	4.98	2.84	0.52	0.05	0.04	1.40	14.14	15.77
SM-24	12.6	dark grey platy shale	9.45	5.67	3.14	0.41	0.09	0.05	1.52	20.22	15.04
SM-25	12.9	dark grey platy shale	7.36	6.52	3.18	0.29	0.35	0.04	1.18	7.81	10.50
SM-1	13.1	limestone	7.75	5.89	2.73	0.20	0.25	0.03	1.15	17.82	11.49
SM-26	13.4	black shale	6.20	7.30	2.78	0.27	0.06	0.04	1.31	16.81	13.55
SM-3	13.6	mudstone	1.51	6.37	3.11	0.27	0.40	0.02	1.80	29.29	10.41
SM-4	13.8	shale	5.34	3.48	3.65	0.96	0.20	0.02	2.01	7.37	11.64
SM-27	14.1	platy shale	5.65	3.60	3.20	1.23	0.07	0.02	1.31	4.40	11.00
SM-5	14.3	shale	9.85	2.91	1.15	0.19	0.23	0.02	0.22	5.34	43.90
SM-28	14.6	platy shale	4.27	3.30	1.64	0.35	0.03	0.02	0.98	37.71	12.25
SM-7	15.1	shale	4.16	1.74	5.61	0.95	0.29	0.04	2.64	70.37	25.78
SM-29	15.3	platy shale	3.80	2.50	5.01	1.08	0.08	0.03	3.74	64.87	24.15
SM-30	15.8	flaky shale	6.09	3.23	3.46	0.67	0.24	0.02	2.16	55.42	26.67
SM-31	16.2	flaky shale	3.18	3.95	3.82	0.71	0.06	0.03	2.68	13.04	10.47
SM-32	16.5	flaky shale	7.15	7.36	3.24	0.39	0.13	0.02	1.61	6.36	13.02
SM-10	17.1	shale	8.01	3.32	2.65	0.39	0.04	0.01	1.97	63.38	29.13
SM-33	17.2	med grey flaky	8.69	3.13	2.38	0.40	0.51	0.03	1.15	53.34	21.01
SM-34	17.5	platy shale	7.97	4.74	4.13	0.64	0.04	0.03	3.07	52.99	21.67
SM-35	17.6	micrite	ND	0.09	1.71	0.38	0.03	0.01	1.19	4.86	5.87
SM-12	17.8	shale	4.46	4.53	3.27	0.60	0.11	0.02	1.94	61.30	18.51
SM-36	18	dark micrite	2.37	1.50	5.59	1.54	0.09	0.03	3.29	42.94	46.11
SM-37	18.2	platy shale	6.07	4.83	2.54	0.49	0.08	0.02	1.24	6.50	10.69
SM-13	18.3	micrite	ND	1.92	1.34	0.71	0.17	0.01	0.25	1.25	2.80
SM-14	18.5	shale	6.35	2.34	1.47	0.27	0.04	0.01	0.98	31.24	25.65
SM-38	18.9	platy shale	6.02	1.37	0.84	0.23	0.02	0.02	0.39	17.15	11.56
SM-39	19.4	platy shale	3.04	2.28	1.74	0.47	0.02	0.02	1.12	11.58	10.35

SM-40	19.6	platy shale	3.60	6.72	8.00	1.53	0.08	0.05	6.10	39.21	10.64
SM-41	20.7	platy shale	6.11	3.08	4.13	1.05	0.05	0.03	2.93	100.0	19.06
SM-42	20.8	shale	4.69	4.18	2.26	0.77	0.10	0.05	1.03	7.19	37.88
SM-43	21.3	platy shale	5.08	3.83	3.09	1.41	0.07	0.04	1.08	9.46	21.82

Appendix D Detailed petrological logging in the field

Cow Close (CC) SD 908 622

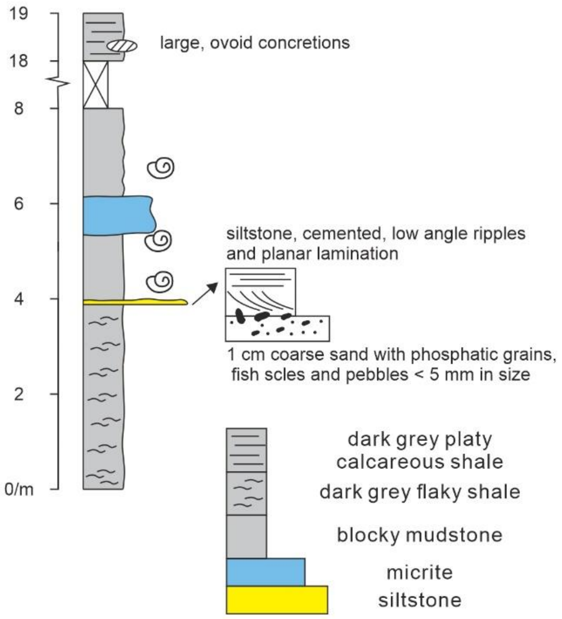

Clough Head Beck (CH) SD 822 438

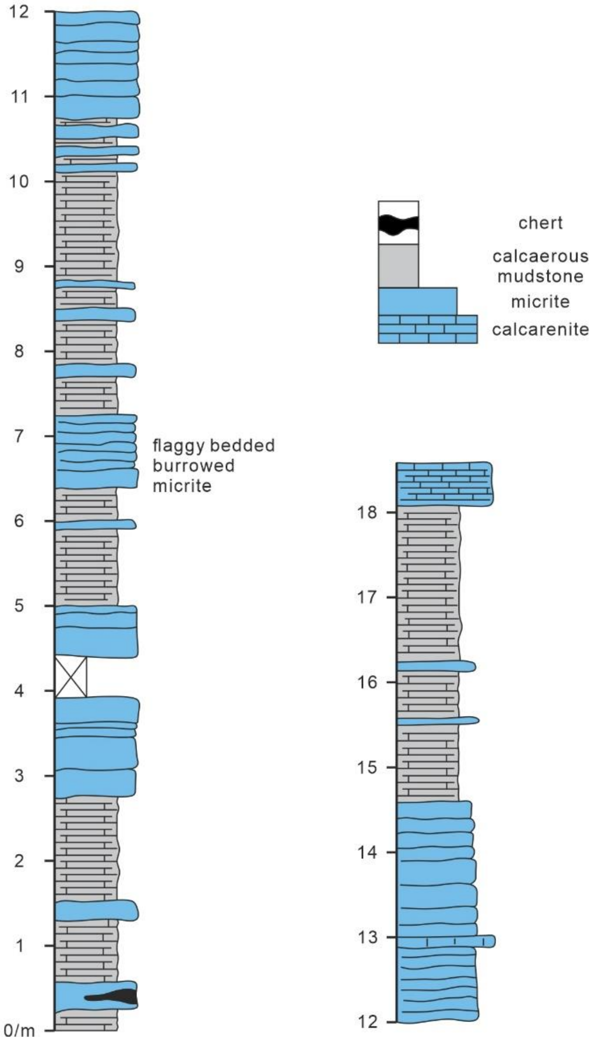

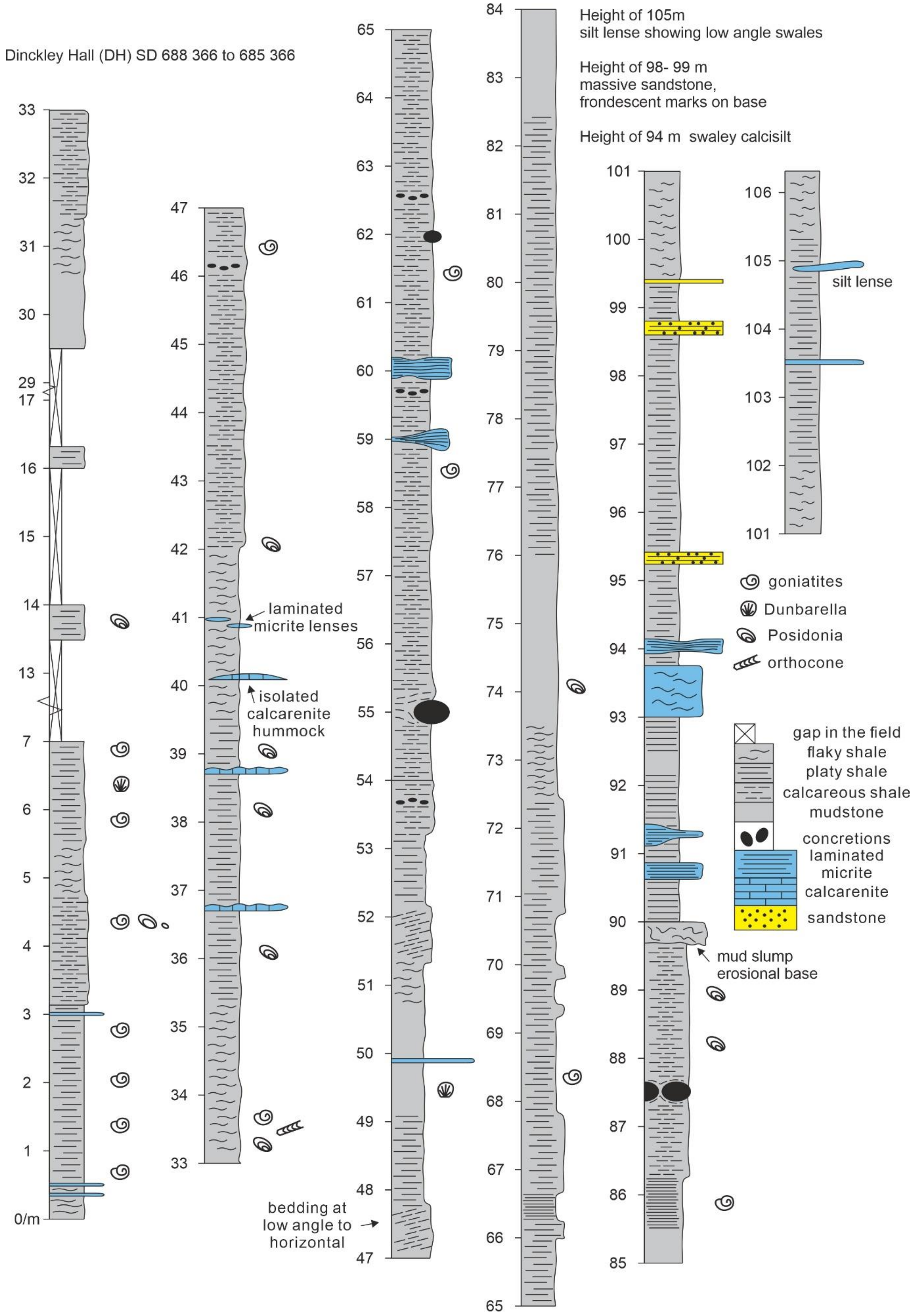
Dinckley Hall (DH) SD 688 366 to 685 366
0/m
1
2
3
4
5
6
7
13
14
15
16
17
29
30
31
32
33
33
34
35
36
37
38
39
40
41
42
43
44
45
46
47
laminated micrite lenses
isolated calcarenite hummock
47
48
49
50
51
52
53
54
55
56
57
58
59
60
61
62
63
64
65
bedding at low angle to horizontal
65
66
67
68
69
70
71
72
73
74
75
76
77
78
79
80
81
82
83
84
Height of 105m
silt lense showing low angle swales
Height of 98- 99 m
massive sandstone,
frondescent marks on base
Height of 94 m swaley calcisilt
85
86
87
88
89
90
91
92
93
94
95
96
97
98
99
100
101
mud slump
erosional base
101
102
103
104
105
106
silt lense
goniatites
Dunbarella
Posidonia
orthocone
gap in the field
flaky shale
platy shale
calcareous shale
mudstone
concretions
laminated micrite
calcarenite
sandstone

Dob Dale Beck (SF) SD 752 596 to 754 596

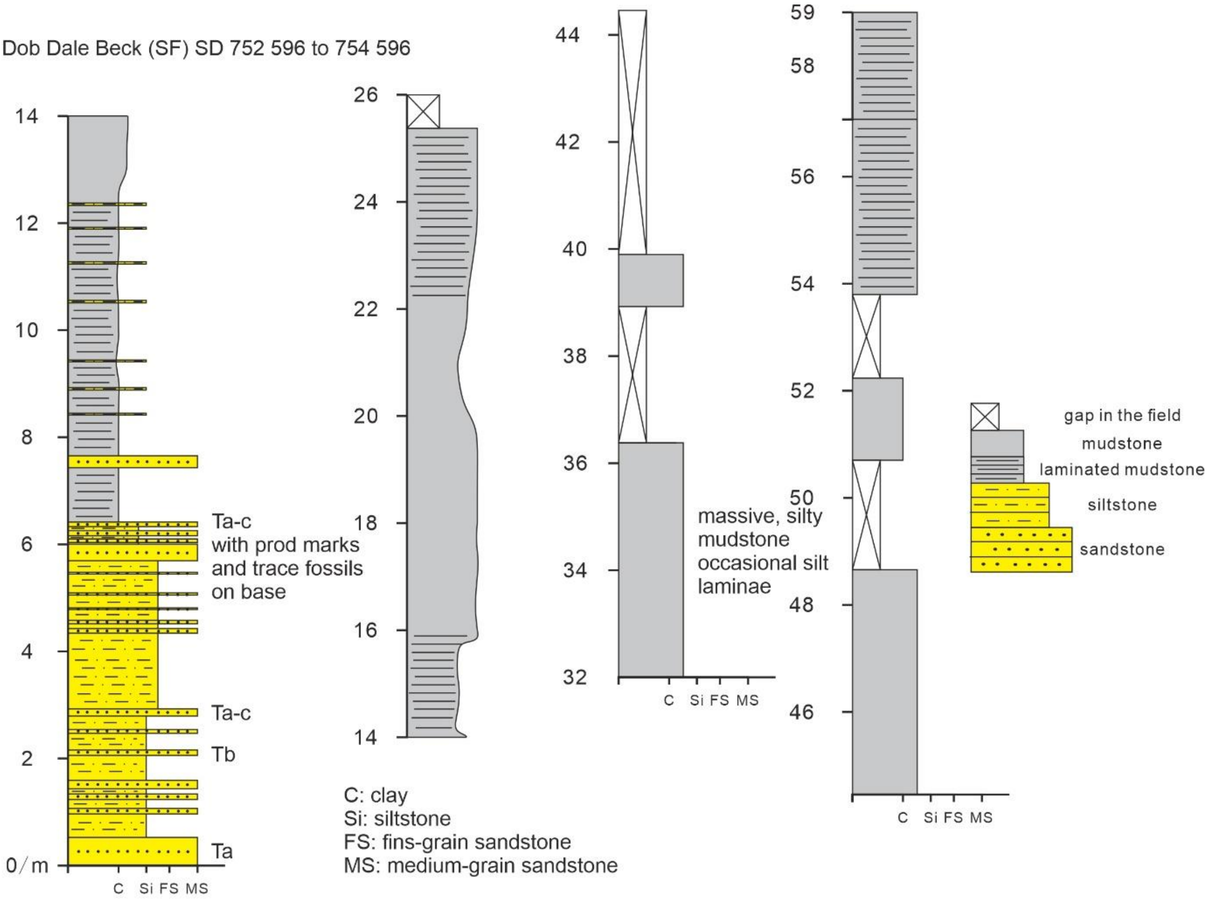

Dobson Brook (DB) SD 619 441

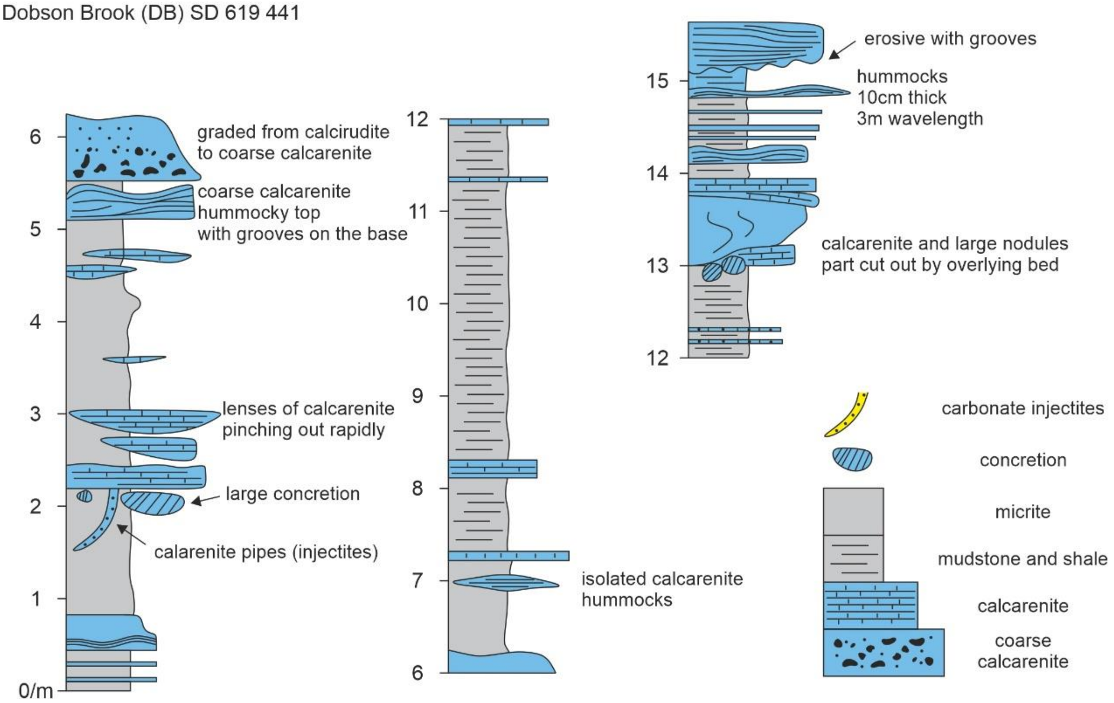

Fountain Fell (FF) SD 873 718

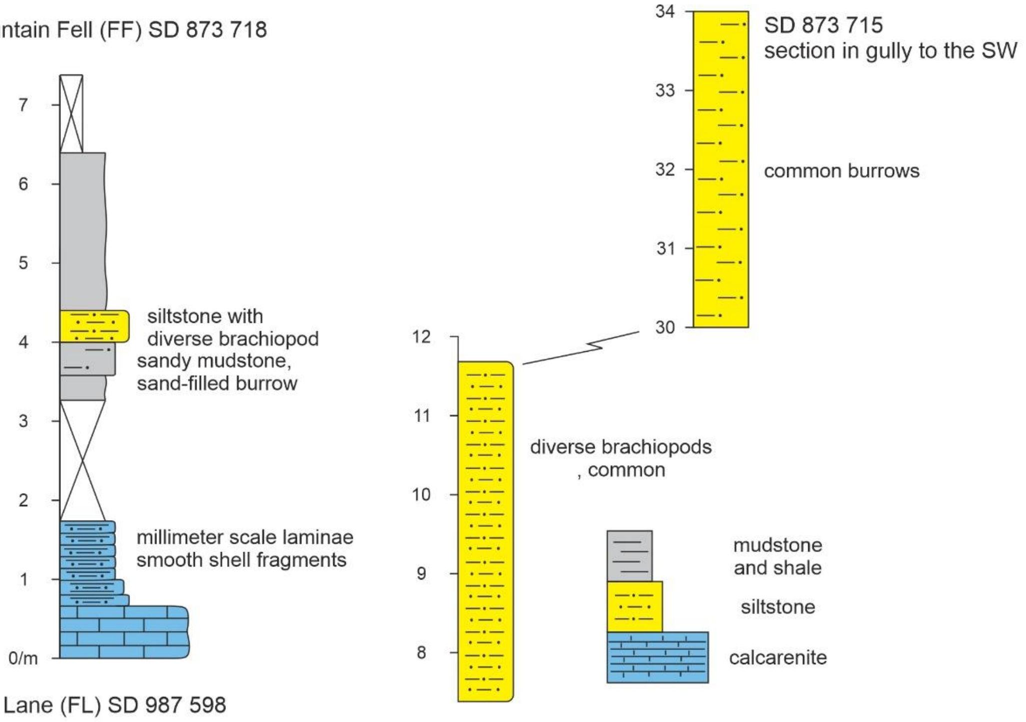

Fell Lane (FL) SD 987 598

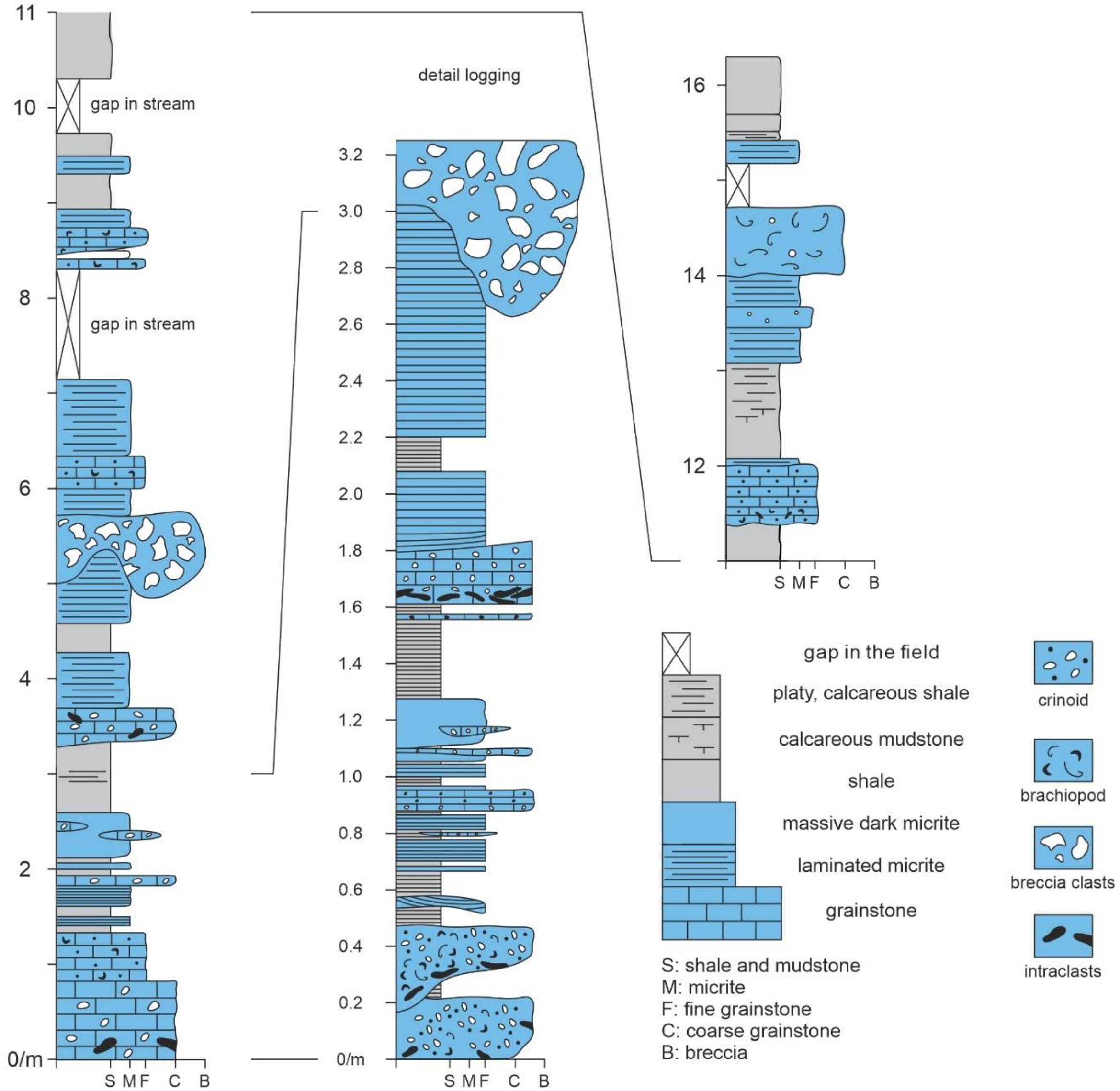

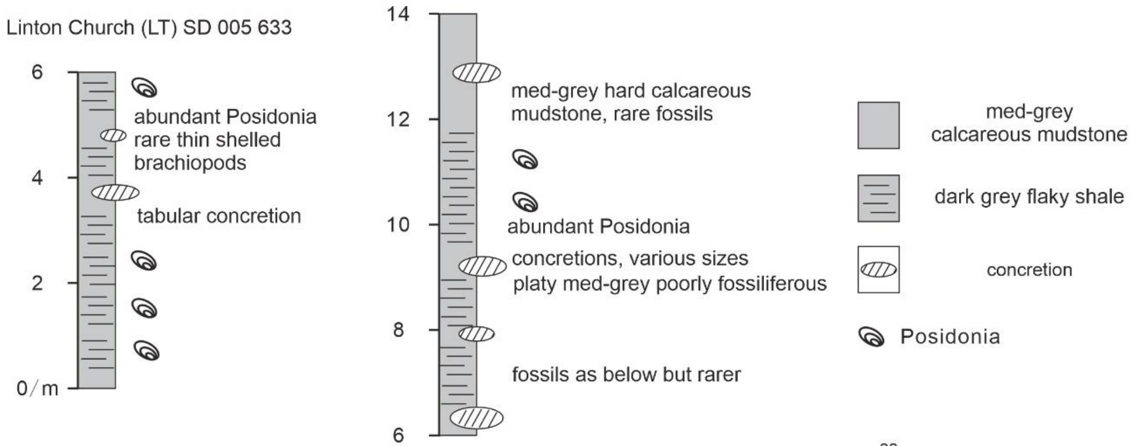
Linton Church (LT) SD 005 633

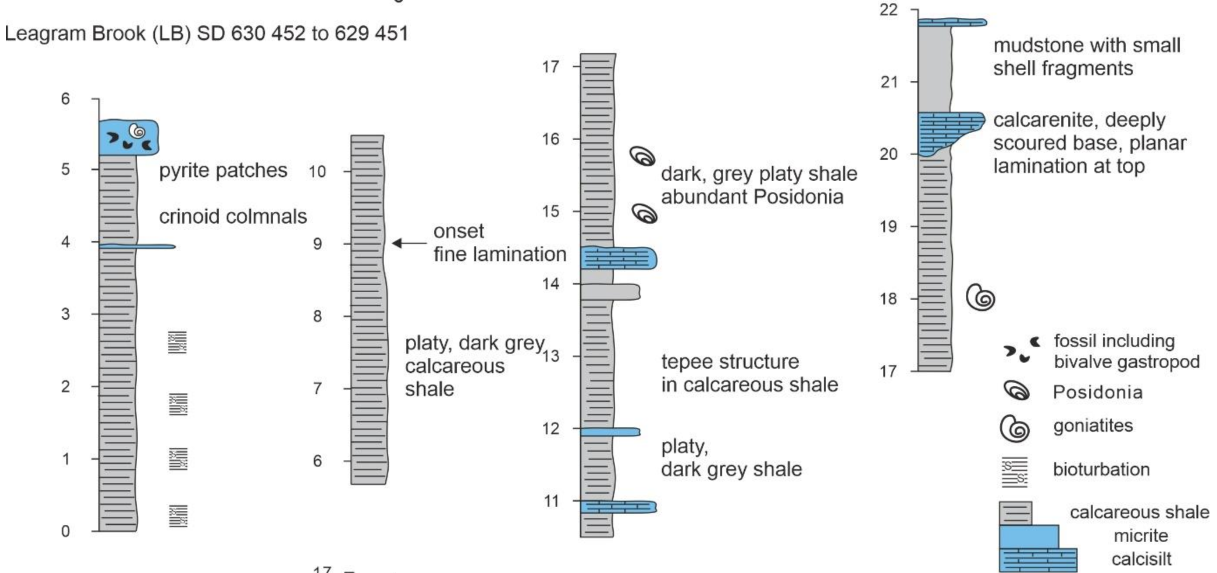
Leagram Brook (LB) SD 630 452 to 629 451

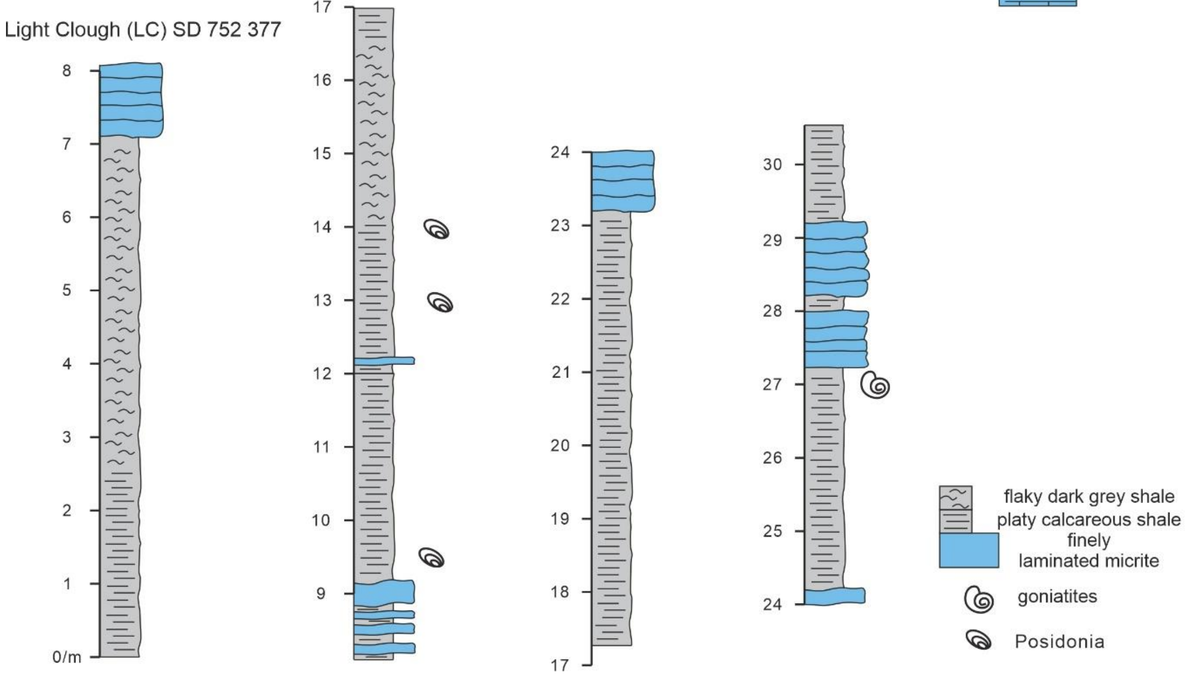
Light Clough (LC) SD 752 377

Moor Close Gill (MC) SD 933 639 to 935 640

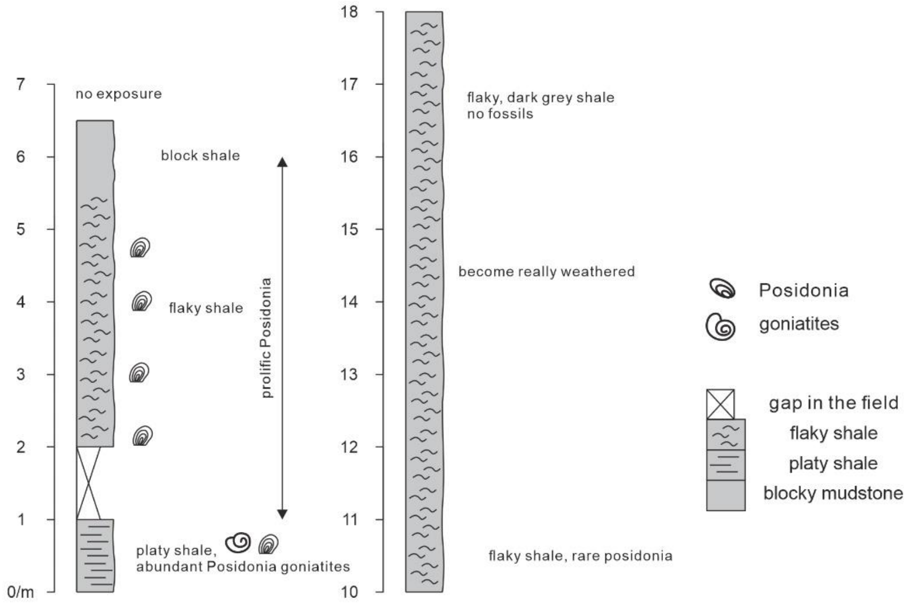

School Share (SS) SD 846 623

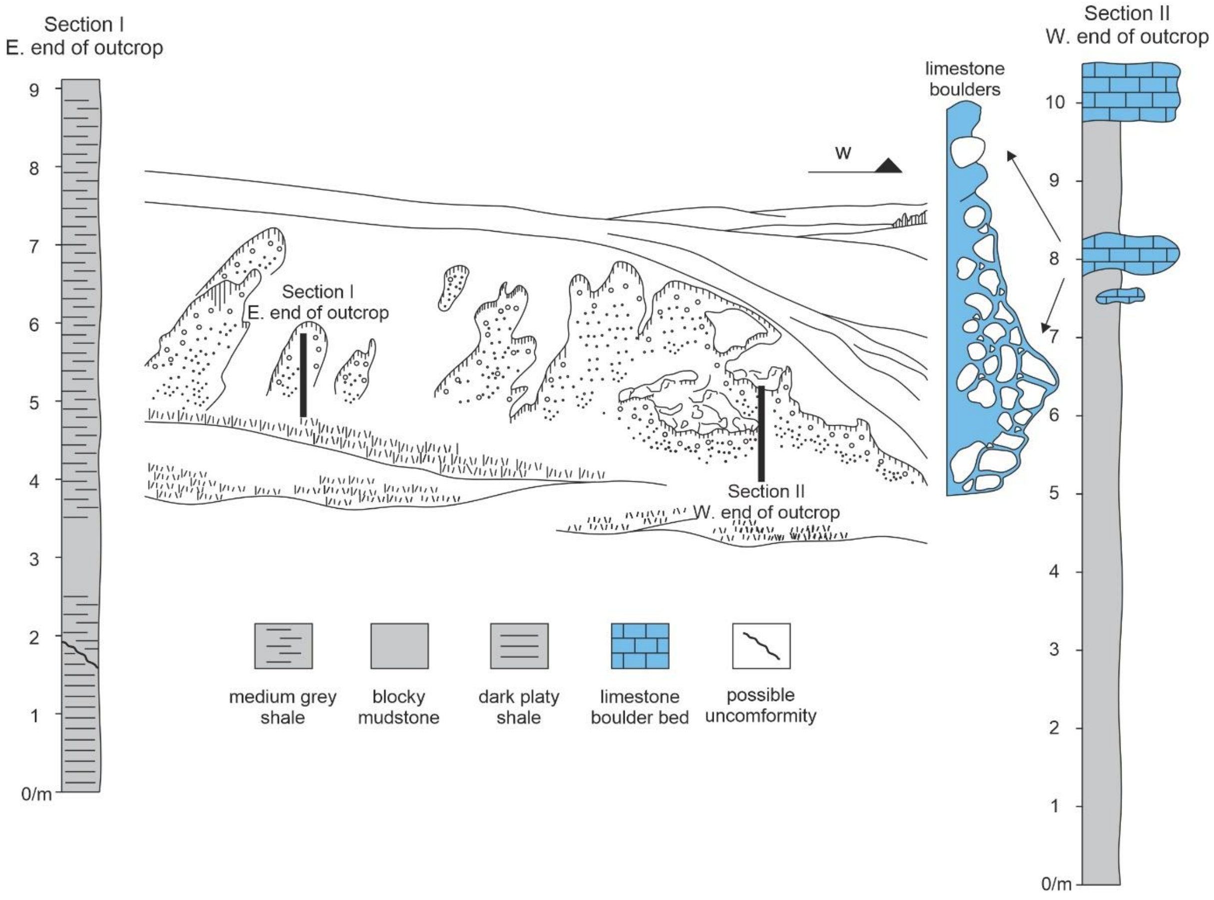

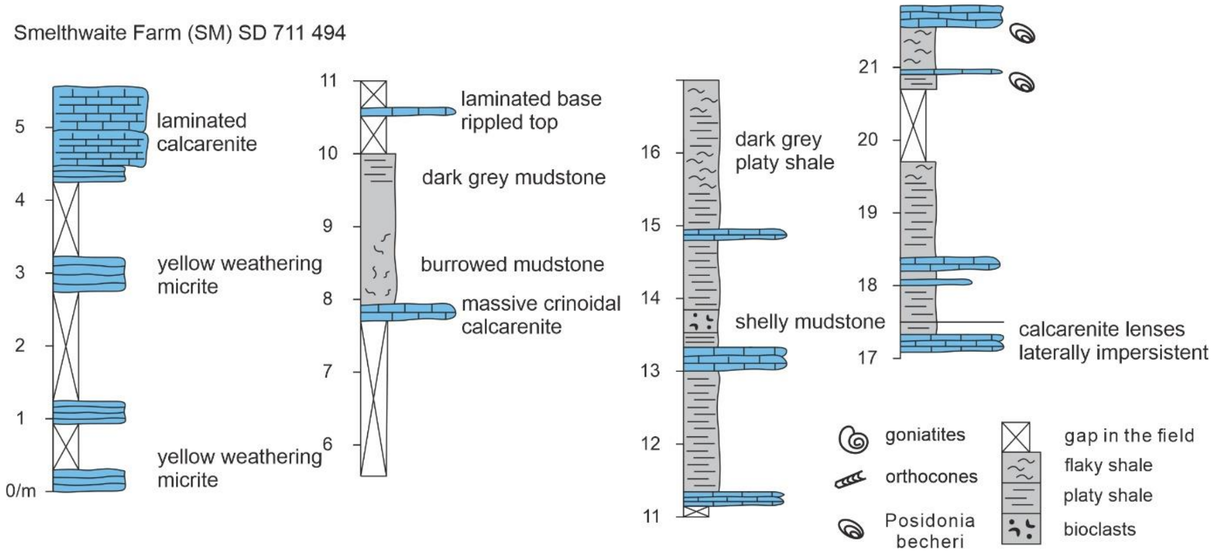
Smelthwaite Farm (SM) SD 711 494
0/m
1
2
3
4
5
laminated calcarenite
yellow weathering micrite
yellow weathering micrite
6
7
8
9
10
11
laminated base rippled top
dark grey mudstone
burrowed mudstone
massive crinoidal calcarenite
11
12
13
14
15
16
dark grey platy shale
shelly mudstone
17
18
19
20
21
calcarenite lenses laterally impersistent
goniatites
orthocones
Posidonia becheri
gap in the field
flaky shale
platy shale
bioclasts

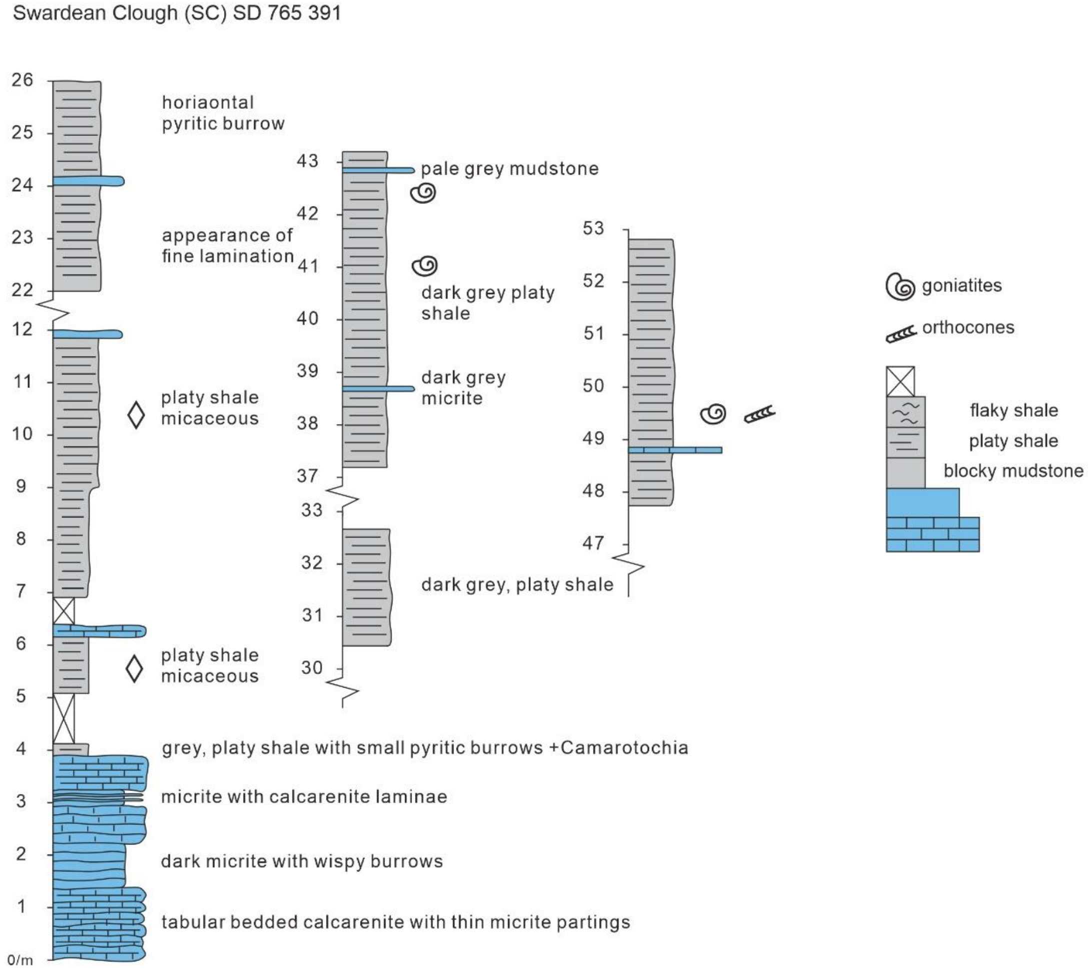
Swardean Clough (SC) SD 765 391
0/m
1
2
3
4
5
6
7
8
9
10
11
12
22
23
24
25
26
horiaontal pyritic burrow
appearance of fine lamination
platy shale micaceous
platy shale micaceous
grey, platy shale with small pyritic burrows +Camarotochia
micrite with calcarenite laminae
dark micrite with wispy burrows
tabular bedded calcarenite with thin micrite partings
30
31
32
33
37
38
39
40
41
42
43
pale grey mudstone
dark grey platy shale
dark grey micrite
dark grey, platy shale
47
48
49
50
51
52
53
goniatites
orthocones
flaky shale
platy shale
blocky mudstone

Tory Log Clough (TLC) section part 1 SD 833 447

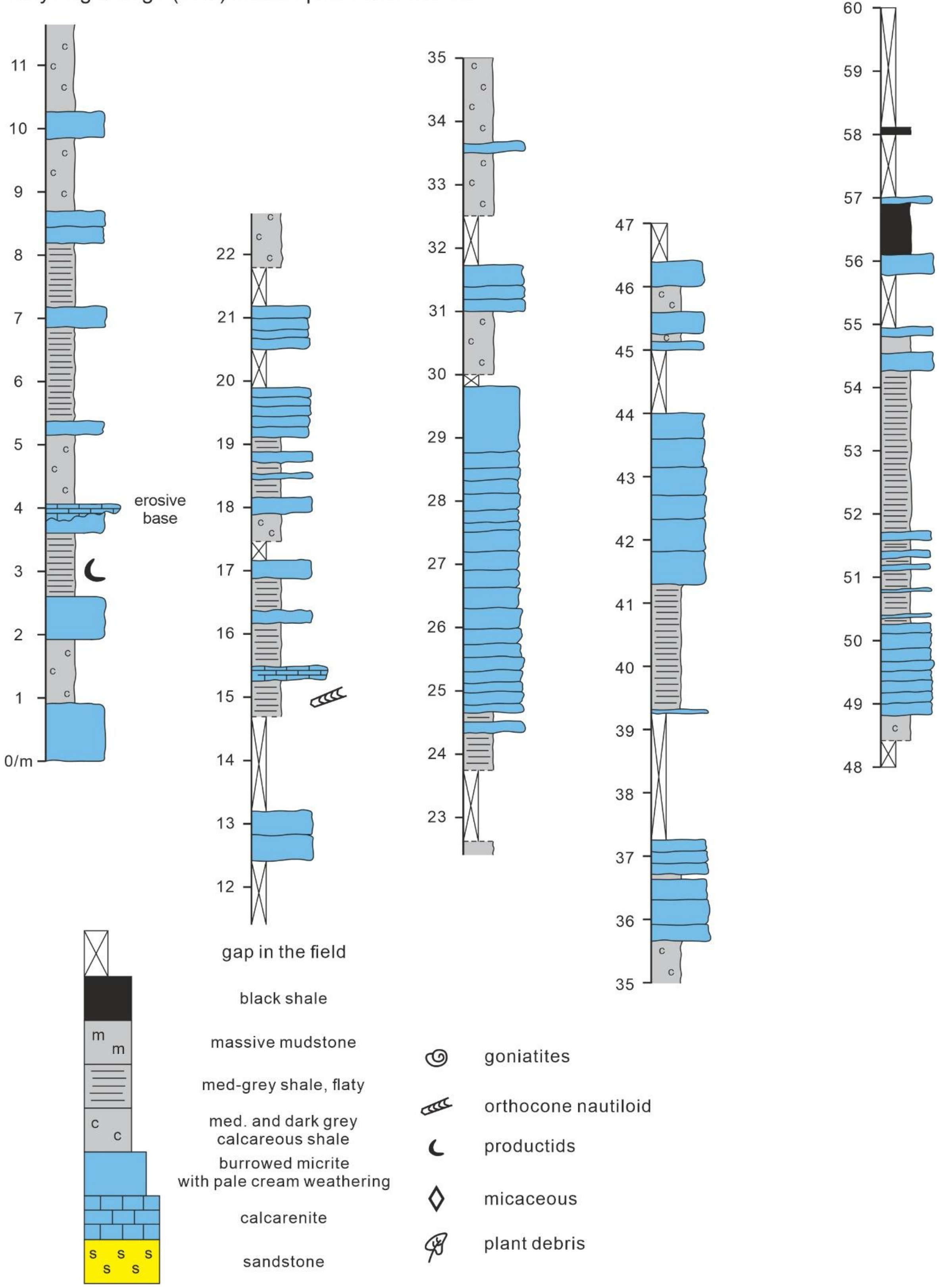

TLC section part 2 SD 833 447